Newcastle University
School of Engineering
Geotechnics and Structures

Investigating Sand Inelasticity and Breakage Alongside Its Role in Enhancing Rail Adhesion

A thesis submitted in fulfilment

of the requirements for the degree of

Doctor of Philosophy

Bin Zhang

Newcastle upon Tyne, UK

January 2025

Abstract

Understanding the strength of particles is essential for enhancing the efficiency, sustainability, and performance of applications involving their breakage. Despite valuable insights gained from extensive laboratory testing, a shared agreement on crushing strength estimation has yet to be achieved, as the geometric and material anisotropy, combined with inherent heterogeneity, pose significant challenges to the standardisation of testing methods.

This thesis aims to advance state-of-the-art research by developing a micro-scale computational framework to investigate the inelasticity and breakage behaviour of sand particles. The framework begins with image acquisition, where the morphology of natural sand particles is virtualised using micro-computed tomography. To simulate their mechanical response, a combined discrete-finite element method is employed to represent them as continuum bodies, while capturing fragment-to-fragment interactions during breakage. This integrated framework is referred to as the micro finite element (μFE) analysis.

Validation of the μFE model yields results that compare well with experimental data from the Brazilian tests and the single particle compression tests. The breakage behaviour of single particles is further examined through a point-loading test using spherical indenters with different radii. The actual contact area between particle and indenter normalised by its corresponding Hertzian area is found to be independent of indenter size, providing new insights into harmonising variations in crushing strength estimated using different indenters.

One application directly controlled by sand breakage is the adjustment of adhesion level at the wheel-rail interface. By reproducing the train operation environment, sand breakage under extreme load is studied, and its effect on adhesion enhancement, considering surface roughness and plastic deformation of the rail, is explored. It reveals the fact that adhesion enhancement is primarily influenced by the number of fragments at the wheel-rail interface, which is directly related to the newly generated surface area.

Acknowledgements

I would like to express my greatest gratitude to my supervisor, Dr. Sadegh Nadimi, for his unwavering support and guidance throughout this research. His encouragement and understanding during my struggles to balance research and family responsibilities have been invaluable. I would not have reached this point or written these words without his constant motivation and dedication. This thesis is a testament to his enthusiasm and mentorship.

I am deeply thankful to Prof. Mohamed Rouainia for his valuable internal collaboration, insightful comments, and constructive feedback, particularly on the work presented in Chapter 3. His expertise, guidance, and thoughtful discussions have significantly enhanced the depth and clarity of my research.

I also greatly appreciate the external collaboration with Dr. Budi Zhao from University College Dublin. His generosity in providing the particle scan images and experimental data formed the foundation for validating the micro finite element model discussed in Chapter 4.

My sincere thanks go to Prof. Roger Lewis from the University of Sheffield for his collaboration during the numerical simulation and experimental study of the sanding process in Chapter 5. His feedback, based on extensive experimental experience and practical knowledge, has been instrumental in refining this work to address the current research gaps, ensuring that the findings are both scientifically rigorous and practically relevant.

I am honored to have been part of the postgraduate research community in the Faculty of Science, Agriculture & Engineering at Newcastle University. My time there has been profoundly meaningful and rewarding. I would like to express my sincere gratitude to all academics, with special thanks to Dr. Chao Zhang for his support during the early stages of my research and Dr. Sadaf Maramizonouz for her assistance with code utilisation. My appreciation also extends to the laboratory technicians, Mr. Stuart Patterson, Mr. Gareth Wear, and Mr. Michael Finley, for their invaluable support during my demonstrations.

This journey would not have been possible without the financial support of the China Scholarship Council - Newcastle University Scholarships. I am deeply grateful for this opportunity and would like to once again express my heartfelt gratitude to Dr. Sadegh Nadimi for making this possible.

Lastly, I want to express my deepest gratitude to the most important people in my life. My wife, Sarentuya, has been my closest friend, partner, and advisor, providing unconditional love and support. My daughter, Nona, has brought immeasurable joy to my life and has taught me the true value of patience. To my parents, who have given me life and unwavering encouragement, thank you for your sacrifices and belief in me.

Thank you all.

Bin Zhang
Newcastle upon Tyne, UK
January 2025

Table of Contents

List of Figures

List of Tables

List of Symbols

a	Parameter used for estimating the compressive and tensile strength
A	Surface area of a particle
A_c	Contact area
A_{cs}	Cross-sectional area
b	Hardening parameter
C_i	Backstress modulus
d	Diameter of the Brazilian disc
$\bar{d}$	Average diameter of a particle
d_1	Longest dimension of a particle
d_2	Intermediate dimension of a particle
d_3	Loading distance / shortest dimension of a particle
d_a	Area equivalent circle diameter
d_i	Indentation depth
D	Damage scalar
D_{90}	90% of the particles are finer than this size
E	Young's modulus
F	Force
F_f	Fracture force
F_N	Normal force
F_T	Tangential force
G^c	Critical mixed-mode fracture energy
G_n	Mode I fracture energy
G_n^c	Critical mode I fracture energy

G_s Mode II fracture energy

G_s^c Critical mode II fracture energy

G_t Mode III fracture energy

k Coefficient used for calculating the tensile strength of flat-to-flat contact

k_n Normal stiffness

k_n^o Initial normal stiffness

k_s First shear stiffness

k_s^o Initial first shear stiffness

k_t Second shear stiffness

ℓ Evaluation length

m Weibull modulus

n Number of particles

N Total number of particles

P_s Survival probability

Q_∞ Saturation stress

r Radius of the equivalent volume sphere of a particle

R Radius of a sphere

R_1 Radius of an indenter

R_2 Half of the longest dimension of a particle

R_a Arithmetical mean height

R_{dq} Root mean square gradient

R_{ku} Kurtosis

R_q Root mean square height

R_{sk} Skewness

t	Thickness of the Brazilian disc
t_n	Nominal traction stress in the normal direction
t_n^0	Initial nominal traction stress in the normal direction
$\overline{t_n}$	Predicted nominal traction stress in the normal direction
t_s	Nominal traction stress in the shear direction
t_s^0	Initial nominal traction stress in the shear direction
$\overline{t_s}$	Predicted nominal traction stress in the shear direction
T	Threshold value
V	Volume of a particle
V_{CH}	Volume of convex hull
α	Angular distance of arch-to-arch and flat-to-flat contacts
α_i	Backstress
$\dot{\alpha}_i$	Backstress rate
β	Crack angle used in the crack extension test
γ_i	Dissipation rate parameter
δ_m	Effective displacement
δ_m^0	Initiation of crack effective displacement
δ_m^{max}	Maximum effective displacement
δ_m^{sep}	Completion of crack effective displacement
δ_n	Crack opening displacement
δ_n^o	Initiation of crack opening displacement
δ_n^{sep}	Completion of crack opening displacement
δ_s	Crack sliding displacement
δ_s^o	Initiation of crack sliding displacement

δ_s^{sep}	Completion of crack sliding displacement
$\bar{\varepsilon}_{pl}$	Equivalent plastic strain
η	Semi-empirical criterion exponent
θ	Fracture angle used in the crack extension test
θ_1	Angle used for estimating the compressive and tensile strength
μ	Friction coefficient
μ_a	Adhesion coefficient
$\Delta\mu_a$	Adhesion enhancement
ρ	Density
σ	Stress
σ_0	Characteristic tensile strength
σ_1	Maximum principal stress
σ_2	Intermediate principal stress
σ_c	Compressive strength
σ_t	Tensile strength
σ_v	Equivalent stress
σ_y	Yield stress
σ_{y0}	Initial yield stress
χ	Empirical parameter to consider heterogeneity
υ	Poisson's ratio

List of Abbreviations

1D	One dimension / one-dimensional
2D	Two dimensions / two-dimensional
3D	Three dimensions / three-dimensional
ASTM	American Society for Testing and Materials
CIE	Cohesive interface element
COH2D4	4-node two-dimensional cohesive interface element
CPE3	3-node linear plane strain triangle element
DEM	Discrete element method
DER	Dark etching regions
DIC	Digital image correlation
eCDF	Empirical cumulative distribution function
EBSD	Electron backscatter diffraction
FE	Finite element
FEM	Finite element method
HR-pQCT	High-resolution peripheral quantitative computed tomography
ISRM	International Society for Rock Mechanics
LBS	Leighton Buzzard Sand
MRI	Magnetic resonance imaging
OM	Optical microscopy
PAT	Photoacoustic tomography
PFC2d	Particle Flow Code in Two Dimensions
RSSB	Rail Safety and Standards Board
SEM	Scanning electron microscopy

SH	Spherical harmonics
XFEM	Extended finite element method
μCT	Micro-computed tomography
μFE	Micro-finite element

Publications

- **Zhang, B.**, Nadimi, S., Eissa, A. and Rouainia, M., 2023. Modelling fracturing process using cohesive interface elements: theoretical verification and experimental validation. *Construction and Building Materials*, **365**, p.130132. https://doi.org/10.1016/j.conbuildmat.2022.130132

- **Zhang, B.**, Nadimi, S. and Lewis, R., 2024. Modelling the adhesion enhancement induced by sand particle breakage at the wheel-rail interface. *Wear*, **538**, p.205232. https://doi.org/10.1016/j.wear.2023.205232

- **Zhang, B.**, Lewis, R. and Nadimi, S., 202X. Modelling the adhesion enhancement at the wheel-rail interface: the role of surface roughness and plastic deformation during rail sanding operation (submitted to *Railway Engineering Science*).

- **Zhang, B.** and Nadimi, S., 202X. Insights on particle breakage variability. *Géotechnique* (in preparation).

- **Zhang, B.**, Farhad, F., Oila, A., Joyce, T. J., Hashim, M., Akid, R., Withers, P. J. and Nadimi, S., 202X. Micro finite element analysis in engineering mechanics over the last three decades. *Journal of Engineering Mechanics* (in preparation).

Chapter 1 Introduction

1.1 Motivation and Background

The strength of individual particles plays a pivotal role in determining their mechanical response to loading and their ability to resist failure. Particle strength, as a fundamental property, is governed by intricate interactions between internal structural features and external forces. The inherent heterogeneity of particles, including variations in size, shape, and material composition, introduces significant variability in their strength. This variability makes it essential to establish a deeper understanding of the factors influencing particle strength and to develop systematic approaches for studying this critical property across different scales.

In the case of sand particles, significant advancements have been made in understanding particle strength through laboratory testing and numerical simulation (McDowell and Bolton, 1998; Nakata *et al.*, 2001; Coop *et al.*, 2004; Tang *et al.*, 2004; Russell and Muir Wood, 2009; Cavarretta and O'Sullivan, 2012; Zhao *et al.*, 2015; Zhang *et al.*, 2020; Zhou *et al.*, 2020; Wei *et al.*, 2022; Liu *et al.*, 2023). Inspired by the Brazilian test (Fairhurst, 1964), traditional compression tests using flat platens have been employed to investigate the tensile strength of sand particles. These tests have highlighted differences in results when considering particle shape effects in one dimension (1D) and two dimensions (2D) (Hiramatsu and Oka, 1966; Lee, 1992; Cavarretta *et al.*, 2017). With the advent of micro-computed tomography (μCT), the failure modes of sand particles have been explored in greater detail, revealing intricate relationships with tensile strength and providing deeper insights into breakage mechanisms (Wang and Coop, 2016). Furthermore, a point load apparatus was introduced to examine the influence of loading conditions on particle breakage, resulting in more consistent tensile strength measurements by reducing the effect of particle shape. However, point load tests present practical challenges, including point-to-particle contact and frequent replacement of loading apparatuses (Wang and Coop, 2018).

Numerical simulations have emerged as a powerful tool to overcome these experimental limitations. To achieve a more accurate representation of sand particles, micro-finite element (μFE) analysis incorporating μCT-derived morphology has been utilised to provide detailed insights into stress transmission within sand particles (Nadimi and Fonseca, 2018a). By coupling cohesive interface elements (CIEs), μFE models enable the investigation of sand particle breakage under rotational point

loading (Wei *et al.*, 2019). This approach demonstrates that traditional compression tests with flat platens tend to overestimate tensile strength, though no universally recommended test method has yet been established.

While progress in understanding the breakage mechanisms of sand particles continues, their practical application in the railway industry underscores the significance of this research. Sand particles, deployed from onboard devices, are widely used to mitigate low adhesion at the wheel-rail interface caused by wet weather, surface contamination, and variations in rail and wheel conditions (Broster *et al.*, 1974; Beagley *et al.*, 1975; Wang *et al.*, 2011; Tao *et al.*, 2020). Experimental investigations at various scales, including twin-disc setups, full-scale rigs, and field tests, have explored the role of sand particles in restoring adhesion and removing leaf layers (Skipper *et al.*, 2018). Beyond sand particles, factors such as rail surface roughness (Wang *et al.*, 2023) and rail plastic deformation (Zhao and Li, 2015) have also been studied for their effects on adhesion. However, comprehensive studies integrating the combined effects of sand particles, rail surface roughness, and plastic deformation are still lacking, leaving a critical gap in understanding their collective impact on adhesion.

1.2 Aim and Objectives

This thesis aims to advance the understanding of sand particle breakage behaviour, with particular attention to the influence of particle morphology, contact curvature, and loading conditions. Rather than focusing solely on particle strength, the work investigates how different loading configurations, specifically point load and compression tests, influence fracture initiation and propagation in granular materials. A key objective is to bridge the gap between these testing methods and to provide new insights into the estimation of tensile strength, which has long been a challenge in laboratory studies of granular systems.

To achieve this, a μFE model coupled with CIEs is proposed to investigate the breakage behaviour of sand particles under varying contact curvatures. The model is carefully calibrated and validated to ensure reliability and accuracy. A comprehensive relationship between particle morphology, contact curvature, contact area, and fracture load is established across different tested samples. Building on this, a new method is proposed to estimate tensile strength, providing more consistent values across different contact curvatures.

To expand the application of the developed μFE model and deepen the understanding of particle breakage in real-world scenarios, the breakage mechanism

of particles and the distribution of their fragments over the rail during the sanding process is investigated using boundary conditions that replicate train traction and braking operations. By incorporating rail surface roughness and plastic deformation data, the study quantitatively examines the adhesion enhancement caused by sand breakage at the wheel-rail interface, an aspect that has not been explored numerically before. The insights gained here could help optimise the sanding process and contribute to safer train operations, which is difficult to achieve through experimental testing alone.

The main objectives of this thesis are as below:

- **O_1:** To conduct a state-of-the-art review of μFE analysis in engineering mechanics, understand the fundamental steps involved in μFE analysis, and identify its advancements, limitations, and the latest techniques to address these limitations.
- **O_2:** To verify the breakage model theoretically against crack extension tests and validate the breakage model experimentally against the Brazilian test. To explore the breakage mechanisms associated with different contact topologies on single particles.
- **O_3:** To analyse how contact curvatures impact the breakage behaviour of individual particles through point load tests. To propose a new method for better estimating tensile strength, accounting for variations in particle morphology and contact curvature.
- **O_4:** To examine the breakage mechanisms of sand particles and their fragment distribution on the rail surface. To investigate the adhesion enhancement caused by particle breakage, considering the effects of rail surface roughness and plastic deformation.

1.3 Outline of Thesis

This thesis consists of six chapters and four appendices in total. The current section is part of Chapter 1, which introduces the background and motivation of the research, the aims and objectives, the thesis outline, and the research contributions from each chapter. Chapters 2 through 5 each focus on a specific aspect of the thesis, beginning with a background review relevant to that topic. Drawing on the key findings from these chapters, Chapter 6 concludes the thesis and offers suggestions for future studies that could extend this research.

Below is a brief summary of the content covered in the main chapters and

appendices:

Chapter 2 provides a state-of-the-art review of μFE analysis in engineering mechanics, which forms the foundation for developing a framework utilising the μFE model to address the research objectives. This chapter begins with the evolution of μFE analysis in biomedical research and introduces the fundamental steps involved, including image preparation, mesh generation, model setup, calibration and validation. Applications in various fields such as orthopaedics, dental research, implant design, material science, granular materials, industrial manufacturing, structural engineering, and corrosion science are reviewed to provide deeper insights into the progress and challenges of μFE analysis, paving the foundation for the framework development in subsequent chapters.

Chapter 3 develops a μFE model to simulate particle breakage using CIEs. The model is refined through a mesh sensitivity study to achieve a balance between computational efficiency and accuracy. Crack initiation and propagation are validated through crack extension tests and cohesive zone analysis. A parametric study is conducted to calibrate the CIE parameters. For further validation, three different contact topologies from the Brazilian test, referred to as point-to-point, arch-to-arch, and flat-to-flat contacts, are numerically reproduced. Load-strain curves, strain distribution, crack initiation and propagation, and tensile strength are compared across topologies. Recommendations are made for a contact topology that better estimates tensile strength.

Chapter 4 numerically reproduces the point loading test using rigid indenters of varying radii. The influence of contact curvature on particle breakage behaviour is analysed. A new equation is proposed to estimate tensile strength independently of contact curvature while accounting for particle morphology. This improved estimation is verified using the Weibull distribution. A fracture mode analysis is performed based on the volume of child fragments. Morphological parameters of child fragments are compared to those of parent particles to investigate the impact of contact curvature on fragment formation. Additionally, two in-house MATLAB codes are developed: one for three-dimensional (3D) CIEs embedment and another for fragment analysis.

Chapter 5 examines the breakage mechanisms of sand particles and their fragment distribution on the rail. To evaluate the effect of particle morphology on adhesion, a smooth wheel-rail interface is employed to minimise the influence of surface irregularities. This approach isolates the specific impact of particle size and shape on adhesion levels before and after fragmentation. The model is subsequently enhanced

by incorporating rail roughness and plastic deformation to create a more realistic representation of the wheel-rail interface, providing deeper insights into associated adhesion enhancement. Furthermore, this methodology is extended to 3D simulations to facilitate future studies.

Appendix A presents key algorithmic implementations for embedding 3D CIEs, with inline comments to enhance understanding.

Appendix B contains the main function of the fragment analysis code, enabling the capture of individual fragments and mass loss.

Appendix C displays 21 silica sand and 21 crushed glass samples reconstructed from μCT images, along with their morphology parameters.

Appendix D lists 37 representative rail surface profiles with their roughness descriptors.

1.4 Contributions

This section outlines the contributions of the candidate to each chapter and the corresponding published or submitted works, where applicable, along with the contributions of the main supervisor, Dr. Nadimi, as well as collaborators, Prof. Rouainia from Newcastle University and Prof. Lewis from the University of Sheffield.

In Chapter 2, the candidate critically reviewed μFE applications across various fields, summarised the fundamental setup of the μFE model, and discussed its advantages and limitations. Dr. Nadimi reviewed this work and provided feedback on potential improvements. The corresponding manuscript is currently under review by external co-authors for submission to the *Journal of Engineering Mechanics*.

In Chapter 3, the candidate proposed a μFE model coupled with CIEs to investigate particle breakage and calibrated the model using mesh sensitivity analysis, crack extension tests, and parametric studies. The candidate also validated the model against the Brazilian test by reproducing different contact topologies. Dr. Nadimi and Prof. Rouainia provided guidance throughout the process and reviewed the accompanying manuscript, which has been published in *Construction and Building Materials* (Zhang *et al.*, 2023).

In Chapter 4, the candidate developed a MATLAB code for embedding 3D CIEs, allowing the proposed μFE model to simulate particle breakage in 3D. To examine the effect of contact curvature on tensile strength, the candidate numerically reproduced the point loading test using loading balls with varying radii. Additionally, the candidate created a MATLAB code for fragment analysis, enabling the capture of individual

fragments throughout the simulation. Dr. Nadimi facilitated collaboration with Dr. Zhao from University College Dublin, who provided μCT images of Leighton Buzzard Sand (LBS) for model validation. Dr. Nadimi also provided feedback during the early stages of code development and reviewed the work. The accompanying manuscript is currently under Dr. Nadimi's review for submission to *Géotechnique*.

In Chapter 5, the candidate extended the μFE model to investigate the breakage mechanisms of sand particles and their fragment distribution on the rail, incorporating rail surface roughness and plastic deformation, to better understand adhesion enhancement at the wheel-rail interface. Dr. Nadimi and Prof. Lewis provided feedback throughout the process and reviewed the accompanying manuscripts. Following a presentation at the 12th International Conference on Contact Mechanics and Wear of Rail/Wheel Systems (CM 2022) in Melbourne, Australia, a paper (Zhang *et al.*, 2024) was published by invitation in the special issue of *Wear*. Another manuscript, which examines the impact of rail roughness and plastic deformation, has been submitted to *Railway Engineering Science* and is under review.

Chapter 2 The Evolution of Micro Finite Element Analysis in Engineering Mechanics

2.1 Introduction

The finite element method (FEM) has been a foundational tool in numerical modelling, offering solutions to complex problems in engineering and science. Despite its versatility, the accurate representation of geometric and material anisotropy, along with heterogeneity, remains a significant challenge. To consider these, the μFE analysis was developed, integrating high-resolution μCT to investigate engineering behaviour at the microscale.

Originally introduced in orthopaedic research to study trabecular bone (van Rietbergen *et al.*, 1995), μFE analysis has since evolved into a powerful tool applied across diverse fields, including dental research, implant design, material science, granular materials, industrial manufacturing, structural engineering, and corrosion science. By bridging microstructural details and macroscopic behaviours, μFE analysis has opened new avenues for understanding and solving engineering and scientific problems.

The goal of this chapter is to critically review the methodology and applications of μFE analysis, with a primary focus on its use in medical research and an exploration of its growing role in other fields. This review aims to summarise current advancements, identify methodological trends, and evaluate the strengths and limitations of μFE analysis. The insights gained from this review will inform the development of a μFE-based breakage model in the following chapters, where the mechanical behaviour of particles under different loading conditions will be investigated.

2.2 Background

In 1972, about fifteen years after the FEM revolutionised stress analysis in engineering mechanics, Brekelmans *et al.* (1972) employed this method for analysing the mechanical behaviour of skeletal parts within the orthopaedic literature. Since then, it has facilitated data evaluation and parametric studies across experiments. Additionally, it predicts hard-to-measure variables and provides a framework for numerical experimentation that closely mirrors lab-based studies in orthopaedic research (Huiskes and Chao, 1983; Huiskes and Hollister, 1993). However, these early implementations lacked the microstructural detail needed to accurately model trabecular bone, missing localized mechanical behaviour and microscale elastic

properties, which led to less precise predictions of bone strength and load response (Fyhrie, 1992; Hollister *et al.*, 1994; van Rietbergen *et al.*, 1995).

The μFE method was first introduced as a solution to address these limitations. Bert van Rietbergen and his colleagues (van Rietbergen *et al.*, 1995) were among the pioneers in applying the μFE model to trabecular bone analysis. Their landmark studies in the 1990s demonstrated how μFE analysis, when combined with high-resolution μCT, could accurately capture the microstructural architecture of trabecular bone and simulate its mechanical behaviour under load (van Rietbergen *et al.*, 1995; Rietbergen, 1996; Ulrich *et al.*, 1998; Van Rietbergen, Majumdar, *et al.*, 1998; Van Rietbergen, Odgaard, *et al.*, 1998; Van Rietbergen *et al.*, 1999). This approach allowed for more accurate predictions of localized stress distributions and mechanical properties, setting the foundation for the μFE method as a critical tool in biomechanics and orthopaedic research.

Since the concepts and frameworks of FEM have been well developed over the past several decades, developments of the μFE method mainly laid out two parts regarding image-based mesh reconstruction. The first development is the techniques to capture high-resolution images. The images used in the early study can only provide a typical voxel size of 50μm using μCT (Hollister *et al.*, 1994), but now the resolution can achieve up to 0.1μm (Withers *et al.*, 2021), which has tremendously improved the quality of images and therefore the mechanical prediction based on the reconstructed mesh becomes more accurate. Meanwhile, advancements in imaging technologies have enabled a transition from ex vivo imaging, which was previously limited to laboratory settings, to capturing high-quality in vivo images. This progress now supports clinical monitoring and longitudinal studies, providing non-invasive, real-time insights into biological structures within living organisms. (Boutroy *et al.*, 2008; Vilayphiou *et al.*, 2010, 2011; Christen *et al.*, 2013; Cheuk *et al.*, 2015). The second development is on mesh reconstruction. The voxel conversion approach is one of the most commonly used methods in orthopaedic research. It converts voxels representing bone tissue into equally sized brick elements, while voxels representing bone marrow are ignored. As a result, the generated FE model consists of millions of elements, each matching the voxel size in the μCT images. This FE model is therefore referred to as the μFE model (van Rietbergen, 2001; van Rietbergen and Ito, 2015).

With the advancement of μFE analysis, this method has been increasingly adopted to address practical mechanical problems at the microscale, yielding effective solutions across various disciplines. In orthopaedic research, the μFE method has been

employed to investigate bone strength (Newitt *et al.*, 2002; Pistoia *et al.*, 2002; Verhulp *et al.*, 2006, 2008; Hazrati Marangalou *et al.*, 2012; Zhang *et al.*, 2013; Christen *et al.*, 2014; Tang *et al.*, 2014; Wen *et al.*, 2016; Rieger *et al.*, 2018; Knowles *et al.*, 2019; Stipsitz *et al.*, 2021; Guha *et al.*, 2022) and its variations due to diseases (Hansen, Brixen, *et al.*, 2012; Stein *et al.*, 2013; Chen *et al.*, 2014; Arias-Moreno *et al.*, 2016; Costa *et al.*, 2020), treatments (Burghardt *et al.*, 2010; Macdonald *et al.*, 2011; Hansen, Hauge, *et al.*, 2012; Rizzoli *et al.*, 2012; Hansen *et al.*, 2013), physical activity (Schipilow *et al.*, 2013; Synek and Pahr, 2018), and growth (Chevalley *et al.*, 2012; Farr *et al.*, 2014; Griesbach *et al.*, 2024). In dental research, it has been utilized to study tooth conditions (Chen *et al.*, 2012; Chang *et al.*, 2014; Ortún-Terrazas *et al.*, 2018; Wan *et al.*, 2022), and the effect of disease treatments (Magne, 2007; Della Bona *et al.*, 2013; Shahrbaf *et al.*, 2013; Silva *et al.*, 2015; Allen *et al.*, 2018; Cen *et al.*, 2018; Chang *et al.*, 2018; Aslan *et al.*, 2021; Smoljan *et al.*, 2021; Mert Eren *et al.*, 2023; Rahmatian *et al.*, 2023). In implant research, the μFE method has been used to explore implant stability (Chevalier *et al.*, 2021; Zupancic Cepic *et al.*, 2022; Epifania *et al.*, 2023), mechanical behaviour (Lin *et al.*, 2010; Frisardi *et al.*, 2012; Ren *et al.*, 2012; Williams and McCullough, 2016; Marcián *et al.*, 2018, 2021; Ovesy *et al.*, 2019; Syed *et al.*, 2021), and the effects on surrounding tissues and structures (Limbert *et al.*, 2010; Lee *et al.*, 2014; MacGinnis *et al.*, 2014; Moon *et al.*, 2015; Chevalier *et al.*, 2016; Jin *et al.*, 2020; Su *et al.*, 2021; Akhlaghi *et al.*, 2023). For porous materials, it has been applied to examine mechanical performance (Maire *et al.*, 2003; Youssef *et al.*, 2005; Aziz *et al.*, 2006; Lacroix *et al.*, 2006; Tsafnat *et al.*, 2008, 2009, 2011; Veyhl *et al.*, 2011; Lin *et al.*, 2014; Tagliabue *et al.*, 2017; Boniotti *et al.*, 2019; Lei *et al.*, 2019; Farina *et al.*, 2021; Hu *et al.*, 2021; D'Andrea *et al.*, 2022), deformation and breakage behaviours (Singh *et al.*, 2010; Basista *et al.*, 2017; Wang *et al.*, 2018; Patel *et al.*, 2019; Ai *et al.*, 2021), and fluid flow permeability (Gunde *et al.*, 2010; Zhang *et al.*, 2019). In granular material research, the μFE method has provided insights into the effects of particle morphology (Zhao and Wang, 2016; S. Nadimi and Fonseca, 2017; Kim and Yun, 2018; Fei *et al.*, 2019), breakage behaviour (Zhao *et al.*, 2015; Ma *et al.*, 2017; Imseeh and Alshibli, 2018; Wei *et al.*, 2019, 2022b; Zhou *et al.*, 2020; Lin *et al.*, 2023), and constitutive behaviour (Nadimi *et al.*, 2020; Nadimi and Fonseca, 2019; Fonseca *et al.*, 2019, 2012; Nadimi *et al.*, 2015; Chen *et al.*, 2021; Thakur and Penumadu, 2020; Nadimi and Fonseca, 2018b, 2018a). Generally, some key features and properties of the μFE method identified to date include:

- μFE analysis allows for detailed modelling of complex structures at the microscale, incorporating high-resolution imaging data such as μCT scans to capture complicated geometries.
- This method effectively accounts for the heterogeneous nature of materials, enabling the accurate simulation of localised mechanical responses within structures.
- It provides robust predictive insights into mechanical performance, such as stress-strain relationships, crack initiation and propagation, and failure points under various loading conditions.
- μFE method can couple mechanical, thermal, and fluid interactions, enabling the study of complex material behaviours in multidisciplinary applications.
- It enables precise quantification of material properties, such as stiffness, strength, and porosity, directly from microscale structures.
- While computationally intensive, advancements in software and hardware have improved its efficiency, allowing for faster analysis of large datasets.
- Widely applied in orthopaedics, dental research, material science, and engineering, it provides solutions to practical problems like bone strength assessment, implant design, and granular material behaviour.
- μFE models are often validated against experimental results, enhancing their reliability and applicability in real-world scenarios.

In this chapter, the μFE analysis is comprehensively reviewed, covering both its methodology and applications. The structure of the paper is as follows: Section 2.3 introduces the fundamental steps of the μFE method; Section 2.4 explores its major applications across a range of problems; Section 2.5 discusses the primary limitations of the μFE model. Finally, Section 2.6 concludes the review with key remarks.

2.3 Fundamental Steps

Since the key strength of the μFE analysis lies in its ability to computationally represent real-world objects with greater accuracy, it creates a seamless pathway from laboratory tests to numerical simulations. To ensure the digital object is representative and the computational result is reliable, four steps are generally applicable across different disciplines: 1) image preparation, 2) mesh generation, 3) model setup, and 4) calibration and validation.

2.3.1 Image Preparation

The image preparation is a critical step that involves image acquisition and image processing to ensure high-quality data for analysis. Image acquisition focuses on capturing visual information using techniques such as μCT, High-resolution peripheral quantitative computed tomography (HR-pQCT), or Magnetic Resonance Imaging (MRI), according to the specific requirements of the study. Following acquisition, image processing techniques are applied to enhance the quality and extract meaningful features. This includes steps like noise reduction, contrast adjustment, and segmentation to isolate regions of interest. Together, a robust foundation can be created for accurate analyses in subsequent stages of the workflow.

Image Acquisition

The microstructure, especially the internal structure and morphological features, of an object plays a critical role in determining its mechanical and physical properties and behaviours. However, two-dimensional (2D) imaging methods are limited in providing spatial information about the structure being examined. On the other hand, three-dimensional (3D) imaging offers insights into the volume, shape, and pore distribution. Commonly used 3D imaging techniques, including confocal optical microscopy (OM), MRI, scanning electron microscopy (SEM), 3D photoacoustic tomography (PAT), μCT, electron tomography, and neutron tomography, are listed in Figure 2.1 and compared in terms of acquisition cost, operational cost, resolution, measurement time, sample size adaptability, and information depth (Vásárhelyi *et al.*, 2020).

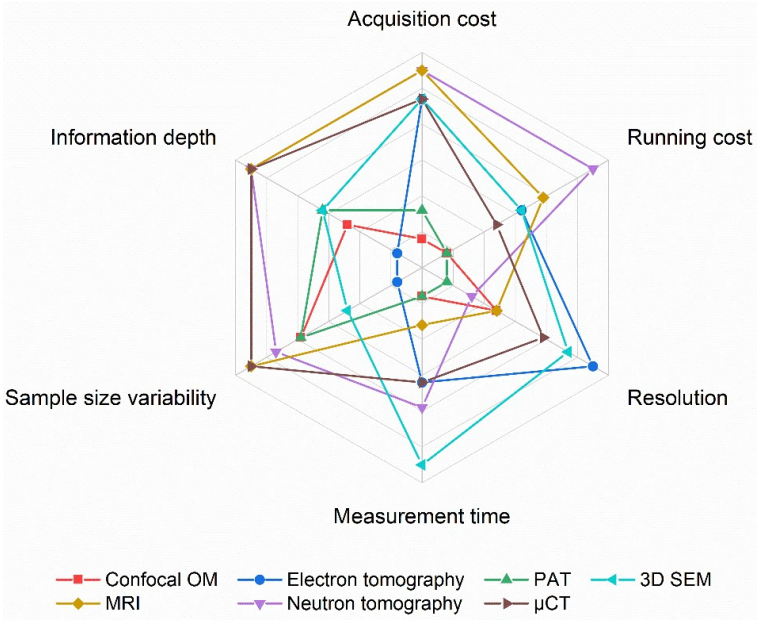

Figure 2.1. Radar chart of the comparison of 3D imaging techniques (adapted with

permission from Vásárhelyi *et al.* (2020)).

In this review, the majority of studies utilise μCT for ex vivo or material imaging, while HR-pQCT (μCT-based) or MRI is commonly employed for in vivo imaging. Here, μCT is used to demonstrate the typical image acquisition process and related information.

As shown in Figure 2.2, the three basic physical components of a CT scanner are the X-ray source, the X-ray detector, and the sample stage. By exploiting the penetration power from an X-ray source, a series of 2D radiographs of the object are captured from many different directions. Depending on the objective of the study, different configurations are used for X-ray imaging. For clinical observations, the X-ray source and detector rotate around the stationary patient (see Figure 2.2a). In contrast, when imaging centimetre- or millimetre-sized specimens, it is more effective to keep the X-ray source and detector stationary while the specimen rotates (see Figure 2.2b). Similar to how 2D images consist of pixels, 3D images are composed of cubic volume elements known as voxels. To accurately characterise features such as shape and volume, the voxel size must be significantly smaller than the expected features or their separation. The μCT system can achieve voxel sizes as small as 0.1 μm (Withers *et al.*, 2021). However, opting for a smaller voxel size typically requires compromising on the size of the object being imaged. This trade-off arises because reducing the effective pixel size often results in a smaller field of view on the detector.

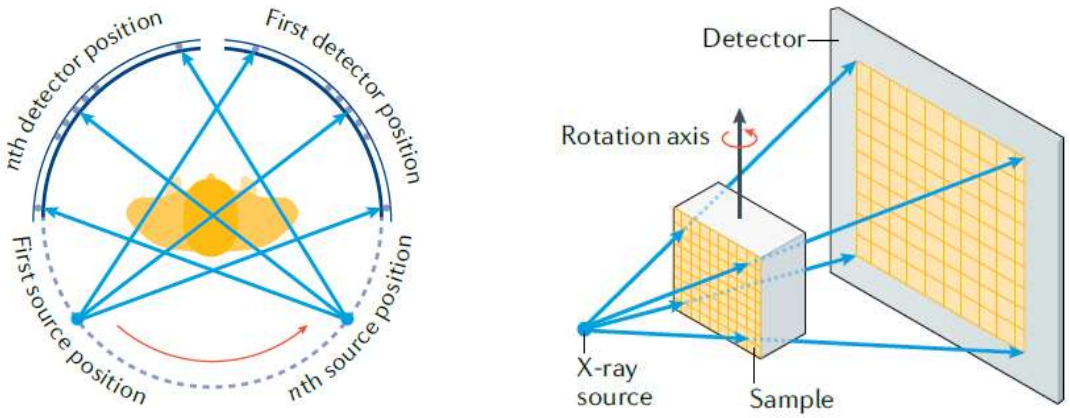

(a) (b)

Figure 2.2. Common X-ray computed tomography configurations. (a) gantry system where the source and the detector rotate in tandem around the patient, animal or specimen. (b) cone beam system typical of laboratory systems (adapted with permission from Withers *et al.* (2021)).

Image Processing

Image processing is an essential step for extracting meaningful information from raw image data (Kuruvilla *et al.*, 2016). Image processing techniques, such as noise removal, contrast enhancement, and normalization, are applied to enhance image quality and ensure consistency. Segmentation methods, including threshold-based, region-based, and edge-based techniques, involve dividing an image into distinct regions or objects to simplify analysis and highlight areas of interest. For the sake of brevity, this section focuses on introducing noise removal, threshold-based segmentation, and region-based segmentation.

Typically, the raw CT image consists of the original image combined with a noise component from acquisition hardware, as illustrated in Figure 2.3. The goal of image denoising is to suppress the noise from the CT images by preserving interesting details so that the filtered image can be used for future analysis. Techniques such as median filters or other advanced filtering methods can be employed to achieve this goal (Withers *et al.*, 2021). Additionally, the development of machine learning techniques can enhance the denoising process by balancing noise reduction with the preservation of important features (Diwakar and Kumar, 2018).

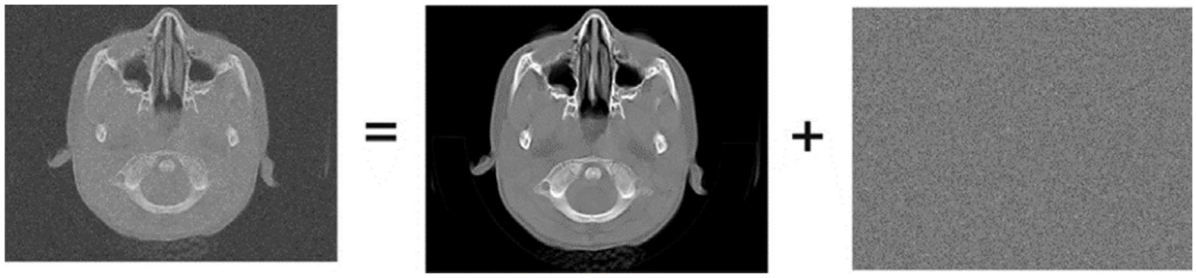

Figure 2.3. A noisy image is the sum of the clean image and the noise component (adapted with permission from Diwakar and Kumar (2018)).

Once the image is clear and cleaned, the next step is to highlight the features of interest, which can be achieved using threshold segmentation. This is a simple yet powerful technique for segmenting images, particularly those with bright objects against a dark background. Threshold segmentation converts a multi-level image into a binary image by selecting an appropriate threshold value T. This value divides image pixels into distinct regions, effectively separating objects from the background (Kuruvilla *et al.*, 2016). T is often determined based on the grayscale histogram, which graphically represents the pixel intensity distribution. The most widely used approach is the Otsu method (Otsu, 1975), originally developed to binarise images by minimising

the weighted sum of variances between two classes. For example, in granular materials, it can effectively separate sand particles from other materials (Zhao and Wang, 2016).

In the presence of multiple phases, such as voids, solids, and liquids, multiple threshold values can be applied to effectively segment these regions (see Figure 2.4). This technique, known as multi-threshold segmentation (Kaur and Kaur, 2014), classifies distinct components within a material by dividing the intensity range into discrete intervals, with each interval corresponding to a specific phase or material type. By providing a detailed and accurate representation of complex multiphase systems, this method enhances analytical capabilities in disciplines such as material science and geotechnical engineering. Alternatively, this task can also be achieved using other segmentation methods, such as watershed (Ramesh *et al.*, 2021) or level set (Cremers *et al.*, 2007) segmentation, which are particularly effective for handling irregular boundaries or topological changes in the data.

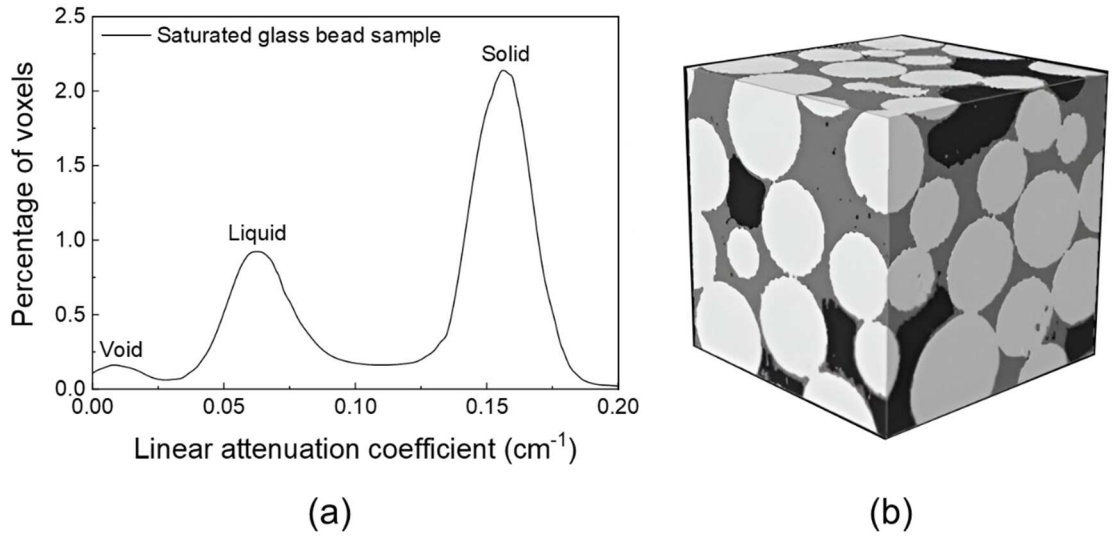

Figure 2.4. Segmentation processes for saturated glass bead sample. (a) linear attenuation histograms of the sample. (b) sub-volumes showing void (dark gray), liquid (medium gray), and solid (light gray) phases (adapted with permission from Vaz *et al.* (2014)).

2.3.2 Mesh Generation

Mesh reconstruction based on prepared images involves converting processed data into a structured representation, such as a 3D surface or volume, using specific reconstruction methods tailored to the application's needs (see Figure 2.5). Among widely used methods, voxel-based conversion (van Rietbergen, 2001), marching

cubes (Frey, 1994; Müller and Rüegsegger, 1995), Delaunay refinement (Nadimi and Fonseca, 2018a), and spherical harmonics (SH) (Shen and Makedon, 2006) are prominent in their respective domains. Voxel-based conversion and marching cubes, both dependent on the filtered back projection method (Willemink and Noël, 2019), are extensively used in medical-related research, offering high accuracy in representing continuous objects such as anatomical structures from CT or MRI data. Conversely, Delaunay refinement operates on point data, making it ideal for reconstructing surfaces from irregularly distributed points, such as those in granular material studies. SH, while not point-based, are often employed for analyzing and representing smooth surfaces, making them useful for granular particle shape analysis or compact surface modeling. While these methods are widely applied, their suitability depends on the specific requirements of the data and the application. Below is a brief overview of each method mentioned.

- Voxel-based conversion directly translates the voxels from processed images into a structured grid and typically generates a very large number of brick elements. For example, representing 1 cm^3 of trabecular bone may involve 10^5 to 10^6 elements (van Rietbergen, 2001). Such complexity requires the development of specialized solvers to execute the simulation efficiently (Van Rietbergen *et al.*, 1996).
- The marching cubes algorithm subdivides the voxels into tetrahedron elements of varying sizes (Frey, 1994; Müller and Rüegsegger, 1995). It is widely recognized for producing smooth, high-quality trabecular surfaces. Drawback includes the lower accuracy due to tetrahedral elements and the higher computational effort required to solve the model.
- Delaunay refinement is a mesh improvement technique that refines a constrained Delaunay triangulation by optimizing triangle quality, specifically by maximizing the minimum angle to avoid "skinny" elements and preserve boundaries (Shewchuk, 2002; Nadimi and Fonseca, 2018b). This approach is particularly important for numerical simulations, as well-shaped elements improve solver convergence and computational efficiency.
- SH is used to characterise and reconstruct the micromorphology of granular materials by representing their surface geometry through spherical harmonic functions. The SH degree provides a means of controlling mesh resolution, while SH descriptors serve as tools for detailed morphological analysis (Shen and Makedon, 2006; Zhou *et al.*, 2015).

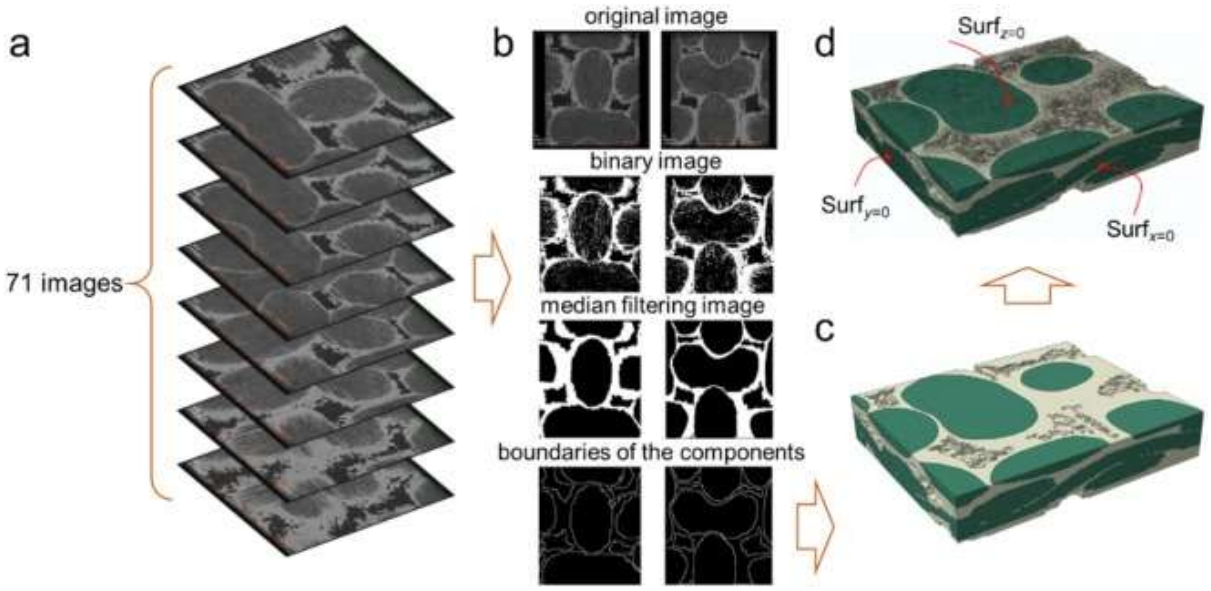

Figure 2.5. The 3D reconstruction process of the plain-woven C/SiC composites. (a) virgin CT images, (b) CT image segmentation, (c) reconstructed geometry model, and (d) reconstructed FE mesh (adapted with permission from Ai *et al.* (2021)).

2.3.3 Model Setup

Once the mesh is prepared, the next step is to establish a numerical framework to simulate the behaviour of the reconstructed object under physical or experimental loading conditions. This step involves defining boundary conditions, assigning material properties, and selecting the appropriate numerical solver based on the objectives.

The first step in the framework is to define and apply the boundary conditions, which are essential for reproducing physical or experimental loading conditions. For instance, to mimic the compression test, a fixed boundary condition is applied to the bottom of the reconstructed object, while an axial load is applied to the top. This setup replicates experimental conditions, enabling the model to simulate material deformation and mechanical response accurately.

The second step involves assigning material properties, such as Young's modulus, Poisson's ratio, and mass density, which are critical for ensuring accurate simulation results. These properties are typically derived from experimental tests and vary significantly between studies. For example, Young’s modulus of bone tissue in μFE analyses has been reported to range from 6.8 to 20 GPa (van Rietbergen and Ito, 2015). This variability underscores the importance of tailoring material properties to reflect the actual mechanical behaviour.

The third step is to determine the appropriate solver. In medical and material-related

research, the primary focus is often on evaluating either the stiffness (using linear analysis) or the strength (using nonlinear analysis) of the reconstructed object. In granular material-related research, sand particles are typically assumed to be rigid due to their high stiffness compared to contact forces (*i.e.,* hard contact). If internal deformation is modelled, it is often approximated using linear elastic behaviour, such as Hooke's Law (Hooke, 1678). In contrast, the contact forces between sand particles are commonly modeled using Hertzian contact theory (Hertz, 1881), which is inherently nonlinear.

To simulate fracturing, additional advanced methods can be coupled with the μFE model, such as the extended finite element method (XFEM) (Druckrey and Alshibli, 2016) or CIEs (Wei *et al.*, 2019). These techniques enhance the model's ability to capture crack initiation, propagation, and interfacial failure, providing a more comprehensive understanding of the mechanical response and fracture mechanics.

Once the model is set up, a μFE solver is required to execute the simulation accurately and efficiently. Table 2.1 provides a summary of commonly used software suites for μFE analysis, categorized by their field of application, highlighting their capabilities tailored to specific requirements in medical, material, and granular research.

Table 2.1. Summary of commonly used software suites for μFE analysis.

Software	Field of applications	References
Abaqus	Orthopaedic research	(Sandino *et al.*, 2017; Rieger *et al.*, 2018; Knowles *et al.*, 2019)
	Dental research	(Chen *et al.*, 2012; Della Bona *et al.*, 2013; Allen *et al.*, 2018; Cen *et al.*, 2018; Ortún-Terrazas *et al.*, 2018; Wan *et al.*, 2022)
	Implant research	(Limbert *et al.*, 2010; Williams and McCullough, 2016; Ovesy *et al.*, 2019; Jin *et al.*, 2020; Su *et al.*, 2021; Zupancic Cepic *et al.*, 2022; Akhlaghi *et al.*, 2023)
	Porous materials	(Maire *et al.*, 2003; Youssef *et al.*, 2005; Berre *et al.*, 2006; Tsafnat *et al.*, 2008, 2009, 2011; Singh *et al.*, 2010; Basista *et al.*, 2017;

		Tagliabue *et al.*, 2017; Wang *et al.*, 2018; Boniotti *et al.*, 2019; Lei *et al.*, 2019; Ai *et al.*, 2021)
	Granular materials	(Kim and Yun, 2018; S. Nadimi and Fonseca, 2017; Imseeh and Alshibli, 2018; Lin *et al.*, 2023; Wei *et al.*, 2022b; Zhou *et al.*, 2020; Wei *et al.*, 2019; Ma *et al.*, 2017; Nadimi *et al.*, 2020; Nadimi and Fonseca, 2019; Fonseca *et al.*, 2019; Nadimi *et al.*, 2015; Thakur and Penumadu, 2020; Druckrey and Alshibli, 2016; Nadimi *et al.*, 2017; Nadimi and Fonseca, 2018b, 2018a)
Ansys	Orthopaedic research	(Wen *et al.*, 2016, 2017; Chen *et al.*, 2017; Costa *et al.*, 2017, 2020; Guha *et al.*, 2022; Revel *et al.*, 2022)
	Dental research	(Chang *et al.*, 2014, 2018; Aslan *et al.*, 2021; Smoljan *et al.*, 2021; Rahmatian *et al.*, 2023)
	Implant research	(Lin *et al.*, 2010; MacGinnis *et al.*, 2014; Moon *et al.*, 2015; Marcián *et al.*, 2018, 2021; Epifania *et al.*, 2023)
	Porous materials	(Patel *et al.*, 2019; Zhang *et al.*, 2019)
COMSOL	Implant research	(Frisardi *et al.*, 2012)
	Porous materials	(Gunde *et al.*, 2010)
	Granular materials	(Fei *et al.*, 2019)
ParOsol	Orthopaedic research	(Synek and Pahr, 2018; Stipsitz *et al.*, 2021; Griesbach *et al.*, 2024)
	Porous materials	(Farina *et al.*, 2021; D'Andrea *et al.*, 2022)

2.3.4 ***Calibration and Validation***

Due to the nature of simulations, results from μFE models must be calibrated and validated against experimental data to better represent real-world behaviours and ensure reliable predictions. Calibration focuses on fine-tuning model parameters to

align the simulation with the experimental data from which these parameters are derived. In contrast, validation evaluates the predictive capability of the calibrated model by comparing its outputs with independent experimental results, ensuring accuracy and robustness.

Calibration

Ideally, μFE models should accurately reproduce experimental results when the sample is properly reconstructed, boundary conditions are appropriately mimicked, and actual material parameters are applied. However, in addition to potential human errors, simplifications, and assumptions are often made to accommodate the challenges of replicating the complexity of real-world conditions, which can lead to discrepancies between numerical and experimental results.

When acceptable numerical results are not achieved, three general steps can be taken to revisit and improve the model. The first step is to ensure that the reconstructed object accurately represents the sample and that the environmental setup is correctly configured. This includes elements such as boundary conditions, contact laws, and analysis time, as these factors are often the primary sources of discrepancies between simulations and experimental results (Deng *et al.*, 2022).

The second step involves reviewing the element type and size used in the model. Since the FEM is based on discretising a continuous domain into smaller finite elements, where the governing equations are solved locally for each element and assembled to approximate the behavior of the entire system, the accuracy of the results is highly dependent on the choice of the element (Hughes, 2003; Rao, 2010). Larger elements may lose important detail, while excessively small elements can increase computational costs without proportional improvements in accuracy. Striking an optimal balance is crucial to ensure reliable simulations.

The third step is to verify the material parameters and make minor adjustments if necessary. Although these parameters are typically derived directly from experimental data and are expected to be the most accurate inputs, slight modifications can help address differences caused by simplifications or assumptions in the model. However, these adjustments should remain within a reasonable range to avoid introducing non-physiological or unrealistic values (Van Rietbergen and Ito, 2015).

To ensure systematic improvement, parametric studies are often employed to evaluate the impact of changes in meshing methods and parameter variations (Knowles *et al.*, 2019; Wei *et al.*, 2019; Zhang *et al.*, 2023). This enables a more

detailed comparison, allowing for the identification of optimal values that enhance accuracy while preserving computational efficiency.

Validation

Once the model has been calibrated, it is necessary to validate it using a range of benchmark experiments within the same research area to extend the applicability and reliability of the model. Validation is typically achieved through both numerical and experimental approaches.

In numerical validation, the model can be checked against theoretical values derived mathematically (Nadimi and Fonseca, 2018b) or compared with other numerical methods addressing the same objective (Van Rietbergen and Ito, 2015; Nadimi *et al.*, 2020). This ensures consistency across different computational frameworks and confirms the robustness of the simulation methodology. In experimental validation, the simulation results are compared with replicated experimental data. Key comparisons include force-displacement curves, deformation behaviour, failure mechanisms, and other measurable parameters that characterise the material's response under specific conditions. If agreement is not achieved, the calibration process is iteratively refined to adjust the model until the numerical results align with experimental observations.

Once the model has been validated, it can be confidently used to provide insights beyond those directly validated by experiments. This includes detailed information at the micro level, such as stress and strain distributions, crack initiation and propagation, and other phenomena that are challenging or impossible to observe experimentally. These validated predictions significantly enhance the understanding and analysis of material behaviour.

2.4 Applications

The μFE analysis provides valuable insights into a sample by leveraging information captured at the micro level, such as stress and strain distribution, deformation behaviour, failure mechanisms, and the effects of microstructural features like porosity, grain boundaries, and inclusions. It enables a comprehensive understanding of mechanical responses and can be extended to analyse thermal, electrical, and fluid-structure interactions. Moreover, it establishes a crucial link between micro-level features and macro-level behaviours, making it an indispensable tool for investigating and optimising material performance. Its applications span a wide range of fields. However, the purpose of this section is not to provide an exhaustive overview of all

possible applications but rather to highlight the type of information that can be obtained, the most suitable numerical models, and the insights that may benefit both readers and potential users.

In each example below, researchers carefully defined the most appropriate numerical framework, including image preparation, mesh generation, and solving software. Typically, the image resolution is set to be about ten times finer than the smallest details of interest within the sample (Withers *et al.*, 2021). Depending on the research objective, either surface meshes or volumetric meshes can be generated to explore the sample's linear or nonlinear behaviour. Finally, selecting an appropriate execution software is essential to ensure that the analysis is both accurate and efficient.

2.4.1 Biomedical Sciences

As one of the earliest applications of μFE analysis, it has been widely utilised in clinical studies to assess the health conditions of patients, particularly in areas such as bones (see Figure 2.6a) and teeth (see Figure 2.6b). With advancements in manufacturing techniques, there is an emerging trend of using implants to replace damaged or diseased organs. The behaviour and performance of implants within the human body can also be effectively investigated using μFE analysis (see Figure 2.6c).

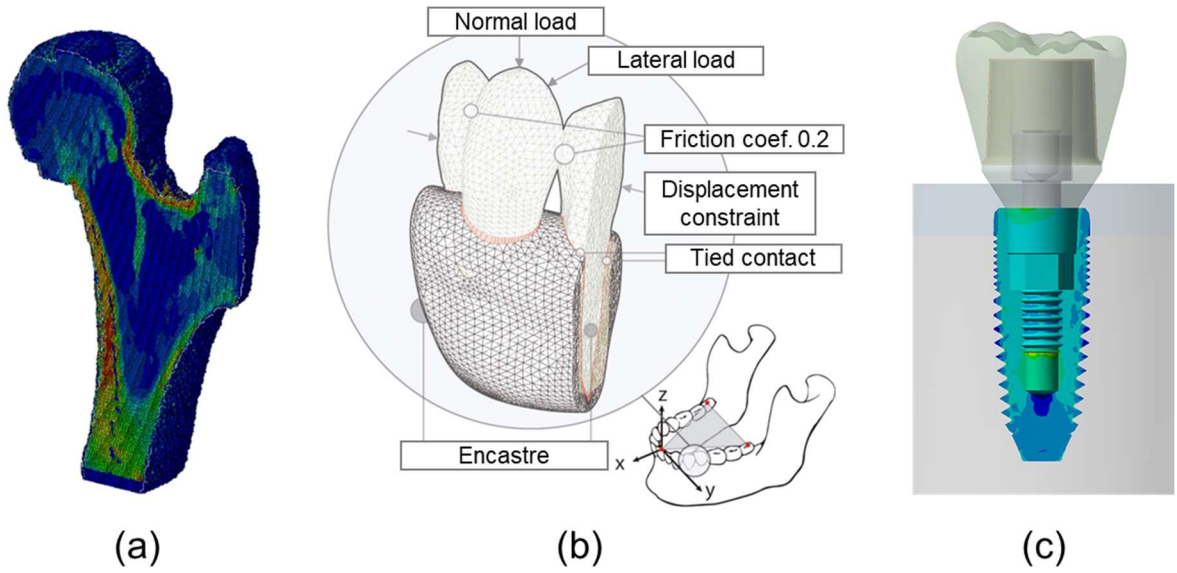

Figure 2.6. Examples of μFE analysis in biomedical sciences. (a) the proximal femur under body weight. (b) loading conditions of the canine tooth. (c) composite resin with prosthetic screw (Part (a) adapted with permission from Majcher *et al.* (2024). Part (b) adapted with permission from Ortún-Terrazas *et al.* (2018). Part (c) adapted with permission from Epifania *et al.* (2023)).

Orthopaedic Research

The apparent mechanical behaviour of trabecular bone depends on properties at the tissue level. To estimate the mechanical properties at the apparent level, two common approaches have been developed using FEM. The first approach applies homogenization theory, constructing trabecular bone models using unit cells with uniform microstructural morphology. However, this method overlooks the heterogeneous nature of bone (Hollister *et al.*, 1991). The second approach uses small pieces of reconstructed trabecular bone to estimate the apparent properties (Fyhrie, 1992, 1993; Hollister and Kikuchi, 1992; Hollister *et al.*, 1992; Edidin *et al.*, 1993), but these samples are not representative of the entire bone (Harrigan *et al.*, 1988). The introduction of μFE models has addressed these limitations, enabling the analysis of reasonably large regions of trabecular bone in full detail, thereby providing a more accurate estimation of mechanical properties (van Rietbergen *et al.*, 1995).

In most clinical studies conducted so far, linear-elastic analyses have been performed (van Rietbergen and Ito, 2015). Although these analyses cannot simulate the actual failure process and, therefore, cannot directly calculate strength, empirical relationships have been developed to predict whole bone strength based on their results. It is assumed that failure will occur if more than 2% of the tissue material in the scanned region is strained beyond 0.7% (Pistoia *et al.*, 2002). Based on this criterion, strength can be back-calculated using linear-elastic analysis. Furthermore, regression models have been developed to predict strength from stiffness (MacNeil and Boyd, 2008). With advancements in supercomputing and the development of efficient solvers, non-linear analyses have become feasible, allowing for more accurate strength estimations (Christen *et al.*, 2014; Wen *et al.*, 2016; Stipsitz *et al.*, 2021; Guha *et al.*, 2022).

Dental Research

The μFE analysis in dental research mainly focuses on evaluating stress distribution and fracture resistance in teeth and restorations, such as porcelain veneers, all-ceramic crowns, and root canal-treated teeth (Chen *et al.*, 2012; Della Bona *et al.*, 2013; Smoljan *et al.*, 2021; Wan *et al.*, 2022; Mert Eren *et al.*, 2023; Rahmatian *et al.*, 2023). For example, it has been used to analyse the effect of resin cement modulus on stress distribution in veneers (Mert Eren *et al.*, 2023) and how access cavity designs and canal preparation techniques affect the fracture resistance of mandibular molars (Smoljan *et al.*, 2021; Rahmatian *et al.*, 2023). Additionally, it plays a significant role in

understanding the porous structure of periodontal ligament (Ortún-Terrazas *et al.*, 2018) and investigating the protective role of periodontal blood flow during dental operation (Cen *et al.*, 2018).

Besides structural analysis, the μFE analysis aids in assessing the long-term performance and failure mechanisms of dental materials. Studies integrate μFE analysis with experimental fatigue testing, to understand the damage and retention behaviours of fiber posts (Silva *et al.*, 2015; Chang *et al.*, 2018). Furthermore, it has been employed to evaluate and optimize dental restoration and crown design (Magne, 2007; Shahrbaf *et al.*, 2013).

Implant Research

With the emergence of implants in dental and orthopedic fields, the μFE analysis has become a valuable tool for investigating the biomechanical behaviour of implants and their interactions with surrounding bone tissues. For example, studies have explored the impact of crown stiffness, implant positioning, and neck microthread design on peri-implant mechanics, revealing critical factors that influence stress concentration and bone health (Jin *et al.*, 2020; Su *et al.*, 2021; Epifania *et al.*, 2023).

Additionally, the μFE analysis has been used in predicting mechanical outcomes such as insertion torque and micromotion. By simulating realistic loading conditions, non-linear analysis accurately captures peri-implant bone damage and deformation, providing valuable insights into the long-term performance of implants in trabecular bone environments (Ovesy *et al.*, 2019; Akhlaghi *et al.*, 2023). Furthermore, it has been applied to evaluate the effects of bone density and anisotropy on the mechanical behaviour of the implant-bone system, offering a deeper understanding of how patient-specific factors influence peri-implant bone stability (Chevalier *et al.*, 2016).

Beyond dental applications, the μFE analysis has demonstrated its value in studying orthopedic implants, such as pedicle screws augmented with cement under various loading scenarios (Chevalier *et al.*, 2021). Furthermore, it has been used to evaluate novel implant materials, such as bioactive ceramics and biodegradable magnesium-alloy screws, providing a basis for material selection and design improvements (Ren *et al.*, 2012; Williams and McCullough, 2016).

2.4.2 Materials Science

Traditional methods in materials science, such as 2D sections combined with stereology (DeHoff and Rhines, 1968), have long been relied upon to study material

behaviour. However, these techniques are inherently limited in resolving complex 3D phenomena, such as the degree of percolation of a phase in a sample (Asghar *et al.*, 2011), fluid transport through porous networks (Atwood *et al.*, 2004), or the architecture of cellular materials (Maire, 2012). After appropriate segmentation, the μFE analysis overcomes these limitations by providing detailed 3D models that account for key features such as porosity, number of phases, and their spatial distribution within the material. This approach enables a deeper understanding of how these microstructural characteristics influence the material's overall behaviour and performance.

One prominent application of μFE analysis is in the characterisation of porous and cellular materials. μFE models have been widely employed to investigate how features like porosity, pore connectivity, and morpho-architectural characteristics influence the mechanical performance of various materials under loading conditions. Studies on scaffolds, including those made of hydroxyapatite (D'Andrea *et al.*, 2024), glass (Farina *et al.*, 2021; D'Andrea *et al.*, 2022), titanium dioxide (Zhang *et al.*, 2019), and glass-ceramic materials (Tagliabue *et al.*, 2017), have demonstrated that defects and porosity significantly impact their elastic and strength properties (see Figure 2.7). Similarly, cellular materials, including metal foams (Singh *et al.*, 2010), polymer-based foams (Youssef *et al.*, 2005), and coke blends (Tsafnat *et al.*, 2008), have been modelled to understand their deformation behaviour, stress distributions, and anisotropic properties.

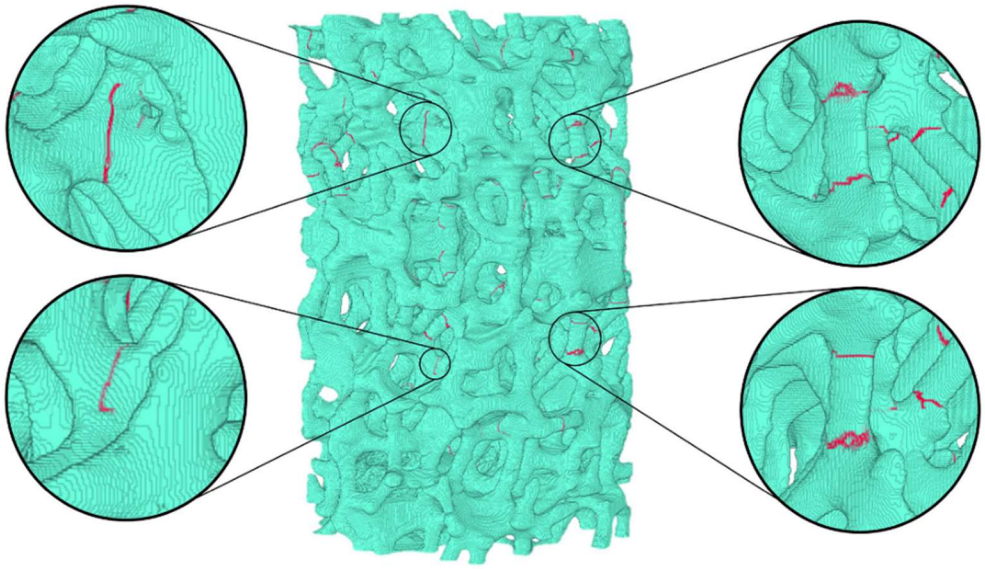

Figure 2.7. The crack pattern of highly porous scaffold after uniaxial compressive load (adapted with permission from D'Andrea *et al.* (2024)).

In addition, μFE models have been applied to composites. For example, ceramic matrix composites (CMC) have been modelled to assess localised stress fields and their relation to matrix cracking using advanced meshing techniques derived from 3D imaging data (Aziz *et al.*, 2006). Additionally, μFE analysis has been adopted in the study of metal-ceramic composites to assess residual stresses and fracture behaviour, leveraging μCT images for detailed simulations (Basista *et al.*, 2017). It has also been employed to evaluate thermal conductivity in materials like wood, enabling high-resolution modelling of the effects of grain orientation, porosity, and water content on thermal performance (Qiu, 2023). In advanced applications, μFE models generated from synchrotron X-ray CT imaging have been used to study carbon fiber-reinforced composites, offering high-fidelity insights into their mechanical behaviour and structural integrity (Sencu *et al.*, 2016).

2.4.3 Granular Materials

In granular materials, the discrete element method (DEM) (Cundall and Strack, 1979) has been widely used for modeling mechanical behaviour. However, the traditional DEM approach, which often relies on spherical particles, simplifies contact detection and force calculations but fails to capture the variation in effective stiffness caused by particle rotation and inter-particle sliding observed in real sand (Cavarretta and O'Sullivan, 2012). Moreover, the rigid body assumptions and associated contact laws inherent in the DEM approach limit its ability to model the contact interaction of irregular particles (Zheng *et al.*, 2012). Additionally, the diverse grain morphologies found in natural sands lead to complex contact topologies that significantly influence stress distribution and deformation within granular assemblies (Fonseca *et al.*, 2013; Druckrey *et al.*, 2016).

The adoption of μFE analysis allows for a more precise spatial representation of particle shapes and distributions through μCT imaging while enabling a more realistic simulation of granular behaviour by integrating deformable bodies into the finite element (FE) framework (Nadimi and Fonseca, 2018b). At the micro level, the μFE analysis reveals the critical role of morphology in particle interactions, such as contact behaviour and force transmission (Nadimi *et al.*, 2015; S. Nadimi and Fonseca, 2017), as shown in Figures 2.8a and 2.8b. At the macro level, it has been employed to study the stress distribution and deformation of granular assemblies under loading conditions, such as triaxial (see Figure 2.8c) and one-dimensional compression tests, uncovering the influence of particle morphology and microstructural features on bulk mechanical

responses (Nadimi and Fonseca, 2018b, 2019; Fonseca *et al.*, 2019; Nadimi *et al.*, 2020). By comparing with DEM simulations, numerical validations of μFE models demonstrate their superior ability to accurately capture stress distributions and deformation within granular assemblies (Nadimi *et al.*, 2017; Nadimi and Fonseca, 2018a).

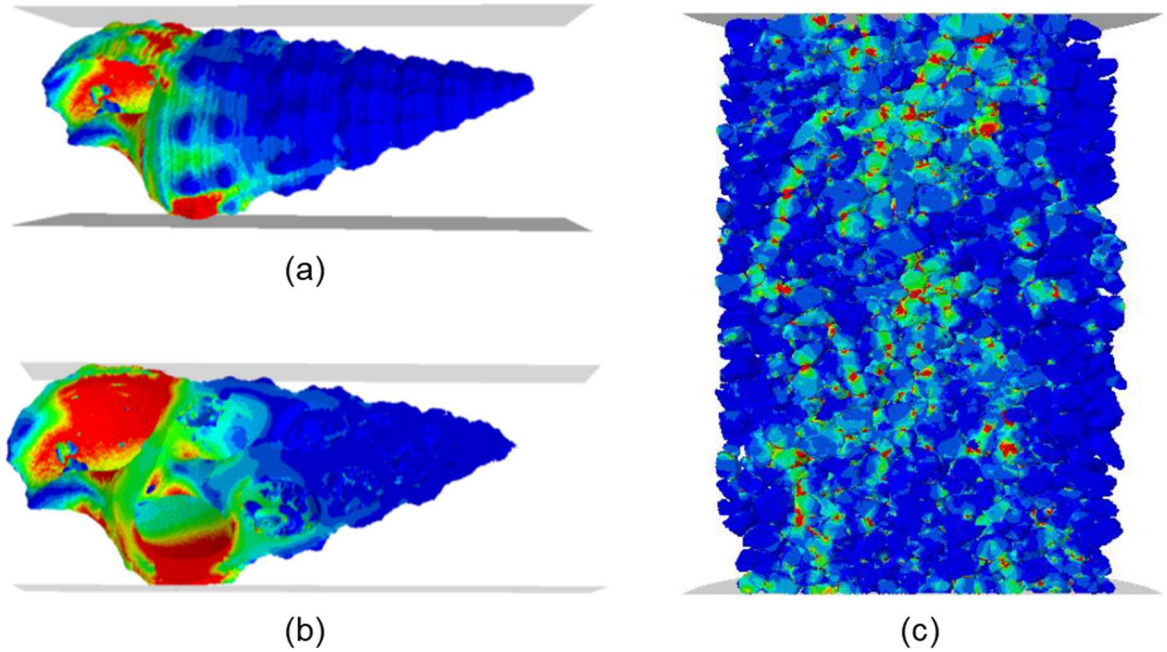

Figure 2.8. The μFE model of granular material at micro and macro levels. (a) the stress distribution of Carbonate sand, side view. (b) the stress distribution of Carbonate sand, cross-section view. (c) Eglin sand under triaxial compression (Part (a) and (b) adapted with permission from Nadimi and Fonseca (2019). Part (c) adapted with permission from Nadimi (2017)).

Besides analysing the constitutive behaviour of granular materials, the μFE model can also be applied to investigate the breakage phenomenon, particularly when coupled with CIEs (Zhang *et al.*, 2023). At the micro level, single particle compression tests have been used to study the effects of particle morphology and loading directions on crack initiation, propagation, and fracture patterns, highlighting the critical influence of morphology on breakage strength and failure modes (Wei *et al.*, 2019; Zhou *et al.*, 2020). At the macro level, beyond particle rearrangement, particle fragmentation during triaxial compression can be simulated to provide more realistic bulk mechanical responses (Lin *et al.*, 2023). In addition to CIEs, XFEM has also been employed in particle breakage studies by coupling with μFE models to simulate particle fracture

mechanics (Druckrey and Alshibli, 2016). See Figure 2.9 for an illustration of the simulation results against experimental observations.

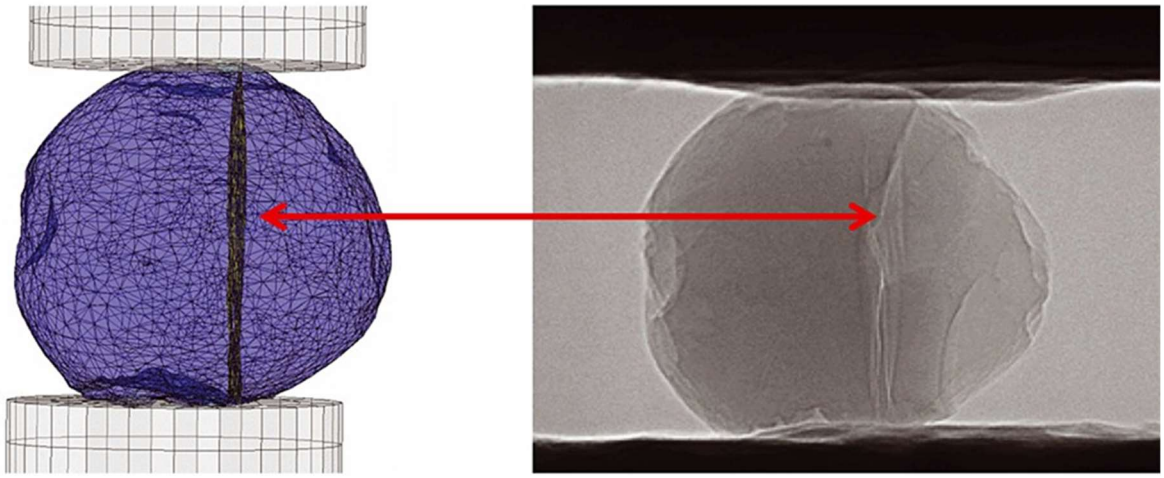

Figure 2.9. Crack locations of XFEM results compared to radiographs during experiments (adapted with permission from Druckrey and Alshibli (2016)).

2.4.4 Industrial Manufacturing

The evaluation of structural performance and reliability under mechanical and thermal loading conditions can be achieved through the μFE analysis. One major application is the analysis of fracture mechanisms in systems subjected to contact fatigue. For instance, μFE models generated using electron backscatter diffraction (EBSD) images, which provide high-resolution crystallographic information and phase separation, have been used to investigate stress states in gears under rolling and sliding fatigue, identifying critical stress regions and aiding design optimization (Farhad and Oila, 2015), as shown in Figure 2.10. Similarly, μFE-based fracture analysis of additive-manufactured interlocked structures has revealed the impact of manufacturing defects on stress evolution and failure modes, enhancing design optimisations and process improvements (Ni *et al.*, 2023).

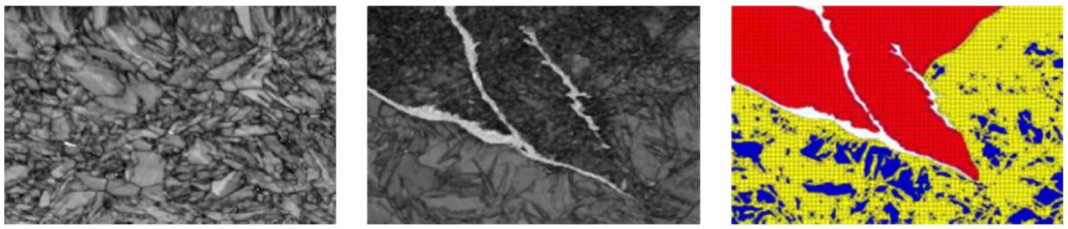

Figure 2.10. (a) EBSD images of a gear before fatigue testing. (b) EBSD images of a gear exhibiting dark etching regions (DER) resulting from microstructural changes. (c) μFE result of crack propagation in gear with DER. Red, yellow, blue, and white colours

represent DER, martensite, retained austenite, and cracks respectively. (adapted with permission from Farhad and Oila (2015)).

Another significant application is the study of lattice structures and metamaterials. High-resolution synchrotron X-ray tomography and μFE models have been employed to analyse failure modes, such as curved surface buckling and fracture, in gyroid-based metamaterials under compression (Hu *et al.*, 2021). For selective laser melting (SLM) fabricated multi-layer lattice structures, the μFE analysis has revealed the effects of defects and layer numbers on compressive strength and failure modes like layer-by-layer crushing (Lei *et al.*, 2019). Fatigue resistance in micro-lattices has also been evaluated, linking defects and crack propagation to fatigue strength through μFE models of as-manufactured geometries (Boniotti *et al.*, 2019).

Composite materials and thermal systems have also greatly benefited from the μFE analysis. For chemical-vapor-infiltrated C/SiC composite, the μFE model has revealed damage initiation at defects and propagation to fiber-matrix interfaces, aligning with in situ CT experiment results (Ai *et al.*, 2021). Likewise, the μFE analysis has been adopted for carbon fiber composites-Cu monoblocks in fusion reactors and has captured manufacturing defects such as debonding, providing high-resolution insights into thermal performance and component lifespan (Evans *et al.*, 2015).

2.4.5 Structural Engineering

By leveraging advanced imaging techniques, μFE models offer precise representations of structural geometries, including defects and voids, which are critical for evaluating mechanical performance and structural integrity.

The μFE model has been instrumental in analysing concrete's heterogeneous behaviour. Mesoscale μFE models accurately predicted concrete compressive strength by capturing the heterogeneity of aggregates, cement paste, and voids (Khormani *et al.*, 2020). Similarly, a μFE analysis revealed 3D fracture mechanisms, highlighting the impact of aggregate content on crack propagation and load-bearing capacity (Huang *et al.*, 2023), illustrated in Figure 2.11. For high strain-rate impacts, μFE models coupled with continuum-discrete simulations effectively captured fragmentation, discrete fractures, and crushing, providing insights for designing impact-resistant structures (Zhang, Z.-J. Yang, *et al.*, 2021). Ex-situ μCT tests integrated with μFE models further advanced the understanding of ultra-high-performance fiber-reinforced concrete, analysing the effects of fiber distribution and matrix interactions on fracture processes, with results aligning closely with

experimental data (Zhang, Z. Yang, *et al.*, 2021).

Beyond traditional construction materials, the μFE analysis has extended to bio-inspired systems such as bamboo and Toucan beaks. Bamboo, a natural composite material, exhibits remarkable axial compressive strength due to its parenchyma foam-like matrix and helically arranged sclerenchyma bundles. The μFE model has been used to simulate bamboo's microstructural performance under compression, providing insights into sustainable material design and bionic engineering (Palombini *et al.*, 2016, 2020). Similarly, the Toucan beak, a sandwich composite structure with a keratinous shell and bony foam core, has been analysed using the μFE model. It revealed the hierarchical structure-property relationships that contribute to its lightweight yet mechanically robust design (Seki *et al.*, 2012).

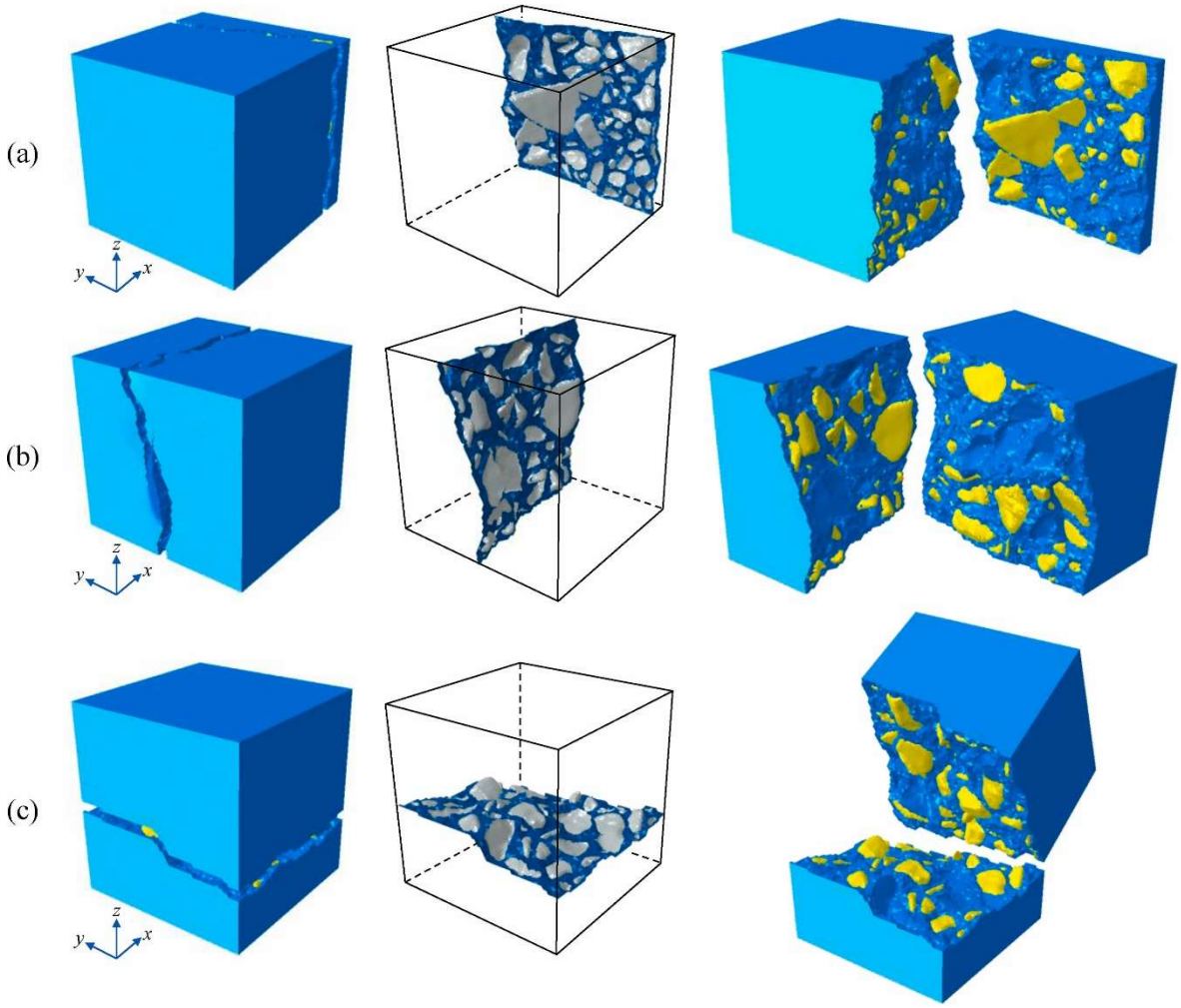

Figure 2.11. Fractured specimens ($f_a = 30\%$) under (a) x-tension, (b) y-tension, and (c) z-tension. The second column extracts the crack surfaces: the grey colour indicates the interfacial cracks around aggregates and the blue shows the cracks in the mortar (adapted with permission from Huang *et al.* (2023)).

2.4.6 *Corrosion Science*

Pitting corrosion presents a significant challenge to material reliability, characterised by its localised nature and its role as a precursor to stress corrosion cracking and fatigue failure. Traditional techniques are unable to accurately capture the stress environment around corrosion pits, which is essential for understanding crack nucleation and growth. This gap has been addressed through the μFE analysis, which combines high-resolution imaging techniques with advanced simulations to provide detailed insights into strain localisation and stress distribution.

For 316L stainless steel, the μFE model has been used to study corrosion pits under cyclic loading. Simulations revealed that crack initiation sites shift from the base of shallow pits to the shoulder and mouth in deeper pits, corresponding to localised stress concentrations, as demonstrated in Figure 2.12. These findings align with experimental observations and demonstrate the capability of the μFE model to predict fatigue life and identify critical failure regions (Hashim *et al.*, 2019).

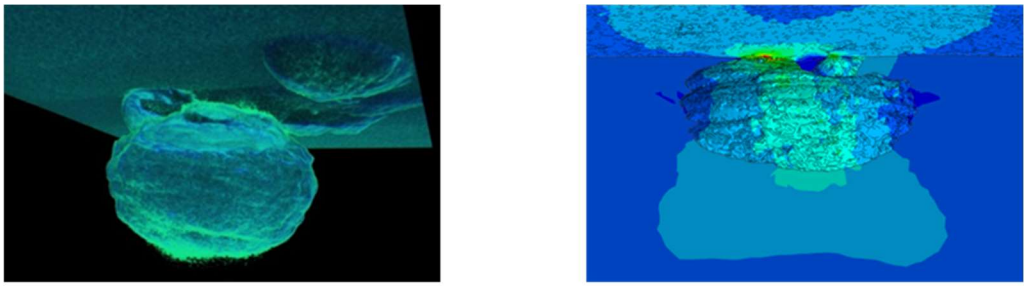

(a) (b)

Figure 2.12. (a) 3D Profile of the corrosion pit as seen from the inside of the metal and (b) stress distribution around the pit.

Similarly, the μFE model has been applied to aluminum alloys to analyse stress distributions caused by pitting corrosion. The analysis revealed a significant increase in stress levels with sensitisation time, which eventually plateaued due to material deformation and crack formation around the pits. This underscores the value of the μFE model in capturing the progression of corrosion damage and providing critical insights for designing corrosion-resistant materials and enhancing structural durability (Pidaparti *et al.*, 2009).

2.4.7 *Other applications*

Although the fields discussed below are not as prominent in μFE analysis as the

previously highlighted areas, they have nonetheless benefited significantly from its advancements. These applications, while less common, showcase the adaptability of μFE in uncovering valuable insights and deepening the understanding of complex structures and mechanisms.

Biological Engineering

In biology, the μFE model can be used to simulate human structures. A validated FE model of the human middle ear, developed using μCT images, serves as a valuable tool for hearing loss research (Nie *et al.*, 2011). Additionally, the μFE model of reconstructed 3D pathways of cochlear neurons aids in the study of cochlear implants and advances the understanding of electrical stimulation and neuron responses (Potrusil *et al.*, 2020).

Electrical Engineering

The μFE analysis can be applied to non-destructively evaluate integrated circuit bond wiring and electronic packaging. Using μCT data, bond wire geometries can be accurately modelled to predict stress concentrations and failure locations (Favata and Shahbazmohamadi, 2018). Similarly, the μFE model of Ball Grid Array packages under thermal cycling enables precise analysis of stress, strain, and manufacturing variations, improving reliability predictions in semiconductor assemblies (Lall and Wei, 2016).

Paleontology

The mechanical behaviour of dromaeosaurid theropod claws, such as those of Velociraptor, can be analysed using the μFE model. It was revealed that the claws were well-adapted for climbing, resisting longitudinal forces, and efficiently transferring stress through trabecular and cortical bone, supporting a potential scansorial phase in the evolution of flight (Manning *et al.*, 2009).

2.5 Limitations

Despite the significant advancements in the μFE analysis, several limitations exist to hinder its broader application and accuracy. One of the primary challenges is the high computational demand associated with the processing of high-resolution μCT images and detailed FE meshes. This computational complexity not only restricts scalability but also results in prohibitively long computational time, particularly for simulations involving entire bone investigations or granular assemblies (van Rietbergen and Ito,

2015; Nadimi and Fonseca, 2018a). Additionally, the reliance on simplified material properties, such as linear elasticity or homogenized assumptions, fails to fully capture the inherent anisotropy and heterogeneity observed in real-world materials (Chung *et al.*, 2019).

Another limitation lies in the challenges associated with applying realistic boundary conditions. Many simulations, particularly those involving triaxial or one-dimensional compression tests, rely on idealised boundary conditions, such as assuming rigid loading platens and fixed or frictionless constraints at the sample edges. These simplifications often fail to accurately replicate the complexities of experimental or field conditions, potentially leading to discrepancies between simulated and observed behaviours (Nadimi and Fonseca, 2019; Nadimi *et al.*, 2020). Moreover, the preparation of high-quality μCT data for analysis is time-consuming and prone to errors. Image processing and mesh generation often require significant manual effort, and inaccuracies in these steps can propagate through the modeling process, compromising the reliability of the results (Withers *et al.*, 2021).

Finally, the validation of the μFE model remains a critical challenge. While experimental data is often used for comparison, input parameters such as Young's modulus are often adjusted to achieve accurate results. However, this approach can result in inconsistencies when varying boundary conditions or mechanical tests are applied, leading to potentially unrealistic parameter adjustments (van Rietbergen and Ito, 2015; Nadimi and Fonseca, 2018b). Furthermore, dynamic behaviours, such as crack propagation and cyclic loading, are often oversimplified or entirely excluded from current models. These limitations highlight the need for further advancements in computational techniques, material modelling, and validation frameworks to fully realise the potential of the μFE analysis in addressing complex material behaviour.

2.6 Summary

This chapter has explored the advancement of μFE analysis as a powerful tool for understanding the microstructural behaviour of materials across various fields, By integrating high-resolution μCT imaging with advanced FE modelling, μFE analysis has proven its broad applicability, including the study of mechanical interactions in bone and implant systems, the deformation and fracture of granular materials, and the thermal and structural performance of composite materials.

- It is highly effective at modelling complex geometries with exceptional precision, allowing for detailed simulations of challenging structures. This capability is

particularly valuable in applications involving biological tissues and granular assemblies, providing critical insights into their mechanical behaviour.

- It excels in simulating interfaces between biological and non-biological materials, such as bone-implant systems, to reveal mechanical interactions and optimise designs. It also supports fracture mechanics by analysing crack initiation, propagation, and failure patterns to assess structural integrity.
- It incorporates microscale variations in material properties, capturing localised mechanical responses and accurately representing material anisotropy. It further facilitates the study of interactions within granular assemblies or porous networks, linking microstructural details to macroscopic performance.
- A research gap has been identified in the medical field, where μFE is widely used to study failure mechanisms, yet no generalised breakage model has been adopted. The μFE-based breakage model developed in this thesis addresses this limitation and may serve as a reference or foundation for future efforts to simulate material fragmentation in biomedical applications.

Considering the advantages outlined above, this thesis establishes a comprehensive framework based on the μFE method to investigate the breakage behaviour of sand particles. The following chapter focuses on the development of the μFE model, including the implementation of CIEs. It explores their theoretical foundation and presents the calibration and validation procedures essential for constructing a robust and reliable breakage modelling approach.

Chapter 3 The Development of the Micro Finite Element Model for Particle Breakage

3.1 Introduction

In this chapter, a framework incorporating μFE analysis with cohesive interface elements (CIEs) is developed to investigate the fracture behaviour of samples under various contact topologies. The adoption of CIEs is first verified theoretically using crack extension tests and subsequently validated experimentally against Brazilian tests. The estimation of tensile strength in brittle materials through the Brazilian test is critically influenced by the contact topology between the sample and the loading platens. Various contact topologies, including flat-to-point, arch-to-arch, and flat-to-flat, have been proposed and examined in the literature.

A comprehensive mesh sensitivity analysis and parametric study are conducted to calibrate the μFE model. Through simulating Brazilian tests using different contact topologies, the numerical results demonstrate the effectiveness of CIEs in capturing critical aspects of fracture behaviour, such as stress-strain response, strain distribution, crack initiation, and crack propagation.

3.2 Background

Tensile strength is the critical design parameter that can provide an in-depth understanding of the mechanisms of crack initiation and propagation. Due to the practical difficulties in performing a direct tensile test, the tensile strength of rock is often inferred indirectly. In 1943, the Brazilian disc test was independently proposed by Akazawa (1943) and Carneiro (1943) to perform an indirect tensile test. Although Fairhurst (1964) doubted the validity of the Brazilian test due to the location of failure which may occur away from the disc centre, it has been gradually accepted in the rock engineering community. In 1978, The International Society for Rock Mechanics (ISRM) established a guideline to perform the test using manufactured loading platens (Bieniawski and Hawkes, 1978), and in 1988 the American Society for Testing and Materials (ASTM) published a standard for the sample preparation and test procedure (ASTM, 1988). Subsequently, Wang and Xing (1999) proposed a flattened Brazilian disc to conduct the test.

The ISRM guideline suggests using curved loading platens of radius 1.5 times that of the disc sample. Thus, manufactured loading platens with different curvatures are required based on the sample diameter. The stress distribution and fracture behaviour

of the Brazilian disc under different arc loading angles have been investigated experimentally and numerically (Yu *et al.*, 2009; Erarslan and Williams, 2012; Erarslan *et al.*, 2012). The results indicated that the Brazilian test with curved loading caused the stress concentration to be lower at the loading ends but cannot promise that cracks initiate from the disc centre due to the non-uniform stress distribution at curved contact. Additionally, different sample size requires different manufactured loading platens.

To simplify the experimental preparation, the ASTM standard proposes a simplified setup of the Brazilian test where flat platens are used to apply loads to the disc at diametrically opposite ends. However, this loading method results in a crushing failure of the disc caused by the stress concentration at the loaded area. To minimise this failure behaviour, Andreev (1991) and Yu *et al.* (2009) modified the test by introducing cushions between the flat platens and the disc to reduce the stress concentration. They performed the test with different cushions that contained various stiffness relative to the sample. The results proved that the cushion works for the purpose of reducing stress concentration, but it also generates a new variable for the tensile strength calculation.

Inspired by the cushion, Wang and Xing (1999) proposed a flattened Brazilian disc sample, where the top and the bottom have been cut parallel to provide better contact at the loading ends. The angular distance of 2α, which can guarantee central crack initiation in the flattened disc, has been studied theoretically and numerically (Wang *et al.*, 2004; Meng *et al.*, 2013; Huang *et al.*, 2015). They found that the optimal angular distance is $20° \leq 2\alpha \leq 30°$. This conclusion has been verified through the flattened Brazilian test in laboratory tests by Wang and Wu (2004).

Besides the existing research on validations and improvements, numerous studies have been undertaken to solve the engineering practical problems by utilising the Brazilian test with different contact topologies (Sarfarazi *et al.*, 2017; Liu *et al.*, 2018; Yang *et al.*, 2019; Haeri *et al.*, 2020). For example, Sarfarazi *et al.* (2017) used Particle Flow Code in Two Dimensions (PFC2d) to study multiple parallel cracks in the ASTM setup. By increasing the joint spacing, they found that the crack initiation stress and failure stress increased for horizontal distribution and decreased for vertical distribution. Their findings, showing that crack initiation and failure stress depend on joint orientation and spacing, highlight the sensitivity of fracture patterns due to internal structure variability, an insight directly relevant to the role of mesh regularity in this study.

Liu *et al.* (2018) found that the fatigue failure modes of flattened Brazilian discs are independent of cycling loads by using the DEM. This demonstrates the robustness of the flattened geometry and supports its use in simulations where repeated loading is not the focus. In the ISRM setup, Yang *et al.* (2019) used PFC2d to reveal that tensile fracture and shear fracture along the bedding plane are the major fracture patterns of shale materials. Their study reinforces the importance of contact conditions in determining fracture mode, which has been carefully accounted for in the present μFE-based modelling. Haeri *et al.* (2020) applied the XFEM to study pre-cracked mortar samples in the ASTM setup. While XFEM effectively captures crack propagation, it is less suited for modelling progressive fragmentation and interface debonding, which are better handled by CIEs used in this study.

The ISRM, ASTM, and flattened Brazilian disc contact topologies have been studied extensively through theoretical, experimental, and numerical simulations, but comparative studies under unified modelling frameworks remain rare. Stirling *et al.* (2013) is one of the few works that examines these loading configurations side-by-side. This gap underscores the need for a consistent modelling approach that can directly compare contact topologies under equivalent conditions, which is an objective this study aims to address.

Informed by this literature, a μFE model combined with CIEs is developed in this chapter to investigate the fracture behaviour between different Brazilian test contact topologies. The ability of μFE to represent material heterogeneity and microstructure, along with the fracture-tracking capability of CIEs, allows for realistic simulation of crack propagation without predefining failure paths (Ma *et al.*, 2017; Chen *et al.*, 2020, 2022). The fracture angle of the model was validated against the crack extension test proposed by Erdogan and Sih (1963). A mesh sensitivity study and parametric calibration are conducted to enhance numerical stability and reliability.

Finally, the ISRM, ASTM, and flattened Brazilian disc contact topologies are simulated and compared to the experimental tests (Stirling *et al.*, 2013), in terms of load-strain curves, strain distribution, crack initiation and propagation, and tensile strength. These comparisons provide critical insights into the strengths and limitations of each loading topology and contribute to improving the design of fracture tests in granular materials.

3.3 Materials and Methods

By employing CIEs, the contact detection and interaction of the μFE model is not

limited to simulating the continuum behaviour within the object but also has the ability to replicate the initiation and propagation of internal cracks. Abaqus/Explicit is adopted to perform FEM simulations due to its computational efficiency for the analysis of models consisting of numerous elements experiencing large deformation within relatively short dynamic response times and for the analysis of discontinuous events within the model.

3.3.1 Cohesive Interface Elements

During the fracture process, the energy dissipation within the cohesive zone, where CIEs exist, can be simulated using the cohesive crack model established by Barenblatt (1959) and Dugdale (1960) and the frictional crack model proposed by Hillerborg *et al.* (1976). Based on their hypothesis, there is a normal traction t_n and a tangential traction (shear) t_s at the fracture surfaces through mechanical behaviours such as material bonding, aggregate interlocking, and surface friction within the cohesive zone. Tension or strain-softening occurs once the tractions of crack surfaces drop constantly as a function of their relative displacements (crack opening displacement δ_n and crack sliding displacement δ_s). Figure 3.1 illustrates typical linear softening curves where δ_n^o, δ_s^o and δ_n^{sep}, δ_s^{sep} denote the displacements at crack initiation and fracture completion, respectively. To capture the pre-crack initiation stage, a linear ascending branch is included in each softening curve. The unloading paths are also shown and are assumed to be linear and elastic, returning to the origin without any residual displacement. This simplification implies that the model does not account for plastic or permanent deformation during unloading, which may limit its ability to capture irreversible damage mechanisms observed in real materials. Once the material enters the softening regime governed by k_n and k_s, it cannot return to the initial stiffness k_n^o and k_s^o, indicating that the stiffness degradation is irreversible in this model. The regions under the curves represent the mode I fracture energy, G_n, and the mode II fracture energy, G_s, both treated as material properties in this study. The initial normal stiffness k_n^o and shear stiffness k_s^o. are set sufficiently high to approximate the undamaged elastic behaviour. However, excessively large values may lead to numerical instability or unrealistic stress concentrations. Therefore, a trial-and-error approach is adopted to select appropriate values fork_n^o and k_s^o.

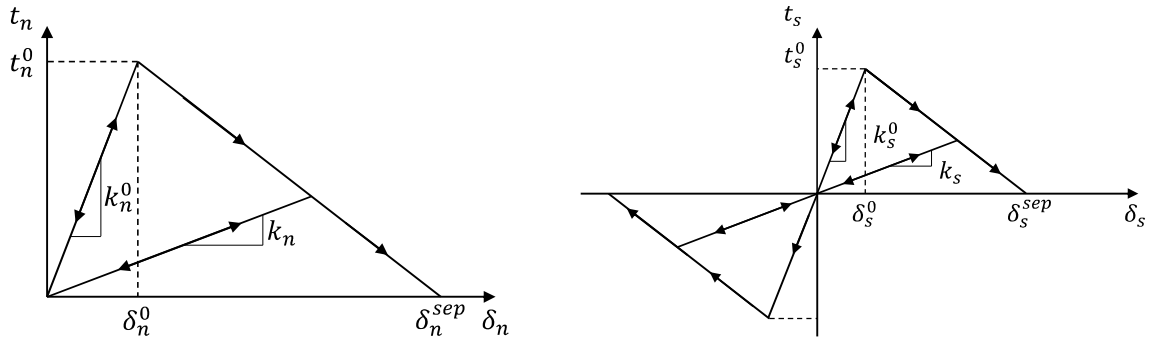

(a) (b)

Figure 3.1. Linear softening laws for the CIEs. (a) the normal direction and (b) the shear direction.

In Abaqus/Explicit, the 4-node two-dimensional cohesive interface element (COH2D4) has zero in-plane thickness and is based on the cohesive crack model. The softening laws shown in Figure 3.1 are applied to define the constitutive behaviour of the cohesive element. Since the progressive damage within the material is irreversible, the feature of COH2D4 is that it can make this happen by setting stiffness k_n and k_s degrade while δ_n and δ_s increase, during the unloading and reloading process. A scalar damage variable D is used to describe the material's overall damage caused by all active mechanisms. It can be derived from the effective displacement δ_m:

$$D = \frac{\delta_m^{sep}(\delta_m^{max} - \delta_m^0)}{\delta_m^{max}(\delta_m^{sep} - \delta_m^0)} \tag{3.1}$$

where δ_m^{max} refers to the maximum effective displacement attained during the loading history. δ_m^0 and δ_m^{sep} are effective relative displacement referring to δ_n^o, δ_s^o and δ_n^{sep}, δ_s^{sep}. δ_m can be defined as a combination of δ_n and δ_s:

$$\delta_m = \sqrt{\langle \delta_n \rangle^2 + \delta_s^2} \tag{3.2}$$

where $\langle\ \rangle$ is the Macaulay bracket and is defined as:

$$\langle \delta_n \rangle = \begin{cases} \delta_n, & \delta_n \geq 0 \text{ (tension)} \\ 0, & \delta_n < 0 \text{ (compression)} \end{cases} \tag{3.3}$$

Based on Equation 3.1, D monotonically evolves from 0 to 1 upon further loading after the initiation of damage. Then, the k_n and k_s can be calculated as:

$$k_n = (1 - D)k_n^o, k_s = (1 - D)k_s^o \tag{3.4}$$

The nominal traction stresses t_n in the normal direction and t_s in the shear direction are also affected by the scalar damage variable D, as described by:

$$t_n = \begin{cases} (1-D)\bar{t_n}, & \bar{t_n} \geq 0 \text{ (tension)} \\ \bar{t_n}, & \bar{t_n} < 0 \text{ (no damage to compressive stiffness)} \end{cases} \quad (3.5)$$

$$t_s = (1-D)\bar{t_s} \quad (3.6)$$

where $\bar{t_n}$ and $\bar{t_s}$ are the nominal traction stress components predicted by the elastic traction-separation behaviour for the current separation without damage.

In addition to the damage evolution explained by the scalar damage variable D, a damage evolution definition is needed to specify the energy dissipated due to fracture. Since mixed-mode (mode I + mode II) fractures are the dominant failure behaviours of brittle materials compared to single-mode fractures, the Benzeggagh-Kenane (B-K) fracture criterion (Benzeggagh and Kenane, 1996) is adopted to define the mixed-mode fracture energy:

$$G^c = G_n^c + (G_s^c - G_n^c)\left\{\frac{G_s}{G_n + G_s}\right\}^\eta \quad (3.7)$$

where G^c is critical mixed-mode fracture energy. G_n^c and G_s^c are critical mode I and mode II fracture energies, respectively. η is a semi-empirical criterion exponent applied to delamination initiation and growth. Since there are limited studies on η of geotechnical materials, the parameter values of resin ranging from 2 (brittle) to 3 (ductile) are used in this study (Aboura, 1993).

Apart from the damage evolution, a damage initiation criterion that refers to the beginning of stiffness degradation is required. The maximum nominal stress criterion is suggested by da Rocha (2016) to simulate materials with lower tensile strength; *i.e.*, the damage is assumed to initiate when the maximum nominal traction ratio reaches a value of one, as defined in the following expression.

$$\max\left\{\frac{\langle t_n \rangle}{t_n^0}, \frac{t_s}{t_s^0}\right\} = 1 \quad (3.8)$$

where t_n^0 and t_s^0 are the initial nominal traction stresses in the normal and shear directions, respectively.

3.3.2 Crack Extension Test

Erdogan and Sih (1963) examined the crack extension in a large plate subjected to general plane loading theoretically and experimentally. They found that crack extension starts at its tip and propagates in a direction that is dependent on the existing crack angle. This fracture behaviour can be illustrated using the following equation:

$$\sin\theta + (3\cos\theta - 1)\cot\beta = 0 \tag{3.9}$$

where β is the crack angle and θ is the fracture angle.

According to Equation 3.9, when $0 < \beta < \frac{\pi}{2}$, θ is negative and the crack propagates in the directions indicated by the black curved lines at the crack tip in Figure 3.2a. Figure 3.2b shows the solution of Equation 3.9 in graphical format versus some experimental results.

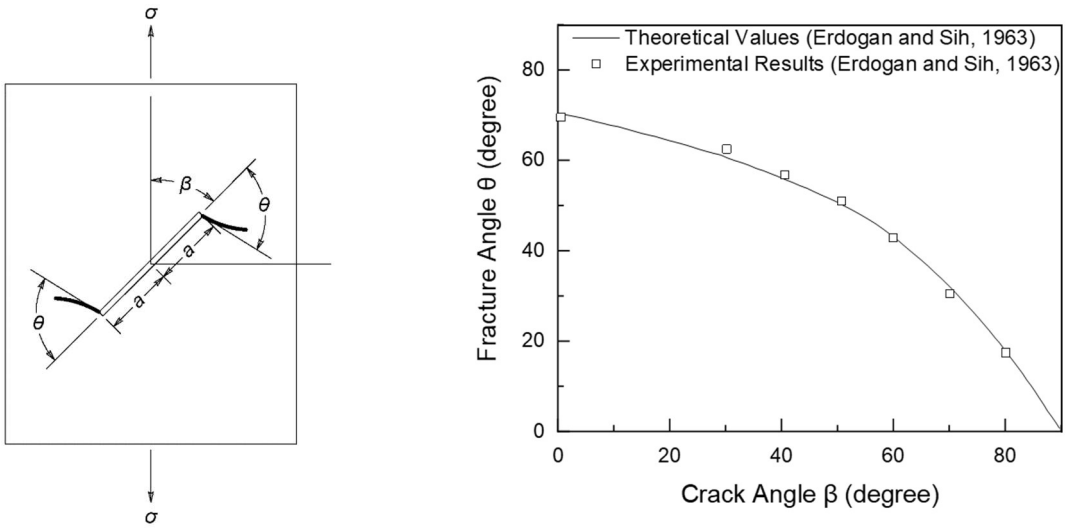

(a) (b)

Figure 3.2. (a) the cracked plate under uniform tension. (b) fracture angle-crack angle plot.

3.3.3 Numerical Model of Crack Extension Test

The cracked plate under uniaxial tension is modelled using the developed method as a validation. The simulation is performed in Abaqus/Explicit. A 228.6 mm by 457.2 mm rectangular mesh with an existing crack of 50.8 mm by 1 mm is generated using 3-node linear plane strain triangle element (CPE3) elements to reproduce the sample used in the crack extension test (Erdogan and Sih, 1963). COH2D4 elements are inserted between CPE3 elements using open-source software developed by Zare-Rami and Kim (2019). Since the COH2D4 elements have zero in-plane thickness, the mesh geometry is not changing. Each element can locally deform depending on the current nodal forces and the traction-separation relation allows crack initiation and propagation where CIEs exist. A constrained bottom and a uniform displacement over the top are assigned to the mesh to reproduce the loading condition.

The material parameters used in the model are listed in Table 3.1. The properties of the solid elements (density, Young's modulus, and Poisson's ratio) were adopted from

Nadimi and Fonseca (2018b). The fracture energies, the semi-empirical criterion exponent, and the friction coefficient were taken from Wei *et al.* (2019). The remaining parameters, including stiffness and strength values for CIEs, were calibrated to best fit the experimental results.

Table 3.1. Material parameters of quartz sand particles.

Solid Elements		
Density	$\rho\ (kg/m^3)$	2500
Young's modulus	$E\ (GPa)$	63
Poisson's ratio	υ	0.22
CIEs		
Normal stiffness	$k_n\ (N/mm^2)$	63000
First shear stiffness	$k_s\ (N/mm^2)$	31500
Tensile strength	$N_{max}\ (MPa)$	25
First shear strength	$S_{max}\ (MPa)$	12
Mode I fracture energy	$G_n\ (N/mm)$	0.1
Mode II fracture energy	$G_s\ (N/mm)$	0.2
Semi-empirical criterion exponent	η	2
Contact law		
Friction coefficient	μ	0.5

3.3.4 ***Brazilian Test***

To investigate the crack propagation, failure load, and strain during the Brazilian test, three different contact topologies of the experimental setup are used and illustrated in Figure 3.3. Flat-to-point, arch-to-arch, and flat-to-flat contact topologies are following the guidance of ASTM (1988), ISRM (Bieniawski and Hawkes, 1978), and Wang and Xing (1999), respectively. The loading is indicated by the letter F and the loaded area is shown by black bold arrows.

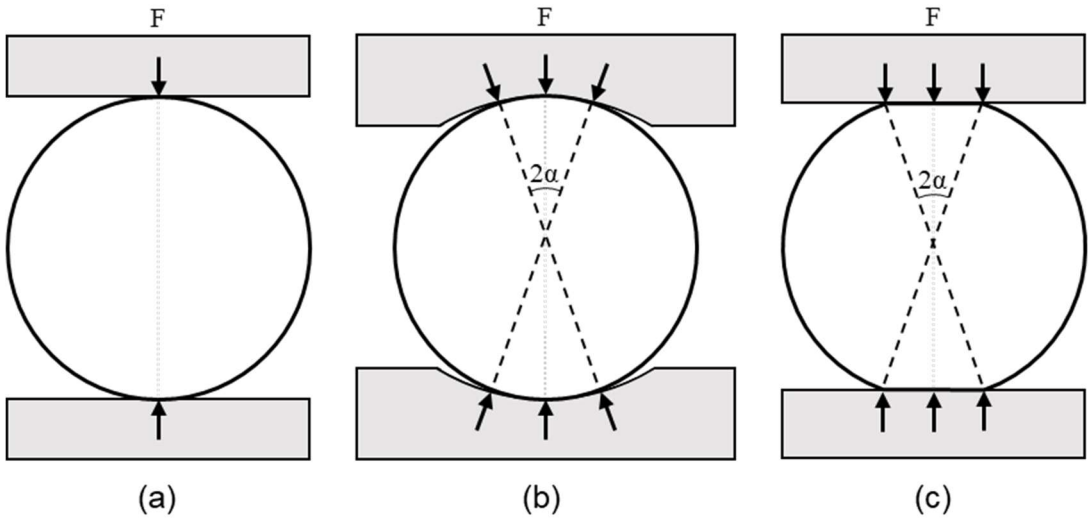

Figure 3.3. Contact topologies. (a) flat-to-point, (b) arch-to-arch, and (c) flat-to-flat.

Flat-to-point contact topology suggests the use of flat platens, applying load to the sample at diametrically opposite ends (Figure 3.3a), and recommends the thickness over diameter (t/d) ratios between 0.2 to 0.75 as being valid. The arch-to-arch and flat-to-flat contact topologies share a common angular distance 2α, which defines the boundary of the loading area (Figures 3.3b and 3.3c). To maintain the same angular distance, the loading platens in arch-to-arch contact topology are manufactured to provide a curve contact where the radius is 1.5 times bigger than the radius of the disc, and loading ends of the disc in flat-to-flat contact topology are cut to a depth where 2α is achieved. The area subject to loading in the arch-to-arch contact topology is comparatively greater than that of the flat-to-flat contact topology as it is applied over a curved surface.

3.3.5 ***Numerical Model of Brazilian Test***

Following the same procedure mentioned in the previous section, three models are generated in Abaqus/Explicit. CPE3 elements are used to create the mesh sample and COH2D4 elements are inserted to simulate crack initiation and propagation. The sphere meshes in the first two models, which reproduced the flat-to-point and arch-to-arch contact topologies, are 74 mm in diameter following the dimension used in the experiments (Stirling *et al.*, 2013). Therefore, the radius of the curved platen in the arch-to-arch model is 55.5 mm. In the flat-to-flat model, the 74 mm sphere is cut to a width of 12.8 mm at the top and the bottom with a depth of 72.9 mm. Two loading platens in each model are set to be discrete rigid, without any deformation during the loading process. The bottom platen is fully constrained, and a negative displacement

is assigned to the top platen to mimic the compression load. The friction coefficient between the platens and the sample is set to 0.5, based on values commonly used in similar particle breakage simulations. (Ma *et al.*, 2017; Wei *et al.*, 2019; Zhou *et al.*, 2020). This value was selected to balance realism with numerical stability and to reflect the contact conditions typically observed in lab-scale uniaxial compression tests.

The material parameters assigned to the meshes are identical to those listed in Table 3.2. The density, Young's modulus, Poisson's ratio, and tensile strength were adopted from Stirling *et al.* (2013), while the fracture energies, the semi-empirical criterion exponent, and the friction coefficient were taken from Wei *et al.* (2019). The remaining parameters were calibrated to best fit the experimental results.

Table 3.2. Material parameters of Springwell Sandstone.

Solid Elements		
Density	$\rho\ (kg/m^3)$	2226
Young's modulus	$E\ (GPa)$	7.527
Poisson's ratio	υ	0.261
CIEs		
Normal stiffness	$k_n\ (N/mm^2)$	10000
First shear stiffness	$k_s\ (N/mm^2)$	5000
Second shear stiffness	$k_t\ (N/mm^2)$	5000
Tensile strength	$N_{max}\ (MPa)$	3.725
First shear strength	$S_{max}\ (MPa)$	16
Second shear strength	$T_{max}\ (MPa)$	16
Mode I fracture energy	$G_n\ (N/mm)$	0.1
Mode II fracture energy	$G_s\ (N/mm)$	0.2
Mode III fracture energy	$G_t\ (N/mm)$	0.2
Semi-empirical criterion exponent	η	2
Contact law		
Friction coefficient	μ	0.5

All simulations were performed using Abaqus/Explicit on a standard office PC running Windows 10, equipped with an Intel(R) Core(TM) i5-10310U CPU @ 1.70 GHz

and 16 GB of RAM. Each simulation took approximately 5 hours of wall-clock time.

3.4 Results and Discussion

3.4.1 Mesh Sensitivity Study

One limitation of using CIEs in breakage simulation is that crack initiation and propagation can only occur along predefined element interfaces. As a result, the simulated crack path is composed of secant lines connecting element nodes, rather than the smooth curved trajectories typically observed in experiments (Erdogan and Sih, 1963). The accuracy of the simulated fracture path is therefore strongly influenced by mesh regularity and element size.

To reduce mesh-induced artefacts and better approximate realistic fracture behaviour, it is important to minimise mesh bias and ensure mesh convergence. For mesh regularity, default meshing parameters in Abaqus are used to generate a randomised mesh pattern across the particle shape, and the same meshing strategy is applied to all cases to avoid discrepancies due to mesh orientation or morphology. Moreover, by refining the mesh, the influence of mesh regularity diminishes, allowing the discrete secant lines to more closely approximate a continuous crack path (Tvergaard and Hutchinson, 1992; Bazant and Planas, 2019).

While the application of a very fine mesh yields more accurate results, it increases computational time (Nadimi and Fonseca, 2018b). It is necessary to optimise and find a balance between the accuracy of results and simulation time. A mesh size sensitivity study is performed to ensure the accurate representation of fracture behaviour, with acceptable computation costs. To investigate the effect of mesh size and find the optimal mesh size value, three different mesh sizes are examined from coarse to fine, as shown in Figure 3.4. All other environment setups are kept the same during the simulations.

The trends of crack propagation in Figure 3.4 are similar for each different mesh tested, while the fracture angles are decreasing from $70°$ to $60°$ and then to $58°$. Based on the theoretical values from Erdogan and Sih (1963), the fracture angle is around $57°$ when the crack angle is $40°$. It is noteworthy that the fracture angle difference is significant when the element size changes from 4 mm to 2 mm, and then becomes negligible when the element size changes from 2 mm to 1 mm. Thus, the fracture behaviour of the mesh with an element size of 1 mm was selected.

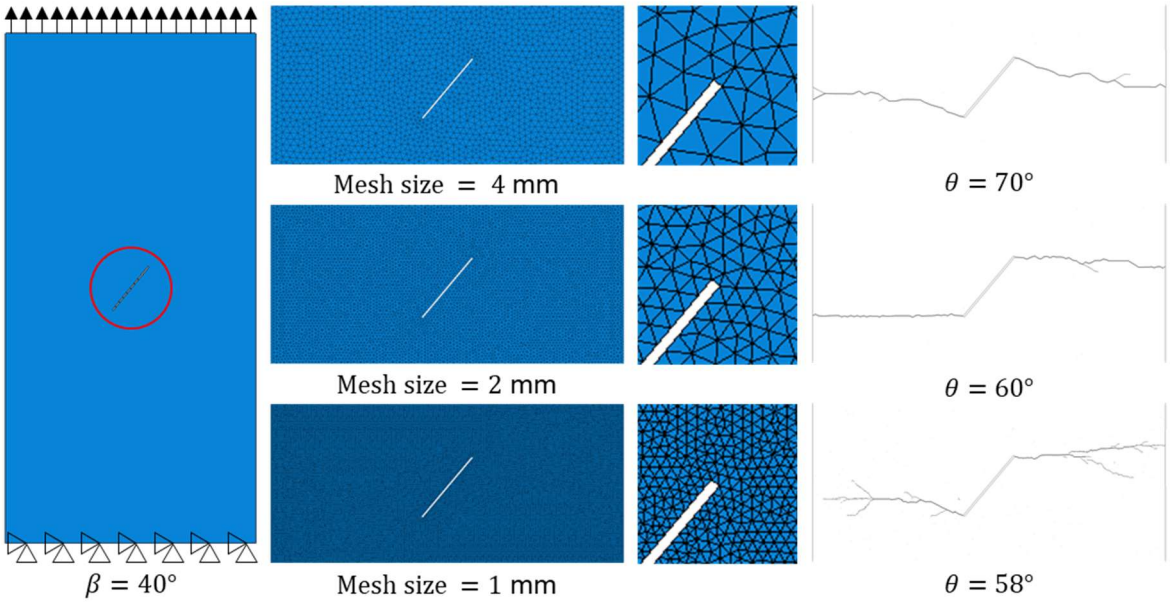

Figure 3.4. The fracture angles for test samples were discretised with different element sizes.

The element size of 1 mm, corresponding to 213,164 CPE3 elements and 319,007 COH2D4 elements, is chosen for simulations of the crack extension test. Several studies in the literature also used 1 mm element size in their investigations (Wang *et al.*, 2015; Hao and Hao, 2016; Trawiński *et al.*, 2016; Wu *et al.*, 2019).

3.4.2 Fracture Angle-Crack Angle Analysis

Numerical models with eight different representative crack angles, from $10°$ to $80°$, are generated to verify the fracture angle against theoretical values and experimental results. A good agreement between numerical and theoretical values is shown in Figure 3.5. The fracture angle is measured from the existing crack to a straight line which balances the dynamic crack propagating direction caused by multiple secant lines, at 4, 6, 8, and 10 nodes away from the crack tip. This straight line behaves as a potential direction where a crack propagates through the elements. The numerical predictions in Figure 3.5 indicate the average value of every four fracture angle measurements and the flat-end bar indicates the standard deviation.

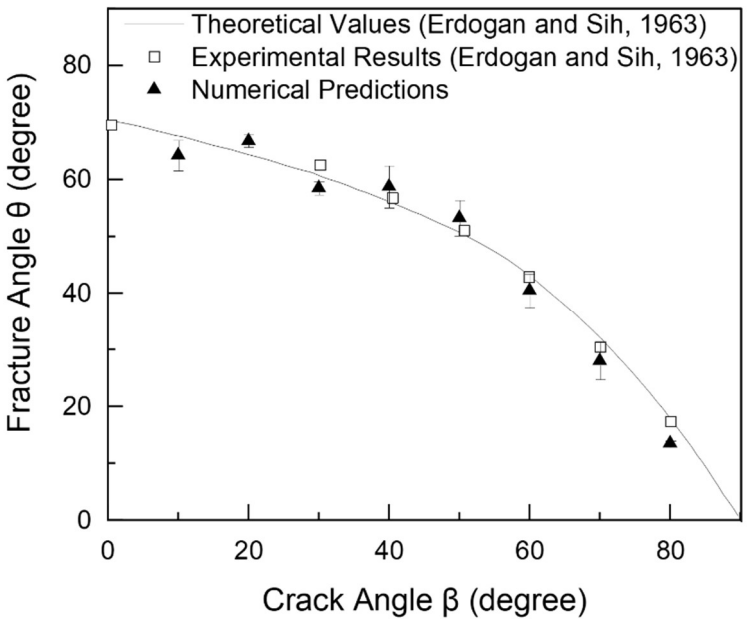

Figure 3.5. Numerical prediction of fracture angle-crack angle plot against experimental and theoretical results.

3.4.3 ***Cohesive Zone Analysis***

It is possible to further optimise the model by limiting the number of CIEs. Given this, it is important to establish a rational cohesive zone that enables simulation to reproduce crack distribution and propagation observed experimentally. Models using flat-to-point contact topology with three different cohesive zones are investigated, ranging from no cohesive zone to a cohesive zone width that equals the sample width (full cohesive zone). Material parameters of Springwell Sandstone are assigned to the models. The mesh information of each model is listed in Table 3.3.

Table 3.3. Mesh information of models using different cohesive zones.

	Mesh size (mm)	CPE3 element	COH2D4 element
No cohesive zone	1	9,000	0
Partial cohesive zone	1	8,832	4,372
Full cohesive zone	1	9,000	13,384

When no cohesive zone exists, the mesh behaves like a deformable body without any cracks during the simulation as expected (Figures 3.6a and 3.6d). A partial cohesive zone resulted in fewer CIEs along which cracks can propagate and thus simulated fracture patterns in a confined and restricted zone (Figures 3.6b and 3.6e).

Such simulations produced crack paths that are controlled by the cohesive zone width. Their results are distinct from what was observed during experiments and are influenced by boundary conditions. A wider cohesive zone could reduce this issue and allow the linear softening laws to be applied over a wider area and develop a crack where traction is greatest. Thus, the full cohesive zone allowed randomized crack initiation and propagation within the mesh (Figures 3.6c and 3.6f).

Since different fracture behaviours caused by sample-apparatus geometries of the Brazilian test lead to distinct load-strain curves from test to test, the full cohesive zone is selected for simulations in the next section.

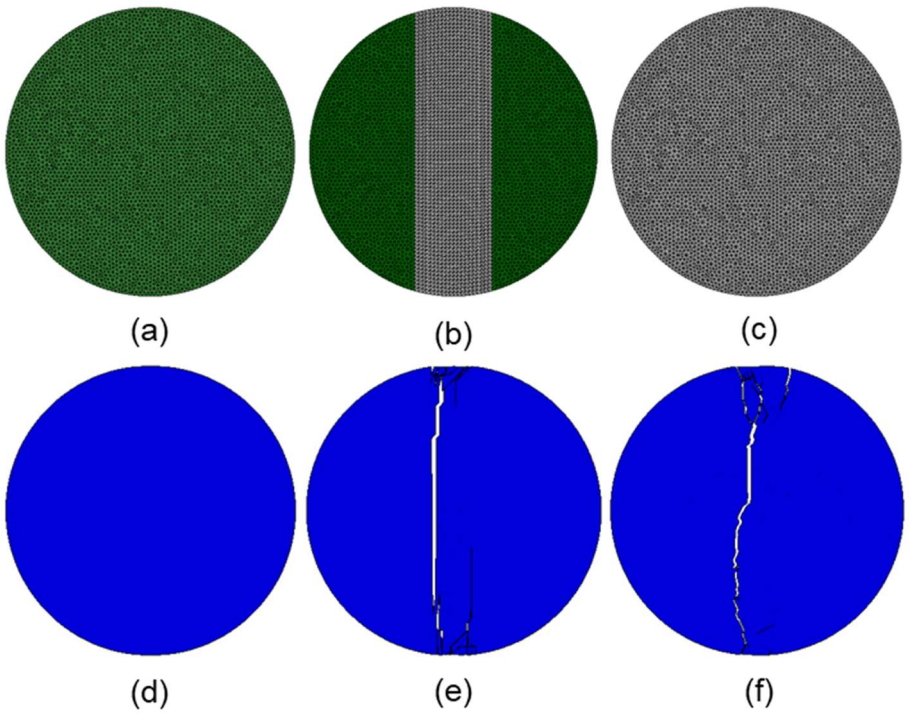

Figure 3.6. Fracture behaviours of different cohesive zones. (a) no cohesive zone, (b) partial cohesive zone, (c) full cohesive zone, (d) no cohesive zone mesh under uniaxial compression, (e) partial cohesive zone mesh under uniaxial compression, and (f) full cohesive zone mesh under uniaxial compression.

3.4.4 ***Parametric Study of CIE Parameters***

One major challenge of using CIEs to simulate fracture behaviour is parameter calibration. Due to limited experimental information for the targeted materials, a parametric study using flat-to-flat contact topology is performed to have an enhanced understanding of the parameters of CIEs and how they affect the failure load and strain. Except for the semi-empirical exponent η which only affects the post-fracture behaviour (Xiong and Xiao, 2019), key parameters including stiffness k_n, k_s, k_t, tensile

strength N_{max}, shear strength S_{max}, T_{max} and fracture energy G_n, G_s, G_t are investigated by varying the target parameter and leaving the rest constant.

Figure 3.7a shows that increasing stiffness leads to a steeper load-strain curve such that the sample fails at lower strain with a slightly lower load. Since the stiffness remains constant for Figures 3.7b, 3.7c, and 3.7d, the slopes of load-strain curves are the same before failure. By increasing the tensile strength and shear strength simultaneously, the fracture occurs at a higher strain with a higher load (Figure 3.7b). Increasing shear strength initially leads to a rise in the failure load, but beyond a certain point, further increases in shear strength have a negligible effect (Figure 3.7c) and a similar trend happens to the fracture energy (Figure 3.7d). The failure load continues to increase till $G_s = G_t = 8G_n$.

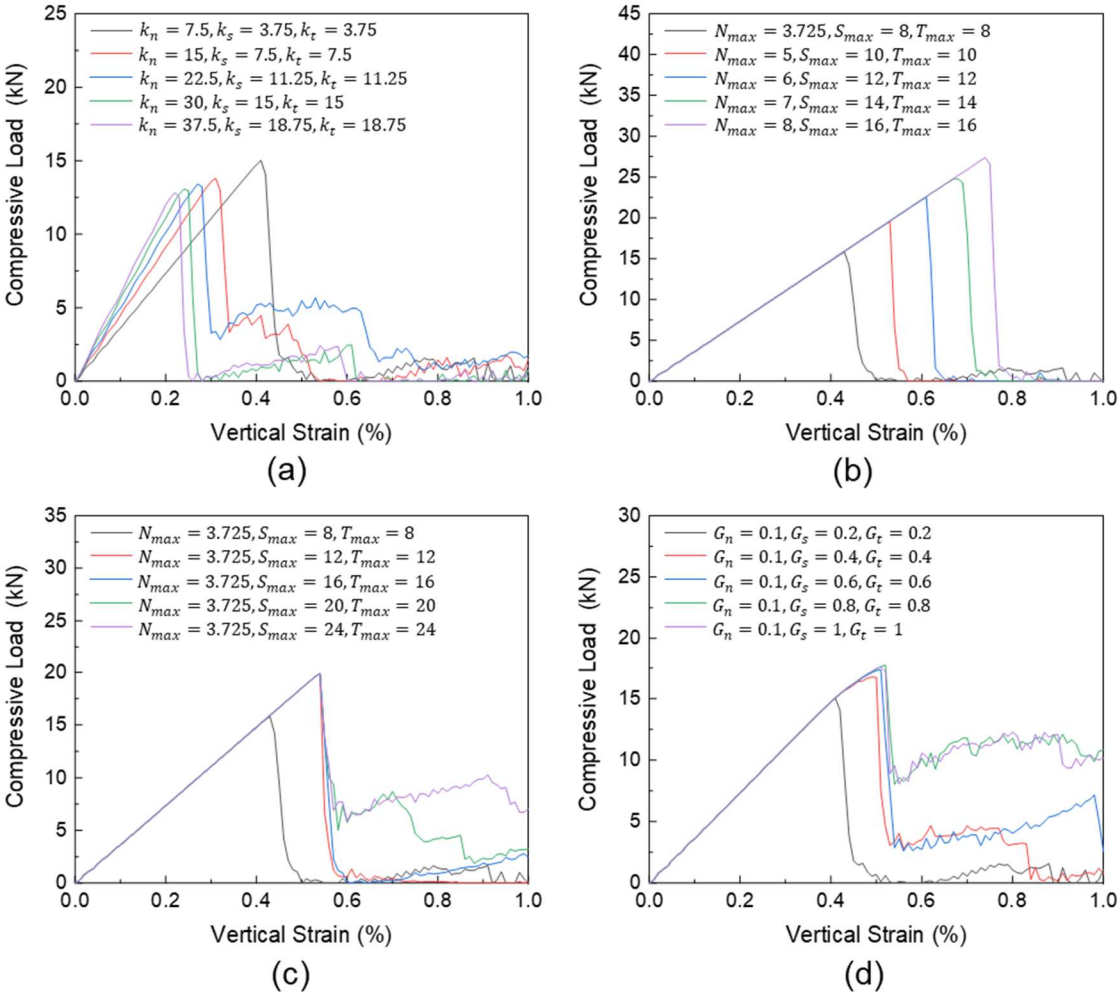

Figure 3.7. Load-strain curves affected by CIEs parameters. (a) stiffness (GPa), (b) tensile strength (MPa), (c) shear strength (MPa), and (d) fracture energy (N/mm).

3.4.5 ***Brazilian Tests***

The flat-to-point, arch-to-arch, and flat-to-flat contact topologies are reproduced

numerically for the Brazilian test. For comparison, the same displacement is applied to all tests in Abaqus/Explicit to obtain the load-strain curves, strain distribution, crack initiation & propagation, and tensile strength of the models using different contact topologies. The mesh information of each model is listed in Table 3.4.

According to the observations made during the simulations, the flat-to-point and arch-to-arch models both start with negligible initial contact area. However, their contact area evolves differently during loading due to the geometry of the loading platens. In the flat-to-point contact, the contact region gradually increases in a localised circular shape as the load progresses. In contrast, the arch-to-arch contact rapidly forms a wider contact area, developing into a substantial portion of the spherical surface. This results in more distributed stress at the early stage of loading. Meanwhile, the flat-to-flat model begins with a predefined, finite contact area, which largely remains unchanged until failure. These differences in initial and evolving contact conditions significantly affect the stress distribution, strain localisation, and crack initiation mechanisms across the models.

Load-Strain Relationships

The load-strain curves of the Brazilian test simulations using different contact topologies just before breakage are shown in Figure 3.8. For arch-to-arch and flat-to-flat contact topologies, the simulated failure loads and strains are comparable to the experimental results. However, the breakage in the model using flat-to-point contact topology occurred at a higher strain with a lower failure load compared to the experiment. Overall, the simulation results illustrate a trend that the failure load is increasing when sample-apparatus geometry changes from flat-to-point contact topology to arch-to-arch contact topology and then to flat-to-flat contact topology. Although this relationship is not the same as the experimental data measured externally in Figure 3.8, it is identical to the experimental results observed using the digital image correlation (DIC) method, which provides local strain measurements (Stirling *et al.*, 2013). Simulation representing the model with flat-to-flat contact topology shows the stiffest response to loading, failing at higher loads while experiencing less vertical strain than the other two contact topologies.

Table 3.4. Mesh information of models using different contact topologies.

Test	Mesh size (mm)	CPE3 element	COH2D4 element

Flat-to-point	1	9,000	13,384
Arch-to-arch	1	9,000	13,384
Flat-to-flat	1	8,853	13,164

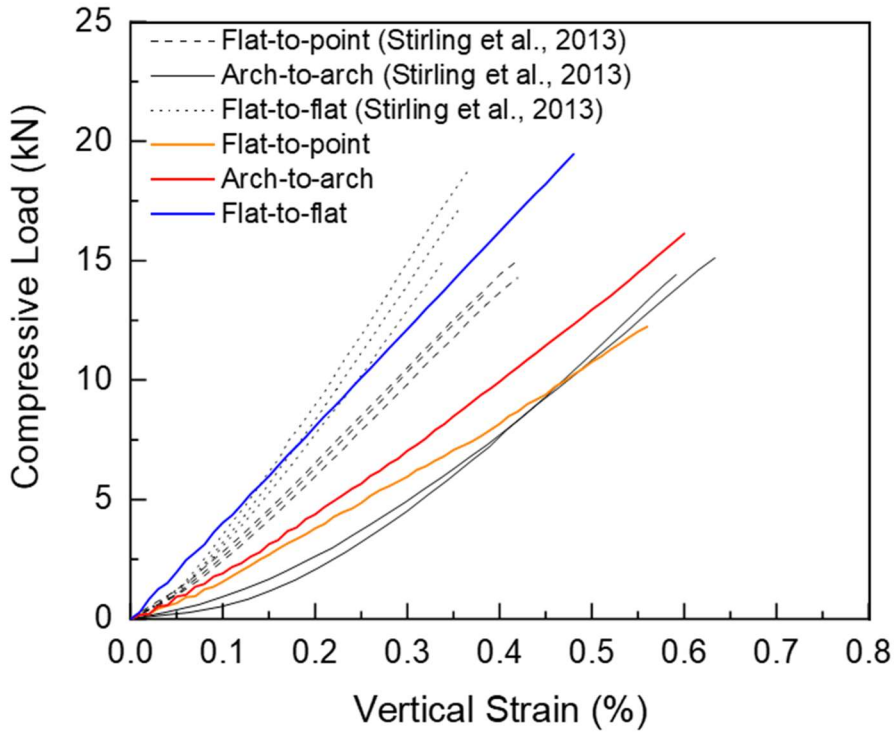

Figure 3.8. Simulated load-strain curves of different sample-apparatus geometries.

Strain Distribution Analysis

Since strain concentration induces crack initiation, the horizontal and vertical strain distribution of models using different contact topologies were generated in Abaqus/Explicit. Contour plots represent the captured state immediately prior to failure are shown in Figure 3.9. The dark red area indicates the strain concentration due to tension and the dark blue area indicates the strain concentration due to compression.

For the model using flat-to-point contact topology, Figure 3.9a highlights the two areas of dominant horizontal extension located at the top and bottom of the sample. The greatest vertical compressive strain occurs at the loading ends and can be clearly seen in Figure 3.9d. Therefore, the highest horizontal strain and largest vertical strain share the same region. This supports the observation of crushing occurring at the loading ends during the experiment (Stirling *et al.*, 2013).

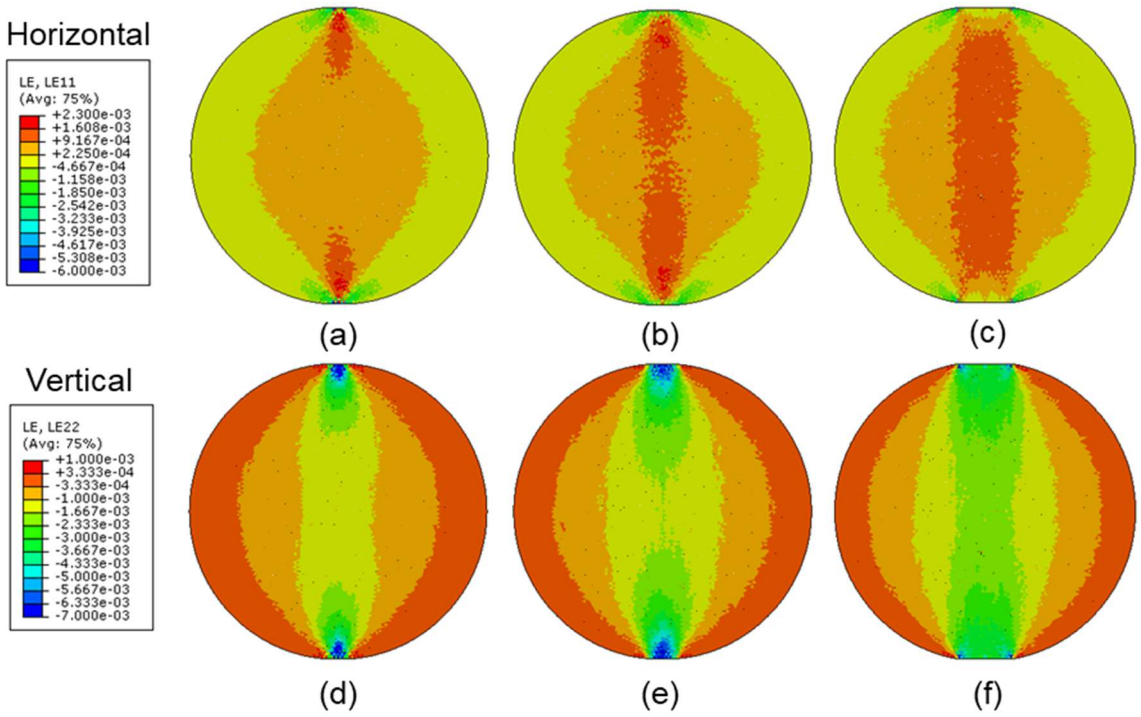

Figure 3.9. Simulated strain distributions of different contact topologies. (a), (d) flat-to-point contact topology. (b), (e) arch-to-arch contact topology. (c), (f) flat-to-flat contact topology.

For the model using arch-to-arch contact topology, the strain concentration in both horizontal (Figure 3.9b) and vertical (Figure 3.9e) plots are similar to the ones using flat-to-point contact topology. Additionally, the higher horizontal strains due to extension are well spread along the vertical axis (Figure 3.9b). It is noteworthy that the DIC results from the experiment indicated that the strain distribution is not perfectly, diametrically opposed within the disc (Stirling *et al.*, 2013). This eccentric behaviour has also been reported by several authors (Hondros, 1959; Wang and Xing, 1999; Wang *et al.*, 2004; Jianhong *et al.*, 2009) and is due to the imperfect contact between the sample and curved loading platens. The eccentric strain distribution is not observed in the contour plots and is not a problem in numerical simulation.

For the model using flat-to-flat contact topology, compared to the first two contact topologies, the strain is distributed broadly along the vertical axis in both horizontal (Figure 3.9c) and vertical (Figure 3.9f) plots, without any strain concentration at the loading ends. This reveals the reason why the crack initiated at the centre of the disc and propagated to the loading ends (Stirling *et al.*, 2013). Such behaviour represents the greatest compliance with the idealized theoretical failure criteria.

Crack Initiation and Propagation Study

Since the tensile strength is estimated according to the assumptions that failure occurs at the point of maximum tensile stress (*i.e.,* at the disc centre) and that the radial compressive stress has no influence on failure (Fairhurst, 1964), the study of crack initiation and propagation is necessary for the purpose of validating a Brazilian test. Post-fracture behaviours of different contact topologies have been captured photographically in Abaqus/Explicit, as shown in Figure 3.10.

For flat-to-point contact topology, the crack occurs at one loading end caused by the greatest compressive strain and propagates to the other loading end (Figure 3.10a). For arch-to-arch contact topology, the crack also starts from the disc top and grows towards the bottom due to the strain concentration at the loading ends (Figure 3.10b). Notably, since the higher strains are well distributed along the diameter, there are some secondary cracks at the disc centre. For flat-to-flat contact topology, the strain is distributed broadly across the diameter and the strain concentration is negligible owing to the flattened disc geometry. The crack begins from the disc centre and propagates to the loading ends. This fracture behaviour is identical to the assumptions used for tensile strength estimation.

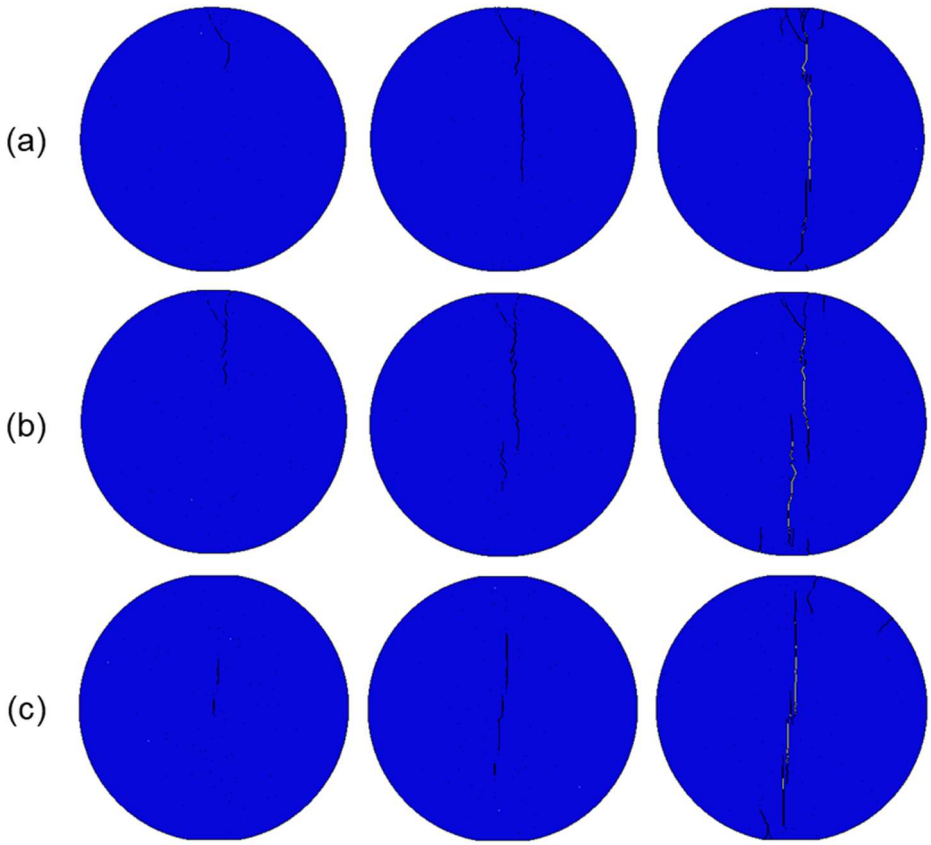

Figure 3.10. Crack initiation and propagation. (a) flat-to-point contact topology, (b) arch-to-arch contact topology, and (c) flat-to-flat contact topology.

Tensile Strength Comparison

According to the guidance of flat-to-point and arch-to-arch contact topologies, the tensile strength σ_t of the discs were calculated based on Equation 3.10, where F_f is the fracture force, d is the diameter, and t is the thickness. It assumes the materials maintain linear elasticity until failure and the maximum tensile stresses are induced normally to the loaded diameter. The tensile strength of the disc using flat-to-flat contact topology was calculated using Equation 3.11, which introduces a coefficient k that is related to the angular distance 2α. When $2\alpha = 20°$, as it was applied in the flattened Brazilian disc within this paper, $k = 0.9644$ (Wang *et al.*, 2004).

$$\sigma_t = \frac{2F_f}{\pi dt} \tag{3.10}$$

$$\sigma_t = k \times \frac{2F_f}{\pi dt} \tag{3.11}$$

Tensile strengths calculated by Stirling *et al.* (2013) using experimental results were used and averaged in Table 3.5, to compare with tensile strengths calculated from the simulations.

Table 3.5. Tensile strengths calculated for experiments (average) and simulations.

Test	Experimental results (Stirling *et al.*, 2013)		Simulation results	
	Failure load $F_f\ (kN)$	Tensile strength $\sigma_t\ (MPa)$	Failure load $F_f\ (kN)$	Tensile strength $\sigma_t\ (MPa)$
Flat-to-point	14.35	3.34	12.24	2.85
Arch-to-arch	14.32	3.33	16.14	3.75
Flat-to-flat	17.53	3.93	19.46	4.37

In Table 3.5, the observed failure loads and calculated tensile strengths from both experimental results and numerical simulations are comparable. Notably, the failure load and tensile strength from experimental results using arch-to-arch contact topology are slightly less than those using flat-to-point contact topology, whereas the failure load and tensile strength from simulation results increase gradually when switching from flat-to-point to arch-to-arch and then to flat-to-flat contact topology. One possible reason is the eccentric loading behaviour of arch-to-arch contact topology during the

experiment.

3.5 Summary

This chapter presented a computational modelling approach to simulate crack initiation and propagation in brittle materials with homogeneous, isotropic, and linear elastic properties. The key feature of this method is the application of CIEs, which enable the μFE model to effectively simulate fracturing behaviour. The feasibility of this approach was verified theoretically through crack extension tests and validated experimentally using Brazilian tests under different contact topologies. The main remarks from this chapter are as follows:

- The fracture angles obtained from the simulations show good agreement with theoretical predictions and experimental results of the crack extension test.
- The load-strain curves, strain distributions, crack initiation and propagation, and tensile strength obtained in simulations using different contact topologies align closely with those from Brazilian tests with equivalent experimental setups.
- The flat-to-flat contact topology is preferred for the Brazilian test, as it produces fracture behaviour where cracks initiate at the disc's centre and propagate toward the loading ends, consistent with assumptions used for tensile strength estimation.

The results and findings in this chapter provide a numerical framework for fracture simulation and offer a promising approach to identifying the optimal contact topology for the Brazilian test. The next chapter will build on this framework by exploring the breakage behaviour of sand particles, incorporating real particle morphology and different contact curvatures.

Chapter 4 Insights on Particle Breakage Variability

4.1 Introduction

The strength of individual particles is a crucial factor influencing their mechanical behaviour under loading and their ability to resist failure. As a fundamental property, particle strength arises from complex interactions between their internal structural characteristics and external forces. Variability in particle strength is driven by inherent heterogeneity, including differences in size, shape, and material composition. This diversity underscores the need for a comprehensive understanding of the factors affecting particle strength.

To address these challenges, this chapter proposes the use of point load tests with varying indenter sizes to investigate the effect of contact curvature on particle breakage behaviour, focusing on silica sand and crushed glass. The developed μFE model is utilised to accurately capture particle morphology while incorporating CIEs to simulate particle breakage.

4.2 Background

Accurate measurement of particle strength is critical for understanding and predicting breakage under various loading conditions. However, measuring the strength of individual irregular particles presents a challenge. The variability in particle size and shape makes sample preparation for laboratory testing challenging. Additionally, even when using the ideal morphology, the internal structure and mineralogy of each particle differ, requiring a significant number of tests to quantify particle strength (Zhang ***et al.***, 2020). This further exacerbates the already challenging situation, adding to the complexity.

Fairhurst (1964) used the Brazilian test to indirectly estimate the tensile strength σ_t of disc-shaped rock samples:

$$\sigma_t = \frac{2F_f}{\pi dt} \tag{4.1}$$

where F_f is the fracture force; d and t are the diameter and thickness of the disc sample, respectively. Later, Hiramatsu and Oka (1966) advanced this approach for irregular rock samples by considering the loading distance d_3 between two loading platens:

$$\sigma_t = 0.9\frac{F_f}{{d_3}^2} \tag{4.2}$$

Note that d_3 is also the shortest dimension of the sample, accounting for the size effect in irregular materials.

Lee (1992) performed diametrical compression of particles using two flat platens. He defined the F_f of a particle and calculated the corresponding tensile strength σ_t as follows:

$$\sigma_t = \frac{F_f}{\bar{d}^2} \tag{4.3}$$

where $\bar{d}$ is the average diameter of the particle. Furthermore, using Christensen's multiaxial failure criterion (Christensen, 2000), Russell and Muir Wood (2009) proposed an approximate expression for the compressive and tensile strength of an elastic sphere under compression:

$$\sigma_c = \frac{aF_f}{\pi R^2 \sin^2\theta_1}, \sigma_t = \frac{-aF_f}{\chi\pi R^2 \sin^2\theta_1} \tag{4.4}$$

where σ_c is the compressive strength, R is the radius of the sphere, θ is the contact area in degrees, and χ is an empirical parameter to consider heterogeneity. The parameter a can be defined, and the θ_1 can be derived by using the Hertzian contact theory as follows:

$$a = \frac{3\left(\frac{3}{32} + \frac{\sqrt{2}}{24} + \left(\frac{\sqrt{2}}{12} - \frac{1}{4}\right)\mu + \left(\frac{1}{2} - \frac{\sqrt{2}}{3}\right)\mu^2\right)}{(2-\sqrt{2})(1+\mu)}, \theta_1 = 2\cos^{-1}\left(1 - \left(\frac{3F(1-\upsilon^2)}{4ER}\right)^{2/3}\right) \tag{4.5}$$

where μ is the coefficient of friction, F is the normal force, E is Young's modulus, and υ is the Poisson's ratio. A few more recent studies improve the estimation of tensile strength by considering the shape effect. Cavarretta *et al.* (2017) mathematically examined Equation 4.3 by replacing d and t in Equation 4.1 with $\bar{d}$, finding that Lee (1992) overestimated the maximum tensile stress by 60% and suggesting that their calculated result represents a nominal strength. To address this, they proposed incorporating the intermediate dimension d_2 in Equation 4.2 to better capture the shape effect:

$$\sigma_t = 0.9\frac{F_f}{d_2 d_3} \tag{4.6}$$

indicating that the maximum tensile stress should act on the smallest vertical cross-

section of the particle, represented by d_2 and d_3. More recently, Liu *et al.* (2023) critiqued Equations 4.2 and 4.6, arguing that considering only one or two principal dimensions is insufficient to account for the irregular particles. They proposed an equivalent diameter d_a as an improvement on Equation 4.3 to represent overall particle morphology:

$$\sigma_t = \frac{F_f}{{d_a}^2} \tag{4.7}$$

where d_a is the diameter of a circle with an area equivalent to the particle's projected area, averaged from 10-20 perspectives. These perspectives were captured as the particle fell freely by gravity and rotated. This method shows expected correlations between fracture forces and nominal tensile strengths across particles of various morphologies within a similar size range.

However, the contact between the particle and loading platens is complex and may lead to varied mechanical behaviours, resulting in different fracture forces and breakage patterns, which complicates the estimation of tensile strength. By analysing the silica sand after the oedometer test, Nakata *et al.* (2001) defined the particle breakage behaviours in five classes: (1) no visible damage, (2) single abrasion, (3) multi-abrasion, (4) major splitting, and (5) further fragmentation of sub-particles. Later, Cavarretta and O'Sullivan (2012) investigated the breakage of irregular single particles subject to uniaxial compression and found that it involves four main stages to crush the sample: (1) initial rotation, (2) damage, (3) elastic response, (4) fragmentation, and (5) crushing. With the advancement of technology, Wang and Coop (2016) successfully captured real-time images of crack initiation and propagation on a single particle using a high-speed microscope camera. Based on the rapidity of failure and associated fragments, they categorised the particle failure mode into four types: (1) splitting, (2) explosive, (3) explosive-splitting, and (4) chipping. They proposed a local roundness parameter to evaluate the contact between the particle and loading platens. They suggested that high local roundness (*i.e.,* flatter contact area with flat platens) tends to cause explosive breakage with higher strength, whereas low local roundness triggers splitting breakage. Following this conclusion, they replaced the flat platens with rigid balls to minimise the effect of the loading apparatus (Wang and Coop, 2018). They found that the point loading test provides slightly more consistent strength measurements by minimising the effects of contact topology. However, they also noted that the point loading test is more difficult to perform and requires frequent replacement of the loading balls.

Alternatively, numerical simulation has been proven to be a reliable approach to overcome the difficulties faced in experiments. Tang *et al.* (2004) numerically investigated the particle breakage under point-to-point, multipoint, point-to-plane, and plane-to-plane loading in 2D. They found that the particle strength increases sequentially from point-to-point to plane-to-plane loading. Later, Zhu and Zhao (2019) extended the breakage analysis in 3D by using a spherical particle. They concluded that the number of fragments generated from a crushed particle does not exhibit any significant correlation with the coordination number (*i.e.,* the number of contact points between particles). By considering particle morphology, Liu *et al.* (2020) conducted a point load test using the DEM. They observed two crack zones developed from the compressive contact points and propagated toward each other until complete breakage occurred, resulting in the particle splitting into several pieces. However, the use of spherical particles in DEM fails to replicate the variety of particle morphologies, which plays a significant role in creating complex contact topologies that directly influence stress distribution and particle deformation (Fonseca *et al.*, 2013; Druckrey *et al.*, 2016). With the emergence of the μCT approach, Nadimi and Fonseca (2017, 2018a, 2019) adopted the μFE model from biomedical applications to investigate particle-to-particle interactions under loading. They highlighted its ability to compute the map of stress distribution inside each grain. Furthermore, Wei *et al.* (2019) applied the μFE model, coupling it with CIEs for numerically reproducing the point loading test. They compressed particles from different directions and observed that particles generally break along the smaller dimensions without experiencing chipping. They also concluded that traditional compression tests using platens tend to overestimate the breakage stresses.

While tensile strength measured from traditional compression tests is often overestimated, no universally accepted criterion has been established for conducting particle strength tests to achieve consistent results. According to observations of particle breakage, before major breakage, the particle cracks during point loading and crushes under platen loading (Tang *et al.*, 2004). Thus, a transition likely exists between these two behaviours, which can be linked by altering the contact topologies. Additionally, according to fracture mechanics, the crack should initiate at the sample centre and propagate towards the loading ends to best estimate the tensile strength (Fairhurst, 1964), whereas point loading induces crush at the loading ends and platen loading triggers off-centre breakage due to chipping and local roughness. Therefore, altering the radius of the indenters during the compression test enables this study to

observe variations in the breakage behaviour of particles. By utilising the μFE model enriched with CIEs, the same particle is compressed under various indenters, a scenario that cannot be studied experimentally, to uncover the relationship between contact curvature and fracture behaviour. Forty-two particles are tested using seven different indenters, resulting in 294 simulations. A novel equation is developed to estimate the particle tensile strength, an inherent property independent of both particle morphology and contact curvature. Furthermore, morphology analyses are carried out both before and after particle breakage to provide deeper insights into the influence of particle shape on its breakage behaviour.

4.3 Model Setup

The μFE model captures particle morphology with high fidelity while providing a more realistic representation of granular behaviour through a finite-element formulation that accounts for deformable bodies (Nadimi and Fonseca, 2018a). The breakage of particles under external loading can happen at the element-to-element interface where CIEs are incorporated. The interactions between fragments occur following Newton's second law, hard contact in normal and frictional contact in tangential directions.

4.3.1 Image Acquisition and Processing

In this study, two samples were prepared for image scanning. The first is silica sand (British rail sand) obtained from Network Rail, United Kingdom. The second is recycled crushed glass, produced by washing and crushing various types of glass bottles, then sieved using a mesh size of 1.18 mm. The μCT system, SkyScan 1176, located at the Preclinical *in-Vivo* Imaging Facility at Newcastle University Medical School was employed to capture the particle morphology. Scans were performed with a source current of 357 μA and a voltage of 70 kV. The 3D shape of the particles was obtained by reconstructing the μCT images into greyscale cross-sectional slices, achieving a voxel resolution of 8.81 μm. This resulted in 3D images with dimensions of approximately 7444 × 7444 × 7117 voxels. To improve computational efficiency during image processing, the μCT images were resized to reduce the 3D matrix dimensions while preserving the particles' size and shape characteristics (Maramizonouz, Nadimi, W. Skipper, *et al.*, 2023).

To accurately represent the complex and irregular shapes of particles while maintaining repeatability, an advanced surface reconstruction algorithm is employed, utilising the open-source Computational Geometry Algorithms Library (Rineau and

Yvinec, 2012) through a Matlab (The MathWorks Inc., 2020) based workflow comprising two stages. The first stage focuses on surface mesh extraction, where triangular iso-surfaces are generated from 3D segmented images using a refinement of the constrained Delaunay triangulation (Shewchuk, 2002). Pre-set values for density and the smallest angle are applied to control the size and number of triangles, allowing fine meshes to detail angular features while larger triangles to approximate flat surfaces. In the second stage, the sub-volumes bounded by these iso-surfaces are filled with tetrahedral elements to create a volumetric mesh. This integrated approach ensures that the volumetric mesh preserves the original boundaries of the particles while optimising the element size according to geometric constraints. It overcomes the limitations of voxel-based meshes, such as stepped boundaries, and produces high-quality elements that enhance computational efficiency and solver performance, even for complex topologies.

4.3.2 3D Cohesive Interface Elements Embedment

CIEs are embedded between adjacent elements without altering the overall mesh morphology due to their geometric zero-thickness. However, as no existing code was available for embedding CIEs in 3D, an in-house code is developed based on the framework proposed by Zhang *et al.* (2023) to implement CIEs in a volumetric mesh. The general process includes three main steps as illustrated in Figure 4.1. To begin with, every pair of tetrahedral elements in the targeted region is identified. Each pair, by definition, shares a common face consisting of three nodes. To ensure that no faces share the same nodes, the nodes of the shared face are duplicated, and the element connectivity matrix is updated accordingly (Figure 4.1b). The CIE is then inserted between the adjacent tetrahedral elements, using the nodes of the duplicated face, as shown in Figure 4.1c. Due to the definition used in Abaqus, a correction algorithm is applied to check the connectivity of CIE as described below:

1) Compute the normal of CIE based on current connectivity. For example, in Figure 4.1c: $n = Edge_{9,10} \times Edge_{9,11}$
2) Compute the centre of each element in the pair (e.g., C_1 and C_2).
3) Compute $n \cdot C_1C_2$ (scalar product):
   $n \cdot C_1C_2 > 0$, the current connectivity is consistent with the definition in Abaqus.
   $n \cdot C_1C_2 < 0$, the current connectivity is incorrect, switch the position of the 2nd and 5th nodes with the 3rd and 6th nodes, receptively. For example, the new connectivity of CIE would be $\{9\ 11\ 10\ 6\ 8\ 7\}$.

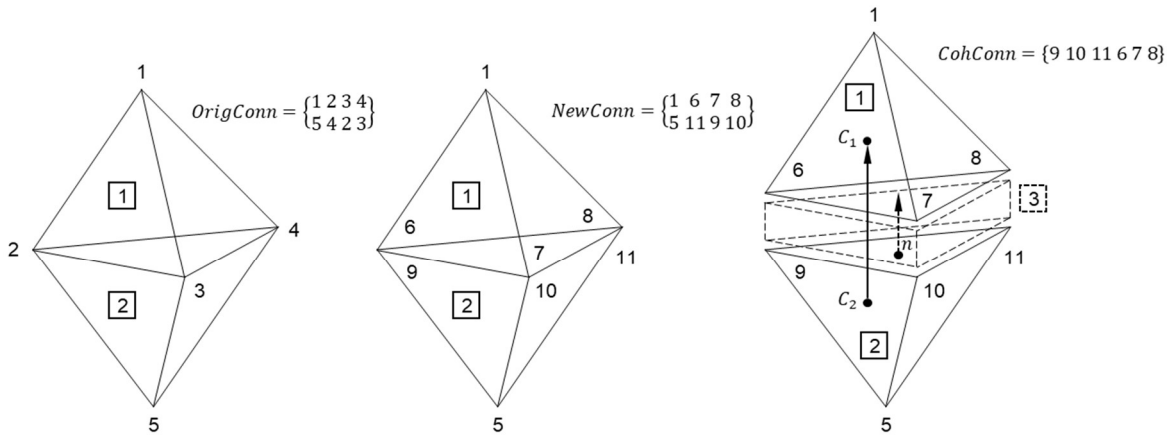

(a) Original mesh (b) Duplicating nodes (c) Embedding CIE

Figure 4.1. Embedding CIE between each pair of tetrahedral elements.

4.3.3 ***Model Validation***

Using the proposed particle reconstruction framework outlined in Section 4.3.1, the mesh for the LBS particle was generated from the original data obtained by Zhao *et al.* (2015) through μCT imaging during a single particle crushing test. Two loading platens were created in the numerical domain to simulate the uniaxial compression. The bottom platen was assigned fixed boundary conditions in all directions, while the top platen was allowed to move only in the vertical direction. According to the experimental observation, no plastic deformation occurred in the loading platens during the test. Therefore, to avoid the significant heavy computational burden that would be obtained, the loading platen was considered as a rigid body during the simulation. The material properties of LBS particles were determined using the calibrated parameters of quartz sand from Table 3.1 in Chapter 3, with consideration of breakage in the tangential direction, as shown in Table 4.1.

Table 4.1. Material parameters of LBS particles

Solid Elements		
Density	$\rho\ (kg/m^3)$	2500
Young's modulus	$E\ (GPa)$	63
Poisson's ratio	υ	0.22
CIEs		
Normal stiffness	$k_n\ (N/mm^2)$	63000

First shear stiffness	$k_s\ (N/mm^2)$	31500
Second shear stiffness	$k_t\ (N/mm^2)$	31500
Tensile strength	$N_{max}\ (MPa)$	25
First shear strength	$S_{max}\ (MPa)$	12
Second shear strength	$T_{max}\ (MPa)$	12
Mode I fracture energy	$G_n\ (N/mm)$	0.1
Mode II fracture energy	$G_s\ (N/mm)$	0.2
Mode III fracture energy	$G_t\ (N/mm)$	0.2
Semi-empirical criterion exponent	η	2
Contact law		
Friction coefficient	μ	0.5

The simulation results, including the fracture pattern and force-displacement curve, are presented in Figure 4.2 for comparison with the lab tests. The simulated force-displacement curve and particle fracture pattern show a good agreement with the experimental results. This confirms that the selected physical parameters are reasonable and that the μFE model is reliable for subsequent simulations examining the effect of contact curvature on breakage behaviour.

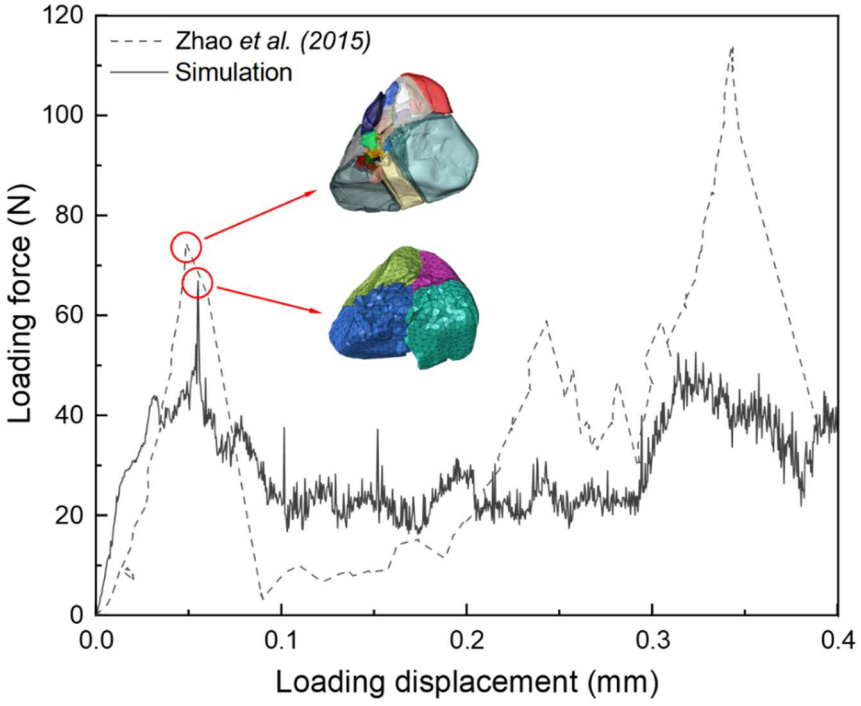

Figure 4.2. Validation of μFE model against experimental data.

4.3.4 ***Modified Point Load Tests***

Tensile strength estimated from traditional compression tests with flat platens is often higher than that obtained from point load tests, as demonstrated both experimentally and numerically. In the following study, the breakage behaviour of single particles under different contact curvatures is investigated, bridging the gap between point loading and platen loading. As illustrated in Figure 4.3, the radius of indenters is increasing from 0.1 mm to 0.2 mm, 0.4 mm, and up to 6.4 mm The curvature of 0.2 mm matches the point ends used by Wang and Coop (2018), while the curvature of 6.4 mm approximates a flat contact, given the relatively small size of the tested particle. For comparison, all tested particles were rotated around their geometric center to achieve the most stable contact with the smallest indenter. This orientation was then preserved for subsequent tests using larger indenters.

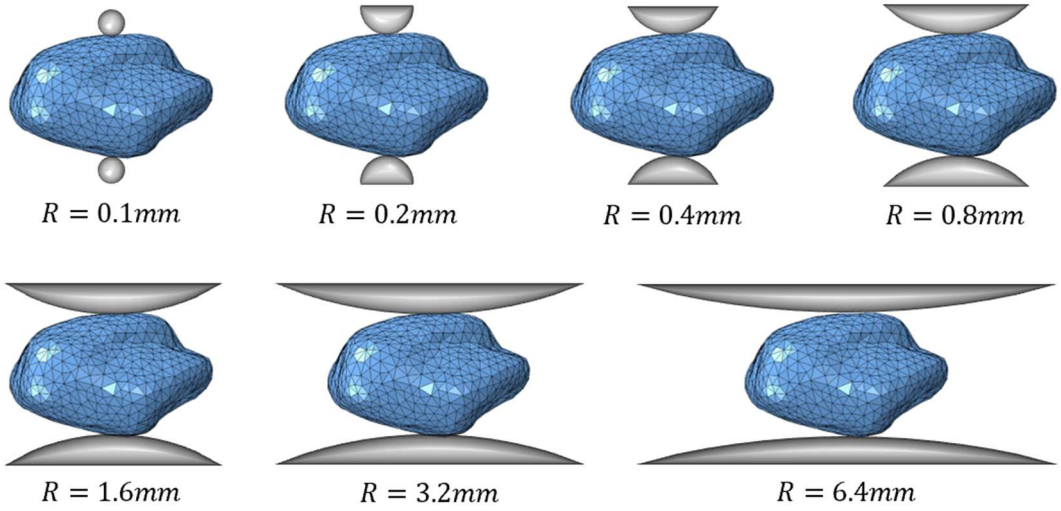

Figure 4.3. Modified point loading test using different indenters.

Two types of material are used in this study: silica sand and crushed glass. Given that tensile strength is significantly influenced by particle size (Nakata, Kato, *et al.*, 2001), the size of each particle was adjusted during reconstruction to match the surface area of a reference sphere with a 0.5 mm radius. This normalisation ensures a more consistent contact area across particles and minimises the influence of size-related effects. To further isolate the influence of particle morphology and contact curvature on breakage behaviour, differences in material microstructure and intrinsic mechanical properties between silica sand and crushed glass are deliberately disregarded. Instead, both materials were assigned identical material properties, as listed in Table 4.1. This simplification is justified by the study's objective: to understand how morphological

characteristics govern the breakage mechanisms, independent of material composition. By controlling for size and material, the observed differences in breakage behaviour can be more confidently attributed to variations in particle morphology and contact curvature.

In order to quantify the particle morphology, four characteristics listed in Table 4.2 have been measured via an open source software SHAPE (Angelidakis *et al.*, 2021). The results are plotted in Figure 4.4 using the empirical cumulative distribution function (eCDF). It highlights the distinct differences in shape characteristics between the two groups, with crushed glass generally exhibiting more elongated shapes compared to the more spherical and convex silica sand.

Table 4.2. Four key characteristics of particle morphology.

	Formula	Range	Parameters
Flatness	$\frac{{d_2}^2}{d_1 \cdot d_3 + {d_2}^2} - \frac{d_3}{d_1 + d_3}$	(0,1]	d_1: Longest dimension d_2: Intermediate dimension
Elongation	$\frac{d_1 \cdot d_3}{d_1 \cdot d_3 + {d_2}^2} - \frac{d_3}{d_1 + d_3}$	(0,1]	d_3: Shortest dimension
Sphericity	$\frac{\sqrt[3]{36\pi V^2}}{A}$	(0,1]	V: Volume; A: Surface area
Convexity	$\frac{V}{V_{CH}}$	(0,1]	V_{CH}: Volume of convex hull

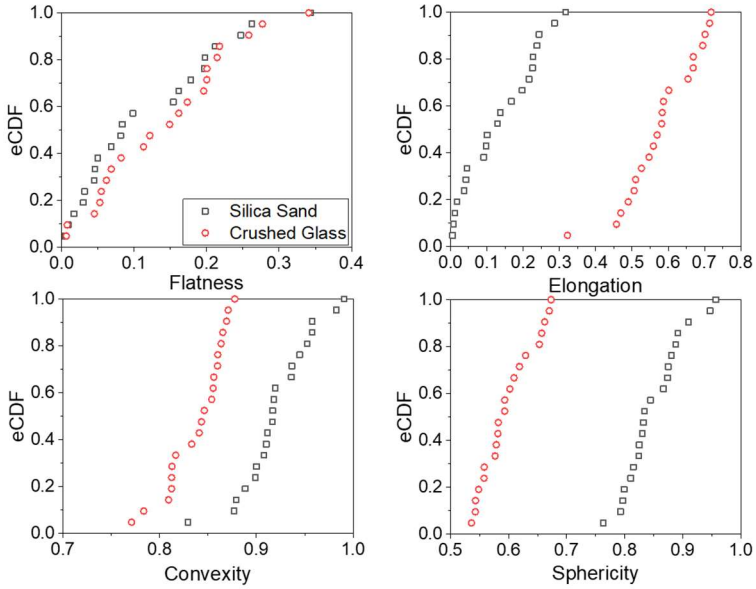

Figure 4.4. eCDF of the morphological characteristics of silica sand and crushed glass.

4.4 Results and Discussion

This section focuses on the statistical analysis and discussion of the results, exploring how contact curvature correlates with breakage behaviour by considering particle morphology.

4.4.1 Fracture Force

Figures 4.5a and 4.5b present the typical force-strain curves from particle breakage simulations for silica sand and crushed glass, respectively. The simulations show convergence when the indenter radius exceeds 1.6 mm for both materials, indicating that an indenter radius of 6.4 mm sufficiently represents a flat contact area, and larger radii are unnecessary. For both materials, a clear trend can be observed that as the indenter size increases, the peak force also increases, while its occurrence shifts to a smaller strain range.

In the case of silica sand in Figure 4.5a, the peak force corresponds to the fracture force, as indicated by a substantial drop in load following the peak. This behaviour suggests that fragments lose contact with the indenter after crushing occurs. However, for crushed glass in Figure 4.5b, this abrupt load drop is only observed with smaller indenters. For larger indenters, the load exhibits a gradual increase until the end of the simulation. The inset in Figure 4.5b provides insights into the contact behaviour during breakage: although significant fragmentation occurs, the elongated shape of the fragments maintains contact with the larger indenters, resulting in a smoother load

transition.

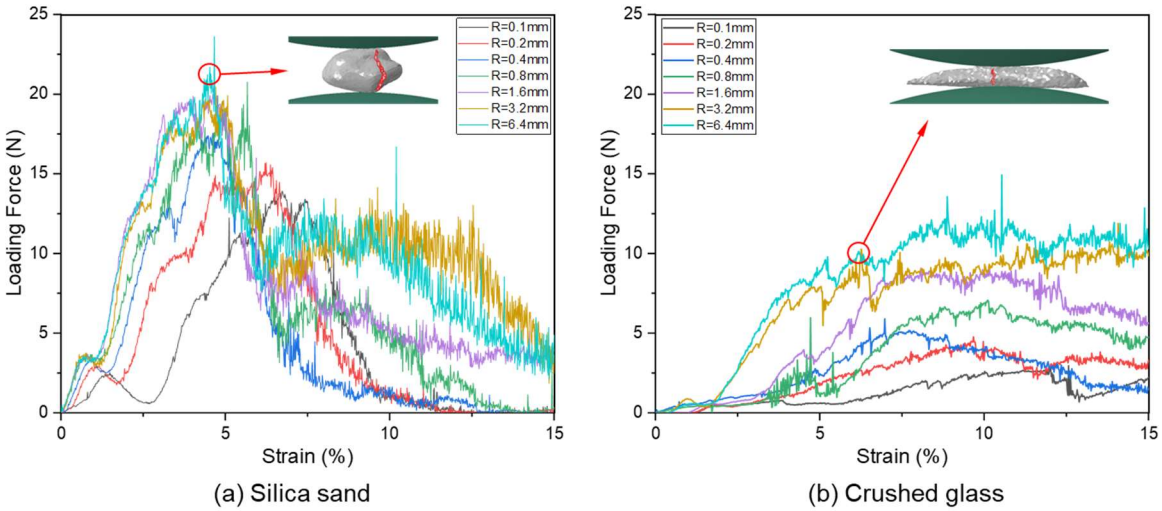

Figure 4.5. Typical load-strain curves of silica sand and crushed glass.

Figure 4.6 summarises the fracture forces experienced by particles at the time of major breakage. For both silica sand and crushed glass, the fracture force increases with indenter size. The data distribution is more concentrated with smaller indenters, while it becomes more dispersed as the indenter radius increases. This is due to more complex interactions between particles and larger indenters as the local roundness plays a more significant role. Comparing the two materials, silica sand exhibits higher fracture forces than crushed glass, which is attributed to its particle shape contributing to a greater loading distance. In conclusion, contact area and loading distance have a more pronounced effect on fracture force compared to particle roundness.

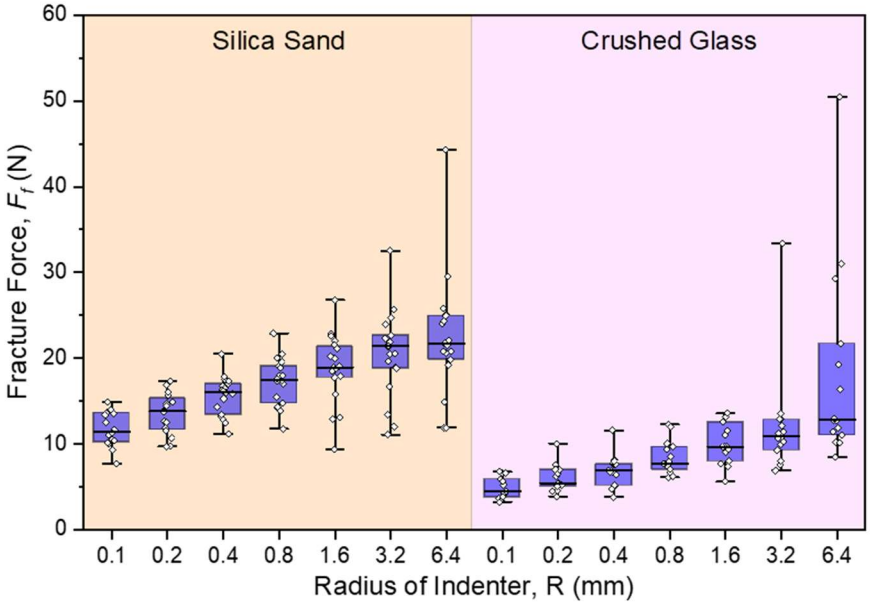

Figure 4.6. The fracture force of silica sand and crushed glass.

4.4.2 ***Contact Area***

The contact area between the tested particles and the indenters was recorded throughout the simulations. To investigate its effect on the mechanical behaviour of the particle, its relationships with fracture force, particle morphology, and indenter size are examined.

Effect of Fracture Force on Contact Area

When the particle experiences major breakage, the associated contact area is captured and plotted against its fracture force, as shown in Figure 4.7. When the tested particle is exposed to the same contact area, silica sand usually requires a higher force to trigger the breakage process compared to crushed glass. This is because the stress in silica sand, owing to its compacted shape, could be distributed more evenly across the contact area, whereas the crushed glass tends to experience higher stress concentrations at the points of contact due to its irregular geometry. Thus, for the same contact area, crushed glass breaks at lower forces compared to silica sand.

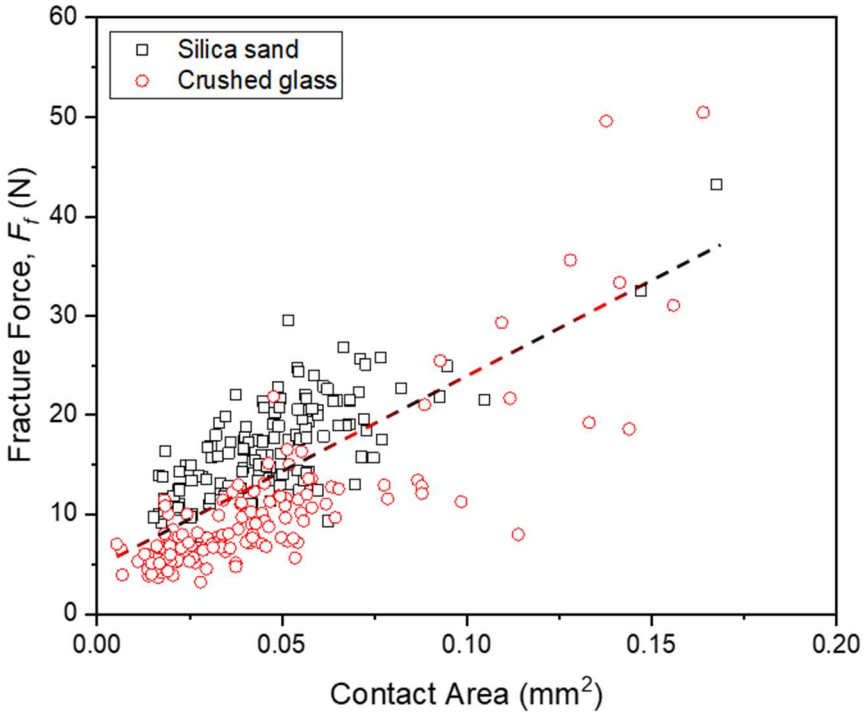

Figure 4.7. Relationship between contact area and fracture force.

Effect of Indenter Size on Contact Area

The contact area between the particle and indenter throughout the simulation has been visualised for silica sand in Figure 4.8a and crushed glass in Figure 4.8b. The solid lines represent the mean contact area values across simulations using the same indenter size, while the shaded regions indicate the standard deviation. As expected, larger indenters generate a larger contact area for both materials. However, the trends differ between the two materials.

For silica sand in Figure 4.8a, as the indenter size increases, the slope of the contact area curve increases, peaking at a later strain stage. Convergence is observed for larger indenters (*i.e.*, 3.2 mm and 6.4 mm), confirming that no larger radii are required. In contrast, crushed glass in Figure 4.8b shows no peak in the contact area curve, with the slope gradually increasing as the indenter size grows. This trend is attributed to the elongated shape of the crushed glass, allowing larger indenters to create a more extensive contact area.

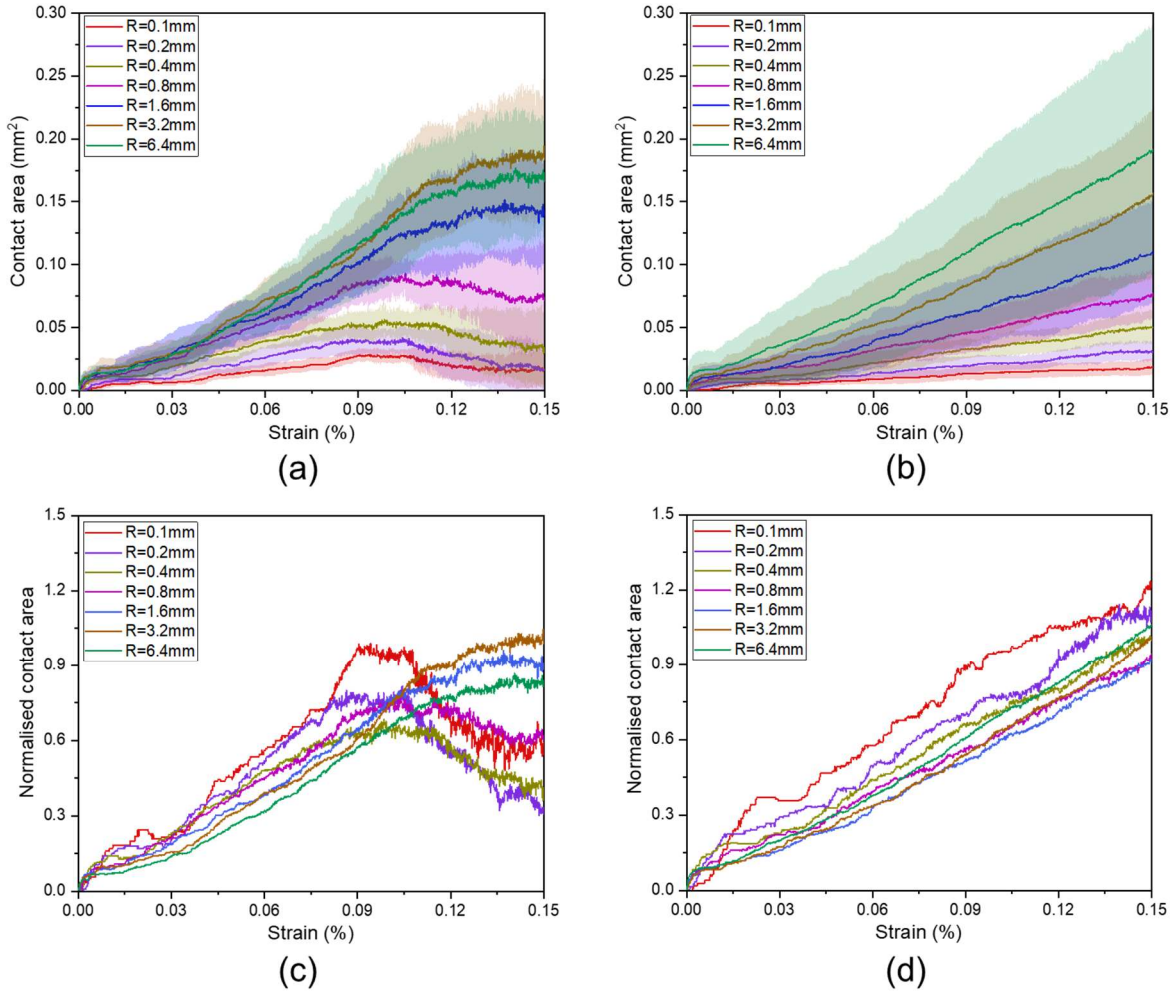

Figure 4.8. Relationship between contact area and indenter size. (a), (c) silica sand and (b), (d) crushed glass.

To better understand the relationship between indenter size and contact area, the extracted contact area values are normalised based on the theoretical contact area, A_H, derived from Hertzian contact theory below:

$$A_H = \pi d_i \left(\frac{R_1 R_2}{R_1 + R_2} \right) \tag{4.8}$$

where d_i is the indentation depth, R_1 is the radius of each indenter, and R_2 is half of the d_1 of the tested particle. After normalisation, the contact areas from different indenters begin to converge, as shown in Figure 4.8c for silica sand and Figure 4.8d for crushed glass. The normalised contact area for smaller indenters becomes more pronounced compared to larger indenters, with a decreasing trend as the radius increases. Throughout the simulation, most data exhibit an increasing trend, except for the peaks observed with smaller indenters, particularly in Figure 4.8c. This is due to the smaller indenter surfaces not being large enough to maintain contact with the

fragments during particle breakage, causing significant drops in the plots.

Despite these fluctuations, the overall converging trend remains consistent for all tested particles before breakage. This suggests a potential method for estimating tensile strength, independent of the specific loading methods used, which will be further discussed in the following section.

4.4.3 Tensile Strength

Determination of Tensile Strength

The tensile strength of the silica sand and crushed glass under different indenters is first calculated using the method of Hiramatsu and Oka (1966), with the corresponding results displayed in Figure 4.9a. The white dots represent the estimated tensile strength, while the flat-end bars indicate the minimum and maximum values. The box shows the upper and lower quartiles of the data, with the horizontal line representing the median value.

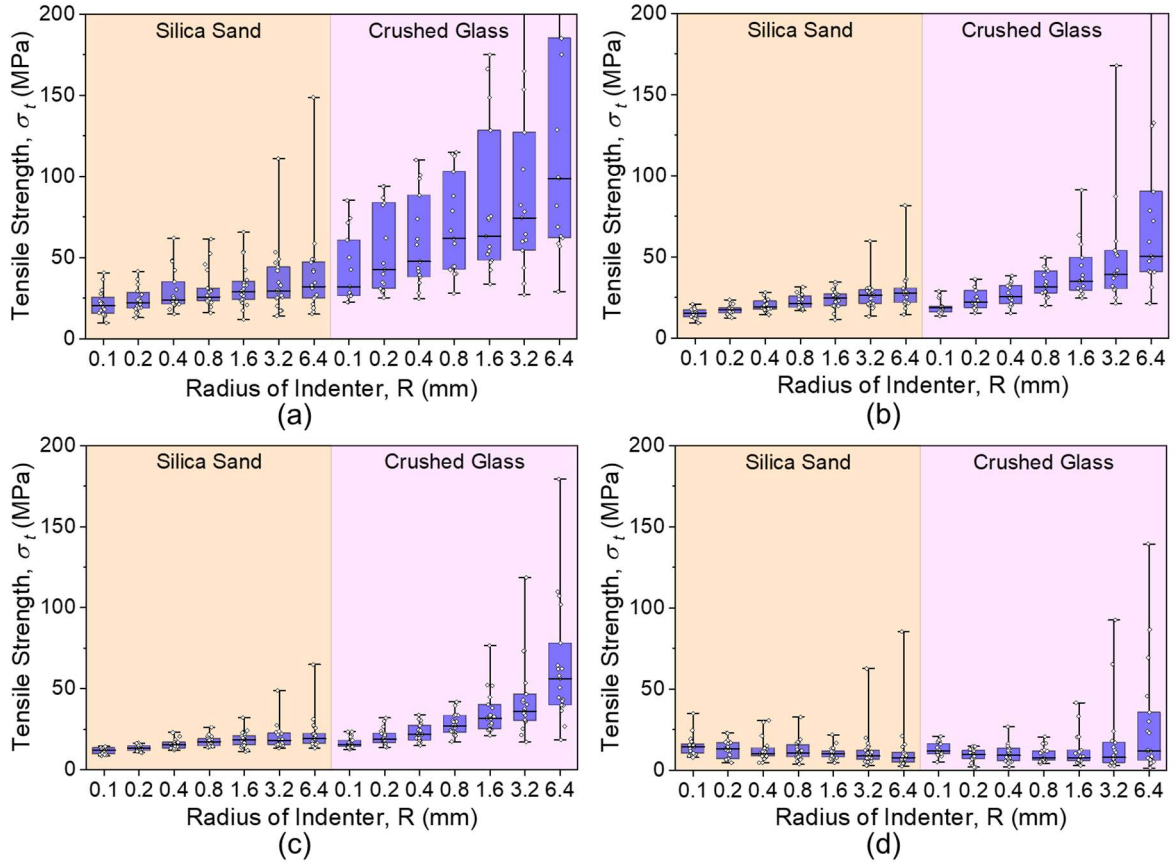

Figure 4.9. Estimated tensile strength using different methods: (a) Hiramatsu and Oka (1966), (b) Cavarretta *et al.* (2017), (c) cross-sectional area, and (d) present study.

In Figure 4.9a, the estimated tensile strength for silica sand across different indenters shows a consistent median value and a similar range of variation. However, the data for crushed glass display a wider distribution, with median values increasing as the indenter size grows. This indicates that the loading distance d_3 used in Equation 4.2 by Hiramatsu and Oka (1966) can capture the size effect but has limited capability to account for the shape effect.

$$\sigma_t = 0.9\frac{F_f}{{d_3}^2} \tag{4.2}$$

To better quantify the shape effect, the Equation 4.6 provided by Cavarretta *et al.* (2017) incorporating the measurements of the two principal axes of the particle is used and the results are shown in Figure 4.9b. By considering the shape effect in two dimensions, the variation range of the data and the differences between median values for crushed glass are reduced. This result is further validated in Figure 4.9c, where the tensile strength is calculated directly using the cross-sectional area where the crack initiated and propagated.

$$\sigma_t = 0.9\frac{F_f}{d_2 d_3} \tag{4.6}$$

Both Figures 4.9b and 4.9c show an increase in data variation and median values as the indenter size increases. This agrees with experimental observations, where traditional compression tests using flat platens (with a radius approaching infinity) tend to overestimate the tensile strength, while point load tests with smaller indenters provide more consistent strength measurements (Wang and Coop, 2018). However, because tensile strength is an inherent material property, the estimated values for the same particle should be independent of indenter size.

Using the normalised contact area, which is independent of loading curvatures, the fracture force is normalised to estimate the tensile strength. A new equation is proposed:

$$\sigma_t = F_f \times \frac{A_c}{A_H} \times \frac{1}{A_{cs}} \times \frac{2r}{d_1} \tag{4.9}$$

where A_c denotes the contact area measured at the moment of breakage, while A_{cs} represents the cross-sectional area subjected to tension (see Figure 4.10). The factor $2r/d_1$ accounts for the shape effect, in which r is the radius of the equivalent volume sphere of the particle.

Based on Equation 4.9, the corresponding results are shown in Figure 4.9d. It is

evident that when the fracture force is normalised by the contact area, the estimated tensile strength from different indenters becomes more consistent, offering a more reliable method for estimating tensile strength independently of the loading method. While this approach provides higher accuracy by accounting for the actual contact area at failure, it requires μCT imaging during the test to capture precise geometric details. This results in increased processing time and may not be practical for large-scale testing involving many particles. In contrast, methods proposed by Hiramatsu and Oka (1966) and Cavarretta et al. (2017) offer simpler and faster estimations using basic geometric measurements, making them more suitable for high-throughput experiments, although with reduced accuracy.

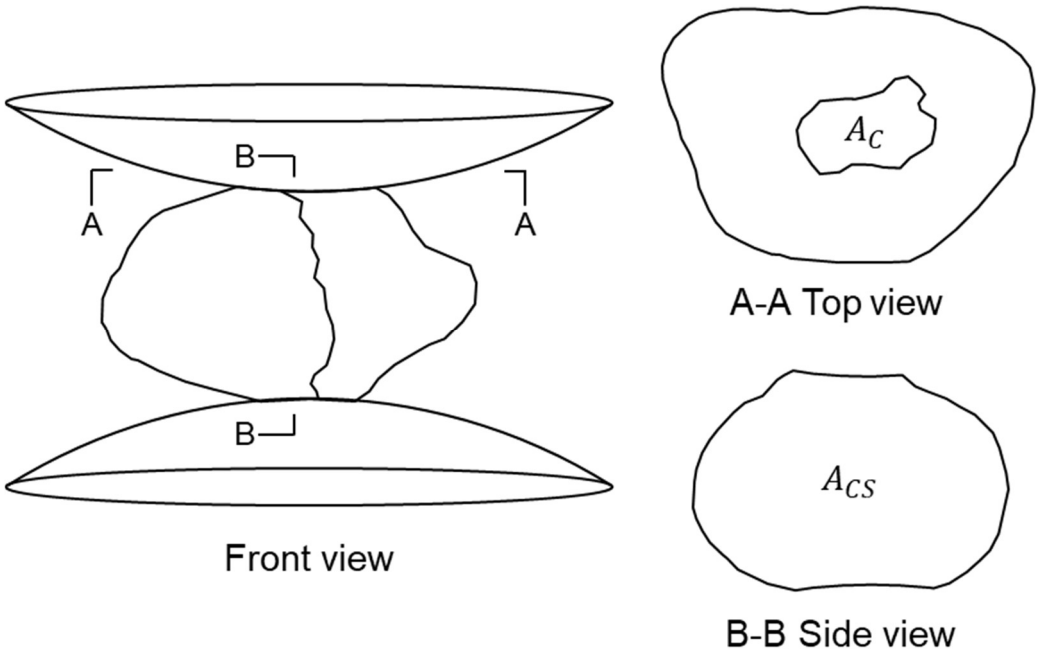

Figure 4.10. Schematic diagram of the moment when particle breakage occurs.

Distribution of Tensile Strength

The survival probability P_s is used to analyse the estimated tensile strength according to the equation below proposed by Nakata *et al.* (1999):

$$P_s = \frac{n(\sigma_t \geq \sigma)}{N} \tag{4.10}$$

where n is the number of particles with σ_t equal or greater than a given σ, and N is the total number of particles. The results shown in Figure 4.11a indicate that silica sand behaves similarly to crushed glass, with a slightly higher survival probability at higher tensile strength. Most of the computed tensile strength values fall within the range of 0~20 MPa. These high values have been retained to reflect the full output of

simulations, but they are not representative of the overall distribution. In practice, such extreme values may be due to rare contact configurations or localised mesh artefacts.

Compared to experimental values commonly reported in the literature (i.e., 30~40 MPa), the simulated strength values are generally lower. This discrepancy may stem from differences in material parameters, such as stiffness, tensile/shear strength, and fracture energy, used in the numerical model. Additionally, assumptions made in the simulation setup, including friction coefficient and boundary conditions, can influence the results. It's also important to note that the tensile strength in this study is based on Equation 4.9, which provides a more precise estimate by accounting for the contact area. In contrast, experimental values reported in the literature are typically derived from tests involving rapid manual measurements, which can lead to higher but less accurate apparent strengths.

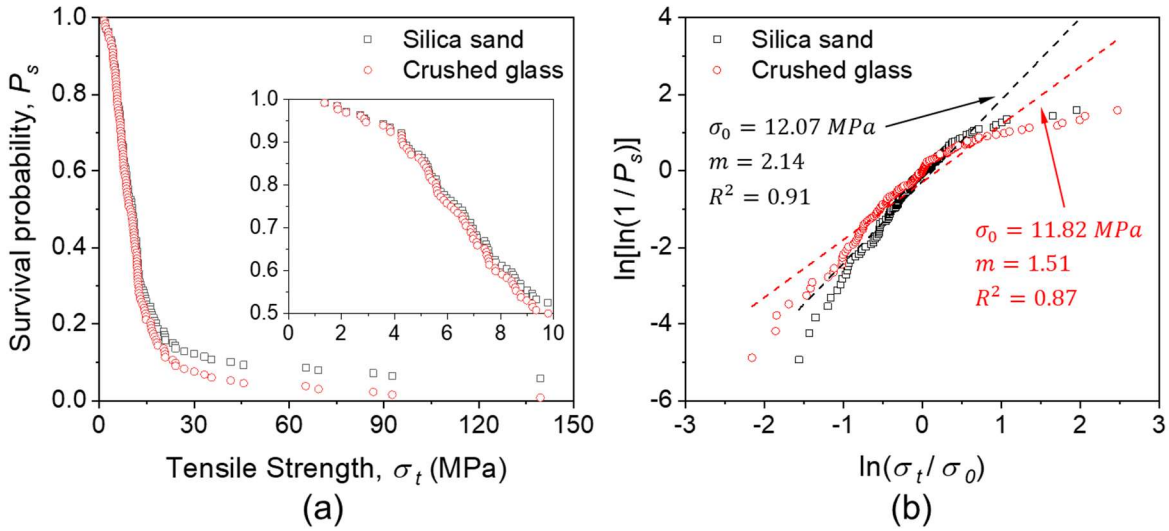

Figure 4.11. (a) Particle survival probability. (b) Weibull distribution of tensile strength.

Furthermore, the Weibull function (Weibull, 1951) is used to characterise the relationship between P_s and σ_t:

$$P_s = exp\left[-\left(\frac{\sigma_t}{\sigma_0}\right)^m\right] \tag{4.11}$$

where σ_0 is the characteristic tensile strength and corresponds to σ_t at $P_s = 37\%$. The Weibull modulus m is a shape parameter that describes the distribution, with a higher value indicating less variation in tensile strength. By taking the natural logarithm twice on both sides of Equation 4.11, the Weibull function transforms into a linear relationship:

$$ln\left[ln\left(\frac{1}{P_s}\right)\right] = m\ ln\frac{\sigma_t}{\sigma_0} \tag{4.12}$$

According to Equation 4.12, the Weibull distribution is plotted in Figure 4.11b. Linear

relationships are established for both silica sand and crushed glass, indicating that the estimated tensile strength for both materials follows the Weibull distribution. The smaller m of crushed glass suggests a wider dispersion in tensile strength compared to silica sand.

4.4.4 Particle Fracture Pattern

In this study, three fracture modes—local crushing, major splitting, and chipping—were commonly observed during particle breakage with different indenters, as illustrated in Figure 4.12. The local crushing mode occurs when the indenter penetrates the particle, causing localised breakage and generating small fragments (see Figure 4.12a). The major splitting mode is characterised by the particle breaking into two nearly equal major fragments (see Figure 4.12b). The chipping mode is defined when the particle produces two or more fragments, with at least one major fragment and one or more minor fragments (see Figure 4.12c).

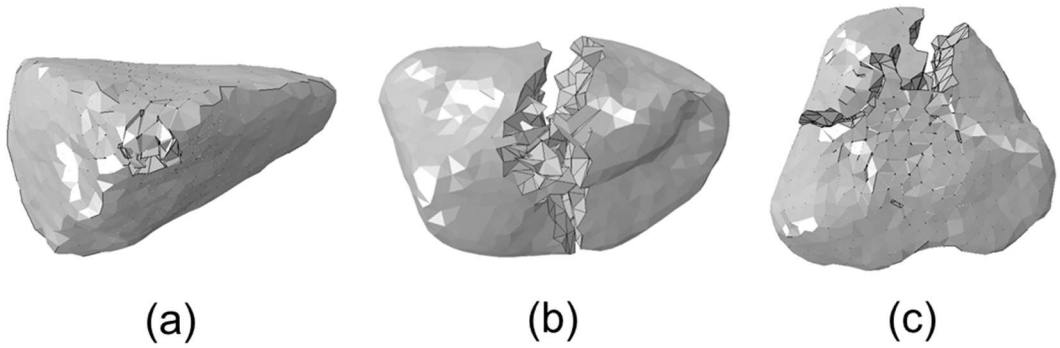

Figure 4.12. Different fracture modes: (a) local crushing, (b) major splitting, and (c) chipping.

According to the observations, when the indenter size is small, particle breakage often initiates with local crushing and then progresses to major splitting. However, when the indenter is larger, the increased contact area minimises local stress concentration and leads to the chipping mode of fracture.

To quantify the fracture modes of major splitting and chipping across all simulations, an in-house code is developed to capture the fragments generated during particle breakage. Through trial and error, the volume ratio between the major and minor fragments is set at 0.7 to better reflect the transition from major splitting to chipping. Using this threshold, the fracture modes for all particles are summarised in Figure 4.13. The results align with the mentioned observations: the dominant fracture mode is major splitting with smaller indenters, transitioning to chipping as the indenter size increases.

This transition is more pronounced in silica sand compared to crushed glass, likely due to its more compact shape.

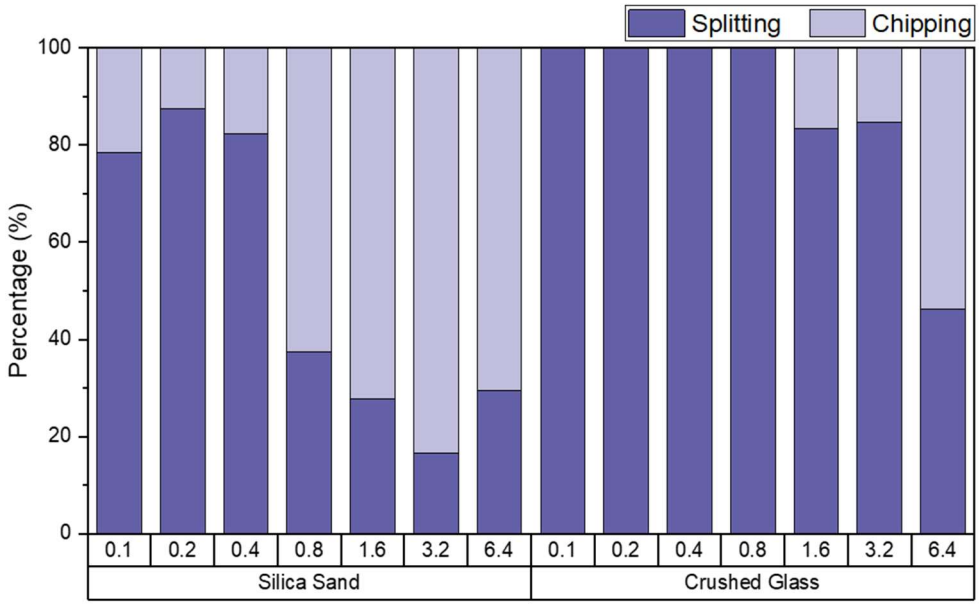

Figure 4.13. Percentage histogram of fracture mode using different indenters.

4.4.5 Characterisation of Fragment Morphology

Furthermore, the morphological characteristics of fragments are plotted in Figure 4.14 to compare with their parent particles. Based on the results, the fragmentation patterns of silica sand and crushed glass differ significantly. The fragments of silica sand tend to become more angular after breakage, showing lower convexity and sphericity values, indicating more irregular breakage. In contrast, the fragments of crushed glass maintain more self-similar shapes, displaying a more uniform fragmentation pattern, particularly with reduced elongation.

The radius of indenters plays a key role in influencing convexity and sphericity: larger indenters generally produce fragments with smaller convexity and sphericity values, leading to more irregular fragmentation. This trend is particularly pronounced in silica sand. However, an exception is observed in crushed glass, where sphericity actually increases after breakage, suggesting a more uniform fragmentation process. Overall, crushed glass, with its isotropic nature, retains more consistent fragment shapes across different indenter sizes, making its fragmentation more predictable.

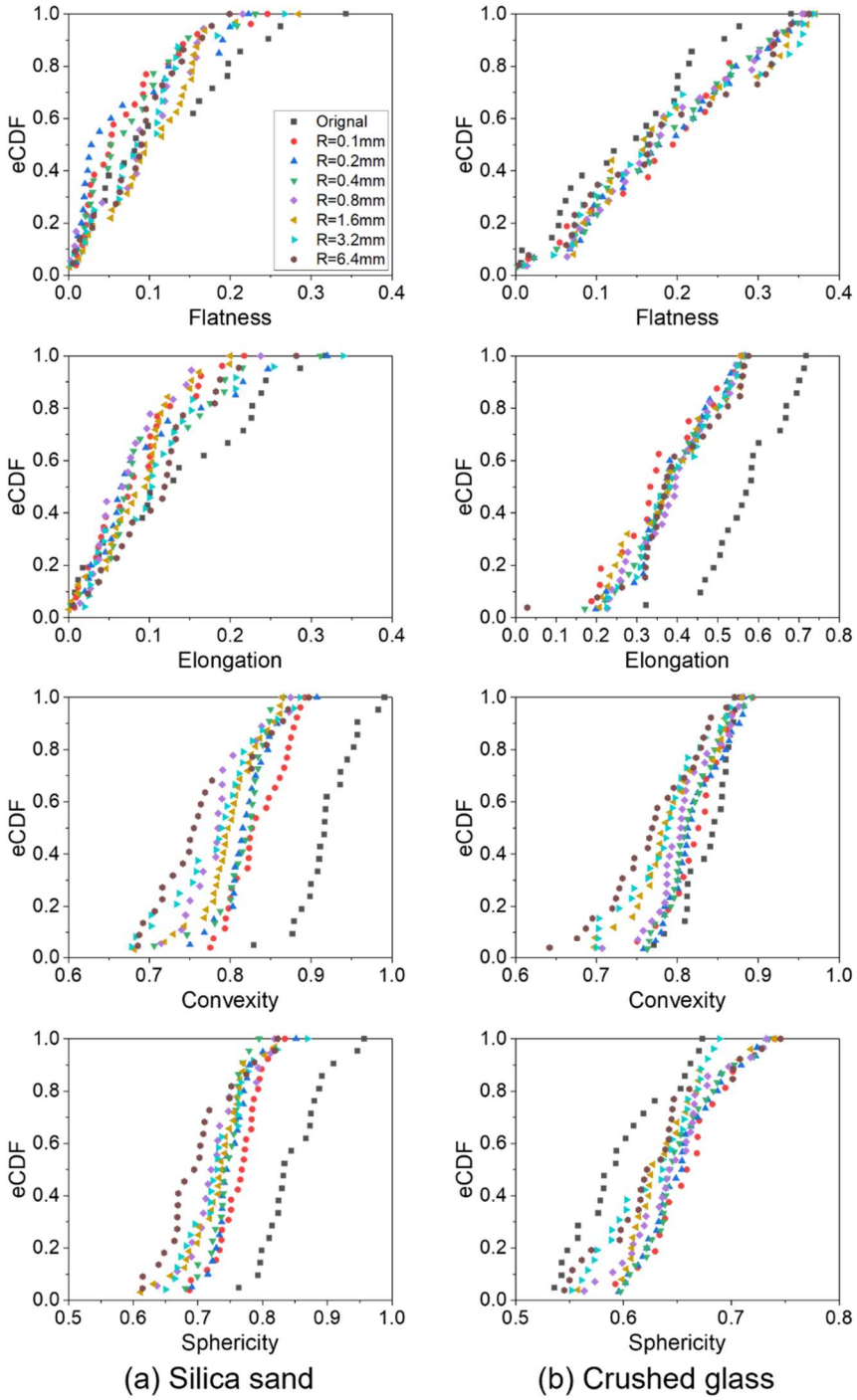

Figure 4.14. eCDF of the morphological characteristics of parent and child particles.

4.5 Summary

In this chapter, silica sand with compact shapes and crushed glass with elongated shapes were tested through a point loading test using different indenters, with radius sizing from 0.1 mm to 6.4 mm, to investigate the effect of contact curvature on particle breakage behaviour. The key findings are summarised as follows.

- The μFE approach coupled with CIEs is able to simulate particle breakage behaviour effectively.

- The load-strain curves from silica sand and crushed glass behave differently.
- A new method has been proposed to estimate particle tensile strength, independent of contact curvatures.
- The fracture mode of single particles loaded by a small indenter is major splitting and the fracture mode shifts to chipping when a larger indenter is involved.
- Silica sand tends to generate irregular fragments with lower convexity and sphericity values. In contrast, the fragments of crushed glass maintain more self-similar shapes with reduced elongation.

The results and findings in this chapter demonstrate the ability of the developed μFE approach to model particle breakage in 3D effectively. The study highlights how contact curvature influences fracture modes and particle strength, providing a deeper understanding of breakage mechanisms.

Chapter 5 The Impact of Sand Particle Breakage on Adhesion at the Wheel-Rail Interface

5.1 Introduction

In the railway industry, the term “adhesion” is defined as the amount of traction present in the wheel-rail interface. It plays a vital role in providing controlled slip and slide during acceleration and braking, respectively. This makes adhesion a critical factor in train performance, enabling efficient acceleration and responsive braking to ensure safe operation. However, insufficient adhesion can lead to prolonged acceleration and braking distances, significantly increasing the risk of accidents. To address these challenges, sand particles are often applied at the wheel-rail interface from an on-board device to enhance adhesion levels, particularly under adverse conditions such as contamination.

This chapter explores the mechanisms behind adhesion enhancement at the wheel-rail interface through the developed μFE model. To isolate the effects of sand particles, the wheel and rail are modelled with smooth surfaces. Then, the mechanical behaviour of sand particles during wheel-rail interaction is investigated in 2D. Particular attention is given to how particle morphology, including size and aspect ratio, influences adhesion levels during traction and braking (pure sliding) operations. To provide a more realistic simulation of the rail, the model is refined through the introduction of additional parameters. Rail roughness is first introduced to quantify its effect on adhesion level, followed by the inclusion of rail plastic deformation. By incorporating these parameters, the model provides a comprehensive framework for evaluating the complex mechanisms influencing the adhesion level at the wheel-rail interface. Furthermore, the methodology is extended to 3D for future investigation.

By addressing existing knowledge gaps, this integrated framework provides valuable guidance for optimising railway maintenance strategies and improving operational safety and efficiency.

5.2 Background

Efficient and safe train operation relies on the adhesion coefficient in the wheel-rail interface. The level of adhesion coefficient in the wheel-rail interface significantly influences the performance and reliability of railway transportation systems (Zhu *et al.*, 2012; Chen, 2024). However, challenges such as wet weather, surface contamination, and variations in rail and wheel conditions can lead to reduced adhesion, posing

significant operational risks (Broster *et al.*, 1974; Beagley *et al.*, 1975; Wang *et al.*, 2011; Tao *et al.*, 2020). In particular, low adhesion during traction operation leads to delays and general disruption due to a longer acceleration time. During braking operation, insufficient adhesion results in extended braking distances and may lead to signals passed at danger or collisions in extreme cases (Ishizaka *et al.*, 2017; Buckley-Johnstone *et al.*, 2020). When low adhesion is detected, rail sanding from an on-board device is utilised to increase the adhesion level during the wheel-rail contact (Skipper *et al.*, 2018, 2020).

Rail grinding, employed as a maintenance measure to restore the worn rail surface (Magel and Kalousek, 2002; Uhlmann *et al.*, 2016; Wang *et al.*, 2024), results in a very rough rail contact surface which can affect the adhesion coefficient and the influence of contamination. In order to evaluate the restored rail, roughness parameters have been adopted from metrology to characterise the rail surface after grinding. Mesaritis *et al.* (2020) used a laboratory grinding process to investigate the effect of grinding parameters on the post-grinding roughness of the rail. Later, they utilised a full-scale testing facility to evaluate the performance of three rail grades after the grinding process (Mesaritis *et al.*, 2023). Besides the quality control of the grinding process, Lundmark *et al.* (2009) used surface roughness to quantify the tribological performance of the wheel/rail interface in the laboratory by using a two-disc rolling/sliding machine. They found that rougher wheel specimens resulted in lower wear compared to smoother specimens, particularly reducing the wear on the rail disc. Furthermore, Wang *et al.* (2023) investigated the effect of surface roughness on friction and wear of the rail by adding different lubrications at the nanoscale. Their results indicate that reducing surface roughness, up to a critical point, can effectively reduce friction and wear under mixed lubrication conditions.

However, a roughness parameter by itself is not enough to monitor the adhesion level during train operation. Although the rail is made of steel, it is subjected to cyclic loading that leads to permanent deformation, which also affects the adhesion level during the wheel-rail contact. Tomlinson *et al.* (2021) used twin disc tests to simulate cyclic loading experienced by rail steel in service, from which a shear yield stress–plastic shear strain relationship can be generated for the tested sample. Later, Zhao and Li (2015) used a 3D transient FE approach considering elasto-plasticity to explore the frictional rolling contact between the wheel and rail. They found the contact patch increased in size, shifted forward in the rolling direction, and changed from an ellipse into an asymmetric oval. Recently, Meyer *et al.* (2021) developed a new methodology

for FE simulations of elasto-plastic rolling contact loading. It could provide higher accuracy for a given rolling length due to periodic boundary conditions.

Since the wear and plastic deformation of the rail occurs simultaneously during train operation, it is not adequate to investigate the adhesion level at the wheel-rail interface by considering only one of them. As a result, Pletz *et al.* (2014) developed a 3D FE model of the full-scale test rig. Its result can be transferred to different 2D models to calculate crack tip loading and cyclic deformations of rough surfaces. Following this, they introduced a quasistatic FE model to calculate the plastic deformations of rails caused by rolling/sliding wheels (Pletz *et al.*, 2019). By employing a 3D dynamic model, Vo *et al.* (2014) found that higher adhesion levels enlarge slip regions and surface damage, while worn profiles increase contact pressure and alter the contact patch geometry. Recently, Spiryagin *et al.* (2023) developed an algorithm to calculate the contact stresses with different surface roughness considering elastic and plastic deformations at the wheel-rail interface.

Besides wear and plastic deformation of the rail, the presence of a third body at the wheel-rail interface also affects the adhesion level, particularly during sanding operations. Over the past few years, research has focused on investigating the effects of sand particles entrained into the wheel-rail contact. Experiments have been established across a range of scales (e.g., twin-disc setup, linear full-scale rig, and field tests) to investigate the adhesion restoration and leaf layer removal induced by sand particles, as well as the traction enhancers (Skipper *et al.*, 2018). In order to optimise the railway sanding system, sand entrainment has been investigated for different hose types, hose positions, and crosswinds using an experimental approach (Lewis *et al.*, 2018). Furthermore, numerical simulations have been conducted to investigate the sander efficiency affected by the coefficient of restitution, coefficient of friction, particle size, particle shape, and crosswinds (Maramizonouz, Nadimi, W. A. Skipper, *et al.*, 2023; Maramizonouz *et al.*, 2025). Recently, alternative materials have been tested and compared for the purpose of replacing the original sand (C. Zhang, Maramizonouz, *et al.*, 2024). All these studies explain the advantages and limitations of sanding application in railway operation well.

When it comes to the morphological effect of sand particles, the size distribution and shape features are specifically described in the Rail Safety and Standards Board (RSSB) standard GMRT2461 for traction and braking operations (RSSB, 2018). According to operational experience, fine-particle sand is better for acceleration, while coarse-particle sand is better for braking (RSSB, 2018). Additionally, particle size is

proportional to the degree of adhesion increase (Cooper, 1972; Skipper *et al.*, 2019). Fine and medium-sized sand particles (0.06-0.3 mm and 0.3-0.6 mm, respectively) are more likely to result in isolation (good electrical contact between wheel and rail is essential for train detection in signal systems), according to research on the relationship between particle size and risk of isolation (Arias-Cuevas *et al.*, 2010). They suggested that this might be due to smaller particles not breaking up and being ejected upon entering the contact, thus allowing a layer of sand to build up. The particle-size effects based on standard sand and its micro-fragments were examined by Shi *et al.* (2020) using a twin-disc set-up. They discovered that the micro-fragments enhance adhesion at a smaller cost of wheel-rail wear and damage. Skipper *et al.* (2023) performed particle characterization followed by high-pressure torsion (HPT) testing. Based on the outcomes, a less circular particle is preferable for low adhesion conditions, and an optimum particle size exists when mitigating against leaf layers.

Although it is well established that roughness, plastic deformation, and third body layers influence adhesion level at the wheel-rail interface, existing studies have primarily focused on the effects of individual factors or pairwise combinations. However, there is a notable lack of research that integrates all three aspects—rail surface roughness, rail plastic deformation, and third body layers—to examine their combined impact, which would offer a more realistic understanding of the breakage mechanism of sand and how fragments distribute over the rail.

In this chapter, by introducing the wheel-rail contact with boundary conditions assigned to reproduce actual traction and braking operations, the developed μFE model for particle breakage analysis is utlised to study the influence of third body layers, specifically sand particles, on adhesion level at wheel-rail interface in 2D. To examine the effect of particle morphology on adhesion, a smooth wheel-rail interface is utilised to minimise the influence of surface irregularities. This method isolates the specific impact of particle size and shape on adhesion levels before and after fragmentation. Then, the roughness is introduced to the rail surface to quantify its effect on adhesion level. Finally, the plastic deformation due to cyclic loading is assigned to the rail for an integrated analysis of the adhesion level during the sanding process. Furthermore, a 3D version of the enhanced μFE model is established with some preliminary findings.

5.3 Methodology

5.3.1 Breakage Modelling

The breakage of sand particles is modelled through CIEs, which are treated as the

zero thickness intermediate glue elements that follow the traction-separation laws. For detailed information, please refer to Chapter 3.3.1 for CIEs in 2D.

5.3.2 Elastic and Plastic Behaviours

Elasticity indicates the capacity of a material to undergo deformation when subjected to a load and subsequently regain its initial shape upon load removal. For example, during the wheel-rail contact, the rail deforms elastically to a certain degree, allowing for better contact and adherence. The occurrence of excessive permanent deformation (plastic deformation) in rail materials is undesirable. Plastic deformation can lead to wear and surface irregularities on the rail, negatively affecting adhesion and overall performance. Therefore, it is critical to utilise a constitutive model that accurately represents how the material responds to loading. In this study, the rail is modelled with an elastic/plastic material description that uses a combination of isotropic and kinematic hardening.

The equivalent stress σ_v established by Von Mises is employed to check the behaviour of a material in the principal plane stress case. Therefore, the yield stress σ_y can be expressed as follows to predict the plastic deformation.

$$\sigma_y = \sigma_v = \sqrt{\sigma_1^2 - \sigma_1\sigma_2 + \sigma_2^2} \tag{5.1}$$

where the σ_1 and σ_2 are the two principal stresses. When $\sigma_v \leq \sigma_y$, the material is dominated by the elastic deformation. As soon as the σ_v becomes bigger than σ_y, the mechanical behaviour of material transmits from elastic to plastic.

The flow rule is another fundamental concept of plastic deformation that defines how the material behaves after the yielding point. It not only describes the relationship between stress and strain but also specifies the direction and rate of plastic deformation.

Two flow rules are adopted in this study: a) isotropic hardening, where the σ_y increases uniformly in all directions with the accumulation of plastic strain. It increases uniformly through the entire plastic deformation process; b) kinematic hardening, where the shape of the yield surface remains constant but its centre shifts. It is influenced by the accumulated plastic strain and past loading history. Figure 5.1 shows the changes in yield surface when the plastic deformation follows different flow rules.

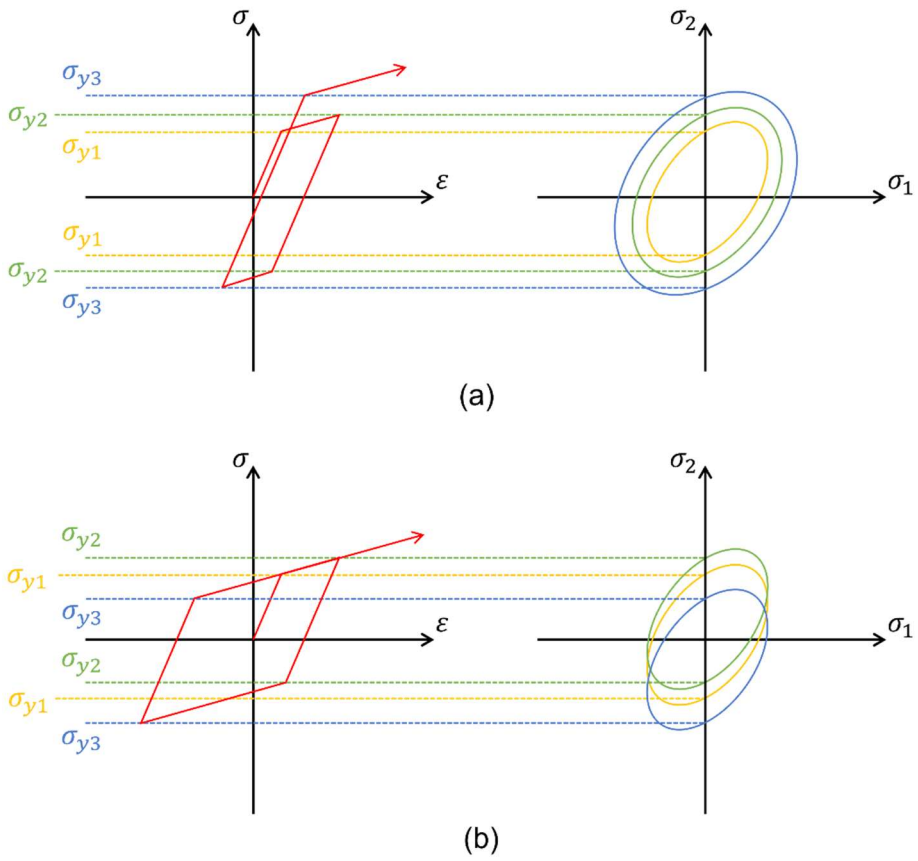

Figure 5.1. Two adopted flow rules: (a) isotropic hardening and (b) kinematic hardening.

5.3.3 Roughness

Surface roughness is characterised by the variances in the orientation of a real surface's normal vector from its idealized shape. In railway engineering, the roughness with a broad spectrum of wavelengths is present on the running surface of the rail. This rail roughness, in turn, triggers the generation of vibrations and rolling noise. When the rails are worn beyond the specific allowable limits, their profiles must be restored to avoid undesired contact conditions in the wheel-rail interface. According to BS EN13231-3-2012 (BS EN 13231-3, 2012), the arithmetic mean surface roughness R_a of the rail should not exceed $10\ \mu m$ along more than 16% of the measure length after grinding.

Data Acquisition

Surface roughness data for rail profiles following grinding were provided by colleagues at the University of Sheffield. These data were obtained using 3D surface replication and optical profilometry methods, as described by Mesaritis *et al.* (2020). Two representative surface areas measuring $24mm \times 2mm$ were extracted from the

scanned data and classified based on their average roughness (R_a):

- Case A: a surface with medium roughness ($R_a < 10\ \mu m$);
- Case B: a surface with very high roughness ($R_a \approx 20\ \mu m$), as shown in Figure 5.2.

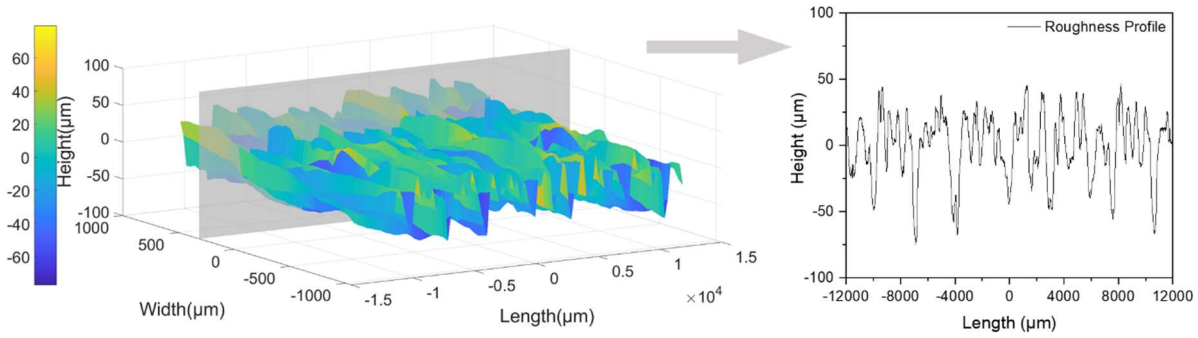

Figure 5.2. Representative 3D surface profile of the rail from Case B (high roughness, $R_a \approx 20\ \mu m$).

Data Analysis

Each $24mm \times 2mm$ surface region was sampled at a lateral resolution of 4 μm, yielding five hundred 2D roughness profiles per case. To reduce computational cost while preserving key surface features, the number of profiles was reduced to 100 per case through uniform sub-sampling.

Roughness descriptors used for quantitative analysis are listed in Table 5.1, including R_a, R_q, R_{dq}, R_{sk}, and R_{ku}. In Case B, as shown in Figure 5.3, the descriptors R_a, R_q, R_{sk}, and R_{ku} showed consistent trends across the profiles, whereas R_{dq}, which captures local slope variation, exhibited notable fluctuations. To identify representative profiles, a turning point analysis was performed on the R_{dq} data. Based on this, 35 profiles from Case B.

The limited number of Case A profiles were selected, specifically two, reflects both the lower variability in surface characteristics and the supporting role of this case within the study. The selection strategy was aligned with the study's aim to address industry concerns by focusing on the worst-case grinding outcomes (Case B). Nevertheless, including a few profiles that met the grinding standard ($R_a < 10\ \mu m$) ensured a basis for comparison with compliant surface conditions.

The roughness descriptors corresponding to all selected profiles are provided in Appendix D.

Table 5.1. Supported rail roughness descriptors.

Descriptor	Formula	Range	Comments
Arithmetical mean height R_a	$R_a = \frac{1}{\ell}\int_0^{\ell} \lvert Z(x)\rvert \, dx$	$[0, +\infty)$	Units of length
Root mean square height R_q	$R_q = \sqrt{\frac{1}{\ell}\int_0^{\ell} Z^2(x) \, dx}$	$[0, +\infty)$	Units of length
Root mean square gradient R_{dq}	$R_{dq} = \sqrt{\frac{1}{\ell}\int_0^{\ell} \left[\frac{d}{dx}Z(x)\right]^2 dx}$	$[0, +\infty)$	Unitless
Skewness R_{sk}	$R_{sk} = \frac{1}{{R_q}^3}\left[\frac{1}{\ell}\int_0^{\ell} Z^3(x) \, dx\right]$	$(-\infty, +\infty)$	Unitless
Kurtosis R_{ku}	$R_{ku} = \frac{1}{{R_q}^4}\left[\frac{1}{\ell}\int_0^{\ell} Z^4(x) \, dx\right]$	$[0, +\infty)$	Unitless

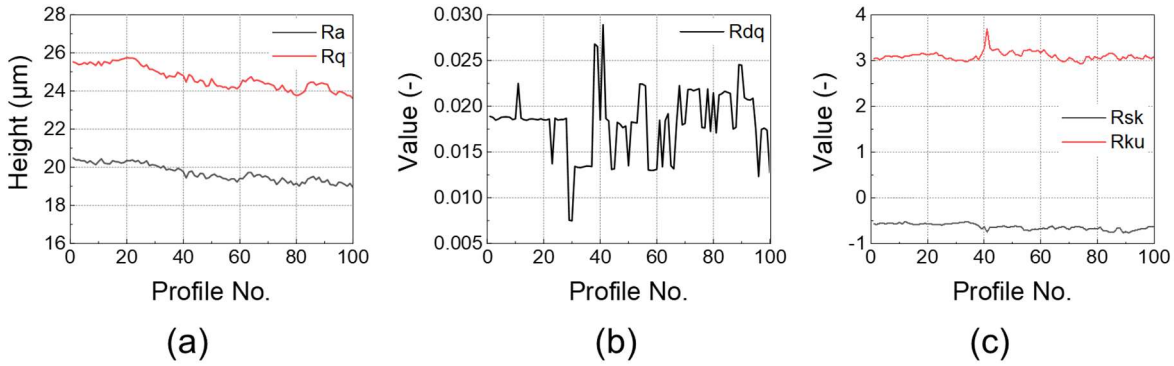

Figure 5.3. The roughness descriptors of 100 profiles from Case B. (a) R_a and R_q. (b) R_{dq}. (c) R_{sk} and R_{ku}.

Profile Regeneration

The next step is to generate the rail roughness in the numerical software. Each representative profile consists of over six thousand points. Therefore, a progressive data reduction has been conducted on each profile to reduce the geometrical complexity while still maintaining accuracy. The procedure is down sampling the data iteratively by selecting every nth point, where n starts from 2. For each downsampled dataset, R_a of the simplified profile has been calculated to compare with the original one. This downsampling process will continue until the relative difference between the current and previous R_a exceeds 1%, at which point the previous downsampled dataset will be adopted. Now, the representative profiles have been simplified while

retaining the essential roughness characteristics within a certain error threshold. A Python script has been developed to create rail parts reflecting the extended roughness profiles in Abaqus.

5.4 Model Setup and Materials

The objective of this numerical study is twofold: 1) to investigate the effect of particle size and shape on adhesion level, and 2) to analyse the impact of sand fragmentation on adhesion level by incorporating rail conditions such as surface roughness and plastic deformation. To achieve these objectives, the developed model incorporates two types of rail surfaces: one featuring a flat surface that undergoes elastic deformation, and another characterised by a rough surface that initially undergoes elastic deformation, followed by elastic-plastic deformation.

In this section, a simplified 2D model is reintroduced for two main reasons. First, setting up and refining a new model is considerably more efficient in 2D, particularly during the early stages of development. Second, 2D simulations offer significantly lower computational demands, enabling results to be obtained within a practical time frame. As this is a preliminary study, the aim is to explore the general behaviour of sand particles at the wheel–rail interface rather than to produce precise quantitative predictions. Therefore, a 2D model is more appropriate for capturing qualitative trends, testing modelling assumptions, and guiding the development of more advanced 3D models in future work.

5.4.1 Numerical Model

A revised version of the developed μFE model is used to simulate the wheel-rail contact, as shown in Figure 5.4. The inset provides a magnified view of the sand particle and rail surface for detailed visualisation. Ideally, the wheel should be considered as a deformable body with horizontal displacement and rotation to reproduce actual operation. However, in modelling, all the motions will be located at every single element after the wheel has been meshed, which is expensive to simulate numerically and needs tremendous computational power. Therefore, the wheel is simplified as a rigid body to avoid complex elastic deformations due to multiple motions. It is assigned with a displacement in the x direction (ca. 110 mm, which is an adequate length for the wheel to break particles in element-size fragments and pass them entirely) and with a 60 kN concentrated force at the centre, which is a typical load for a passenger train (Skipper *et al.*, 2021). For traction operation, the wheel is subjected to an angle of

rotation equal to 0.242 radians to simulate the 10% slip used in experiments (Arias-Cuevas *et al.*, 2011). For braking operation, no rotation is provided to the wheel in order to simulate pure sliding, which is an extreme case of this operation. The rail is modelled as a deformable body to allow the sand particle and fragments to enter the wheel-rail contact. It has a fixed boundary condition at the bottom to limit the motion of the rail from all directions. From some preliminary simulation results, the stress distribution and associated deformations only occur within the rail sub-surface area, therefore the rail depth has been reduced from the actual size to 50 mm to expedite the simulation. The sand particles are deformable bodies as well but have been enriched with CIEs to simulate the fracture behaviour. Table 5.2 provides a summary of the components and their corresponding boundary conditions.

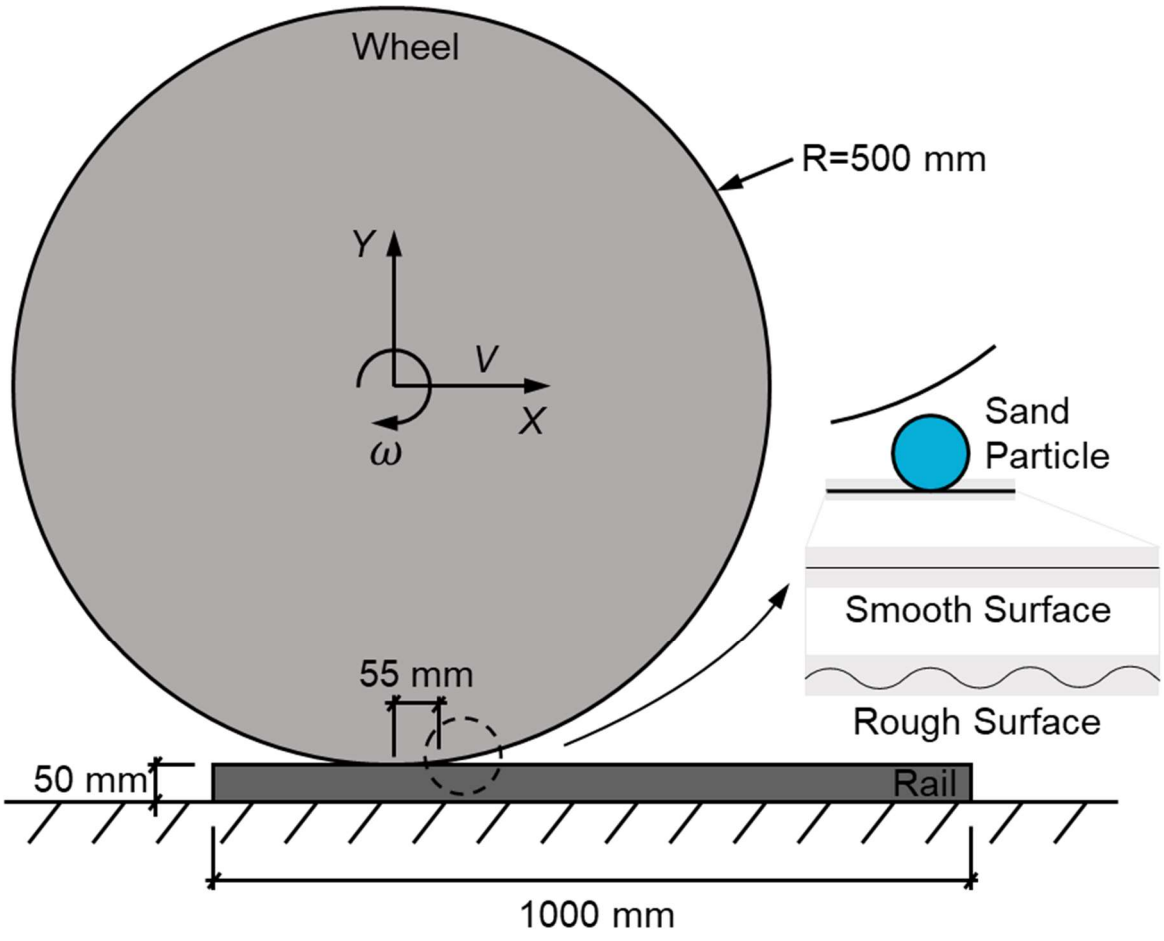

Figure 5.4. Schematic diagram of the numerical model.

Table 5.2. Summary of the model.

Wheel	Rail	Sand particles

Part type	Discrete rigid	Deformable	Deformable (CIEs added)
Geometry	Circle	Rectangle	Circle/Ellipse
Boundary conditions	Horizontal displacement	Encastre	Free
	Concentrated force		
	Traction operation (0.242 radians)		
	Braking operation (0 radians)		

All deformable bodies are created using CPE3 elements, which can undergo local deformation based on the current nodal forces. In the case of sand particles, COH2D4 elements are positioned at the interface of CPE3 elements. Since CIEs are of zero thickness, the overall mesh geometry remains unaltered, but every element is now connected by the CIEs. When the normal stress or shear stress at the CIEs reaches a predefined threshold, the CIEs initiate a process of cracking, resulting in debonding between elements.

During the simulation, the 60 kN concentrated force is considered the normal force. The tangential force along the moving direction is recorded throughout the entire simulation. The overall traction can be quantified using the equation below:

$$\mu_a = \frac{F_T}{F_N} \tag{5.2}$$

where μ_a is the adhesion coefficient, F_T is the tangential force and F_N is the normal force.

The wheel-rail contact is assumed to be frictionless, the coefficient of friction between fragment-to-wheel, fragment-to-rail, and fragment-to-fragment is set to 0.5, which is the value for dry contact observed from experiments (Shi *et al.*, 2020) and applied in numerical simulations (Zhao and Li, 2011). As a result, the calculated μ from this model only considers the traction force that comes from these micro frictional contacts and interlocking of the fragments. To separate this value from the common adhesion coefficient μ, a parameter termed adhesion enhancement $\Delta\mu$ is defined in this chapter to represent the calculated results.

5.4.2 Mesh Forms

The variation of sand morphology alters their mechanical properties, such as the ultimate strength, friction, fracture behaviour, fragment distribution, etc., which could influence the adhesion level at the wheel-rail interface. In this study, it is assumed that all sand particles are regular shapes (*i.e.,* circles and ellipses). Circular meshes are generated to investigate the size effect and ellipsoidal meshes are created to explore the shape effect. The diameters of circular meshes vary from 0.71 mm to 2.80 mm according to the RSSB standard GMRT2461 (RSSB, 2018; Skipper *et al.*, 2021). The aspect ratios of ellipsoidal meshes are increasing from 1:1 to 4:1. The generated sand particle meshes in different sizes and aspect ratios are illustrated in Figure 5.5.

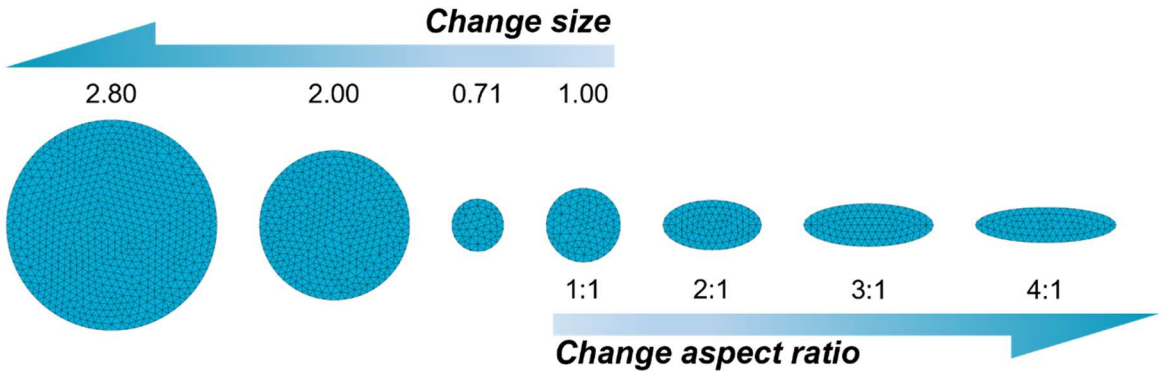

Figure 5.5. Particles mesh in different sizes and shapes.

To determine the size of fragments, Zhang *et al.* (2024) reported that the particle size distribution of crushed sand collected from the railhead shows $D_{90} < 100\ \mu m$. Considering that the computational cost of FEM simulations is highly dependent on element size, a constant element size of $100\ \mu m$ is assigned to all particle meshes to ensure the simulations can be completed within a reasonable time frame. This element size has a good representation of the real fragmentation process of sand particles at the wheel-rail interface, as it allows all particle meshes to break into element-size fragments during the simulation. The data reported by Zhang *et al.* (2024) were obtained from a field test conducted at Wensleydale, North Yorkshire, which is described later in this chapter, thereby ensuring consistency between the experimental observations and the numerical model inputs.

Additionally, based on the mesh sensitivity study from Chapter 3, the element size to mesh size ratio used here is in the acceptable range. The composition of all the sand particle meshes used in this chapter is listed in Table 5.3.

Table 5.3. Mesh composition of sand particles based on size and shape.

	Mesh dimension (mm)	Element size (mm)	CPE3 elements
Size	0.71	0.10	92
	1.00	0.10	179
	2.00	0.10	733
	2.80	0.10	1388
Shape	1:1 (1.00 / 1.00)	0.10	179
	2:1 (1.36 / 0.68)	0.10	170
	3:1 (1.80 / 0.60)	0.10	186
	4:1 (2.00 / 0.50)	0.10	174

5.4.3 Material Properties

Since the wheel is modelled as a rigid body and does not require material properties, only two materials need to be defined: a) the sand particle, which uses the parameters specified in Table 3.1 of Chapter 3, and b) the rail, which incorporates both elastic and plastic deformation and will be discussed in detail here.

When the rail is only deformed elasticly (*i.e.,* flat surface), Young's modulus and Poisson's ratio of 210 GPa and 0.3 are used, respectively. The density of the rail is 7800 kg/m^3. When the rail involves plastic deformation, besides the parameters used for elastic deformation, the combined isotropic/kinematic model in Abaqus/Explicit package has been adopted. It provides a more accurate approximation to the stress-strain relation and therefore a better prediction of the adhesion enhancement.

Isotropic parameters

According to the work of Chaboche (1989), the isotropic hardening can be described by a change in the yield stress σ_y shifting from its initial value σ_{y0}, corresponding to the equivalent plastic strain $\bar{\varepsilon}_{pl}$ in the following manner:

$$\sigma_y = \sigma_{y0} + Q_\infty\left(1 - e^{-b\bar{\varepsilon}_{pl}}\right) \tag{5.3}$$

where, according to Pletz *et al.* (2014), the saturation stress Q_∞ and hardening parameter b were established at $-40\ MPa$ and 0.04, respectively. The initial yield stress σ_{y0} was measured as $320\ MPa$ from the same study.

Kinematic parameters

The kinematic component of the hardening is represented through the yield function Y. In this function, the backstress tensor α is deducted from the stress tensor σ to simulate the kinematic hardening $Y(\sigma - \alpha)$. The α is calculated as the sum of each backstress α_i. The increment of α_i during plastic deformation is computed using the backstress rate $\dot{\alpha}_i$, which is derived from σ and the equivalent plastic strain rate $\dot{\bar{\varepsilon}}_{pl}$ according to:

$$\dot{\alpha}_i = C_i \frac{1}{\sigma_y}(\sigma - \alpha)\dot{\bar{\varepsilon}}_{pl} - \gamma_i \alpha_i \dot{\bar{\varepsilon}}_{pl} \tag{5.4}$$

where the values of backstress modulus C_i and dissipation rate parameter γ_i are listed in Table 5.4. A final hardening curve is generated by combining the listed six backstress curves to provide a better capture of the shape of the plastic behaviour.

Table 5.4. Backstress parameters of the railhead part (Pletz *et al.*, 2014).

i	$C_i\ (GPa)$	$\gamma_i\ (1)$
1	350	5000
2	80	1000
3	15	150
4	10	50
5	8	20
6	0.19	0.01

By incorporating these two parameters, the model can simulate the hardened layer that forms on the rail surface due to cyclic loading. However, since the primary objective of this study is to investigate the effect of surface roughness on adhesion at the wheel-rail interface, the analysis focuses exclusively on the critical case of the first loading cycle after grinding, where the yield strength of the rail is lower than that of the hardened rail. Nevertheless, this setup establishes the numerical foundation for future investigations involving cyclic loading.

Simulations were run in Abaqus/Explicit on a Windows 10 office PC equipped with an Intel i5-10310U CPU (1.70 GHz) and 16 GB RAM. The execution time of the simulations, using a 1 mm sand particle as an example, ranged from 2 to 4 hours of wall-clock time, depending on the complexity of the rough rail surface.

5.5 Results and Discussion

The analysis and discussion focus on four key factors influencing adhesion at the wheel-rail interface. First, the effect of particle morphology and quantity is examined on a flat rail surface under elastic deformation, as detailed in Sections 5.5.1 to 5.5.4. Second, a parametric study investigates the influence of particle size on a rough rail surface under elastic deformation, followed by validation using a single particle size across 37 rough surfaces (see Appendix D), covered in Sections 5.5.5 and 5.5.6. Third, the effect of single particle size on 37 rough surfaces is analysed, considering both elastic and plastic deformation, as discussed in Section 5.5.7. Finally, a 3D version of the model is developed with some preliminary results.

5.5.1 Particle Fracture Behaviour

According to the particle state, the whole simulation process can be classified into three stages, as shown in Figure 5.6. The first stage is the prior-to-fracture stage, where the wheel is approaching the particle. The second stage is the fracture stage, where the first contact between the wheel and particle is happening, followed by multiple contacts with particle fragments. The first contact (Figures 5.6a and 5.6d) of each particle occurs slightly differently due to the size difference, as all particles are located 55 mm away from the wheel. For traction operation, the fragments are intended to remain at the original position or move towards the wheel-rail contact, as shown in Figure 5.6b. On the contrary, during the braking operation, fragments have been spread further away from their original place as a consequence of the chopping force induced by the sliding wheel, as illustrated in Figure 5.6e.

The third stage is the post-fracture stage, where the particle is fully fractured and the wheel is only interacting with element-size fragments. For traction operation, all fragments are fed into the wheel-rail interface with the help of the rolling wheel and the deformable rail (Figure 5.6c). However, in the braking case, the majority of fragments have been held and pushed away by the sliding wheel till the end of the simulation and limited fragments are able to pass through the wheel-rail contact (Figure 5.6f).

As shown in Figure 5.6, triangular elements were used to discretise the particle. This element type was chosen because it is well suited for capturing detailed mesh features and allows for finer meshing, which improves the resolution of contact detection between fragments and between fragments and the wheel or rail. Moreover, the CIE subroutines (Zare-Rami and Kim, 2019) employed in this study are compatible only with triangular elements, further justifying their selection.

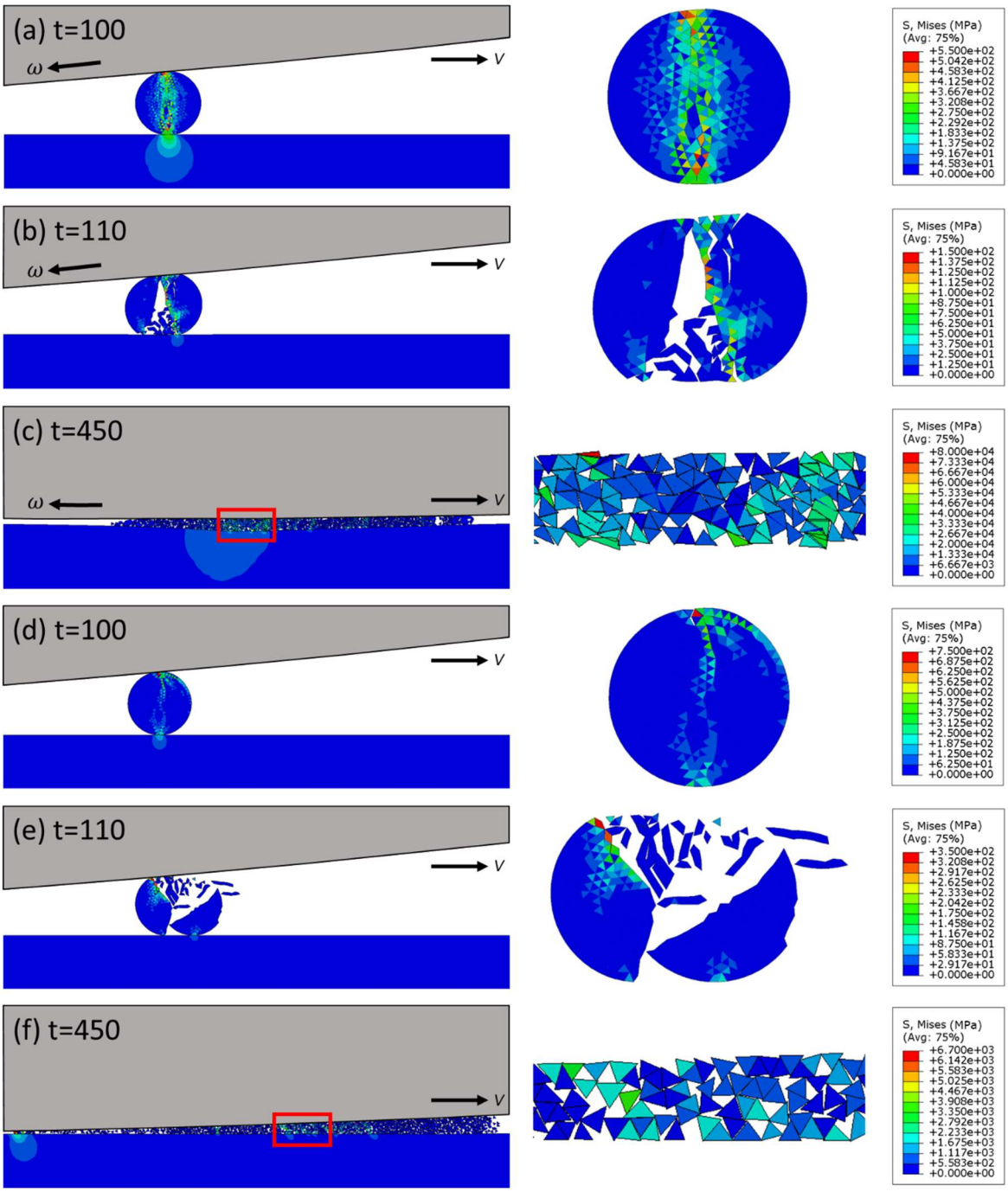

Figure 5.6. Fracture process of a single particle: (a) – (c) traction operation and (d) – (f) braking operation.

5.5.2 Particle Size Analysis

The results of adhesion enhancement for particle sizes from 0.71 mm to 2 mm are given in Figure 5.7a for traction operation. The adhesion enhancement calculated at the fracture stage is negligible for all particles compared with the values from the post-fracture stage. The adhesion enhancement starts to increase sharply due to the wheel rolling on fragments. When all fragments break into element sizes, the adhesion enhancement achieves its peak value and then begins to decline as the wheel passes

the enhanced area. The variation trend of adhesion enhancement observed from different particles is similar, but the magnitude grows when particle size increases.

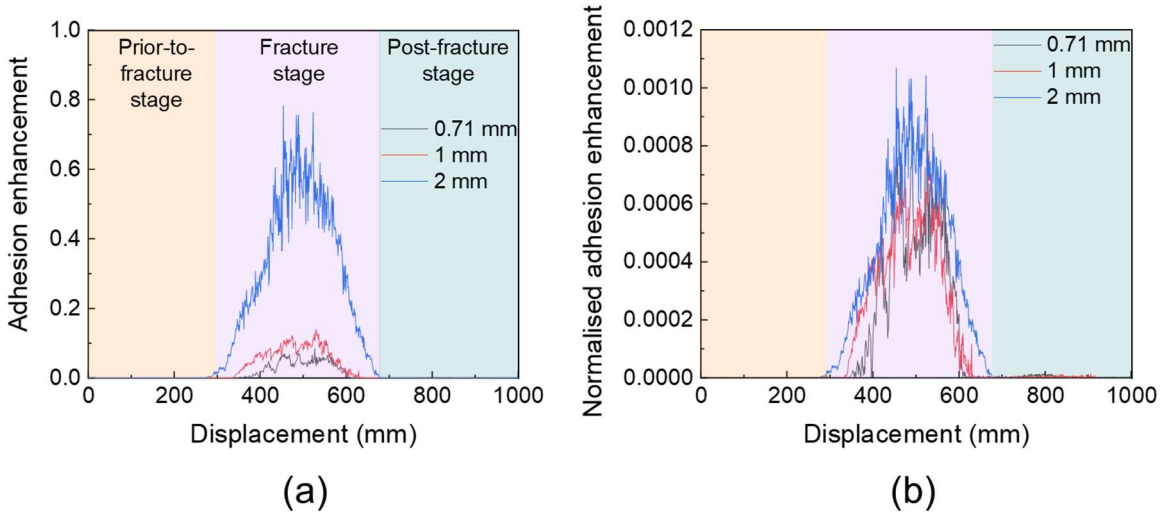

Figure 5.7. Size effect during traction operation. (a) adhesion enhancement of single particles and (b) normalised adhesion enhancement.

Since an element size of 0.1 mm was assigned to all the particle meshes, the number of element-sized fragments generated during the fracture stage varies depending on the size of the mesh. To account for this, the total adhesion enhancement generated in each case has been divided by the corresponding number of fragments, and the normalised results are plotted in Figure 5.7b to evaluate the contribution of fragment number to adhesion behaviour. Although fragment count can be influenced by the element type, the same type was used consistently across all simulations to ensure fair comparison. Moreover, fragment count offers a more direct representation of material degradation than the number of frictional contacts, particularly in cases where multiple fragments interact simultaneously with the wheel or rail surfaces. After the normalisation, the variation trends are similar to the non-normalised ones, but the magnitude is now converging. This can be related to the mass of fragments considering the fact that they are assumed to be homogenous with constant density. In more scientific terms, the new surface area generated as the third body in the contact is similar after the normalisation.

For braking operation, particle sizes ranging from 0.71 mm to 2.8 mm are used and the results are plotted in Figure 5.8. A clear increase for all particles is observed at a bigger displacement owing to chopping fragmentation as fragments further spread along the rail. Due to the different amount of fragments generated, the increment slope

is steep for bigger particles and is gentle for smaller particles, as shown in Figure 5.8a. The smaller particles (*i.e.,* 0.71 mm and 1 mm) achieved a lower plateau quickly. The bigger particles (*i.e.,* 2 mm and 2.8 mm), on the other hand, keep increasing till the end due to the simulation length. This indicates that it takes a larger displacement for a large amount of fragments to achieve a plateau. Normalisation is conducted on the data and the results are indicated in Figure 5.8b. All the increasing trends are overlapping now. The peak value for a single fragment (ca. 0.00025) is smaller than the one (ca. 0.0010) in the traction operation (Figure 5.7b).

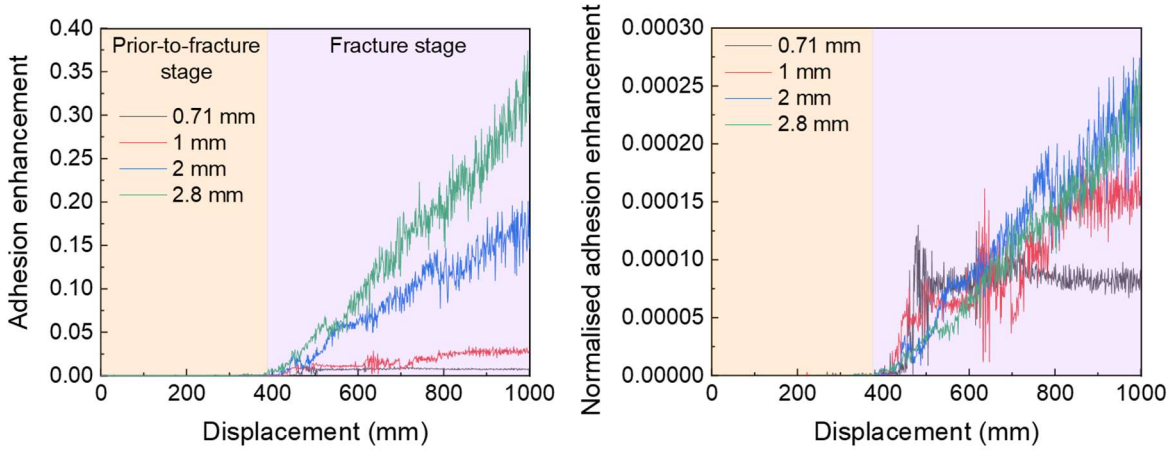

Figure 5.8. Size effect during braking operation. (a) adhesion enhancement of single particles and (b) normalised adhesion enhancement.

The results before and after normalisation reveal the fact that the adhesion enhancement is induced by the fragments generated, not the particle size. Additionally, sand particles during traction operation tend to provide a higher adhesion enhancement than the braking operation. On the other hand, the enhancement lasts longer during braking operation owing to the fragments carryover event.

5.5.3 Particle Shape Analysis

The particle shape is another important morphological parameter affecting mechanical behaviour. Therefore, a set of ellipsoidal meshes with a different aspect ratio ranging from 1:1 to 4:1 are used to study the shape effect on adhesion enhancement. As it was revealed in particle size analysis that different amounts of fragments could lead to different traction enhancement results, certain dimensions were selected to generate meshes to not only meet the different aspect ratios but also to consist of a similar

amount of fragment elements.

During traction operation, four different particle meshes were tested and the results of adhesion enhancement are shown in Figure 5.9a. Overall, the plot of adhesion enhancement from different particle meshes shows the same variation trend with a similar peak value. This indicates that changing the aspect ratio does not affect the adhesion enhancement significantly. Figure 5.9b illustrates the results after normalisation. As fragments generated from different particle meshes are comparable, the plots are similar to the non-normalised ones, however, the values are now for the single fragment. These values are identical to the normalised data in particle size analysis.

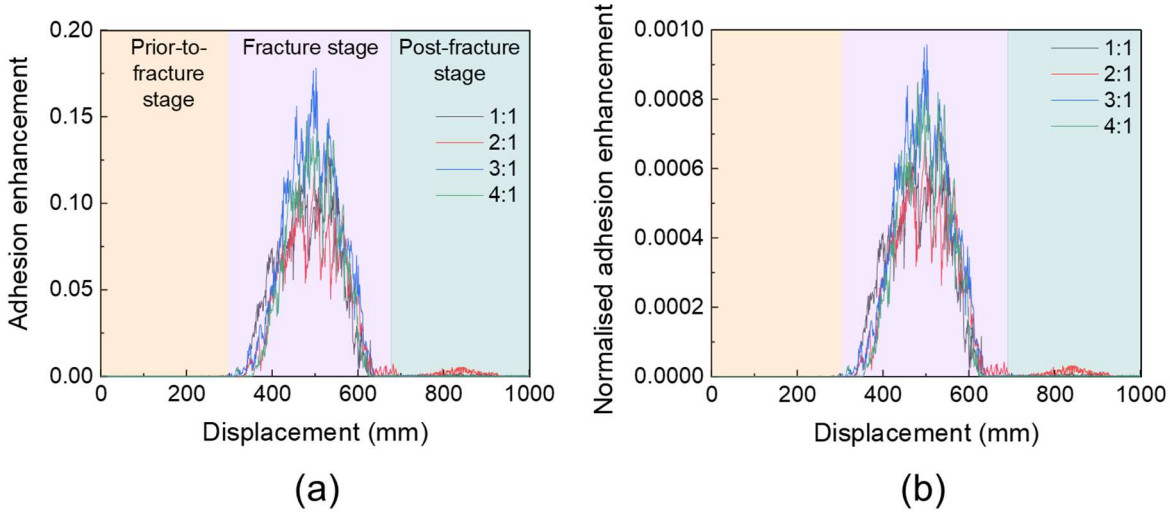

Figure 5.9. Shape effect during traction operation. (a) adhesion enhancement of single particles and (b) normalised adhesion enhancement.

For braking operation, the same particle meshes are used and the results of adhesion enhancement are given in Figure 5.10a. Overall, all plots of adhesion enhancement start to increase at the same location with a similar slope. However, the plots of particle mesh with a smaller aspect ratio (*i.e.,* 1:1 and 2:1) reach a lower peak value earlier and maintain it till the end of the simulation. On the other hand, the plots of particle mesh with a larger aspect ratio (*i.e.,* 3:1 and 4:1) achieve a higher peak value at a later stage. This is owing to the fragments of elongated shape spreading widely along the rail after breakage and thus generating a larger fragment-to-wheel contact area. After the normalisation, the plots are identical to the non-normalised ones due to the similar amount of fragments, however, the separation between each plateau becomes more obvious that the single fragment from the elongated shape tends to

provide a higher adhesion enhancement (Figure 5.10b).

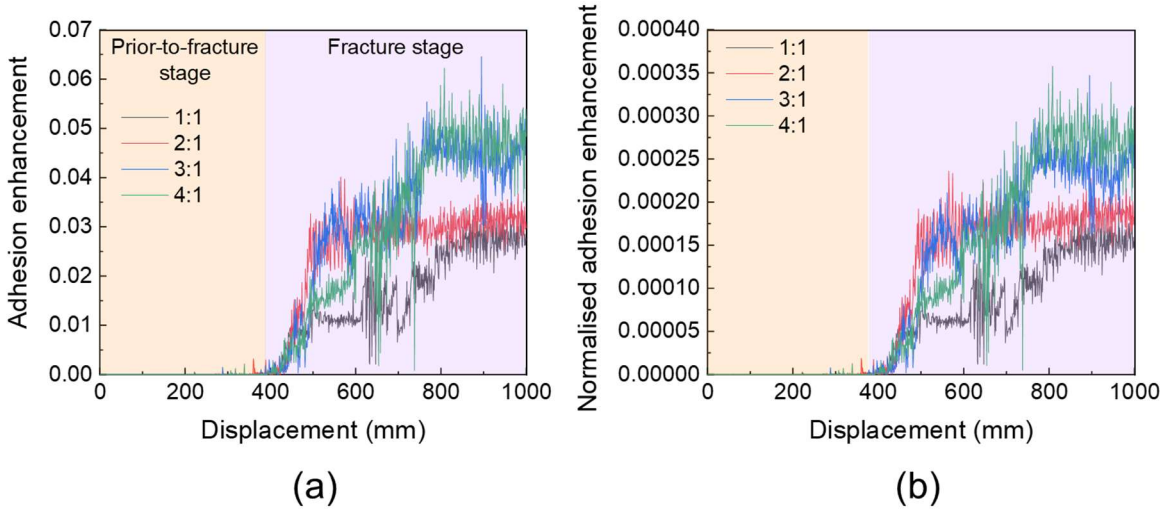

Figure 5.10. Shape effect during braking operation. (a) adhesion enhancement of single particles and (b) normalised adhesion enhancement.

The observed results in particle shape analysis also indicate that the adhesion enhancement during traction operation is higher than the braking operation. Moreover, during the braking operation, the elongated shape is able to generate a higher adhesion enhancement compared to the circular shape.

Notably, some trial simulations have been conducted by assigning the rail with an equivalent Young's Modulus to accommodate less deformation due to the wheel as a rigid body. Similar particle breakage behaviours and plots of adhesion enhancement have been observed, except for the actual values. As preliminary research for studying the sand breakage at the wheel-rail interface, it is more interesting to find the breakage behaviour of sand particles and the variation in adhesion enhancement trends with particle size, aspect ratio, numbers, etc., rather than the actual values.

5.5.4 Multi-Particle Analysis

In addition to the size and shape analysis, the effect of particle number on adhesion enhancement is investigated. Similarly, in order to minimize the influence of fragment number on the adhesion enhancement, different combinations of particles, consisting of a similar amount of CPE3 elements, are used. Thus, a 2 mm circular mesh with 733 elements, four 1 mm circular meshes with a total amount of 716 elements, and eight 0.71 mm circular meshes with a total amount of 736 elements have been adopted in Cases 1, 2, and 3, respectively, as shown in Figure 5.11. Additionally, the fracture

process of Case 2-2 has been illustrated in Figure 5.12 to demonstrate the breakage behaviour of multi-particles.

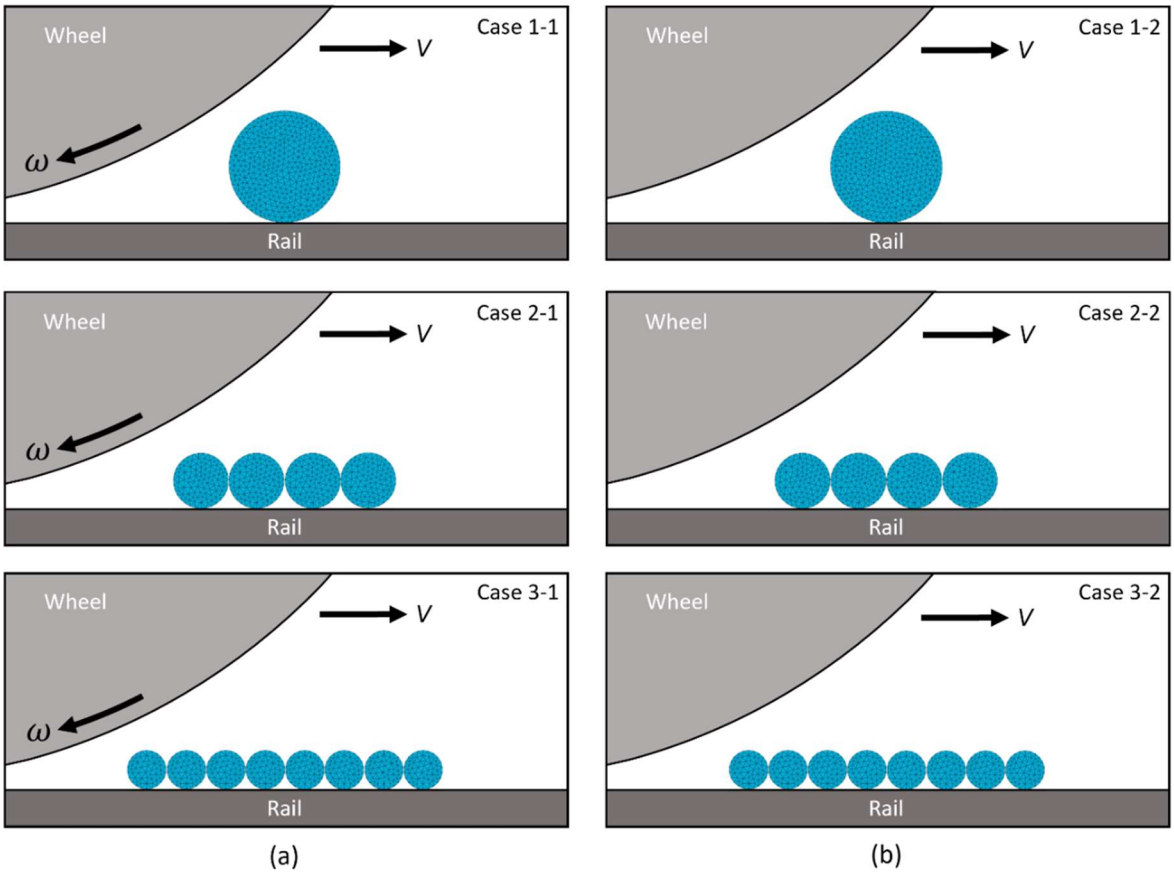

Figure 5.11. Particle combinations during (a) traction operation and (b) braking operation.

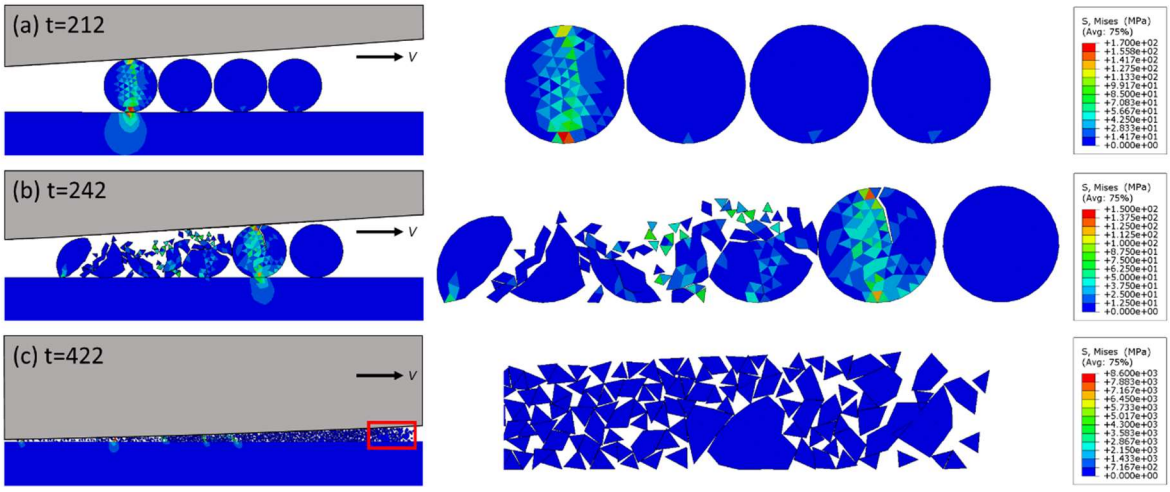

Figure 5.12. Fracture process of Case 2-2.

The results of adhesion enhancement for three cases during traction operation are shown in Figure 5.13a. Despite the differences in particle numbers between the cases,

the adhesion enhancement plots overlap. This is because the rolling movement of the wheel ensures a consistent and steady supply of fragments to the wheel-rail interface, leading to similar total fragment contributions across all cases. In contrast, the braking operation reveals a different trend, as illustrated in Figure 5.13b. While all cases show a similar increasing slope, the case involving a single particle achieves a higher adhesion enhancement. This can be attributed to the fracture behaviour of multi-particle systems. During braking, the sliding motion of the wheel pushes the particles away, causing them to break sequentially. This sequential fragmentation, accompanied by more pronounced rolling movements in the later particles (Figures 5.12b and 5.12c), results in a steady but limited supply of fragments to the wheel-rail interface before all particles are fully fragmented. In comparison, a single larger particle fractures all at once, releasing its full quantity of fragments in a shorter time, thereby creating a greater accumulation of fragments at the wheel-rail interface.

Considering the results from particle size, shape, and number analysis, the traction operation is a fragment-based process as the adhesion enhancement is mainly influenced by the number of fragments at the wheel-rail contact. On the contrary, adhesion enhancement during the braking operation shows all the effects of particle size, shape, and number simultaneously. Based on these simulations, a larger size particle with an elongated shape is preferred for the braking operation.

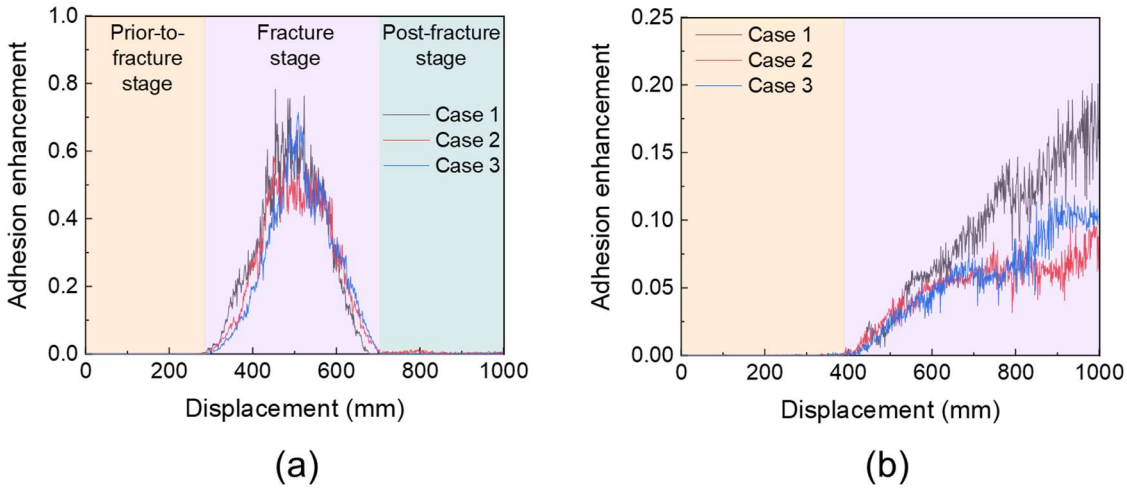

Figure 5.13. Effect of number on adhesion enhancement during (a) traction operation and (b) braking operation.

As part of the PhD study, the candidate participated in field experiments for the rail sanding project funded by the Engineering and Physical Sciences Research Council. These included trials in Great Central Test Track, Loughborough, in 2021 to investigate

different sanding materials, and in Wensleydale, North Yorkshire, in 2024 to test the efficiency of sanding on leaf contamination. In the latest experiment, sand fragments on the rail were observed after each operation. Fragments were passed over by the wheel and left on the rail during traction operation as shown in Figure 5.14a and have been pushed to the end of braking operation as shown in Figure 5.14b. These experimental observations demonstrate a good agreement with the simulation results. It is recommended to record the traction force and normal force from the wheel during a sanding process to establish a link between the field test and the mentioned simulation method.

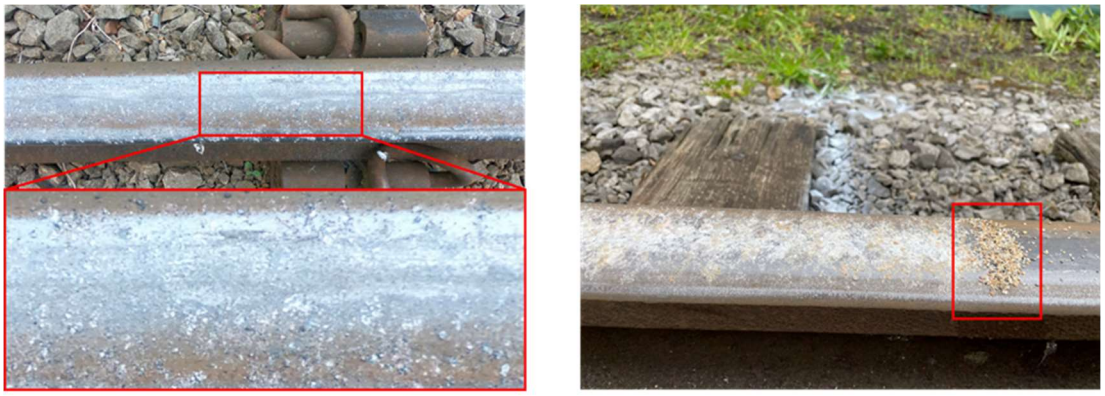

(a) (b)

Figure 5.14. Sand fragments on the rail during (a) traction operation and (b) braking operation.

5.5.5 Parametric study

Three particles with diameters of 0.71 mm, 1 mm, and 2 mm are used to investigate the adhesion level on a selected rough surface, with results compared to those on a flat surface discussed previously.

Traction Operation

The change of adhesion during traction operation is plotted in Figure 5.15. Using Figure 5.15a as an example, displacement smaller than 45 (40 for the flat surface) is defined as the prior-to-fracture stage, and bigger than 70 (65 for the flat surface) is defined as the post-fracture stage. For these two stages, the wheel is only interacting with the rail. From the displacement of 45 to 70 (40 to 65 for the flat surface), the wheel is rolling on top of the sand fragments, which is considered the fracture stage. By comparing the two profiles using the same particle size, although the rough case takes a longer time to achieve the fracture stage due to the uneven surface contact, the durations of the

fracture stage are the same for both flat and rough surfaces. However, when comparing fracture stages for simulations using different particle sizes, the duration becomes longer as a result of particle size increment.

It is noteworthy that the adhesion enhancement on rough surfaces during prior-to-fracture and post-fracture stages are identical for all simulations as no particle is involved. However, the peak value during the fracture stage varies from particle size to particle size. In order to reveal the effect of particle size on adhesion enhancement, the data are normalised based on their respective fragment counts, as shown in Figure 5.15d. During the prior-to-fracture and post-fracture stages, since no fragments are involved, the plots from small particles show higher values than the large particles due to the normalisation. However, the participation of fragments during the fracture stage harmonizes this difference, as the plots from different particle sizes converge. This indicates the new surface area generated in the contact due to fragmentation is similar after the normalisation.

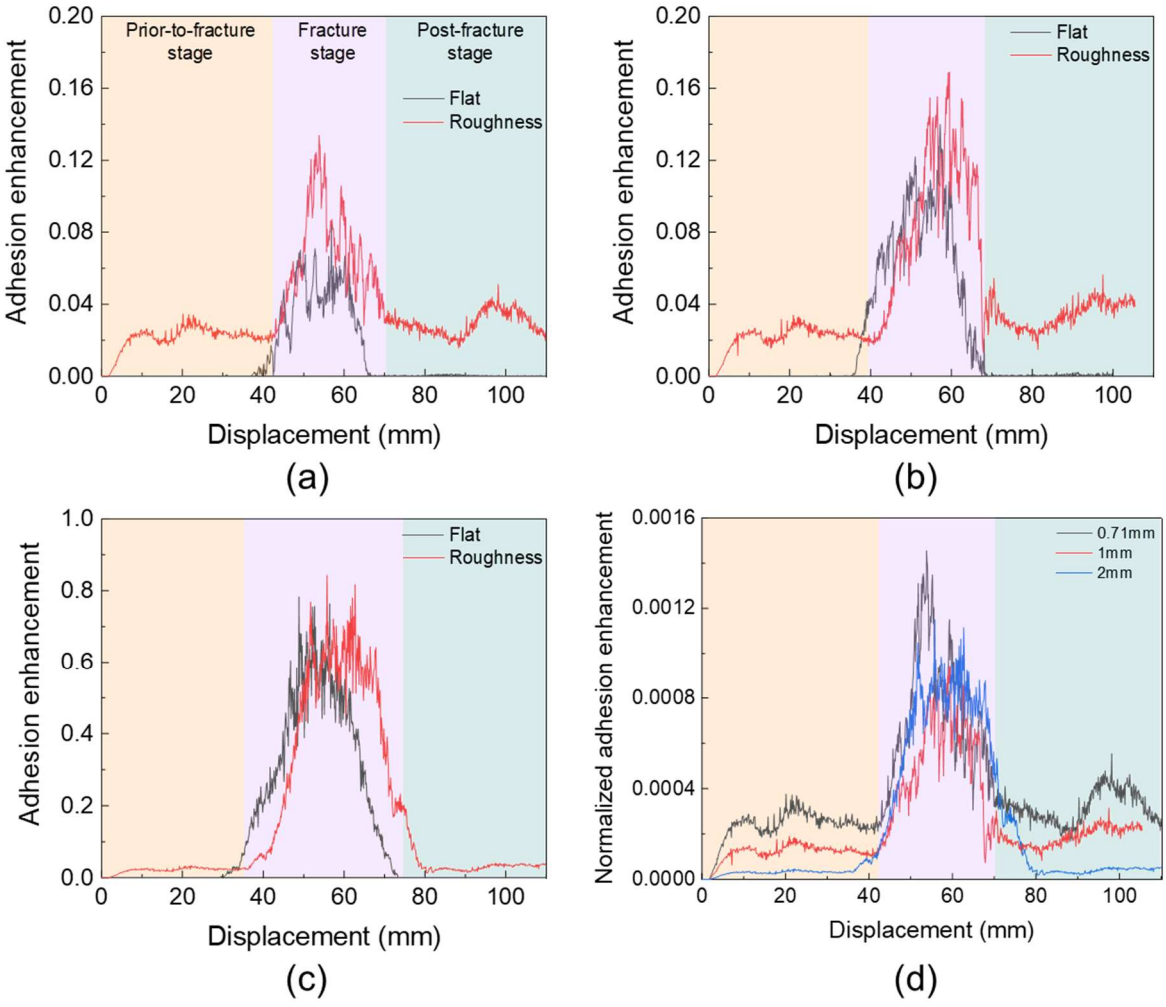

Figure 5.15. Size effect during traction operation: (a) 0.71 mm, (b) 1 mm, (c) 2 mm and (d) normalisation.

Since the same roughness profile is used to investigate adhesion enhancement due to the changing of particle size, the agreements found here also validate the numerical model in terms of repeatability and reliability.

Braking Operation

When the train is approaching a station or designated stop, the wheel is sliding (worst case scenario) to decelerate the train from its current speed to a complete halt. Figure 5.16 shows the observed adhesion enhancements within this operation. Depending on the participation of sand fragments, the braking operation can also be separated into three stages: the prior-to-fracture stage, the fracture stage, and the post-fracture stage. The adhesion enhancement during the prior-to-fracture stage is comparable for particles of different sizes. Compared to traction operation, for the rough surface, the duration of the fracture stage increases tremendously for bigger particles during the braking operation, and therefore the post-fracture stage is not well observed due to the predefined run-length of the model. However, based on the plots from small particles and the stage definition, the post-fracture stage for bigger particles will be similar to its prior-to-fracture stage and only require a longer time to be achieved. This observation introduces a significant difference from the result using the flat surface where the adhesion enhancement increases sharply to its peak value during the fracture stage and then carries the value over into the post-fracture stage till the end of the simulation.

Similarly, a normalisation is conducted on the data and plotted in Figure 5.16d. The initial difference in plots during the prior-to-fracture stage has been discussed in the previous section. Although the fracture stage still lasts longer for bigger particles, its peak value now is comparable to results from small particles.

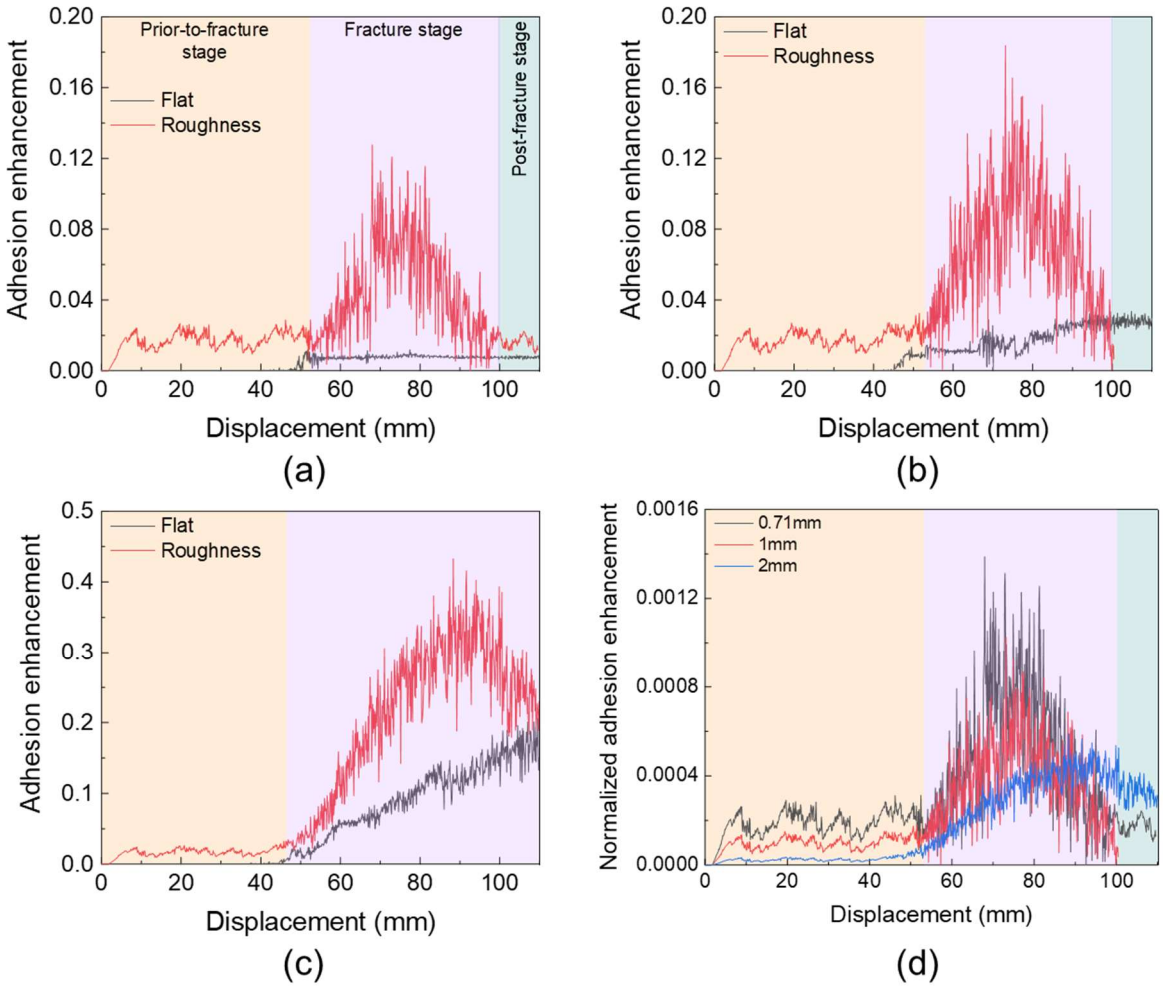

Figure 5.16. Size effect during braking operation: (a) 0.71 mm, (b) 1 mm, (c) 2 mm and (d) normalisation.

Fragment Distribution

During the braking operation, the adhesion enhancement behaves differently on flat and rough surfaces. This requires a further investigation of the fragment distribution during the wheel-rail contact to reveal the underlying facts. The observation has been plotted in Figure 5.17. In the flat case, the sand fragments have been held and pushed away by the sliding wheel till the end of the simulation. Thus, the number of fragments entering the wheel-rail interface starts to increase till a certain value and then this value will be maintained. This explains the reason why adhesion enhancement increases sharply at the beginning and then becomes stable later on. In contrast, the interlocks between the fragments and the uneven surface generate reaction forces which causes the deformation of the rail. Hence, instead of being pushed away, this deformation enables the sand fragments to be passed by the rolling wheel. Consequently, the plots in Figure 5.16 illustrating initial increases in adhesion enhancement, followed by a subsequent decline, have been generated.

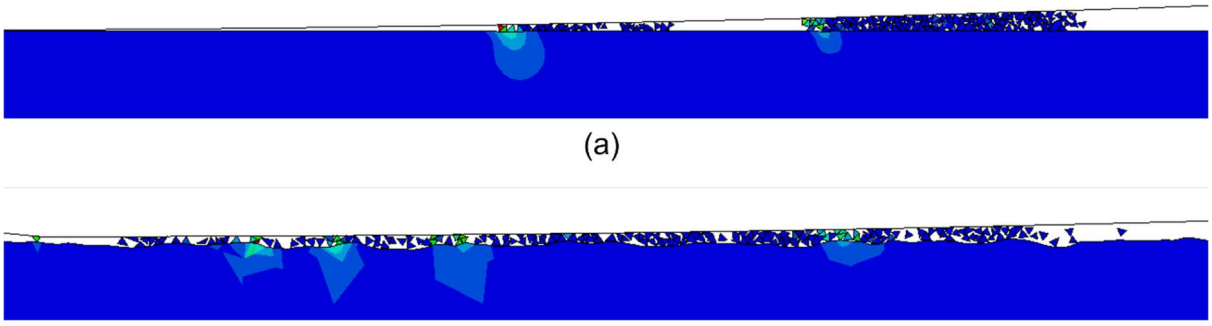

(a)

(b)

Figure 5.17. Fragment distribution during braking operation: (a) flat surface and (b) rough surface.

In summary, the magnitude of adhesion enhancement in the rough case depends on the number of fragments entering the wheel-rail interface rather than the particle size. This aligns with the previous findings using a flat surface. Furthermore, the rough surface permits the wheel to roll over the fragments during braking operation, a feature distinct from the flat surface.

5.5.6 Roughness Effect

A total of 37 representative roughness profiles from cases A and B are analysed to examine the effect of surface roughness on adhesion enhancement. To ensure consistency and comparability, particles with a 1 mm diameter are selected for further investigation.

Traction Operation

The results from 37 simulations using rough surfaces under traction operation have been plotted in Figure 5.18 to compare with the results using the flat surface. The red solid line indicates the average value of the 37 simulations and the pink shade demonstrates its standard deviation. The black line shows the result of adhesion enhancement from the flat surface.

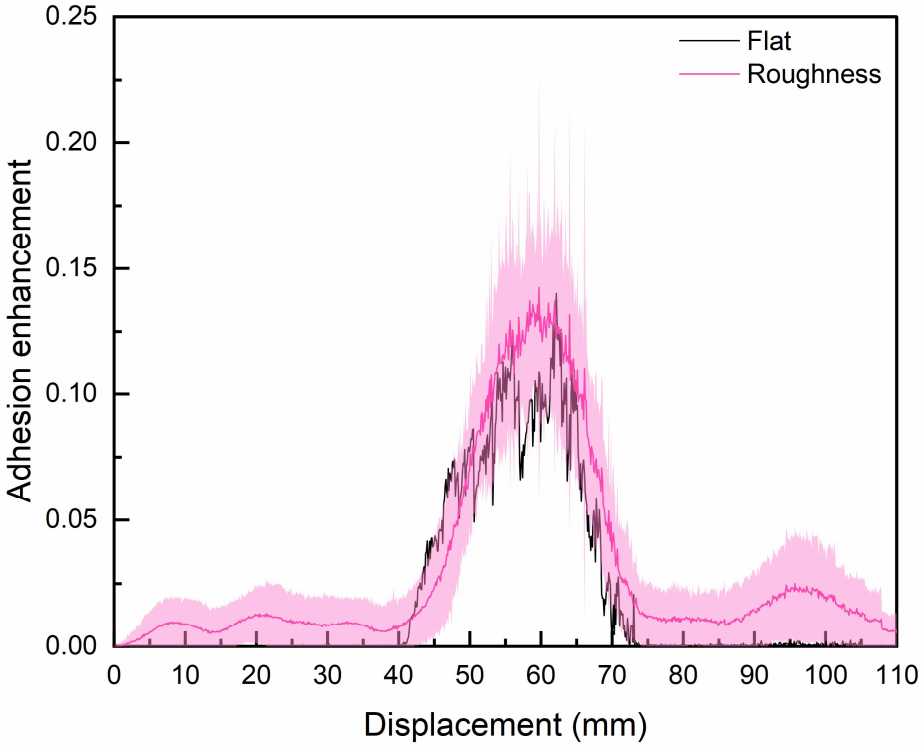

Figure 5.18. Roughness effect during traction operation.

By comparing the two solid lines, the observation from the previous section using the single roughness profile has been confirmed. Furthermore, the smooth portion of the red line during the prior-to-fracture stage indicates a stable improvement of adhesion due to rough surfaces. It begins to rise shortly when the fracture stage occurs. After a sharp curve, the adhesion begins to decrease in a pattern similar to how it had previously increased. It ends with an adhesion enhancement level comparable to that of the prior-to-fracture stage. This variation trend is identical to the black line from the flat surface. The difference in peak values between the two solid lines can be correlated to the initial improvement due to roughness.

Braking Operation

The simulations are repeated for the braking operation. Similarly, as illustrated in Figure 5.19, the average value of adhesion enhancements from 37 simulations is represented by the red solid line, with the pink-shaded area indicating its standard deviation. The adhesion enhancement obtained from the flat surface is depicted by the black line. The hill-shaped plot of average value proves the observation of fragment distribution in the previous section that the mechanical interaction of sand fragments gets changed when switching from the flat surface to the rough surface. Rather than being repelled, the fragments can pass through the wheel-rail interface.

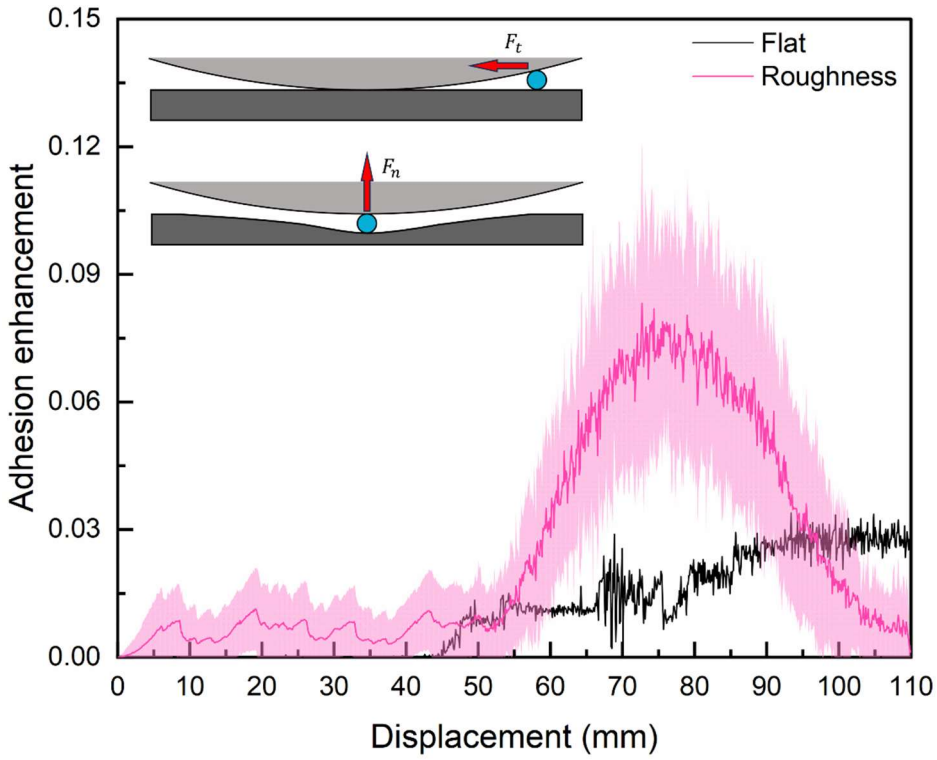

Figure 5.19. Roughness effect during braking operation.

During the prior-to-fracture stage, the plot of the red line indicates the adhesion can be improved during braking operation as well. Although its value is comparable to the enhancement during traction operation, the zigzag shape shows the unstable reaction between the sliding wheel and uneven rail. This phenomenon persists throughout the entire operation, even when sand fragments are present, leading to significant noise in the hill-shaped plot during the fracture stage. Due to the horizontal force from the sliding wheel, it takes longer to complete the fracture stage compared to traction operation. The peak value generated from rough surfaces is about three times higher than the one from the flat surface. This is owing to the total normal force has been reduced by the reaction force generated from the fragments entering the wheel-rail interface, leading to a higher adhesion level compared to the result from the flat surface where no normal force reduction exists, as illustrated by the inset of Figure 5.19. However, this peak value is still lower than the one from the rough surface during traction operation as the rolling wheel contributes to a higher total tangential force.

Roughness Parameter

Based on the earlier discussions, it is evident that rough surface significantly influences

the adhesion in both traction and braking operations. Hence, the widely used descriptor, R_a, is employed here to examine the contribution of roughness to adhesion enhancement. It is a general indicator of surface finish by specifying the average height deviations. Since adhesion enhancement during the post-fracture stage in both traction and braking operations behaves similarly to the prior-to-fracture stage, only the first two stages (*i.e.,* prior-to-fracture stage and fracture stage) are considered here.

As shown in Figure 5.20, the black square indicates the average value of adhesion enhancements during the stage affected by different R_a and the flat end bars represent its standard deviation. By comparing Figures 5.20a and 5.20c, although the adhesion enhancement does not show a significant rise, it is clear that the standard deviation increases with the rise of R_a, suggesting that a rougher surface tends to induce greater fluctuations in adhesion. Additionally, the values exhibit comparability between traction operation and braking operation during the prior-to-fracture stage. It signifies the adhesion level is not affected by the mode of operation when sand fragments are not involved. However, this relationship is changed when the fracture stage begins, as illustrated in Figures 5.20b and 5.20d. While the adhesion enhancement is stable during both operations, the average value and standard deviation of adhesion enhancement are bigger during traction operation than the ones during braking operation. This indicates that adhesion experiences a tremendous fluctuation at the fracture stage during traction operation. In addition, the values of adhesion enhancement are levelled up during the fracture stage compared to the prior-to-fracture stage, as the same amount of fragments were generated during particle breakage. This observation suggests a bigger R_a contributes to a higher adhesion enhancement during the prior-to-fracture stage where no sand particles are involved, and its influence becomes less pronounced compared to the effect of sand fragments during the fracture stage.

5.5.7 Plasticity Effect

The interlocking between sand fragments and the rough surface generates forces that deform the rail profile, allowing more fragments to enter the wheel-rail interface. When only elastic deformation is considered, the recovery of rail deformation introduces reaction forces that increase the adhesion level. However, in practice, plastic deformation, such as wear, typically results in a lower adhesion level. Therefore, it is crucial to use a numerical model that accounts for plastic deformation to further investigate the effects of roughness. Therefore, after defining the plastic parameters of

the rail, the previous model now can be used to further investigate the adhesion level in a more realistic way.

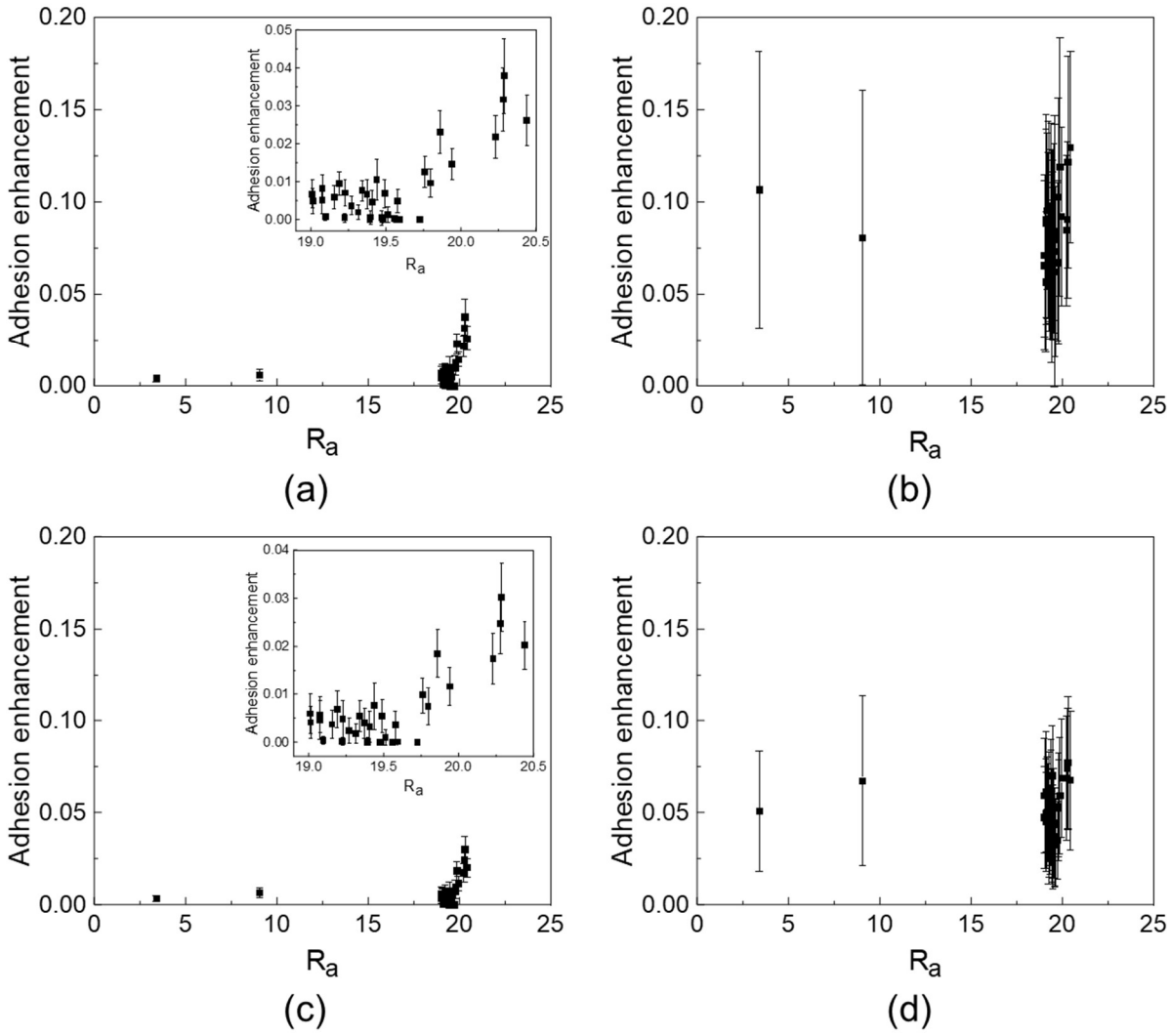

Figure 5.20. Adhesion enhancements influenced by R_a. (a) prior-to-fracture stage and (b) fracture stage during traction operation. (c) prior-to-fracture stage and (d) fracture stage during braking operation.

Traction Operation

As shown in Figure 5.21, the blue shaded area represents the standard deviation of results considering both elastic and plastic deformation, while their mean value is depicted as a continuous blue line. Although the trends of variation are similar, the values from roughness cases that account for plasticity are significantly smaller than those considering only elasticity, with a reduction of approximately 60%. This causes the values to be even smaller than those observed in the flat case. The reduction is attributed to the permanent deformation in the rail caused by its plastic properties,

which diminishes the reaction force generated by the recovery of elastic deformation, thereby reducing the adhesion enhancement. Moreover, compared to the red plots, the width of the blue shaded area becomes narrower, and the noise in the blue solid line appears smoother, with a plateau forming at the peak during the fracture stage. All these observations suggest that the enhanced model, which considers plasticity, results in a more stable adhesion level.

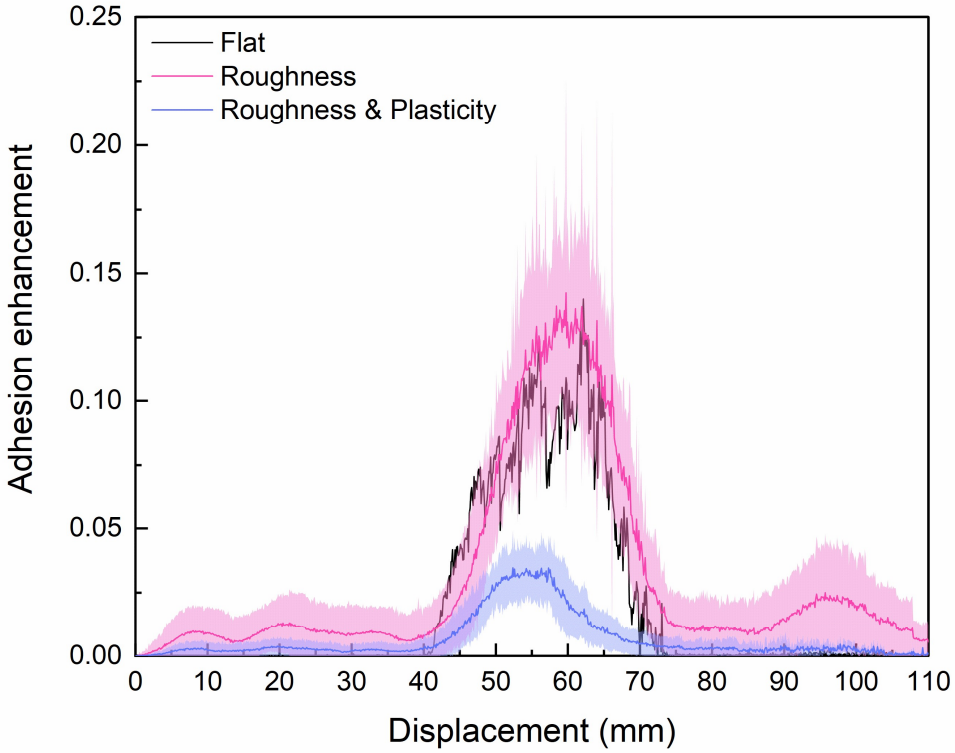

Figure 5.21. Plasticity effect during traction operation.

Braking Operation

The plasticity also affects the adhesion level during braking operation, as shown in Figure 5.22. Due to the sliding wheel during braking operation, the plots from all cases exhibit a persistent vibration throughout the entire simulation. However, their variation trends behave differently.

Divergence starts during the fracture stage. Although all the plots begin to increase at the same time, the slope and peak values vary between cases. For the flat case, the plot starts with a gentle slope and transitions into a plateau that continues until the end. For the roughness case, which only considers elasticity, the plot rises rapidly and falls sharply, reaching a higher peak value compared to the flat case. When plasticity is included in the rough case, the plot ascends with a gentle slope, transitions into a prolonged plateau at half the peak value of the flat case, and then descends with an

even more gradual slope.

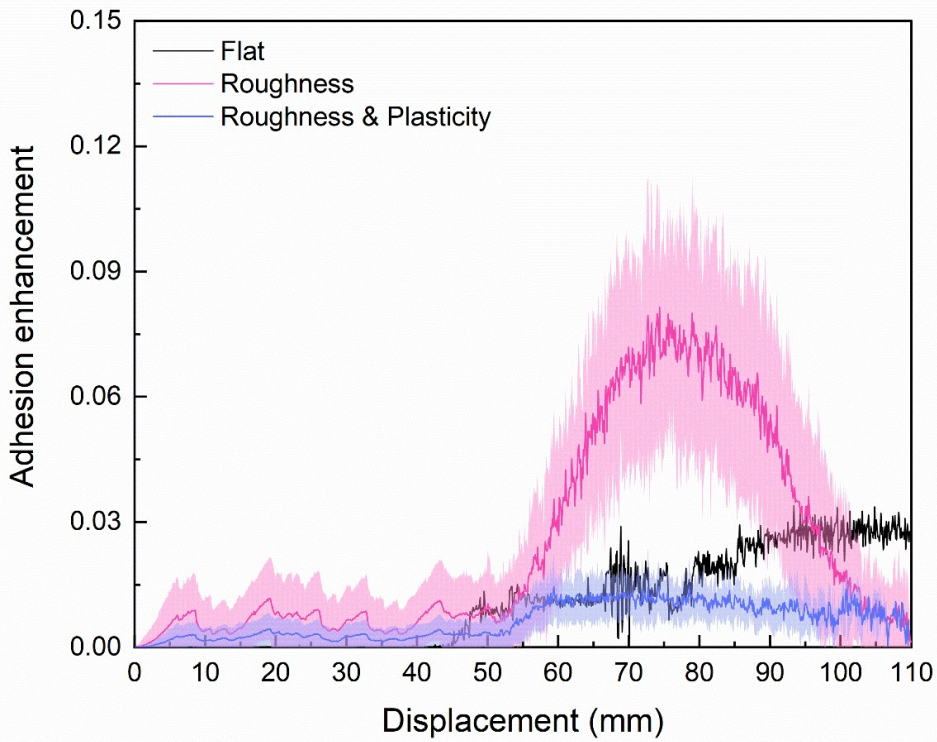

Figure 5.22. Plasticity effect during braking operation.

Overall, this enhanced model reveals the significant impact of plastic deformation on adhesion enhancement during both traction and braking operations. While roughness without plasticity produces higher peak adhesion, it exhibits greater variability and instability, as indicated by the wider shaded regions and sharper transitions. In contrast, the inclusion of plastic deformation in the model leads to a more stable adhesion response, with smoother transitions and prolonged plateaus at lower adhesion levels. However, the reduction in peak adhesion due to plasticity highlights the importance of routine rail grinding to mitigate the effects of wear and maintain the desired surface roughness for optimal adhesion during sanding. These findings emphasize the need for numerical models that incorporate both elastic and plastic behaviours to accurately predict adhesion performance and the importance of consistent rail maintenance to ensure safe and efficient traction and braking in railway operations.

5.5.8 3D Model

Extending the model from 2D to 3D is required to capture the full complexity of the physical processes at the wheel-rail interface. While 2D models provide valuable

insights and serve as a computationally efficient tool for understanding particle fragmentation and adhesion enhancement, they inherently simplify the system by neglecting the third dimension. In real-world scenarios, particle fragmentation and interactions occur in three dimensions, where contact mechanics involve surface areas rather than lines, making 2D representations insufficient for fully describing the system. Transitioning to 3D allows the model to account for volumetric effects and spatial distributions, both of which are essential for accurately simulating adhesion behaviour. Consequently, the existing model has been extended to 3D while maintaining the same boundary conditions and material properties, as illustrated in Figure 5.23.

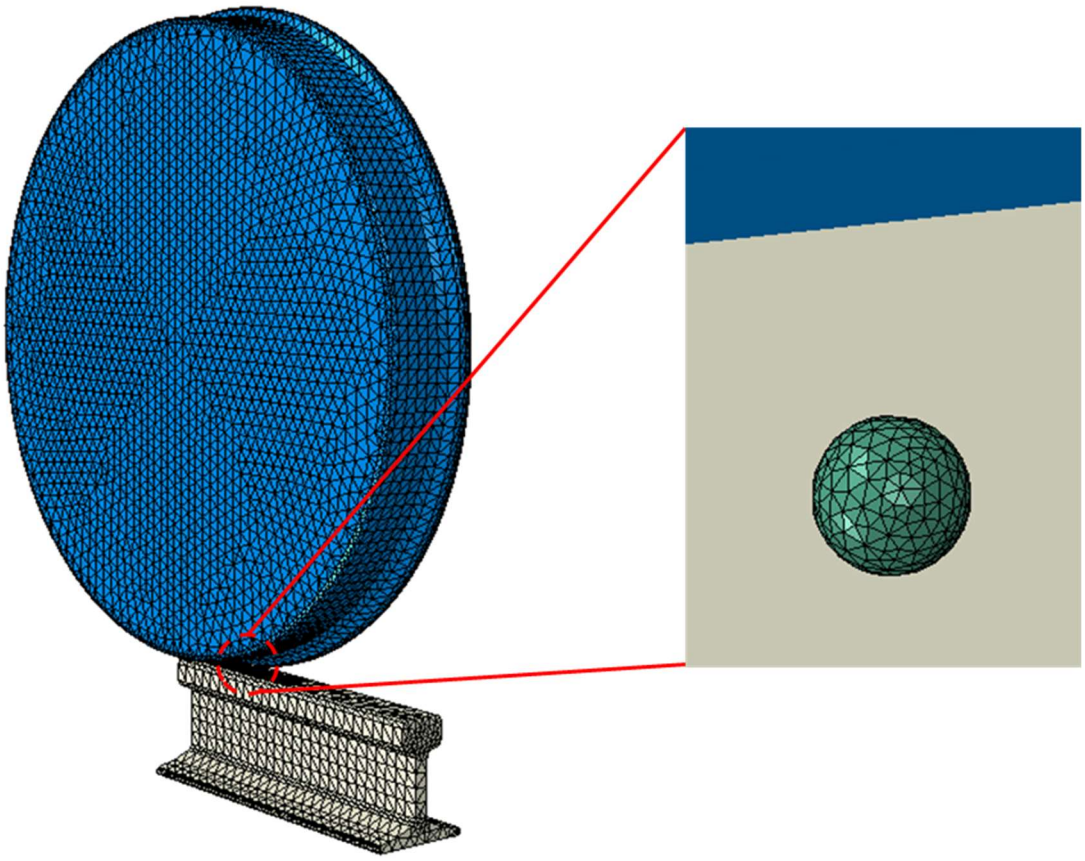

Figure 5.23. The 3D version of the model.

An important consideration is that extending the model to 3D significantly increases the number of elements, leading to a substantial rise in both computational complexity and cost. For example, as shown in Table 5.5, the number of elements needed to mesh a particle with a size of 0.71 mm is much higher in 3D compared to 2D. This highlights the trade-off between model accuracy and computational efficiency when transitioning from 2D to 3D simulations.

Table 5.5. Mesh composition of sand particles in 2D and 3D models.

	Mesh dimension (mm)	Element size (mm)	Element number
2D	0.71	0.10	92 CPE3 elements
3D	0.71	0.10	1978 C3D4 elements

Figure 5.24 presents a preliminary comparison of adhesion enhancement during traction operation using a single particle, modelled in both 2D and 3D conditions. Both curves exhibit a similar trend: a sharp rise, a peak around 500 mm displacement, and a subsequent decline as the fragments pass through the wheel-rail interface. However, the absolute adhesion enhancement values differ significantly, with the 3D simulation showing much higher values than the 2D case. This disparity highlights the limitations of the 2D simulation, where the results are less realistic and serve primarily for trend analysis rather than for representing accurate physical behaviour. In contrast, the 3D simulation captures more complex interactions and incorporates the larger surface contact area resulting from particle fragmentation, providing a more accurate representation of adhesion behaviour.

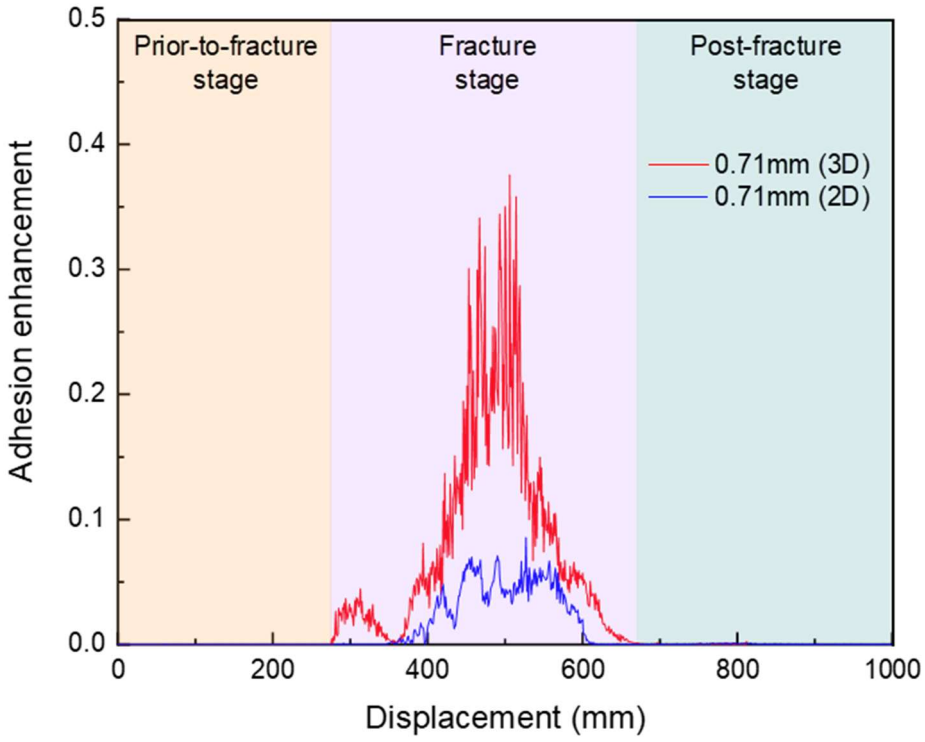

Figure 5.24. Dimensional effect during traction operation.

It is important to note that these results are not normalised by the number of

fragments, due to the fundamental differences in contact mechanics between 2D and 3D simulations. In 2D, contact between fragments and the wheel–rail interface occurs along edges (i.e., lines), and a simplified normalisation could be attempted using the number of fragments directly contributing to contact edges. However, in 3D, for the same initial sand particle size, the number of fragments increases dramatically (e.g., from 92 in 2D to 1,978 in 3D), and the contact conditions become more complex, involving both edge and surface contact. As a result, directly using fragment count for normalisation in 3D is not meaningful or representative of the actual physical interaction. A more appropriate future approach may involve quantifying the actual contact surface area to enable consistent normalisation between 2D and 3D cases.

Furthermore, the advantage of the 3D simulation lies in its ability to visualise the distribution of fragments and the corresponding contact patch on the rail surface as the wheel bypasses through the fragments, as shown in Figure 5.25. The top row of Figure 5.25 illustrates the progressive fragmentation of the particle, transitioning from an intact sphere to a fully fragmented state. The bottom row shows the evolution of contact patches during traction operation. Initially, a small contact area is observed, corresponding to a single point of interaction. As the operation progresses, the contact patch expands, indicating an increase in the effective contact area due to fragmentation and redistribution of particles. This detailed visualisation underscores the complexity of 3D interactions and provides crucial insights into the mechanics of fragment-induced adhesion behaviour at the wheel-rail interface.

The 3D simulation offers a clear advantage over 2D by capturing the complex interactions between fragments and the wheel & rail, including detailed surface contact, stress distribution patterns, and out-of-plane effects. While 2D simulations are valuable for preliminary analysis, they inherently assume plane strain or plane stress conditions and cannot represent true particle geometries, rotational dynamics, or the three-dimensional nature of fragmentation. These limitations reduce their ability to fully replicate the physical response of particles under realistic loading conditions. In contrast, the 3D model offers a more realistic representation of particle fragmentation and inter-particle contact forces, enabling a more comprehensive assessment of their cumulative effect on adhesion behaviour. Future studies will extend this 3D approach to investigate the effects of cyclic loading, surface roughness, and spatial variability in material properties, offering deeper insights into the mechanics of wheel–rail interactions.

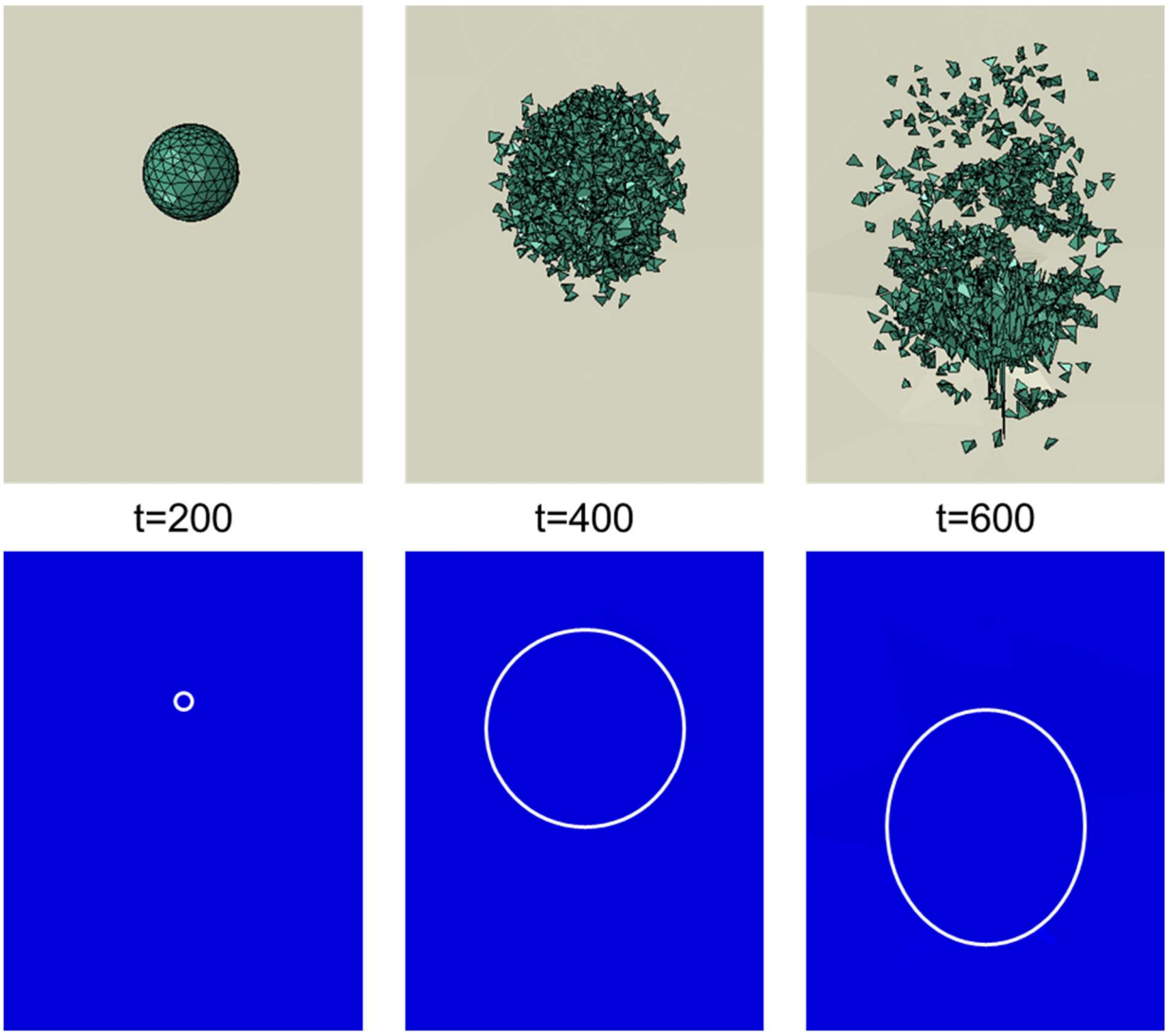

Figure 5.25. Distributions of fragments (top) and contact patches (bottom) during traction operation.

5.6 Summary

This chapter investigated the adhesion enhancement at the wheel-rail interface caused by sand particle breakage using the developed μFE model. The fracture behaviour of sand particles during traction and braking operations was analysed, and the effects of particle size, shape, and number on adhesion improvement were compared. Additionally, the model incorporated surface roughness and plastic deformation of the rail to provide a more realistic representation of wheel-rail interactions. The methodology was extended to 3D modelling to explore the impact of dimensionality on adhesion enhancement. The main conclusions drawn from this chapter are as follows:

- Adhesion enhancement triggered by sand particles is correlated to the number of generated fragments, which can be directly linked to the newly created surface area of the third body.

- Sand particles provide higher adhesion enhancement during traction operations compared to braking operations.
- Surface roughness significantly influences adhesion levels during the pre-fracture stage but becomes less announced in the fracture stage, where the presence of fragments dominates adhesion enhancement.
- Plastic deformation in the rail reduces the reaction forces from fragments during wheel-rail contact, resulting in a lower overall adhesion level.
- Preliminary 3D results demonstrate that dimensionality significantly influences adhesion behaviour, with 3D simulations revealing higher adhesion enhancement due to greater surface contact and more realistic stress distributions compared to 2D.

This chapter demonstrates the critical role of particle fragments in influencing adhesion level at the wheel-rail interface and highlights the importance of dimensionality, surface roughness, and plastic deformation in understanding and optimising adhesion mechanisms for railway systems.

Chapter 6 Conclusions and Future Work

6.1 Summary

This thesis aims to advance the understanding of particle strength, particularly in natural sands with a focus on the influence of particle morphology and contact curvature. The research builds on the limitations of traditional experimental methods, such as flat platen and point-load tests, by employing advanced numerical simulations through μFE analysis. By incorporating CIEs and μCT derived morphology, the research provides a more accurate representation of sand particle breakage behaviour to better estimate the tensile strength, addressing critical gaps in the experimental testing.

The motivation for this work stems from the significant challenges in standardising methods to estimate particle strength, largely due to its geometric and material anisotropy, combined with inherent heterogeneity. While laboratory tests have offered valuable insights, their outcomes are often influenced by experimental constraints, including particle morphology and loading conditions. The introduction of μFE analysis in granular materials has facilitated in-depth investigations of material behaviour, offering valuable insights into failure mechanisms and deformation processes at the microscale. This thesis employs such modelling to investigate both the theoretical and practical aspects of sand particle breakage, including single particle analysis and its application to railway sanding.

Through the review of μFE analysis in engineering mechanics, its transformative capability has been established as a precise tool for linking microstructural features to macroscopic behaviours. By integrating μCT imaging, μFE analysis excels in modelling complex geometries and localised behaviours. Its application across diverse fields, such as biomedical sciences, granular materials, and structural engineering, highlights its broad applicability and effectiveness in addressing challenges that traditional FEM could not resolve. The method's ability to capture microstructural heterogeneity, simulate complex fracture mechanisms, and provide detailed stress-strain analyses has laid the foundation for this thesis, guiding the investigation into sand particle breakage with μFE modelling as the central tool.

Building on this foundation, a robust computational framework using the μFE model enriched with CIEs to simulate crack initiation and propagation has been established. The model was theoretically verified through crack extension tests and experimentally validated using Brazilian tests with different contact topologies such as flat-to-point,

arch-to-arch, and flat-to-flat contacts. A mesh sensitivity analysis was conducted to achieve a balance between computational efficiency and accuracy. The accurate representation of crack initiation and propagation was validated through crack extension tests and cohesive zone analysis. In terms of the calibration of CIEs parameters, a parametric study has been performed to explore their influence on fracture behaviour. Additionally, the study examined load-strain curves, strain distribution, crack initiation and propagation, and tensile strength across different contact topologies, providing a comprehensive understanding of fracture mechanisms. This comprehensive framework not only provides a detailed understanding of fracture mechanisms across diverse contact topologies but also sets the stage for extending the analysis to more complex scenarios, such as the breakage of natural sand particles.

Following the exploration of the fracture behaviour of regular shapes in 2D, the subsequent investigation centered on the breakage behaviour of sand particles under different contact curvatures in 3D, filling the gap between the point-load test and the traditional compression test using flat platens. A modified point-load test was implemented using the developed μFE model, enabling the simulation of particle breakage under varying indenter radii, ranging from 0.1 mm to 6.4 mm. Two samples, silica sand with compact geometries and crushed glass with elongated forms, were numerically tested to analyse how particle morphology and contact curvature influence breakage behaviour. The μCT imaging was employed to reconstruct realistic particle geometries, followed by volumetric mesh generation using an advanced surface reconstruction algorithm. In terms of particle breakage, an in-house code was developed for embedding 3D CIEs into reconstructed meshes. Through 294 simulations of 42 particles with seven different indenters, this study investigated relationships between fracture force, contact area, particle morphology, and indenter size, proposing a novel method to estimate tensile strength independent of contact curvature. Additionally, an in-house code was developed to capture individual fragments for post-breakage analysis. Three distinct fracture modes were identified: local crushing, major splitting, and chipping. By quantifying the morphological changes between parent and child particles under varying contact curvatures, the study provides insights into the factors governing shape evolution during breakage. This enriched μFE model not only bridges the gap between experimental testing and numerical analysis but also establishes a robust framework for investigating complex fracture behaviors and their impact on real-world applications.

One important application directly influenced by sand breakage is the regulation of

adhesion levels at the wheel-rail interface. To investigate this, the developed μFE model for particle breakage analysis was applied to study the role of third-body layers, specifically sand particles, in adhesion enhancement. The numerical environment of the wheel-rail contact was introduced with boundary conditions carefully assigned to replicate realistic traction and braking operations. To isolate the specific effects of particle morphology on adhesion, the initial analysis employed a smooth wheel-rail interface, minimising the influence of surface irregularities and focusing on the impact of particle size and shape before and after fragmentation. Subsequently, rail surface roughness was integrated into the model to quantify its effect on adhesion levels, followed by the inclusion of plastic deformation resulting from cyclic loading to enable a comprehensive analysis of adhesion behaviour during the sanding process. Furthermore, The study expanded into a 3D numerical framework, providing a detailed examination of fragment interactions and contact stress distributions under realistic dimensional conditions.

This research demonstrates the potential of advanced numerical simulations to overcome experimental limitations and provide a comprehensive understanding of particle breakage behaviour. It highlights the importance of integrating particle morphology, contact curvature, and environmental factors to achieve accurate and reliable results. The outcomes are expected to have a significant impact on the design and optimisation of materials and processes in industries ranging from transportation to construction.

6.2 Key Remarks

Specific conclusions are drawn from Chapters 3 through 5, highlighting the key impacts and contributions, which are presented as tangible outcomes.

Chapter 3 The Development of the Micro Finite Element Model for Particle Breakage

- The CIEs can effectively simulate crack initiation and propagation, particularly in measuring the fracture angle, which has been verified through crack extension tests.
- A full cohesive zone approach was identified as optimal for allowing cracks to propagate freely and realistically.
- For flat-to-point contact, the failure occurred at the loading ends due to strain concentration, leading to crushing failure.

- For arch-to-arch contact, the failure also occurred at the loading ends with some secondary cracks at the disc centre, and the eccentric strain distribution caused by practical difficulty is not a problem in the numerical model.
- For flat-to-flat contact, it produces the most ideal fracture behaviour, with crack initiation at the centre and propagation toward the loading ends, aligning with theoretical assumptions.
- Comparisons between different contact topologies highlighted the importance of strain distribution which determines the location of crack initiation and propagation patterns.
- Flat-to-flat contact was identified as the optimal setup, providing the most accurate tensile strength estimation.

Chapter 4 Insights on Particle Breakage Variability

- Silica sand and crushed glass exhibit distinct load-strain behaviours, with silica sand showing abrupt force drops and crushed glass demonstrating smoother transitions due to its elongated fragments.
- Larger indenters lead to higher crushing forces and larger contact areas, highlighting the role of contact curvature in breakage behaviour. The normalization of contact areas shows a consistent converging trend across all tested particles prior to breakage, regardless of indenter size.
- A novel method for estimating tensile strength is proposed, offering consistency across different loading balls. The outcomes for both materials align well with the Weibull distribution.
- Fracture modes shift from major splitting, driven by high local stress concentrations from small indenters, to chipping under larger indenters, which diminish the impact of local stress concentrations.
- Silica sand tends to generate irregular fragments with lower convexity and sphericity values. In contrast, the fragments of crushed glass maintain more self-similar shapes with reduced elongation.
- Two in-house codes were developed: one for embedding 3D CIEs into volumetric meshes to effectively simulate crack initiation and propagation during particle breakage, and another for capturing and analysing individual fragments to perform detailed post-breakage assessments.

Chapter 5 The Impact of Sand Particle Breakage on Adhesion at the Wheel-Rail Interface

- Sand particles enhance the adhesion level at the wheel-rail interface by forming a third-body layer composed of fragments during both braking and acceleration operations.
- Fragmentation during particle breakage is the key contributor to adhesion enhancement, with the number of fragments and their associated newly generated surface area governing the level of improvement.
- Larger and elongated particles produce more fragments and spread widely along the rail, resulting in higher adhesion enhancement during braking operations, while no significant shape effect is observed during traction operations.
- Rail roughness plays a crucial role in adhesion enhancement during the pre-fracture stage by increasing friction but becomes less influential during the fracture stage as sand fragments dominate.
- Plastic deformation in the rail reduces adhesion by limiting reaction forces generated by sand fragments, creating more stable adhesion levels but with lower overall peaks compared to purely elastic rails.
- Fragment distribution varies between flat and rough rail surfaces, with rough surfaces facilitating more effective interlocking of fragments, particularly during braking operations, where higher adhesion enhancement is achieved compared to flat surfaces.
- Sand particles are more effective in traction operations, where rolling wheels maintain consistent fragment contact, compared to braking, where sliding wheels spread fragments over a larger area, weakening their contribution.
- 3D modelling reveals significantly higher adhesion enhancement compared to 2D simulations, capturing the increased surface contact and realistic stress distribution caused by particle fragmentation.
- Field experiments validate the simulation results, demonstrating that sand fragments pass through the wheel-rail interface and spread along the rail, while the majority of fragments during braking operations are pushed away by the sliding wheel.

6.3 Suggestions for Future Work

This section highlights prospective research directions beyond the scope of this thesis. While the developed μFE model has demonstrated its effectiveness in simulating particle breakage behaviour, further advancements in theoretical investigation, numerical modeling, experimental validation, and practical application could deepen the understanding of particle breakage mechanisms and widen the model's applicability.

Theoretical Investigation

The analysis of fracture force in silica sand and crushed glass revealed that data distribution is more concentrated with smaller indenters but becomes increasingly dispersed as the indenter radius increases. This can be attributed to the more intricate interactions between particles and larger indenters, where local roundness exerts a greater influence on fracture behaviour.

Experimental findings by Wang and Coop (2016) aligned with this conclusion, demonstrating that variations in local roundness result in distinct failure modes, which, in turn, influence the estimation of particle tensile strength. Building on this, Zhou *et al.* (2020) further validated this relationship through numerical simulations, confirming a positive correlation between local roundness and particle tensile strength.

Given these findings, it is recommended to incorporate local roundness into investigations of how contact curvature influences particle breakage. The local roundness of sand particles can be effectively captured using μCT-based mesh reconstruction. Subsequently, either an existing open-source code or a custom-developed in-house code could be employed to quantify local roundness values at the loading ends, enabling a deeper understanding of its role in refining the proposed method for estimating tensile strength.

Numerical Simulation

In the point load test reproduced in this research, the tested sand particles were rotated to rest in their most stable position, aligning their minimum principal dimension vertically with the compressive force transmitted by the loading apparatus (Cavarretta *et al.*, 2017). This setup represents the natural resting position of individual particles in a stable state. However, within granular assemblies, particle orientations are continuously rearranged, resulting in a complex and dynamic contact force network that differs significantly from the controlled conditions of isolated particle tests.

A study conducted by Wei *et al.* (2019) on particle breakage under rotational point loading highlighted the significant influence of loading direction on particle fracture behaviour. Fractures vary based on the alignment of the loading direction with the particle's principal dimensions. When loading occurs along the maximum dimension, lower stress and energy lead to minor fractures, such as chipping. Conversely, loading along the minimum dimension requires higher stress and energy, resulting in severe breakage patterns, including the formation of two or three main fragments.

With these conclusions in mind, a further investigation of how contact curvature affects particle breakage is suggested, particularly under varying loading directions that better represent the conditions within granular assemblies. This would allow for a more accurate representation of fracture mechanisms under the realistic force interactions found in granular assemblies.

Experimental Validation

Since the proposed method for estimating particle tensile strength is based solely on simulation results, it is recommended to conduct experimental tests for validation. However, a significant challenge arises from the fact that no two identical sand particles can be found in nature, making it difficult to compress the same particle using loading balls with different radii.

With advancements in 3D printing technology, it is now possible to validate reconstructed objects from numerical models. While pursuing a master’s degree, the candidate and his colleagues successfully reconstructed a natural sand particle in a numerical domain and 3D-printed a simplified sand mesh for a triaxial test. The results showed good agreement when compared with natural sand. The material properties of the 3D-printed particles in that study were comparable to those of typical limestone particles, highlighting the potential of 3D printing for advancing geomechanical studies (Su *et al.*, 2017).

Building on this approach, the particle meshes of silica sand and crushed glass from this research could also be physically reproduced using 3D printing for experimental validation. While there may be differences between the material properties of the 3D-printed particles and natural sand, the material parameters in the μFE model can be adjusted to match those of the printing material for validation purposes. This strategy bridges the gap between numerical modelling and experimental study, enhancing the reliability of simulation results.

Practical Application

During a conversation with guest speaker Dr. Masahide Otsubo from the Port and Airport Research Institute, Japan, the potential application of the developed μFE model in coastal protection was discussed, particularly for assessing the strength of natural boulders used in shoreline defense. Natural boulders are widely utilised for their wave-dissipating properties. However, their effectiveness depends on their mechanical strength and resistance to fracturing under harsh marine conditions. Accurately evaluating their crushing strength and failure behaviour is essential for ensuring long-term durability in coastal environments.

The developed μFE model can be utilised to assess the mechanical properties of natural boulders, providing insights into their durability under repeated wave impacts. Furthermore, this approach can be extended to evaluate alternative materials that may replace natural boulders, such as recycled aggregates or engineered composites.

References

Aboura, Z. (1993) *Etude du processus de délaminage mode I, mode II et mode mixte (I+II) de matériaux composites à renforts tissés à différentes vitesses de sollicitation*. These de doctorat. Compiègne.

Ai, S., Song, W. and Chen, Y. (2021) Stress field and damage evolution in C/SiC woven composites: Image-based finite element analysis and in situ X-ray computed tomography tests, *Journal of the European Ceramic Society*, **41**(4), pp. 2323–2334.

Akazawa, T. (1943) New test method for evaluating internal stress due to compression of concrete (the splitting tension test)(part 1), *Journal of Japan Society of Civil Engineers*, **29**, pp. 777–787.

Akhlaghi, P., Khorshidparast, S. and Rouhi, G. (2023) Investigation on primary stability of dental implants through considering peri-implant bone damage, caused by small and large deformations: A validated non-linear micro finite element study, *Journal of the Mechanical Behavior of Biomedical Materials*, **146**, p. 106062.

Allen, C., Meyer, C.A., Yoo, E., Vargas, J.A., Liu, Y. and Jalali, P. (2018) Stress distribution in a tooth treated through minimally invasive access compared to one treated through traditional access: A finite element analysis study, *Journal of Conservative Dentistry and Endodontics*, **21**(5), p. 505.

Andreev, G.E. (1991) A review of the Brazilian test for rock tensile strength determination. Part I: calculation formula, *Mining Science and Technology*, **13**(3), pp. 445–456.

Angelidakis, V., Nadimi, S. and Utili, S. (2021) SHape Analyser for Particle Engineering (SHAPE): Seamless characterisation and simplification of particle morphology from imaging data, *Computer Physics Communications*, **265**, p. 107983.

Arias-Cuevas, O., Li, Z. and Lewis, R. (2010) Investigating the Lubricity and Electrical Insulation Caused by Sanding in Dry Wheel–Rail Contacts, *Tribology Letters*, **37**(3), pp. 623–635.

Arias-Cuevas, O., Li, Z. and Lewis, R. (2011) A laboratory investigation on the influence of the particle size and slip during sanding on the adhesion and wear in the wheel–rail contact, *Wear*, **271**(1), pp. 14–24.

Arias-Moreno, A.J., Ito, K. and van Rietbergen, B. (2016) Micro-Finite Element analysis will overestimate the compressive stiffness of fractured cancellous bone, *Journal of*

Biomechanics, **49**(13), pp. 2613–2618.

Asghar, Z., Requena, G. and Boller, E. (2011) Three-dimensional rigid multiphase networks providing high-temperature strength to cast AlSi10Cu5Ni1-2 piston alloys, *Acta materialia*, **59**(16), pp. 6420–6432.

Aslan, T., Esim, E., Üstün, Y. and Dönmez Özkan, H. (2021) Evaluation of Stress Distributions in Mandibular Molar Teeth with Different Iatrogenic Root Perforations Repaired with Biodentine or Mineral Trioxide Aggregate: A Finite Element Analysis Study, *Journal of Endodontics*, **47**(4), pp. 631–640.

ASTM (1988) Standard test method for splitting tensile strength of intact rock core specimens, p. 04.08:471-475.

Atwood, R.C., Jones, J.R., Lee, P.D. and Hench, L.L. (2004) Analysis of pore interconnectivity in bioactive glass foams using X-ray microtomography, *Scripta Materialia*, **51**(11), pp. 1029–1033.

Aziz, A.A., Saury, C., Xuan, V.B. and Young, P. (2006) On the material characterization of a composite using micro CT image based finite element modeling, in *Nondestructive Evaluation and Health Monitoring of Aerospace Materials, Composites, and Civil Infrastructure V*. *Nondestructive Evaluation and Health Monitoring of Aerospace Materials, Composites, and Civil Infrastructure V*, SPIE, pp. 32–39.

Barenblatt, G.I. (1959) The formation of equilibrium cracks during brittle fracture. General ideas and hypotheses. Axially-symmetric cracks, *Journal of Applied Mathematics and Mechanics*, **23**(3), pp. 622–636.

Basista, M., Węglewski, W., Bochenek, K., Poniżnik, Z. and Nowak, Z. (2017) Micro-CT Finite Element Analysis of Thermal Residual Stresses and Fracture in Metal-Ceramic Composites, *Advanced Engineering Materials*, **19**(8), p. 1600725.

Bazant, Z.P. and Planas, J. (2019) *Fracture and Size Effect in Concrete and Other Quasibrittle Materials*. New York: Routledge.

Beagley, T.M., McEwen, I.J. and Pritchard, C. (1975) Wheel/rail adhesion — the influence of railhead debris, *Wear*, **33**(1), pp. 141–152.

Benzeggagh, M.L. and Kenane, M. (1996) Measurement of mixed-mode delamination fracture toughness of unidirectional glass/epoxy composites with mixed-mode bending apparatus, *Composites Science and Technology*, **56**(4), pp. 439–449.

Berre, C., Fok, S.L., Marsden, B.J., Babout, L., Hodgkins, A., Marrow, T.J. and

Mummery, P.M. (2006) Numerical modelling of the effects of porosity changes on the mechanical properties of nuclear graphite, *Journal of Nuclear Materials*, **352**(1), pp. 1–5.

Bieniawski, Z.T. and Hawkes, I. (1978) Suggested methods for determining tensile strength of rock materials, *International Journal of Rock Mechanics and Mining Sciences*, **15**(3), pp. 99–103.

Boniotti, L., Beretta, S., Patriarca, L., Rigoni, L. and Foletti, S. (2019) Experimental and numerical investigation on compressive fatigue strength of lattice structures of AlSi7Mg manufactured by SLM, *International Journal of Fatigue*, **128**, p. 105181.

Boutroy, S., Van Rietbergen, B., Sornay-Rendu, E., Munoz, F., Bouxsein, M.L. and Delmas, P.D. (2008) Finite Element Analysis Based on In Vivo HR-pQCT Images of the Distal Radius Is Associated With Wrist Fracture in Postmenopausal Women, *Journal of Bone and Mineral Research*, **23**(3), pp. 392–399.

Brekelmans, W.A.M., Poort, H.W. and Slooff, T.J.J.H. (1972) A New Method to Analyse the Mechanical Behaviour of Skeletal Parts, *Acta Orthopaedica Scandinavica*, **43**(5), pp. 301–317.

Broster, M., Pritchard, C. and Smith, D.A. (1974) Wheel/rail adhesion: its relation to rail contamination on british railways, *Wear*, **29**(3), pp. 309–321.

BS EN 13231-3 (2012) Railway applications-Track Acceptance of works Part 3: acceptance of rail grinding, milling and planning work in tracks, London, BSI-British Standards Institution.

Buckley-Johnstone, L.E., Trummer, G., Voltr, P., Six, K. and Lewis, R. (2020) Full-scale testing of low adhesion effects with small amounts of water in the wheel/rail interface, *Tribology International*, **141**, p. 105907.

Burghardt, A.J., Kazakia, G.J., Sode, M., de Papp, A.E., Link, T.M. and Majumdar, S. (2010) A longitudinal HR-pQCT study of alendronate treatment in postmenopausal women with low bone density: Relations among density, cortical and trabecular microarchitecture, biomechanics, and bone turnover*, *Journal of Bone and Mineral Research*, **25**(12), pp. 2558–2571.

Carneiro, F. (1943) A new method to determine the tensile strength of concrete, in *Proceedings of the 5th meeting of the Brazilian Association for Technical Rules*, pp. 126–129.

Cavarretta, I. and O'Sullivan, C. (2012) The mechanics of rigid irregular particles subject to uniaxial compression, *Géotechnique*, **62**(8), pp. 681–692.

Cavarretta, I., O'Sullivan, C. and Coop, M.R. (2017) The relevance of roundness to the crushing strength of granular materials, *Géotechnique*, **67**(4), pp. 301–312.

Cen, R., Wang, R. and Cheung, G.S.P. (2018) Periodontal Blood Flow Protects the Alveolar Bone from Thermal Injury during Thermoplasticized Obturation: A Finite Element Analysis Study, *Journal of Endodontics*, **44**(1), pp. 139–144.

Chaboche, J.-L. (1989) Constitutive equations for cyclic plasticity and cyclic viscoplasticity, *International journal of plasticity*, **5**(3), pp. 247–302.

Chang, C.-H., Lei, Y.-N., Ho, Y.-H., Sung, Y.-H. and Lin, T.-S. (2014) Predicting the holistic force-displacement relation of the periodontal ligament: in-vitro experiments and finite element analysis, *BioMedical Engineering OnLine*, **13**(1), p. 107.

Chang, Y.-H., Wang, H.-W., Lin, P.-H. and Lin, C.-L. (2018) Evaluation of early resin luting cement damage induced by voids around a circular fiber post in a root canal treated premolar by integrating micro-CT, finite element analysis and fatigue testing, *Dental Materials*, **34**(7), pp. 1082–1088.

Chen, A., Airey, G.D., Thom, N., Li, Y. and Wan, L. (2022) Simulation of micro-crack initiation and propagation under repeated load in asphalt concrete using zero-thickness cohesive elements, *Construction and Building Materials*, **342**, p. 127934.

Chen, G., Fan, W., Mishra, S., El-Atem, A., Schuetz, M.A. and Xiao, Y. (2012) Tooth fracture risk analysis based on a new finite element dental structure models using micro-CT data, *Computers in Biology and Medicine*, **42**(10), pp. 957–963.

Chen, H. (2024) Review of various influencing factors and improvement measures on wheel-rail adhesion, *Wear*, **550–551**, p. 205283.

Chen, X., Yuan, J., Dong, Q. and Zhao, X. (2020) Meso-scale cracking behavior of Cement Treated Base material, *Construction and Building Materials*, **239**, p. 117823.

Chen, Y., Dall'Ara, E., Sales, E., Manda, K., Wallace, R., Pankaj, P. and Viceconti, M. (2017) Micro-CT based finite element models of cancellous bone predict accurately displacement once the boundary condition is well replicated: A validation study, *Journal of the Mechanical Behavior of Biomedical Materials*, **65**, pp. 644–651.

Chen, Y., Ma, G., Zhou, W., Wei, D., Zhao, Q., Zou, Y. and Grasselli, G. (2021) An enhanced tool for probing the microscopic behavior of granular materials based on X-

ray micro-CT and FDEM, *Computers and Geotechnics*, **132**, p. 103974.

Chen, Y., Pani, M., Taddei, F., Mazzà, C., Li, X. and Viceconti, M. (2014) Large-Scale Finite Element Analysis of Human Cancellous Bone Tissue Micro Computer Tomography Data: A Convergence Study, *Journal of Biomechanical Engineering*, **136**(101013).

Cheuk, K.Y., Zhu, T.Y., Yu, F.W.P., Hung, V.W.Y., Lee, K.M., Qin, L., Cheng, J.C.Y. and Lam, T.P. (2015) Abnormal Bone Mechanical and Structural Properties in Adolescent Idiopathic Scoliosis: A Study with Finite Element Analysis and Structural Model Index, *Calcified Tissue International*, **97**(4), pp. 343–352.

Chevalier, Y., Matsuura, M., Krüger, S., Traxler, H., Fleege†, C., Rauschmann, M. and Schilling, C. (2021) The effect of cement augmentation on pedicle screw fixation under various load cases: results from a combined experimental, micro-CT, and micro-finite element analysis, *Bone & Joint Research*, **10**(12), pp. 797–806.

Chevalier, Y., Santos, I., Müller, P.E. and Pietschmann, M.F. (2016) Bone density and anisotropy affect periprosthetic cement and bone stresses after anatomical glenoid replacement: A micro finite element analysis, *Journal of Biomechanics*, **49**(9), pp. 1724–1733.

Chevalley, T., Bonjour, J.P., van Rietbergen, B., Rizzoli, R. and Ferrari, S. (2012) Fractures in Healthy Females Followed from Childhood to Early Adulthood Are Associated with Later Menarcheal Age and with Impaired Bone Microstructure at Peak Bone Mass, *The Journal of Clinical Endocrinology & Metabolism*, **97**(11), pp. 4174–4181.

Christen, D., Melton, L.J., III, Zwahlen, A., Amin, S., Khosla, S. and Müller, R. (2013) Improved Fracture Risk Assessment Based on Nonlinear Micro-Finite Element Simulations From HRpQCT Images at the Distal Radius, *Journal of Bone and Mineral Research*, **28**(12), pp. 2601–2608.

Christen, D., Zwahlen, A. and Müller, R. (2014) Reproducibility for linear and nonlinear micro-finite element simulations with density derived material properties of the human radius, *Journal of the Mechanical Behavior of Biomedical Materials*, **29**, pp. 500–507.

Christensen, R.M. (2000) Yield Functions, Damage States, and Intrinsic Strength, *Mathematics and Mechanics of Solids*, **5**(3), pp. 285–300.

Chung, S.-Y., Kim, J.-S., Stephan, D. and Han, T.-S. (2019) Overview of the use of

micro-computed tomography (micro-CT) to investigate the relation between the material characteristics and properties of cement-based materials, *Construction and Building Materials*, **229**, p. 116843.

Coop, M.R., Sorensen, K.K., Bodas Freitas, T. and Georgoutsos, G. (2004) Particle breakage during shearing of a carbonate sand, *Géotechnique*, **54**(3), pp. 157–163.

Cooper, P.R. (1972) An investigation into the relationship between the Particle Size and the Frictional Performance of Sand (IM-ADH-011)(British Rail Report).

Costa, M.C., Campello, L.B.B., Ryan, M., Rochester, J., Viceconti, M. and Dall'Ara, E. (2020) Effect of size and location of simulated lytic lesions on the structural properties of human vertebral bodies, a micro-finite element study, *Bone Reports*, **12**, p. 100257.

Costa, M.C., Tozzi, G., Cristofolini, L., Danesi, V., Viceconti, M. and Dall'Ara, E. (2017) Micro Finite Element models of the vertebral body: Validation of local displacement predictions, *PLOS ONE*, **12**(7), p. e0180151.

Cremers, D., Rousson, M. and Deriche, R. (2007) A Review of Statistical Approaches to Level Set Segmentation: Integrating Color, Texture, Motion and Shape, *International Journal of Computer Vision*, **72**(2), pp. 195–215.

Cundall, P.A. and Strack, O.D.L. (1979) A discrete numerical model for granular assemblies, *Géotechnique*, **29**(1), pp. 47–65.

D'Andrea, L., Gastaldi, D., Baino, F., Verné, E., Schwentenwein, M., Örlygsson, G. and Vena, P. (2024) Computational models for the simulation of the elastic and fracture properties of highly porous 3D-printed hydroxyapatite scaffolds, *International Journal for Numerical Methods in Biomedical Engineering*, **40**(2), p. e3795.

D'Andrea, L., Gastaldi, D., Verné, E., Baino, F., Massera, J., Örlygsson, G. and Vena, P. (2022) Mechanical Properties of Robocast Glass Scaffolds Assessed through Micro-CT-Based Finite Element Models, *Materials*, **15**(18), p. 6344.

DeHoff, R.T. and Rhines, F.N. (eds) (1968) *Quantitative Microscopy*. New York,: McGraw-Hill.

Della Bona, Á., Borba, M., Benetti, P., Duan, Y. and Griggs, J.A. (2013) Three-dimensional finite element modelling of all-ceramic restorations based on micro-CT, *Journal of Dentistry*, **41**(5), pp. 412–419.

Deng, P., Liu, Q. and Lu, H. (2022) A novel joint element parameter calibration procedure for the combined finite-discrete element method, *Engineering Fracture*

Mechanics, **276**, p. 108924.

Diwakar, M. and Kumar, M. (2018) A review on CT image noise and its denoising, *Biomedical Signal Processing and Control*, **42**, pp. 73–88.

Druckrey, A.M. and Alshibli, K.A. (2016) 3D finite element modeling of sand particle fracture based on in situ X-Ray synchrotron imaging, *International Journal for Numerical and Analytical Methods in Geomechanics*, **40**(1), pp. 105–116.

Druckrey, A.M., Alshibli, K.A. and Al-Raoush, R.I. (2016) 3D characterization of sand particle-to-particle contact and morphology, *Computers and Geotechnics*, **74**, pp. 26–35.

Dugdale, D.S. (1960) Yielding of steel sheets containing slits, *Journal of the Mechanics and Physics of Solids*, **8**(2), pp. 100–104.

Edidin, A.A., Dawson, J.M., Zhu, M. and Chinchalkar, S. (1993) Direct estimation of the modulus of cancellous bone using a variable-stiffness FE model, in *Trans. 39th A. Meeting Orthop. Res. See*, p. 589.

Epifania, E., Lauro, A.E. di, Ausiello, P., Mancone, A., Garcia-Godoy, F. and Tribst, J.P.M. (2023) Effect of crown stiffness and prosthetic screw absence on the stress distribution in implant-supported restoration: A 3D finite element analysis, *PLOS ONE*, **18**(5), p. e0285421.

Erarslan, N., Liang, Z.Z. and Williams, D.J. (2012) Experimental and numerical studies on determination of indirect tensile strength of rocks, *Rock Mechanics and Rock Engineering*, **45**, pp. 739–751.

Erarslan, N. and Williams, D.J. (2012) The damage mechanism of rock fatigue and its relationship to the fracture toughness of rocks, *International Journal of Rock Mechanics and Mining Sciences*, **56**, pp. 15–26.

Erdogan, F. and Sih, G.C. (1963) On the crack extension in plates under plane loading and transverse shear.

Evans, Ll.M., Margetts, L., Casalegno, V., Lever, L.M., Bushell, J., Lowe, T., Wallwork, A., Young, P., Lindemann, A., Schmidt, M. and Mummery, P.M. (2015) Transient thermal finite element analysis of CFC–Cu ITER monoblock using X-ray tomography data, *Fusion Engineering and Design*, **100**, pp. 100–111.

Fairhurst, C. (1964) On the validity of the 'Brazilian' test for brittle materials, *International Journal of Rock Mechanics and Mining Sciences & Geomechanics*

Abstracts, **1**(4), pp. 535–546.

Farhad, F. and Oila, A. (2015) MICROSTRUCTURE STRESS STATE EVALUATION OF CONTACT FATIGUE IN GEARS, *Simulation*, **3**, pp. 413–1.

Farina, E., Gastaldi, D., Baino, F., Vernè, E., Massera, J., Orlygsson, G. and Vena, P. (2021) Micro computed tomography based finite element models for elastic and strength properties of 3D printed glass scaffolds, *Acta Mechanica Sinica*, **37**(2), pp. 292–306.

Farr, J.N., Amin, S., Melton, L.J., III, Kirmani, S., McCready, L.K., Atkinson, E.J., Müller, R. and Khosla, S. (2014) Bone Strength and Structural Deficits in Children and Adolescents With a Distal Forearm Fracture Resulting From Mild Trauma, *Journal of Bone and Mineral Research*, **29**(3), pp. 590–599.

Favata, J. and Shahbazmohamadi, S. (2018) Realistic non-destructive testing of integrated circuit bond wiring using 3-D X-ray tomography, reverse engineering, and finite element analysis, *Microelectronics Reliability*, **83**, pp. 91–100.

Fei, W., Narsilio, G.A. and Disfani, M.M. (2019) Impact of three-dimensional sphericity and roundness on heat transfer in granular materials, *Powder Technology*, **355**, pp. 770–781.

Fonseca, J., Nadimi, S. and Kong, D. (2019) Image-Based Modelling of Shelly Carbonate Sand for Foundation Design of Offshore Structures, in M.F. Randolph, D.H. Doan, A.M. Tang, M. Bui, and V.N. Dinh (eds) *Proceedings of the 1st Vietnam Symposium on Advances in Offshore Engineering*. Singapore: Springer Singapore (Lecture Notes in Civil Engineering), pp. 55–60.

Fonseca, J., O'Sullivan, C., Coop, M. r. and Lee, P. d. (2013) Quantifying the evolution of soil fabric during shearing using scalar parameters, *Géotechnique*, **63**(10), pp. 818–829.

Fonseca, J., O'Sullivan, C., Coop, M.R. and Lee, P.D. (2012) Non-invasive characterization of particle morphology of natural sands, *Soils and Foundations*, **52**(4), pp. 712–722.

Frey, P. (1994) Fully automatic mesh generation for 3-D domains based upon voxel sets, *International Journal for Numerical Methods in Engineering* [Preprint].

Frisardi, G., Barone, S., Razionale, A.V., Paoli, A., Frisardi, F., Tullio, A., Lumbau, A. and Chessa, G. (2012) Biomechanics of the press-fit phenomenon in dental

implantology: an image-based finite element analysis, *Head & Face Medicine*, **8**(1), p. 18.

Fyhrie, D.P. (1992) Direct three-dimensional finite element analysis of human vertebral cancellous bone, in *Trans. 38the Meeting Orthpaedic Research Society, 1992*.

Fyhrie, D.P. (1993) The probability distrbution of trabecular level strains for vertebral cancellous bone, *Trans. Orthop. Res. Soc.*, **18**, p. 175.

Griesbach, J.K., Schulte, F.A., Schädli, G.N., Rubert, M. and Müller, R. (2024) Mechanoregulation analysis of bone formation in tissue engineered constructs requires a volumetric method using time-lapsed micro-computed tomography, *Acta Biomaterialia*, **179**, pp. 149–163.

Guha, I., Zhang, X., Rajapakse, C.S., Chang, G. and Saha, P.K. (2022) Finite element analysis of trabecular bone microstructure using CT imaging and continuum mechanical modeling, *Medical Physics*, **49**(6), pp. 3886–3899.

Gunde, A.C., Bera, B. and Mitra, S.K. (2010) Investigation of water and CO2 (carbon dioxide) flooding using micro-CT (micro-computed tomography) images of Berea sandstone core using finite element simulations, *Energy*, **35**(12), pp. 5209–5216.

Haeri, H., Sarfarazi, V., Ebneabbasi, P., Shahbazian, A., Marji, M.F. and Mohamadi, A.R. (2020) XFEM and experimental simulation of failure mechanism of non-persistent joints in mortar under compression, *Construction and Building Materials*, **236**, p. 117500.

Hansen, S., Brixen, K. and Gravholt, C.H. (2012) Compromised trabecular microarchitecture and lower finite element estimates of radius and tibia bone strength in adults with turner syndrome: A cross-sectional study using high-resolution–pQCT, *Journal of Bone and Mineral Research*, **27**(8), pp. 1794–1803.

Hansen, S., Hauge, E.M., Beck Jensen, J. and Brixen, K. (2013) Differing effects of PTH 1–34, PTH 1–84, and zoledronic acid on bone microarchitecture and estimated strength in postmenopausal women with osteoporosis: An 18-month open-labeled observational study using HR-pQCT, *Journal of Bone and Mineral Research*, **28**(4), pp. 736–745.

Hansen, S., Hauge, E.M., Rasmussen, L., Jensen, J.B. and Brixen, K. (2012) Parathyroidectomy improves bone geometry and microarchitecture in female patients with primary hyperparathyroidism: A one-year prospective controlled study using high-

resolution peripheral quantitative computed tomography, *Journal of Bone and Mineral Research*, **27**(5), pp. 1150–1158.

Hao, Y. and Hao, H. (2016) Finite element modelling of mesoscale concrete material in dynamic splitting test, *Advances in Structural Engineering*, **19**(6), pp. 1027–1039.

Harrigan, T.P., Jasty, M., Mann, R.W. and Harris, W.H. (1988) Limitations of the continuum assumption in cancellous bone, *Journal of biomechanics*, **21**(4), pp. 269–275.

Hashim, M., Farhad, F., Smyth-Boyle, D., Akid, R., Zhang, X. and Withers, P.J. (2019) Behavior of 316L stainless steel containing corrosion pits under cyclic loading, *Materials and Corrosion*, **70**(11), pp. 2009–2019.

Hazrati Marangalou, J., Ito, K. and van Rietbergen, B. (2012) A new approach to determine the accuracy of morphology–elasticity relationships in continuum FE analyses of human proximal femur, *Journal of Biomechanics*, **45**(16), pp. 2884–2892.

Hertz, H. (1881) Über die Berührung fester elastischer Körper., *J reine und angewandte Mathematik*, **92**, p. 156.

Hillerborg, A., Modéer, M. and Petersson, P.-E. (1976) Analysis of crack formation and crack growth in concrete by means of fracture mechanics and finite elements, *Cement and Concrete Research*, **6**(6), pp. 773–781.

Hiramatsu, Y. and Oka, Y. (1966) Determination of the tensile strength of rock by a compression test of an irregular test piece, *International Journal of Rock Mechanics and Mining Sciences & Geomechanics Abstracts*, **3**(2), pp. 89–90.

Hollister, S.J., Brennan, J.M. and Kikuchi, N. (1992) Recent Advantages in Computer Methods in Biomechanics and Biomedical Engineering, *Books & Journals Int. LTD, Swansea, UK*, pp. 308–317.

Hollister, S.J., Brennan, J.M. and Kikuchi, N. (1994) A homogenization sampling procedure for calculating trabecular bone effective stiffness and tissue level stress, *Journal of Biomechanics*, **27**(4), pp. 433–444.

Hollister, S.J., Fyhrie, D.P., Jepsen, K.J. and Goldstein, S.A. (1991) Application of homogenization theory to the study of trabecular bone mechanics, *Journal of biomechanics*, **24**(9), pp. 825–839.

Hollister, S.J. and Kikuchi, N. (1992) Direct analysis of trabecular bone stiffness and tissue level mechanics using an element-by-element homogenization method, in *Trans.*

38th A. Meeting Orthop. Res. Soc, p. 30.

Hondros, G. (1959) The evaluation of Poisson's ratio and the modulus of materials of a low tensile resistance by the Brazilian (indirect tensile) test with particular reference to concrete, *Australian Journal of Applied Science*, **10**, pp. 243–264.

Hooke, R. (1678) *Lectures de potentia restitutiva, or of spring explaining the power of springing bodies*. John Martyn (6).

Hu, W., Cao, X., Zhang, X., Huang, Z., Chen, Z., Wu, W., Xi, L., Li, Y. and Fang, D. (2021) Deformation mechanisms and mechanical performances of architected mechanical metamaterials with gyroid topologies: Synchrotron X-ray radiation in-situ compression experiments and 3D image based finite element analysis, *Extreme Mechanics Letters*, **44**, p. 101229.

Huang, Y., Natarajan, S., Zhang, H., Guo, F., Xu, S., Zeng, C. and Zheng, Z. (2023) A CT image-driven computational framework for investigating complex 3D fracture in mesoscale concrete, *Cement and Concrete Composites*, **143**, p. 105270.

Huang, Y.G., Wang, L.G., Lu, Y.L., Chen, J.R. and Zhang, J.H. (2015) Semi-analytical and numerical studies on the flattened Brazilian splitting test used for measuring the indirect tensile strength of rocks, *Rock Mechanics and Rock Engineering*, **48**, pp. 1849–1866.

Hughes, T.J. (2003) *The finite element method: linear static and dynamic finite element analysis*. Courier Corporation.

Huiskes, R. and Chao, E.Y.S. (1983) A survey of finite element analysis in orthopedic biomechanics: The first decade, *Journal of Biomechanics*, **16**(6), pp. 385–409.

Huiskes, R. and Hollister, S.J. (1993) From Structure to Process, From Organ to Cell: Recent Developments of FE-Analysis in Orthopaedic Biomechanics, *Journal of Biomechanical Engineering*, **115**(4B), pp. 520–527.

Imseeh, W.H. and Alshibli, K.A. (2018) 3D finite element modelling of force transmission and particle fracture of sand, *Computers and Geotechnics*, **94**, pp. 184–195.

Ishizaka, K., Lewis, S.R. and Lewis, R. (2017) The low adhesion problem due to leaf contamination in the wheel/rail contact: Bonding and low adhesion mechanisms, *Wear*, **378–379**, pp. 183–197.

Jianhong, Y., Wu, F.Q. and Sun, J.Z. (2009) Estimation of the tensile elastic modulus

using Brazilian disc by applying diametrically opposed concentrated loads, *International Journal of Rock Mechanics and Mining Sciences*, **46**(3), pp. 568–576.

Jin, Z.-H., Peng, M.-D. and Li, Q. (2020) The effect of implant neck microthread design on stress distribution of peri-implant bone with different level: A finite element analysis, *Journal of Dental Sciences*, **15**(4), pp. 466–471.

Kaur, D. and Kaur, Y. (2014) Various image segmentation techniques: a review, *International Journal of Computer Science and Mobile Computing*, **3**(5), pp. 809–814.

Khormani, M., Kalat Jaari, V.R., Aghayan, I., Ghaderi, S.H. and Ahmadyfard, A. (2020) Compressive strength determination of concrete specimens using X-ray computed tomography and finite element method, *Construction and Building Materials*, **256**, p. 119427.

Kim, Y. and Yun, G.J. (2018) Effects of microstructure morphology on stress in mechanoluminescent particles: Micro CT image-based 3D finite element analyses, *Composites Part A: Applied Science and Manufacturing*, **114**, pp. 338–351.

Knowles, N.K., Ip, K. and Ferreira, L.M. (2019) The Effect of Material Heterogeneity, Element Type, and Down-Sampling on Trabecular Stiffness in Micro Finite Element Models, *Annals of Biomedical Engineering*, **47**(2), pp. 615–623.

Kuruvilla, J., Sukumaran, D., Sankar, A. and Joy, S.P. (2016) A review on image processing and image segmentation, in *2016 international conference on data mining and advanced computing (SAPIENCE)*. IEEE, pp. 198–203.

Lacroix, D., Chateau, A., Ginebra, M.-P. and Planell, J.A. (2006) Micro-finite element models of bone tissue-engineering scaffolds, *Biomaterials*, **27**(30), pp. 5326–5334.

Lall, P. and Wei, J. (2016) PBGA package Finite Element Analysis based on the physical geometry modeling using X-ray micro CT digital volume reconstruction, in *2016 15th IEEE Intersociety Conference on Thermal and Thermomechanical Phenomena in Electronic Systems (ITherm)*. *2016 15th IEEE Intersociety Conference on Thermal and Thermomechanical Phenomena in Electronic Systems (ITherm)*, pp. 285–294.

Lee, D.-M. (1992) The angle friction of granular fills, *Ph. D. dissertation, University of Cambridge* [Preprint].

Lee, H.K., Bayome, M., Ahn, C.S., Kim, S.-H., Kim, K.B., Mo, S.-S. and Kook, Y.-A. (2014) Stress distribution and displacement by different bone-borne palatal expanders

with micro-implants: a three-dimensional finite-element analysis, *European Journal of Orthodontics*, **36**(5), pp. 531–540.

Lei, H., Li, C., Meng, J., Zhou, H., Liu, Y., Zhang, X., Wang, P. and Fang, D. (2019) Evaluation of compressive properties of SLM-fabricated multi-layer lattice structures by experimental test and μ-CT-based finite element analysis, *Materials & Design*, **169**, p. 107685.

Lewis, S., Riley, S., Fletcher, D. and Lewis, R. (2018) Optimisation of a railway sanding system for optimal grain entrainment into the wheel–rail contact, *Proceedings of the Institution of Mechanical Engineers, Part F: Journal of Rail and Rapid Transit*, **232**(1), pp. 43–62.

Limbert, G., van Lierde, C., Muraru, O.L., Walboomers, X.F., Frank, M., Hansson, S., Middleton, J. and Jaecques, S. (2010) Trabecular bone strains around a dental implant and associated micromotions—A micro-CT-based three-dimensional finite element study, *Journal of Biomechanics*, **43**(7), pp. 1251–1261.

Lin, C., Natesaiyer, K. and Miller, J.D. (2014) High resolution X-ray microtomography based micro finite element analysis of mechanical properties of cellular material, *International society for industrial process tomography* [Preprint].

Lin, C.-L., Wang, J.-C., Chang, S.-H. and Chen, S.-T. (2010) Evaluation of Stress Induced by Implant Type, Number of Splinted Teeth, and Variations in Periodontal Support in Tooth-Implant–Supported Fixed Partial Dentures: A Non-Linear Finite Element Analysis, *Journal of Periodontology*, **81**(1), pp. 121–130.

Lin, Y., Ma, J., Lai, Z., Huang, L. and Lei, M. (2023) A FDEM approach to study mechanical and fracturing responses of geo-materials with high inclusion contents using a novel reconstruction strategy, *Engineering Fracture Mechanics*, **282**, p. 109171.

Liu, G.-Y., Xu, W.-J., Sun, Q.-C. and Govender, N. (2020) Study on the particle breakage of ballast based on a GPU accelerated discrete element method, *Geoscience Frontiers*, **11**(2), pp. 461–471.

Liu, X., Li, S. and Yao, T. (2023) Laboratory investigation on the single particle crushing strength of carbonate gravel incorporating size and shape effects, *Géotechnique*, pp. 1–17.

Liu, Y.I., Dai, F., Xu, N., Zhao, T. and Feng, P. (2018) Experimental and numerical investigation on the tensile fatigue properties of rocks using the cyclic flattened

Brazilian disc method, *Soil Dynamics and Earthquake Engineering*, **105**, pp. 68–82.

Lundmark, J., Kassfeldt, E., Hardell, J. and Prakash, B. (2009) The influence of initial surface topography on tribological performance of the wheel/rail interface during rolling/sliding conditions, *Proceedings of the Institution of Mechanical Engineers, Part F: Journal of Rail and Rapid Transit*, **223**(2), pp. 181–187.

Ma, G., Zhou, W., Regueiro, R.A., Wang, Q. and Chang, X. (2017) Modeling the fragmentation of rock grains using computed tomography and combined FDEM, *Powder Technology*, **308**, pp. 388–397.

Macdonald, H.M., Nishiyama, K.K., Hanley, D.A. and Boyd, S.K. (2011) Changes in trabecular and cortical bone microarchitecture at peripheral sites associated with 18 months of teriparatide therapy in postmenopausal women with osteoporosis, *Osteoporosis International*, **22**(1), pp. 357–362.

MacGinnis, M., Chu, H., Youssef, G., Wu, K.W., Machado, A.W. and Moon, W. (2014) The effects of micro-implant assisted rapid palatal expansion (MARPE) on the nasomaxillary complex—a finite element method (FEM) analysis, *Progress in Orthodontics*, **15**(1), p. 52.

MacNeil, J.A. and Boyd, S.K. (2008) Bone strength at the distal radius can be estimated from high-resolution peripheral quantitative computed tomography and the finite element method, *Bone*, **42**(6), pp. 1203–1213.

Magel, E.E. and Kalousek, J. (2002) The application of contact mechanics to rail profile design and rail grinding, *Wear*, **253**(1), pp. 308–316.

Magne, P. (2007) Efficient 3D finite element analysis of dental restorative procedures using micro-CT data, *Dental Materials*, **23**(5), pp. 539–548.

Maire, E. (2012) X-Ray Tomography Applied to the Characterization of Highly Porous Materials, *Annual Review of Materials Research*, **42**(1), pp. 163–178.

Maire, E., Fazekas, A., Salvo, L., Dendievel, R., Youssef, S., Cloetens, P. and Letang, J.M. (2003) X-ray tomography applied to the characterization of cellular materials. Related finite element modeling problems, *Composites Science and Technology*, **63**(16), pp. 2431–2443.

Majcher, K.B., Kontulainen, S.A., Leswick, D.A., Dolovich, A.T. and Johnston, J.D. (2024) Magnetic resonance imaging based finite element modelling of the proximal femur: a short-term in vivo precision study, *Scientific Reports*, **14**(1), p. 7029.

Manning, P.L., Margetts, L., Johnson, M.R., Withers, P.J., Sellers, W.I., Falkingham, P.L., Mummery, P.M., Barrett, P.M. and Raymont, D.R. (2009) Biomechanics of Dromaeosaurid Dinosaur Claws: Application of X-Ray Microtomography, Nanoindentation, and Finite Element Analysis, *The Anatomical Record*, **292**(9), pp. 1397–1405.

Maramizonouz, S., Nadimi, S., Skipper, W. and Lewis, R. (2023) Characterisation of physical and mechanical properties of seven particulate materials proposed as traction enhancers, *Scientific Data*, **10**(1), p. 400.

Maramizonouz, S., Nadimi, S., Skipper, W. and Lewis, R. (2025) CFD–DEM modelling of particle entrainment in wheel–rail interface: a parametric study on particle characteristics, *Railway Engineering Science* [Preprint].

Maramizonouz, S., Nadimi, S., Skipper, W.A., Lewis, S.R. and Lewis, R. (2023) Numerical modelling of particle entrainment in the wheel–rail interface, *Computational Particle Mechanics*, **10**(6), pp. 2009–2019.

Marcián, P., Borák, L., Zikmund, T., Horáčková, L., Kaiser, J., Joukal, M. and Wolff, J. (2021) On the limits of finite element models created from (micro)CT datasets and used in studies of bone-implant-related biomechanical problems, *Journal of the Mechanical Behavior of Biomedical Materials*, **117**, p. 104393.

Marcián, P., Wolff, J., Horáčková, L., Kaiser, J., Zikmund, T. and Borák, L. (2018) Micro finite element analysis of dental implants under different loading conditions, *Computers in Biology and Medicine*, **96**, pp. 157–165.

McDowell, G.R. and Bolton, M.D. (1998) On the micromechanics of crushable aggregates, *Géotechnique*, **48**(5), pp. 667–679.

Meng, J.J., Cao, P., Zhang, K. and Tan, P. (2013) Brazil split test of flattened disk and rock tensile strength using particle flow code, *Journal of Central South University (Science and Technology)*, **44**(6), pp. 2449–2454.

Mert Eren, M., Celebi, A.T., İçer, E., Baykasoğlu, C., Mugan, A., Yücel, T. and Yıldız, E. (2023) Biomechanical Behavior Evaluation of Resin Cement with Different Elastic Modulus on Porcelain Laminate Veneer Restorations Using Micro-CT-Based Finite Element Analysis, *Materials*, **16**(6), p. 2378.

Mesaritis, M., Santa, J.F., Molina, L.F., Palacio, M., Toro, A. and Lewis, R. (2023) Post-field grinding evaluation of different rail grades in full-scale wheel/rail laboratory tests,

Tribology International, **177**, p. 107980.

Mesaritis, M., Shamsa, M., Cuervo, P., Santa, J.F., Toro, A., Marshall, M.B. and Lewis, R. (2020) A laboratory demonstration of rail grinding and analysis of running roughness and wear, *Wear*, **456–457**, p. 203379.

Meyer, K.A., Skrypnyk, R. and Pletz, M. (2021) Efficient 3d finite element modeling of cyclic elasto-plastic rolling contact, *Tribology International*, **161**, p. 107053.

Moon, W., Wu, K.W., MacGinnis, M., Sung, J., Chu, H., Youssef, G. and Machado, A. (2015) The efficacy of maxillary protraction protocols with the micro-implant-assisted rapid palatal expander (MARPE) and the novel N2 mini-implant—a finite element study, *Progress in Orthodontics*, **16**(1), p. 16.

Müller, R. and Rüegsegger, P. (1995) Three-dimensional finite element modelling of non-invasively assessed trabecular bone structures, *Medical Engineering & Physics*, **17**(2), pp. 126–133.

Nadimi, Sadegh and Fonseca, J. (2017) On the tensile strength of soil grains in Hertzian response, in *EPJ Web of conferences*. EDP Sciences, p. 07001.

Nadimi, S. and Fonseca, J. (2017) Single-Grain Virtualization for Contact Behavior Analysis on Sand, *Journal of Geotechnical and Geoenvironmental Engineering*, **143**(9), p. 06017010.

Nadimi, S. and Fonseca, J. (2018a) A micro finite-element model for soil behaviour, *Géotechnique*, **68**(4), pp. 290–302.

Nadimi, S. and Fonseca, J. (2018b) A micro finite-element model for soil behaviour: numerical validation, *Géotechnique*, **68**(4), pp. 364–369.

Nadimi, S. and Fonseca, J. (2019) Image based simulation of one-dimensional compression tests on carbonate sand, *Meccanica*, **54**(4), pp. 697–706.

Nadimi, S., Fonseca, J., Andò, E. and Viggiani, G. (2020) A micro finite-element model for soil behaviour: experimental evaluation for sand under triaxial compression, *Géotechnique*, **70**(10), pp. 931–936.

Nadimi, S., Fonseca, J. and Taylor, N. (2015) A microstructure-based finite element analysis of the response of sand, in *Deformation Characteristics of Geomaterials*. IOS Press, pp. 816–823.

Nadimi, S., Shire, T. and Fonseca, J. (2017) Comparison between a μFE model and DEM for an assembly of spheres under triaxial compression, in *EPJ Web of*

Conferences. EDP Sciences, p. 15002.

Nadimi Shahraki, S. (2017) *Stress Transmission in a Granular System*. PhD Thesis. City, University of London.

Nakata, A.F.L., Hyde, M., Hyodo, H. and Murata (1999) A probabilistic approach to sand particle crushing in the triaxial test, *Géotechnique*, **49**(5), pp. 567–583.

Nakata, Y., Hyodo, M., Hyde, A.F.L., Kato, Y. and Murata, H. (2001) Microscopic Particle Crushing of Sand Subjected to High Pressure One-Dimensional Compression, *Soils and Foundations*, **41**(1), pp. 69–82.

Nakata, Y., Kato, Y., Hyodo, M., Hyde, A.F. and Murata, H. (2001) One-dimensional compression behaviour of uniformly graded sand related to single particle crushing strength, *Soils and foundations*, **41**(2), pp. 39–51.

Newitt, D.C., Majumdar, S., van Rietbergen, B., von Ingersleben, G., Harris, S.T., Genant, H.K., Chesnut, C., Garnero, P. and MacDonald, B. (2002) In Vivo Assessment of Architecture and Micro-Finite Element Analysis Derived Indices of Mechanical Properties of Trabecular Bone in the Radius, *Osteoporosis International*, **13**(1), pp. 6–17.

Ni, Y., Wang, Z., Bai, H., Zeng, Q., Liao, H. and Wu, W. (2023) Investigations of the failure mode for additive manufactured interlocked interface structure based on X-Ray CT image guided finite element analysis and experimental comparisons, *Engineering Fracture Mechanics*, **284**, p. 109220.

Nie, X., Liu, H., Huang, X., Tan, J., Xie, X., Yao, W., Rao, Z. and Duan, M. (2011) Finite element model of human ear reconstruction through micro-computer tomography, *Acta Oto-Laryngologica*, **131**(3), pp. 269–276.

Ortún-Terrazas, J., Cegoñino, J., Santana-Penín, U., Santana-Mora, U. and Pérez del Palomar, A. (2018) Approach towards the porous fibrous structure of the periodontal ligament using micro-computerized tomography and finite element analysis, *Journal of the Mechanical Behavior of Biomedical Materials*, **79**, pp. 135–149.

Otsu, N. (1975) A threshold selection method from gray-level histograms, *Automatica*, **11**(285–296), pp. 23–27.

Ovesy, M., Indermaur, M. and Zysset, P.K. (2019) Prediction of insertion torque and stiffness of a dental implant in bovine trabecular bone using explicit micro-finite element analysis, *Journal of the Mechanical Behavior of Biomedical Materials*, **98**, pp.

301–310.

Palombini, F.L., Kindlein, W., de Oliveira, B.F. and de Araujo Mariath, J.E. (2016) Bionics and design: 3D microstructural characterization and numerical analysis of bamboo based on X-ray microtomography, *Materials Characterization*, **120**, pp. 357–368.

Palombini, F.L., Lautert, E.L., Mariath, J.E. de A. and de Oliveira, B.F. (2020) Combining numerical models and discretizing methods in the analysis of bamboo parenchyma using finite element analysis based on X-ray microtomography, *Wood Science and Technology*, **54**(1), pp. 161–186.

Patel, R., Lu, M., Diermann, S.H., Wu, A., Pettit, A. and Huang, H. (2019) Deformation behavior of porous PHBV scaffold in compression: A finite element analysis study, *Journal of the Mechanical Behavior of Biomedical Materials*, **96**, pp. 1–8.

Pidaparti, R.M., Koombua, K. and Rao, A.S. (2009) Corrosion Pit Induced Stresses Prediction from SEM and Finite Element Analysis, *International Journal for Computational Methods in Engineering Science and Mechanics*, **10**(2), pp. 117–123.

Pistoia, W., van Rietbergen, B., Lochmüller, E.-M., Lill, C.A., Eckstein, F. and Rüegsegger, P. (2002) Estimation of distal radius failure load with micro-finite element analysis models based on three-dimensional peripheral quantitative computed tomography images, *Bone*, **30**(6), pp. 842–848.

Pletz, M., Daves, W., Yao, W., Kubin, W. and Scheriau, S. (2014) Multi-scale finite element modeling to describe rolling contact fatigue in a wheel–rail test rig, *Tribology International*, **80**, pp. 147–155.

Pletz, M., Meyer, K.A., Künstner, D., Scheriau, S. and Daves, W. (2019) Cyclic plastic deformation of rails in rolling/sliding contact–quasistatic FE calculations using different plasticity models, *Wear*, **436**, p. 202992.

Potrusil, T., Heshmat, A., Sajedi, S., Wenger, C., Johnson Chacko, L., Glueckert, R., Schrott-Fischer, A. and Rattay, F. (2020) Finite element analysis and three-dimensional reconstruction of tonotopically aligned human auditory fiber pathways: A computational environment for modeling electrical stimulation by a cochlear implant based on micro-CT, *Hearing Research*, **393**, p. 108001.

Qiu, Q. (2023) Thermal conductivity assessment of wood using micro computed tomography based finite element analysis (μCT-based FEA), *NDT & E International*,

139, p. 102921.

Rahmatian, M., Jafari, Z., Moghaddam, K.N., Dianat, O. and Kazemi, A. (2023) Finite Element Analysis of Fracture Resistance of Mandibular Molars with Different Access Cavity Designs, *Journal of Endodontics*, **49**(12), pp. 1690–1697.

Ramesh, K.K.D., Kumar, G.K., Swapna, K., Datta, D. and Rajest, S.S. (2021) A Review of Medical Image Segmentation Algorithms, *EAI Endorsed Transactions on Pervasive Health and Technology*, **7**(27), pp. e6–e6.

Rao, S.S. (2010) *The finite element method in engineering*. Elsevier.

Ren, L.-M., Arahira, T., Todo, M., Yoshikawa, H. and Myoui, A. (2012) Biomechanical evaluation of porous bioactive ceramics after implantation: micro CT-based three-dimensional finite element analysis, *Journal of Materials Science: Materials in Medicine*, **23**(2), pp. 463–472.

Revel, M., Bermond, F., Duboeuf, F., Mitton, D. and Follet, H. (2022) Influence of loading conditions in finite element analysis assessed by HR–pQCT on *ex vivo* fracture prediction, *Bone*, **154**, p. 116206.

Rieger, R., Auregan, J.C. and Hoc, T. (2018) Micro-finite-element method to assess elastic properties of trabecular bone at micro- and macroscopic level, *Morphologie*, **102**(336), pp. 12–20.

Rietbergen, B. van (1996) *Mechanical behavior and adaptation of trabecular bone in relation to bone morphology*.

van Rietbergen, B. (2001) Micro-FE Analyses of Bone: State of the Art, in S. Majumdar and B.K. Bay (eds) *Noninvasive Assessment of Trabecular Bone Architecture and the Competence of Bone*. Boston, MA: Springer US, pp. 21–30.

van Rietbergen, B. and Ito, K. (2015) A survey of micro-finite element analysis for clinical assessment of bone strength: The first decade, *Journal of Biomechanics*, **48**(5), pp. 832–841.

van Rietbergen, B., Weinans, H., Huiskes, R. and Odgaard, A. (1995) A new method to determine trabecular bone elastic properties and loading using micromechanical finite-element models, *Journal of Biomechanics*, **28**(1), pp. 69–81.

Rineau, L. and Yvinec, M. (2012) 3D surface mesh generation, *CGAL user and reference manual*, **4**(1).

Rizzoli, R., Chapurlat, R.D., Laroche, J.-M., Krieg, M.A., Thomas, T., Frieling, I.,

Boutroy, S., Laib, A., Bock, O. and Felsenberg, D. (2012) Effects of strontium ranelate and alendronate on bone microstructure in women with osteoporosis, *Osteoporosis International*, **23**(1), pp. 305–315.

da Rocha, R.J.B. (2016) *Evaluation of different damage initiation and growth criteria in the cohesive zone modelling analysis of single-lap bonded joints*. Master's Thesis. Instituto Politecnico do Porto (Portugal).

RSSB (2018) Standards Board. GMRT2461 sanding equipment (Issue 2).

Russell, A.R. and Muir Wood, D. (2009) Point load tests and strength measurements for brittle spheres, *International Journal of Rock Mechanics and Mining Sciences*, **46**(2), pp. 272–280.

Sandino, C., McErlain, D.D., Schipilow, J. and Boyd, S.K. (2017) Mechanical stimuli of trabecular bone in osteoporosis: A numerical simulation by finite element analysis of microarchitecture, *Journal of the Mechanical Behavior of Biomedical Materials*, **66**, pp. 19–27.

Sarfarazi, V., Haeri, H., Marji, M.F. and Zhu, Z. (2017) Fracture mechanism of Brazilian discs with multiple parallel notches using PFC2D, *Periodica Polytechnica Civil Engineering*, **61**(4), pp. 653–663.

Schipilow, J.D., Macdonald, H.M., Liphardt, A.M., Kan, M. and Boyd, S.K. (2013) Bone micro-architecture, estimated bone strength, and the muscle-bone interaction in elite athletes: An HR-pQCT study, *Bone*, **56**(2), pp. 281–289.

Seki, Y., Mackey, M. and Meyers, M.A. (2012) Structure and micro-computed tomography-based finite element modeling of Toucan beak, *Journal of the Mechanical Behavior of Biomedical Materials*, **9**, pp. 1–8.

Sencu, R.M., Yang, Z., Wang, Y.C., Withers, P.J., Rau, C., Parson, A. and Soutis, C. (2016) Generation of micro-scale finite element models from synchrotron X-ray CT images for multidirectional carbon fibre reinforced composites, *Composites Part A: Applied Science and Manufacturing*, **91**, pp. 85–95.

Shahrbaf, S., vanNoort, R., Mirzakouchaki, B., Ghassemieh, E. and Martin, N. (2013) Effect of the crown design and interface lute parameters on the stress-state of a machined crown–tooth system: A finite element analysis, *Dental Materials*, **29**(8), pp. e123–e131.

Shen, L. and Makedon, F. (2006) Spherical mapping for processing of 3D closed

surfaces, *Image and Vision Computing*, **24**(7), pp. 743–761.

Shewchuk, J.R. (2002) Constrained Delaunay Tetrahedralizations and Provably Good Boundary Recovery., *IMR*, **193**, p. 204.

Shi, L.B., Wang, C., Ding, H.H., Kvarda, D., Galas, R., Omasta, M., Wang, W.J., Liu, Q.Y. and Hartl, M. (2020) Laboratory investigation on the particle-size effects in railway sanding: Comparisons between standard sand and its micro fragments, *Tribology International*, **146**, p. 106259.

Silva, N.R. da, Aguiar, G.C.R., Rodrigues, M. de P., Bicalho, A.A., Soares, P.B.F., Veríssimo, C. and Soares, C.J. (2015) Effect of Resin Cement Porosity on Retention of Glass-Fiber Posts to Root Dentin: An Experimental and Finite Element Analysis, *Brazilian Dental Journal*, **26**, pp. 630–636.

Singh, R., Lee, P.D., Lindley, T.C., Kohlhauser, C., Hellmich, C., Bram, M., Imwinkelried, T. and Dashwood, R.J. (2010) Characterization of the deformation behavior of intermediate porosity interconnected Ti foams using micro-computed tomography and direct finite element modeling, *Acta Biomaterialia*, **6**(6), pp. 2342–2351.

Skipper, W., Chalisey, A. and Lewis, R. (2020) A review of railway sanding system research: Wheel/rail isolation, damage, and particle application, *Proceedings of the Institution of Mechanical Engineers, Part F: Journal of Rail and Rapid Transit*, **234**(6), pp. 567–583.

Skipper, W., Nadimi, S. and Lewis, R. (2021) Sand consist changes for improved track circuit performance (COF-UOS-03).

Skipper, W.A., Chalisey, A. and Lewis, R. (2018) A review of railway sanding system research: Adhesion restoration and leaf layer removal, *Tribology - Materials, Surfaces & Interfaces*, **12**(4), pp. 237–251.

Skipper, W.A., Nadimi, S., Chalisey, A. and Lewis, R. (2019) Particle characterisation of rail sands for understanding tribological behaviour, *Wear*, **432–433**, p. 202960.

Skipper, W.A., Nadimi, S., Watson, M., Chalisey, A. and Lewis, R. (2023) Quantifying the effect of particle characteristics on wheel/rail adhesion & damage through high pressure torsion testing, *Tribology International*, **179**, p. 108190.

Smoljan, M., Hussein, M.O., Guentsch, A. and Ibrahim, M. (2021) Influence of Progressive Versus Minimal Canal Preparations on the Fracture Resistance of

Mandibular Molars: A 3-Dimensional Finite Element Analysis, *Journal of Endodontics*, **47**(6), pp. 932–938.

Spiryagin, M., Bernal, E., Oldknow, K., Persson, I., Rahaman, M.L., Ahmad, S., Wu, Q., Cole, C. and Mcsweeney, T. (2023) Implementation of roughness and elastic-plastic behavior in a wheel-rail contact modeling for locomotive traction studies, *Wear*, **532**, p. 205115.

Stein, E.M., Silva, B.C., Boutroy, S., Zhou, B., Wang, J., Udesky, J., Zhang, C., McMahon, D.J., Romano, M., Dworakowski, E., Costa, A.G., Cusano, N., Irani, D., Cremers, S., Shane, E., Guo, X.E. and Bilezikian, J.P. (2013) Primary hyperparathyroidism is associated with abnormal cortical and trabecular microstructure and reduced bone stiffness in postmenopausal women, *Journal of Bone and Mineral Research*, **28**(5), pp. 1029–1040.

Stipsitz, M., Zysset, P.K. and Pahr, D.H. (2021) Prediction of the Inelastic Behaviour of Radius Segments: Damage-based Nonlinear Micro Finite Element Simulation vs Pistoia Criterion, *Journal of Biomechanics*, **116**, p. 110205.

Stirling, R.A., Simpson, D.J. and Davie, C.T. (2013) The application of digital image correlation to Brazilian testing of sandstone, *International Journal of Rock Mechanics and Mining Sciences*, **60**, pp. 1–11.

Su, K., Zhou, Y., Hossaini-Zadeh, M. and Du, J. (2021) Effects of implant buccal distance on peri-implant strain: A Micro-CT based finite element analysis, *Journal of the Mechanical Behavior of Biomedical Materials*, **116**, p. 104325.

Su, Y.-F., Zhang, B., Lee, S.J. and Sukumaran, B. (2017) Parametric Sensitivity Study of Particle Shape Effect Through 3D Printing, in X. Li, Y. Feng, and G. Mustoe (eds) *Proceedings of the 7th International Conference on Discrete Element Methods*. Singapore: Springer Singapore (Springer Proceedings in Physics), pp. 593–600.

Syed, A.U.Y., Rokaya, D., Shahrbaf, S. and Martin, N. (2021) Three-Dimensional Finite Element Analysis of Stress Distribution in a Tooth Restored with Full Coverage Machined Polymer Crown, *Applied Sciences*, **11**(3), p. 1220.

Synek, A. and Pahr, D.H. (2018) Plausibility and parameter sensitivity of micro-finite element-based joint load prediction at the proximal femur, *Biomechanics and Modeling in Mechanobiology*, **17**(3), pp. 843–852.

Tagliabue, S., Rossi, E., Baino, F., Vitale-Brovarone, C., Gastaldi, D. and Vena, P.

(2017) Micro-CT based finite element models for elastic properties of glass–ceramic scaffolds, *Journal of the Mechanical Behavior of Biomedical Materials*, **65**, pp. 248–255.

Tang, C.A., Liu, H.Y., Zhu, W.C., Yang, T.H., Li, W.H., Song, L. and Lin, P. (2004) Numerical approach to particle breakage under different loading conditions, *Powder Technology*, **143–144**, pp. 130–143.

Tang, C.Y., Tsui, C.P., Tang, Y.M., Wei, L., Wong, C.T., Lam, K.W., Ip, W.Y., Lu, W.W.J. and Pang, M.Y.C. (2014) Voxel-based approach to generate entire human metacarpal bone with microscopic architecture for finite element analysis, *Bio-Medical Materials and Engineering*, **24**(2), pp. 1469–1484.

Tao, G., Wen, Z., Jin, X. and Yang, X. (2020) Polygonisation of railway wheels: a critical review, *Railway Engineering Science*, **28**(4), pp. 317–345.

Thakur, M.M. and Penumadu, D. (2020) Triaxial compression in sands using FDEM and micro-X-ray computed tomography, *Computers and Geotechnics*, **124**, p. 103638.

The MathWorks Inc. (2020) MATLAB Version: 9.9.0.1495850 (R2020b) Update 1. Natick, Massachusetts: The MathWorks Inc.

Tomlinson, K., Fletcher, D. and Lewis, R. (2021) Measuring material plastic response to cyclic loading in modern rail steels from a minimal number of twin-disc tests, *Proceedings of the Institution of Mechanical Engineers, Part F: Journal of Rail and Rapid Transit*, **235**(10), pp. 1203–1213.

Trawiński, W., Bobiński, J. and Tejchman, J. (2016) Two-dimensional simulations of concrete fracture at aggregate level with cohesive elements based on X-ray μCT images, *Engineering Fracture Mechanics*, **168**, pp. 204–226.

Tsafnat, N., Amanat, N. and Jones, A.S. (2011) Analysis of coke under compressive loading: A combined approach using micro-computed tomography, finite element analysis, and empirical models of porous structures, *Fuel*, **90**(1), pp. 384–388.

Tsafnat, N., Tsafnat, G. and Jones, A.S. (2008) Micro-finite element modelling of coke blends using X-ray microtomography, *Fuel*, **87**(13), pp. 2983–2987.

Tsafnat, N., Tsafnat, G. and Jones, A.S. (2009) Automated mineralogy using finite element analysis and X-ray microtomography, *Minerals Engineering*, **22**(2), pp. 149–155.

Tvergaard, V. and Hutchinson, J.W. (1992) The relation between crack growth

resistance and fracture process parameters in elastic-plastic solids, *Journal of the Mechanics and Physics of Solids*, **40**(6), pp. 1377–1397.

Uhlmann, E., Lypovka, P., Hochschild, L. and Schröer, N. (2016) Influence of rail grinding process parameters on rail surface roughness and surface layer hardness, *Wear*, **366–367**, pp. 287–293.

Ulrich, D., Van Rietbergen, B., Weinans, H. and Rüegsegger, P. (1998) Finite element analysis of trabecular bone structure: a comparison of image-based meshing techniques, *Journal of Biomechanics*, **31**(12), pp. 1187–1192.

Van Rietbergen, B. and Ito, K. (2015) A survey of micro-finite element analysis for clinical assessment of bone strength: The first decade, *Journal of Biomechanics*, **48**(5), pp. 832–841.

Van Rietbergen, B., Majumdar, S., Pistoia, W., Newitt, D.C., Kothari, M., Laib, A. and Rüegsegger, P. (1998) Assessment of cancellous bone mechanical properties from micro-FE models based on micro-CT, pQCT and MR images, *Technology and Health Care*, **6**(5–6), pp. 413–420.

Van Rietbergen, B., Müller, R., Ulrich, D., Rüegsegger, P. and Huiskes, R. (1999) Tissue stresses and strain in trabeculae of a canine proximal femur can be quantified from computer reconstructions, *Journal of Biomechanics*, **32**(2), pp. 165–173.

Van Rietbergen, B., Odgaard, A., Kabel, J. and Huiskes, R. (1998) Relationships between bone morphology and bone elastic properties can be accurately quantified using high-resolution computer reconstructions, *Journal of Orthopaedic Research*, **16**(1), pp. 23–28.

Van Rietbergen, B., Weinans, H., Huiskes, R. and Polman, B.J.W. (1996) Computational Strategies for Iterative Solutions of Large Fem Applications Employing Voxel Data, *International Journal for Numerical Methods in Engineering*, **39**(16), pp. 2743–2767.

Vásárhelyi, L., Kónya, Z., Kukovecz, Á. and Vajtai, R. (2020) Microcomputed tomography–based characterization of advanced materials: a review, *Materials Today Advances*, **8**, p. 100084.

Vaz, C.M.P., Tuller, M., Lasso, P.R.O. and Crestana, S. (2014) New Perspectives for the Application of High-Resolution Benchtop X-Ray MicroCT for Quantifying Void, Solid and Liquid Phases in Soils, in W.G. Teixeira, M.B. Ceddia, M.V. Ottoni, and G.K.

Donnagema (eds) *Application of Soil Physics in Environmental Analyses: Measuring, Modelling and Data Integration*. Cham: Springer International Publishing, pp. 261–281.

Verhulp, E., van Rietbergen, B., Müller, R. and Huiskes, R. (2008) Indirect determination of trabecular bone effective tissue failure properties using micro-finite element simulations, *Journal of Biomechanics*, **41**(7), pp. 1479–1485.

Verhulp, E., Van Rietbergen, B. and Huiskes, R. (2006) Comparison of micro-level and continuum-level voxel models of the proximal femur, *Journal of Biomechanics*, **39**(16), pp. 2951–2957.

Veyhl, C., Belova, I.V., Murch, G.E. and Fiedler, T. (2011) Finite element analysis of the mechanical properties of cellular aluminium based on micro-computed tomography, *Materials Science and Engineering: A*, **528**(13), pp. 4550–4555.

Vilayphiou, N., Boutroy, S., Sornay-rendu, E., Van rietbergen, B., Munoz, F., Delmas, P.D. and Chapurlat, R. (2010) Finite element analysis performed on radius and tibia HR-pQCT images and fragility fractures at all sites in postmenopausal women, *Bone*, **46**(4), pp. 1030–1037.

Vilayphiou, N., Boutroy, S., Szulc, P., van Rietbergen, B., Munoz, F., Delmas, P.D. and Chapurlat, R. (2011) Finite element analysis performed on radius and tibia HR-pQCT images and fragility fractures at all sites in men, *Journal of Bone and Mineral Research*, **26**(5), pp. 965–973.

Vo, K.D., Tieu, A.K., Zhu, H.T. and Kosasih, P.B. (2014) A 3D dynamic model to investigate wheel–rail contact under high and low adhesion, *International Journal of Mechanical Sciences*, **85**, pp. 63–75.

Wan, B., Chung, B.H., Zhang, M.R., Kim, S.A., Swain, M., Peters, O.A., Krishnan, U. and Moule, A. (2022) The Effect of Varying Occlusal Loading Conditions on Stress Distribution in Roots of Sound and Instrumented Molar Teeth: A Finite Element Analysis, *Journal of Endodontics*, **48**(7), pp. 893–901.

Wang, H., Wang, C., You, Z., Yang, X. and Huang, Z. (2018) Characterising the asphalt concrete fracture performance from X-ray CT Imaging and finite element modelling, *International Journal of Pavement Engineering*, **19**(3), pp. 307–318.

Wang, P., Liang, H., Jiang, L. and Qian, L. (2023) Effect of nanoscale surface roughness on sliding friction and wear in mixed lubrication, *Wear*, **530–531**, p. 204995.

Wang, Q.Z., Jia, X.M., Kou, S.Q., Zhang, Z.X. and Lindqvist, P.-A. (2004) The flattened

Brazilian disc specimen used for testing elastic modulus, tensile strength and fracture toughness of brittle rocks: analytical and numerical results, *International Journal of Rock Mechanics and Mining Sciences*, **41**(2), pp. 245–253.

Wang, Q.Z. and Wu, L.Z. (2004) The flattened Brazilian disc specimen used for determining elastic modulus, tensile strength and fracture toughness of brittle rocks: experimental results, *International Journal of Rock Mechanics and Mining Sciences*, **41**, pp. 26–30.

Wang, Q.-Z. and Xing, L. (1999) Determination of fracture toughness KIC by using the flattened Brazilian disk specimen for rocks, *Engineering Fracture Mechanics*, **64**(2), pp. 193–201.

Wang, W. and Coop, M.R. (2016) An investigation of breakage behaviour of single sand particles using a high-speed microscope camera, *Géotechnique*, **66**(12), pp. 984–998.

Wang, W. and Coop, M.R. (2018) Breakage behaviour of sand particles in point-load compression, *Géotechnique Letters*, **8**(1), pp. 61–65.

Wang, W.J., Zhang, H.F., Wang, H.Y., Liu, Q.Y. and Zhu, M.H. (2011) Study on the adhesion behavior of wheel/rail under oil, water and sanding conditions, *Wear*, **271**(9), pp. 2693–2698.

Wang, X.F., Yang, Z.J., Yates, J.R., Jivkov, A.P. and Zhang, C. (2015) Monte Carlo simulations of mesoscale fracture modelling of concrete with random aggregates and pores, *Construction and Building Materials*, **75**, pp. 35–45.

Wang, Y., Xiao, H., Zhang, Z., Cui, X., Chi, Y. and Nadakatti, M.M. (2024) The formation, development and classification of rail corrugation: a survey on Chinese metro, *Railway Engineering Science* [Preprint].

Wei, D., Zhao, B., Dias-da-Costa, D. and Gan, Y. (2019) An FDEM study of particle breakage under rotational point loading, *Engineering Fracture Mechanics*, **212**, pp. 221–237.

Wei, D., Zhao, B. and Gan, Y. (2022) Surface reconstruction with spherical harmonics and its application for single particle crushing simulations, *Journal of Rock Mechanics and Geotechnical Engineering*, **14**(1), pp. 232–239.

Weibull, W. (1951) A Statistical Distribution Function of Wide Applicability, *Journal of Applied Mechanics*, **18**(3), pp. 293–297.

Wen, X.-X., Xu, C., Zong, C.-L., Feng, Y.-F., Ma, X.-Y., Wang, F.-Q., Yan, Y.-B. and Lei, W. (2016) Relationship between sample volumes and modulus of human vertebral trabecular bone in micro-finite element analysis, *Journal of the Mechanical Behavior of Biomedical Materials*, **60**, pp. 468–475.

Wen, X.-X., Yu, H.-L., Yan, Y.-B., Zong, C.-L., Ding, H.-J., Ma, X.-Y., Wang, T.-S. and Lei, W. (2017) Influence of the shape of the micro-finite element model on the mechanical properties calculated from micro-finite element analysis, *Experimental and Therapeutic Medicine*, **14**(2), pp. 1744–1748.

Willemink, M.J. and Noël, P.B. (2019) The evolution of image reconstruction for CT—from filtered back projection to artificial intelligence, *European Radiology*, **29**(5), pp. 2185–2195.

Williams, A.F.O. and McCullough, M.B.A. (2016) Micro-Computed Tomography to Finite Element Analysis of In Vivo Biodegradable Magnesium-Alloy Screw and Surrounding Bone in Rabbit Femurs, in. *ASME 2015 International Mechanical Engineering Congress and Exposition*, American Society of Mechanical Engineers Digital Collection.

Withers, P.J., Bouman, C., Carmignato, S., Cnudde, V., Grimaldi, D., Hagen, C.K., Maire, E., Manley, M., Du Plessis, A. and Stock, S.R. (2021) X-ray computed tomography, *Nature Reviews Methods Primers*, **1**(1), pp. 1–21.

Wu, Z., Cui, W., Fan, L. and Liu, Q. (2019) Mesomechanism of the dynamic tensile fracture and fragmentation behaviour of concrete with heterogeneous mesostructure, *Construction and Building Materials*, **217**, pp. 573–591.

Xiong, X. and Xiao, Q. (2019) Meso-scale simulation of concrete based on fracture and interaction behavior, *Applied Sciences*, **9**(15), p. 2986.

Yang, S.-Q., Yin, P.-F. and Huang, Y.-H. (2019) Experiment and discrete element modelling on strength, deformation and failure behaviour of shale under Brazilian compression, *Rock Mechanics and Rock Engineering*, **52**, pp. 4339–4359.

Youssef, S., Maire, E. and Gaertner, R. (2005) Finite element modelling of the actual structure of cellular materials determined by X-ray tomography, *Acta Materialia*, **53**(3), pp. 719–730.

Yu, Y., Zhang, Jianxun and Zhang, Jichun (2009) A modified Brazilian disk tension test, *International Journal of Rock Mechanics and Mining Sciences*, **46**(2), pp. 421–425.

Zare-Rami, K. and Kim, Y.-R. (2019) MIDAS-VT-Pre: Software to generate 2D finite element model of particle/fiber embedded composites with cohesive zones, *SoftwareX*, **10**, p. 100292.

Zhang, B., Nadimi, S., Eissa, A. and Rouainia, M. (2023) Modelling fracturing process using cohesive interface elements: theoretical verification and experimental validation, *Construction and Building Materials*, **365**, p. 130132.

Zhang, B., Nadimi, S. and Lewis, R. (2024) Modelling the adhesion enhancement induced by sand particle breakage at the wheel-rail interface, *Wear*, **538**, p. 205232.

Zhang, C., Maramizonouz, S., Milledge, D. and Nadimi, S. (2024) An electro-mechanical contact model for particulate systems, *Powder Technology*, **440**, p. 119759.

Zhang, C., Nadimi, S., Maramizonouz, S., Milledge, D. and Lewis, R. (2024) A Discrete Element Model of High-Pressure Torsion Test to Assess the Effect of Particle Characteristics in the Interface, *Journal of Tribology*, **146**(081501).

Zhang, N., Magland, J.F., Rajapakse, C.S., Bhagat, Y.A. and Wehrli, F.W. (2013) Potential of in vivo MRI-based nonlinear finite-element analysis for the assessment of trabecular bone post-yield properties, *Medical Physics*, **40**(5), p. 052303.

Zhang, X., Baudet, B.A. and Yao, T. (2020) The influence of particle shape and mineralogy on the particle strength, breakage and compressibility, *International Journal of Geo-Engineering*, **11**(1), p. 1.

Zhang, X., Tiainen, H. and Haugen, H.J. (2019) Comparison of titanium dioxide scaffold with commercial bone graft materials through micro-finite element modelling in flow perfusion, *Medical & Biological Engineering & Computing*, **57**(1), pp. 311–324.

Zhang, X., Yang, Z., Pang, M., Yao, Y., Li, Q.M. and Marrow, T.J. (2021) Ex-situ micro X-ray computed tomography tests and image-based simulation of UHPFRC beams under bending, *Cement and Concrete Composites*, **123**, p. 104216.

Zhang, X., Yang, Z.-J., Huang, Y.-J., Wang, Z.-Y. and Chen, X.-W. (2021) Micro CT Image-based Simulations of Concrete under High Strain Rate Impact using a Continuum-Discrete Coupled Model, *International Journal of Impact Engineering*, **149**, p. 103775.

Zhao, B. and Wang, J. (2016) 3D quantitative shape analysis on form, roundness, and compactness with μCT, *Powder Technology*, **291**, pp. 262–275.

Zhao, B., Wang, J., Coop, M.R., Viggiani, G. and Jiang, M. (2015) An investigation of

single sand particle fracture using X-ray micro-tomography, *Géotechnique*, **65**(8), pp. 625–641.

Zhao, X. and Li, Z. (2011) The solution of frictional wheel–rail rolling contact with a 3D transient finite element model: Validation and error analysis, *Wear*, **271**(1–2), pp. 444–452.

Zhao, X. and Li, Z. (2015) A three-dimensional finite element solution of frictional wheel–rail rolling contact in elasto-plasticity, *Proceedings of the Institution of Mechanical Engineers, Part J: Journal of Engineering Tribology*, **229**(1), pp. 86–100.

Zheng, Q.J., Zhu, H.P. and Yu, A.B. (2012) Finite element analysis of the contact forces between a viscoelastic sphere and rigid plane, *Powder Technology*, **226**, pp. 130–142.

Zhou, B., Wang, J. and Zhao, B. (2015) Micromorphology characterization and reconstruction of sand particles using micro X-ray tomography and spherical harmonics, *Engineering Geology*, **184**, pp. 126–137.

Zhou, B., Wei, D., Ku, Q., Wang, J. and Zhang, A. (2020) Study on the effect of particle morphology on single particle breakage using a combined finite-discrete element method, *Computers and Geotechnics*, **122**, p. 103532.

Zhu, F. and Zhao, J. (2019) A peridynamic investigation on crushing of sand particles, *Géotechnique*, **69**(6), pp. 526–540.

Zhu, Y., Olofsson, U. and Persson, K. (2012) Investigation of factors influencing wheel–rail adhesion using a mini-traction machine, *Wear*, **292–293**, pp. 218–231.

Zupancic Cepic, L., Frank, M., Reisinger, A., Pahr, D., Zechner, W. and Schedle, A. (2022) Biomechanical finite element analysis of short-implant-supported, 3-unit, fixed CAD/CAM prostheses in the posterior mandible, *International Journal of Implant Dentistry*, **8**(1), p. 8.

Appendix A

This appendix provides key scripts detailing the functions and classes of the in-house code for embedding 3D CIEs, as utilised in Chapter 4.

```
%%
clc;
clear;

%% Select the input file
[FileName, FilePath] = uigetfile('*.inp', 'Select the mesh data');
FilePathFileName = append(FilePath, FileName);

% The main while, read the file line by line.
FileID = fopen( FilePathFileName , 'r');
MeshDataInput = textscan(FileID, '%s', 'delimiter', '\n');
MeshDataInput = MeshDataInput{1,1}; % Get correct size of this matrix.

% Remove empty lines
MeshDataInput=MeshDataInput(~cellfun('isempty',MeshDataInput));

% Reading
LineIndex = {};
LineIndexCounter = 1;
for LL = 1 : size(MeshDataInput,1) % size(,1) return rows
    if ~isempty( strfind( MeshDataInput{LL,1},'*' ) )  % find *, if true(1), then...
        LineIndex(LineIndexCounter,1:2)  =  {LL,  MeshDataInput{LL,1}};  % assign lineIndex(1,1) and (1,2)
        LineIndexCounter = LineIndexCounter + 1;
    end
end
LineIndex(LineIndexCounter,1:2) = {size(MeshDataInput,1)+1, []};

%
% ========================================================================
% find mesh information

Coo_O = [];
Con_O = [];
El_Phase1 = [];
El_Phase2 = [];
El_CZ = [];

for II = 1 : size(LineIndex,1)

    % find Node information
    if ~isempty( strfind( LineIndex{II,2},'*Node' ) )
        for LL = LineIndex{II,1}+1 : LineIndex{II+1,1}-1
            OneNodeCoo_O     =     textscan(MeshDataInput{LL,1},     '%f', 'delimiter', ',');
            Coo_O = vertcat(Coo_O, OneNodeCoo_O{1,1}');  % transpose
        end
    end

    % find Element information
    if ~isempty( strfind( LineIndex{II,2},'*Element' ) )
        for LL = LineIndex{II,1}+1 : LineIndex{II+1,1}-1
            OneElCon_O  =  textscan(MeshDataInput{LL,1},  '%f','delimiter', ',');
            Con_O = vertcat(Con_O, OneElCon_O{1,1}');
        end
    end
```

```
    % find Phase1 information
    if ~isempty( strfind( LineIndex{II,2},'Phase1' ) )
        for LL = LineIndex{II,1}+1 : LineIndex{II+1,1}-1
            OneLineEl_Phase1        =       textscan(MeshDataInput{LL,1},
'%f','delimiter', ',');
            El_Phase1 = vertcat(El_Phase1, OneLineEl_Phase1{1,1});
        end
    end

    if ~isempty( strfind( LineIndex{II,2},'CZ' ) )
        for LL = LineIndex{II,1}+1 : LineIndex{II+1,1}-1
            OneLineEl_CZ = textscan(MeshDataInput{LL,1}, '%f','delimiter',
',');
            El_CZ = vertcat(El_CZ, OneLineEl_CZ{1,1});
        end
    end
end

%
================================================================================

NumRegEl = size(Con_O,1);               % count the rows of Con_O
Con_O = [Con_O zeros(NumRegEl,2)];      % add two columns of 0 to Con_O

El_Phase1(find(isnan(El_Phase1)))=0;
El_Phase1 = setdiff(El_Phase1,0);

El_Phase2(find(isnan(El_Phase2)))=0;
El_Phase2 = setdiff(El_Phase2,0);

El_CZ(find(isnan(El_CZ)))=0;
El_CZ = setdiff(El_CZ,0);


%%

Con=Con_O(:,:);
Coo=Coo_O(:,:);

Coor = [];
Conn = [];
%
================================================================================
% Finding Neighbering Elements
T = Con(:,2:5);
P = Coo(:,2:4);

TR = triangulation(T,P);

N = neighbors(TR);
% i row is the current element, column j is the element that element i
sharing face with.
% By convention, N(i,j) is the neighbor opposite the jth vertex of ti(i).
% If a triangle or tetrahedron has one or more boundary facets,
% the nonexistent neighbors are represented as NaN values in TN.
%       2D                                      3D
%  V1    V2    V3                        V1     V2     V3     V4
% Edge2 Edge3 Edge1                    Face1  Face2  Face3  Face4
% ------------------------------------------------------------------------
```

```
--
% Make the NeiberEl
%    2D                                          3D
% 1      2                                 1      2      3
% El1  El2                                E11    E12    E13

NeiberEl = [];
for EE = 1:size(N,1)
    for VV = 1:size(N,2)
        if ~isnan(N(EE,VV))   && ... % find the shared faces
            EE < N(EE,VV)     && ... % aviod count shared face two times
            (ismember(EE,El_CZ) || ismember(N(EE,VV),El_CZ))

            NeiberEl = [NeiberEl;
                        EE, N(EE,VV)];

        end
    end
end
%
=========================================================================
% Duplicating Nodes

% Find "inner" CZ Nodes (not nodes shared with elements outside CZ)
Node_CZ=[1:size(Coo,1)]';
for EE = 1:NumRegEl
    if ~ismember(EE,El_CZ)     % ~ if EE belongs to El_CZ, yes=1, no=0
        Node_CZ = setdiff(Node_CZ,Con(EE,2:5));
    end
end

% Total Number of required nodes
TotNumReqNode = numel(El_CZ)*4;   % return the number of elements in El_CZ
*4
% -------------------------------------------------------------------------
--
% Making Conn which is connectivity matrix after duplicating new nodes
NewNodeStrorage = [Node_CZ; ...
                   [size(Coo,1)+1      :      size(Coo,1)+(TotNumReqNode-
size(Node_CZ,1))]'];

Conn = Con;
Bin=1;
for AA = 1:numel(El_CZ)
    EE = El_CZ(AA);
    Conn(EE,2:5) = NewNodeStrorage(Bin:Bin+3);
    Bin = Bin+4;
end
% -------------------------------------------------------------------------
--
% Making Coor which inculdes duplicated new nodes
Coor = Coo;
for AA = 1:numel(El_CZ)
    EE = El_CZ(AA);
    for NN = 2:5
        Coor(Conn(EE,NN),1:4)= [Conn(EE,NN)  Coo(Con(EE,NN),2:4)];


    end
```

```
end
%
%=========================================================================

CohEl_Phase1       =[];
CohEl_Phase2       =[];
CohEl_InterPhase12 =[];

CohElCounter = NumRegEl;

% tic
for CE = 1:size(NeiberEl,1)

    % disp(CE/size(NeiberEl,1));

    EE = NeiberEl(CE,1);
    EEE = NeiberEl(CE,2);

    [ El_Cen_A, El_Edge_A, El_EdgeCen_A ] = El_Specs( EE, Coor, Conn );
    [ El_Cen_B, El_Edge_B, El_EdgeCen_B ] = El_Specs( EEE, Coor, Conn );

    [CC,iA,iB] = intersect(El_EdgeCen_A, El_EdgeCen_B, 'rows');

    % find the index of these three nodes of element A and B

    Bin_A = El_Edge_A(iA(1),1);
    Bin_B = El_Edge_B(iB(1),1);

    for i=1:size(iA,1)

        for j=1:size(El_Edge_A,2)

            if ~ismember(El_Edge_A(iA(i),j), Bin_A)

               Bin_A = [Bin_A; El_Edge_A(iA(i),j)];     % find three nodes
of element A

            end
        end
    end

    for i=1:size(iB,1)

        for j=1:size(El_Edge_B,2)

            if ~ismember(El_Edge_B(iB(i),j), Bin_B)

               Bin_B = [Bin_B; El_Edge_B(iB(i),j)];     % find three nodes
of element B

            end
        end
    end


%=========================================================================

    % Defining Coh Elements
```

```
A1 = Bin_A(1);          % EdgeA(NodeA) EdgeB(NodeB)  (3D)

A2 = Bin_A(2);                %   A_1     0-----0    B_1
                              %           /|     /|
A3 = Bin_A(3);                %          / |    / |
                              %         /  |   /  |
                              % A_2   0-----0    |    B_2
n=1;                          %         \  |   \  |
                              %          \ |    \ |
                              %           \|     \|
                              %   A_3     0-----0    B_3
while n<=3
    m=1;
    while m<=3
        if Coor(Bin_B(m),2:4) == Coor(Bin_A(n),2:4)
           B(n) = Bin_B(m);
        end
        m=m+1;
    end
    n=n+1;
end

B1 = B(1);
B2 = B(2);
B3 = B(3);

%============================================================
% Correct Numbering
% A1 A2 A3 B1 B2 B3

A1_A2 = Coor(A2,2:4) - Coor(A1,2:4);
A1_A3 = Coor(A3,2:4) - Coor(A1,2:4);
Bin_normal = cross(A1_A2, A1_A3);

CACB = El_Cen_B - El_Cen_A;
Bin_dot = dot(Bin_normal, CACB);

if Bin_dot>0
   NewCohEl=[A1 A2 A3 B1 B2 B3];
end
if Bin_dot<0
   NewCohEl=[A1 A3 A2 B1 B3 B2];
end

CohElCounter = CohElCounter + 1;
Conn(CohElCounter, 1:7) = [CohElCounter,  NewCohEl];

if     ismember(EE,El_Phase1) && ismember(EEE,El_Phase1)
    CohEl_Phase1= [CohEl_Phase1;    CohElCounter];

elseif ismember(EE,El_Phase2) && ismember(EEE,El_Phase2)
    CohEl_Phase2= [CohEl_Phase2;    CohElCounter];

elseif (ismember(EE,El_Phase1) && ismember(EEE,El_Phase2)) ||...
       (ismember(EE,El_Phase2) && ismember(EEE,El_Phase1))
    CohEl_InterPhase12= [CohEl_InterPhase12;    CohElCounter];
end
```

```
end

% Write output file
MeshData2AbaqusInp(Coor,   Conn,   FileName,   El_Phase1,   CohEl_Phase1,
NumRegEl)

disp('Done!')
```

Appendix B

This appendix includes key scripts showcasing the functions and classes of the in-house code used for fragment analysis in Chapter 4.

```
clc;
clear;

%% Get COH3D6 Node's Information

% Select the input file
[FileName, FilePath] = uigetfile('*.*', 'Select the INP including CIEs
file');
FilePathFileName = append(FilePath, FileName);

% Open the file for reading
fileID = fopen( FilePathFileName , 'r');

% Define the search pattern
search_pattern_1 = '*Element, type=C3D4';
search_pattern_2 = '*Element, type=COH3D6';

% Initialize variables
matching_lines_1 = {};
matching_lines_2 = {};
i=0;
l=0;
C3D4_total = [];
COH3D6_total = [];
A_values = [];
B_values = [];
C_values = [];

% Read the file line by line

while ~feof(fileID)
    % Read the current line
    current_line = fgetl(fileID);

    % Check if the line contains the search pattern
    if contains(current_line, search_pattern_1)
        matching_lines_1{end+1} = current_line;

        % Read the next line to get values for A, B, and C
        next_line = fgetl(fileID);

        % Continue reading lines until a line containing '*' is
encountered
        while ~contains(next_line, '*')
            % Split values using commas
            values_str = strsplit(next_line, ',');

            % Convert string values to numerical values
            i=i+1;
            C3D4_total(i,1) = str2double(values_str{1});
            C3D4_total(i,2) = str2double(values_str{2});
            C3D4_total(i,3) = str2double(values_str{3});
            C3D4_total(i,4) = str2double(values_str{4});
            C3D4_total(i,5) = str2double(values_str{5});

            % Read the next line
            next_line = fgetl(fileID);
        end
    end
```

```
end

frewind(fileID);  % move to the beginning of the file

while ~feof(fileID)
    % Read the current line
    current_line = fgetl(fileID);

    % Check if the line contains the search pattern
    if contains(current_line, search_pattern_2)
        matching_lines_2{end+1} = current_line;

        % Read the next line to get values for A, B, and C
        next_line = fgetl(fileID);

        % Continue reading lines until a line containing '*' is
encountered
        while ~contains(next_line, '*')
            % Split values using commas
            values_str = strsplit(next_line, ',');

            % Convert string values to numerical values
            l=l+1;
            COH3D6_total(l,:) = str2double(values_str);

            A_values(l,1) = str2double(values_str{2});
            A_values(l,2) = str2double(values_str{5});

            B_values(l,1) = str2double(values_str{3});
            B_values(l,2) = str2double(values_str{6});

            C_values(l,1) = str2double(values_str{4});
            C_values(l,2) = str2double(values_str{7});

            % Read the next line
            next_line = fgetl(fileID);
        end
    end
end


% Close the file
fclose(fileID);

%% Get COH3D6 Coordinate's Information

% Select the input file
[FileName, FilePath] = uigetfile('*.*', 'Select the data at certain
strain');
FilePathFileName = append(FilePath, FileName);

% Open the file for reading
fileID = fopen( FilePathFileName , 'r');

% Read the entire file as a cell array of strings
lines = textscan(fileID, '%s', 'Delimiter', '\n');
lines = lines{1};  % Extract the cell array from the result

% Close the file
```

```
fclose(fileID);

% Separate lines into elements based on spaces
all_elements = cellfun(@(line) strsplit(line, ' '), lines,
'UniformOutput', false);

% Count the number of rows
num_rows = numel(all_elements);

% Initialize a matrix with zeros
Node_coordinates_new = zeros(num_rows, 4);

% Assign columns 2, 6, 7, and 8 to the new matrix
for j = 1:num_rows
    % Convert the strings to numbers using str2double
    Node_coordinates_new(j, 1) = str2double(all_elements{j}{2});      %
node
    Node_coordinates_new(j, 2) = str2double(all_elements{j}{6});      % x
    Node_coordinates_new(j, 3) = str2double(all_elements{j}{7});      % y
    Node_coordinates_new(j, 4) = str2double(all_elements{j}{8});      % z
end

% Count the number of rows for A, B and C
[numRows, numCols] = size(A_values);

D = 0;
uD = 0;
COH3D6_Damage = [];

% Check the nodes in A_values;
for k = 1:numRows

    % Calculate the distance between A(k,1) and A(k,2)
    Distance = sqrt((Node_coordinates_new(A_values(k,2), 2) -
Node_coordinates_new(A_values(k,1), 2))^2 + ...
         (Node_coordinates_new(A_values(k,2), 3) -
Node_coordinates_new(A_values(k,1), 3))^2 + ...
         (Node_coordinates_new(A_values(k,2), 4) -
Node_coordinates_new(A_values(k,1), 4))^2);

     % Check the distance > ?, breakage occurs <-------------------

     % 0.001 when can see breakage,
     % 0.0004 when ST=1000 and can't see full breakage GB: P11 0D1
     % 0.0002 when ST=1000 and can't see full breakage GB: P37 0D1

    if Distance > 0.001;
        D = D+1;
        COH3D6_Damage = [COH3D6_Damage; COH3D6_total(k,:)];
    else
        uD = uD+1;
    end
end

% Check the nodes in B_values;
for k = 1:numRows

    % Calculate the distance between A(k,1) and A(k,2)
```

```
    Distance = sqrt((Node_coordinates_new(B_values(k,2), 2) -
Node_coordinates_new(B_values(k,1), 2))^2 + ...
         (Node_coordinates_new(B_values(k,2), 3) -
Node_coordinates_new(B_values(k,1), 3))^2 + ...
         (Node_coordinates_new(B_values(k,2), 4) -
Node_coordinates_new(B_values(k,1), 4))^2);

     % Check the distance > 0.005, breakage occurs
    if Distance > 0.005;
        D = D+1;

        % Check if the first row of A belongs to B
        if ~ismember(COH3D6_total(k,:), COH3D6_Damage, 'rows')

            % If not, append the COH3D6(k,:) to COH3D6_D
            COH3D6_Damage = [COH3D6_Damage; COH3D6_total(k,:)];

        end

    else
        uD = uD+1;
    end
end

% Check the nodes in C_values;
for k = 1:numRows

    % Calculate the distance between A(k,1) and A(k,2)
    Distance = sqrt((Node_coordinates_new(C_values(k,2), 2) -
Node_coordinates_new(C_values(k,1), 2))^2 + ...
         (Node_coordinates_new(C_values(k,2), 3) -
Node_coordinates_new(C_values(k,1), 3))^2 + ...
         (Node_coordinates_new(C_values(k,2), 4) -
Node_coordinates_new(C_values(k,1), 4))^2);

     % Check the distance > 0.005, breakage occurs
    if Distance > 0.005;
        D = D+1;

        % Check if the first row of A belongs to B
        if ~ismember(COH3D6_total(k,:), COH3D6_Damage, 'rows')

            % If not, append the COH3D6(k,:) to COH3D6_D
            COH3D6_Damage = [COH3D6_Damage; COH3D6_total(k,:)];

        end

    else
        uD = uD+1;
    end
end

% Identify rows in COH3D6_Damage that are present in COH3D6_total
rows_to_remove = ismember(COH3D6_total, COH3D6_Damage, 'rows');

% Remove rows from COH3D6_total
COH3D6_connected = COH3D6_total(~rows_to_remove, :);

%% Find the connections between C3D4 elements
```

```
% Initialize the connections
New_C3D4_connections = zeros(size(COH3D6_connected, 1), 2);

% Loop through each row in COH3D6_connected to find 1st C3D4 element
for m = 1:size(COH3D6_connected, 1)
    % Extract the values from columns 2 to 4 in the current row of
COH3D6_connected
    values_to_match = COH3D6_connected(m, 2:4);

    % Loop through each row in C3D4_total
    for n = 1:size(C3D4_total, 1)
        % Extract the values from columns 2 to 5 in the current row of
C3D4_total
        values_to_compare = C3D4_total(n, 2:5);

        % Check if there is an overlap
        if any(ismember(values_to_match, values_to_compare))
            % If there is an overlap, store the value from the first
column of C3D4_total
            New_C3D4_connections(m,1) = C3D4_total(n, 1);
            break;  % Exit the inner loop since a match is found
        end
    end
end

% Loop through each row in COH3D6_connected to find 2nd C3D4 element
for m = 1:size(COH3D6_connected, 1)
    % Extract the values from columns 5 to 7 in the current row of
COH3D6_connected
    values_to_match = COH3D6_connected(m, 5:7);

    % Loop through each row in C3D4_total
    for n = 1:size(C3D4_total, 1)
        % Extract the values from columns 2 to 5 in the current row of
C3D4_total
        values_to_compare = C3D4_total(n, 2:5);

        % Check if there is an overlap
        if any(ismember(values_to_match, values_to_compare))
            % If there is an overlap, store the value from the first
column of C3D4_total
            New_C3D4_connections(m,2) = C3D4_total(n, 1);
            break;  % Exit the inner loop since a match is found
        end
    end
end

% Create a matrix to save all fragments bigger than ?%
Fragments = {};
a = 1;

% Create a graph from the matrix
G = graph(New_C3D4_connections(:,1), New_C3D4_connections(:,2));

% Find connected components
connectedComponents = conncomp(G);

% Count elements in each connected component
```

```
componentCounts = histcounts(connectedComponents,
1:max(connectedComponents)+1);

% Calculate percentages and sum them up
totalPercentage = 0;

% Append "_DamageIndex" to the original FileName
%newFileName = strcat(FileName(1:end-4), '_DamageIndex.txt');  % Assuming
the file extension is always '.txt'
newFileName = strcat(FileName, '_DamageIndex.txt');  % Assuming the file
extension is always '.txt'

% Open the file for writing
fileID = fopen(newFileName, 'w');

fprintf(fileID, 'PARTICLE BREAKAGE INDEX\n\n');

fprintf(fileID, 'Damaged COH3D6 Nodes: %d\n', D);
fprintf(fileID, 'Undamaged COH3D6 Nodes: %d\n', uD);
fprintf(fileID, 'Damage Index based on COH3D6 Nodes: %.2f%%\n\n', D / (D
+ uD) * 100);

fprintf(fileID, 'Damaged COH3D6 Elements: %d\n', size(COH3D6_Damage,1));
fprintf(fileID, 'Undamaged COH3D6 Elements: %d\n',
size(COH3D6_connected,1));
fprintf(fileID, 'Damage Index based on COH3D6 Elements: %.2f%%\n\n',
size(COH3D6_Damage,1) / size(COH3D6_total,1) * 100);

fprintf(fileID, 'Connected Components and Percentages:\n\n');

for i = 1:max(connectedComponents)
    indices = find(connectedComponents == i);
    count = componentCounts(i);

    if count > 1
        percentage = count / (size(C3D4_total, 1)) * 100;
        totalPercentage = totalPercentage + percentage;
        fprintf(fileID, '%s connected components (%d elements): %.2f%%\n
(%s)\n\n', num2str(i), count, percentage, num2str(indices));

    else
        fprintf(fileID, '%s connected components (%d elements): %s\n\n',
num2str(i), count, num2str(indices));
    end

    % set the limit of minimum fragment size to 10% <-------------------
    if percentage >= 10

        Fragments{a} = indices;
        a = a+1;
    end

    percentage = 0;

end

% Display the total percentage
fprintf(fileID, '\nTotal Percentage of Break Elements: %.2f%%\n',
totalPercentage);
```

```
fprintf(fileID, '\nTotal Percentage of Smashed Elements: %.2f%%\n', 100 -
totalPercentage);

% Close the file
fclose(fileID);

disp(['Generate the ' newFileName]);

%% Create input files for selected fragments
Fragments_Nodes = {};
Fragments_C3D4 = {};
Fragments_COH3D6 = {};


% Find all C3D4 for each fragment
for x = 1:size(Fragments,2)

    C3D4_temp = [];

    for y = 1:size(Fragments{x},2)
        C3D4_temp(y,:)= C3D4_total(Fragments{x}(1,y),:);
    end

    Fragments_C3D4{x} = C3D4_temp;

end

% Find all Node's coordinates for each fragment
for x = 1:size(Fragments_C3D4,2)

    Nodes_temp = [];
    b = 1;

    for y = 1:size(Fragments_C3D4{x},1)
        for z = 2:5
        Nodes_temp(b,:)= Node_coordinates_new(Fragments_C3D4{x}(y,z),:);
        b = b+1;
        end
    end

    Fragments_Nodes{x} = Nodes_temp;

end

% Find all COH3D6_Connected with C3D4 infor
COH3D6_C3D4 = [COH3D6_connected,New_C3D4_connections];

% Find all COH3D6 for each fragment
for x = 1:size(Fragments,2)

    COH3D6_temp = [];
    c = 1;

    for y = 1:size(COH3D6_C3D4,2)

        % Find rows where both C3D4 in columns 8 and 9 of COH3D6_C3D4 are
members of Fragments
```

```
        COH3D6_temp = ismember(COH3D6_C3D4(:, 8), Fragments{x}) &
ismember(COH3D6_C3D4(:, 9), Fragments{x});
    end

    Fragments_COH3D6{x} = COH3D6_C3D4(COH3D6_temp,1:7);

end


% Read orignal input file to find nodes & C3D4 (where no CIEs involved)

% Select the input file
[FileName, FilePath] = uigetfile('*.*', 'Select the orignal INP before
adding CIEs file');
FilePathFileName = append(FilePath, FileName);

% Open the file for reading
fileID = fopen( FilePathFileName , 'r');

% Define the search pattern
search_pattern_3 = '*Node';
search_pattern_4 = '*Element, type=C3D4';

% Initialize variables
matching_lines_3 = {};
matching_lines_4 = {};
i=0;
Nodes_orignal = [];
C3D4_orignal = [];

% Get orignal Nodes
while ~feof(fileID)
    % Read the current line
    current_line = fgetl(fileID);

    % Check if the line contains the search pattern
    if contains(current_line, search_pattern_3)
        matching_lines_3{end+1} = current_line;

        next_line = fgetl(fileID);

        % Continue reading lines until a line containing '*' is
encountered
        while ~contains(next_line, '*')
            % Split values using commas
            values_str = strsplit(next_line, ',');

            % Convert string values to numerical values
            i=i+1;
            Nodes_orignal(i,1) = str2double(values_str{1});
            Nodes_orignal(i,2) = str2double(values_str{2});
            Nodes_orignal(i,3) = str2double(values_str{3});
            Nodes_orignal(i,4) = str2double(values_str{4});

            % Read the next line
            next_line = fgetl(fileID);
        end
    end
end
```

```
frewind(fileID);  % move to the beginning of the file

i=0;
% Get orignal C3D4
while ~feof(fileID)
    % Read the current line
    current_line = fgetl(fileID);

    % Check if the line contains the search pattern
    if contains(current_line, search_pattern_4)
        matching_lines_4{end+1} = current_line;

        next_line = fgetl(fileID);

        % Continue reading lines until a line containing '*' is
encountered
        while ~contains(next_line, '*')
            % Split values using commas
            values_str = strsplit(next_line, ',');

            % Convert string values to numerical values
            i=i+1;
            C3D4_orignal(i,1) = str2double(values_str{1});
            C3D4_orignal(i,2) = str2double(values_str{2});
            C3D4_orignal(i,3) = str2double(values_str{3});
            C3D4_orignal(i,4) = str2double(values_str{4});
            C3D4_orignal(i,5) = str2double(values_str{5});

            % Read the next line
            next_line = fgetl(fileID);
        end
    end
end


Fragments_Nodes_orignal = {};
Fragments_C3D4_orignal = {};

% Use the Fragments_C3D4 to find Fragments_C3D4_orignal
for x = 1:size(Fragments,2)

    d = 0;

    for y = 1:size(Fragments_C3D4{x},1)

        d = d+1;
        Fragments_C3D4_orignal{x}(d,1) =
C3D4_orignal(Fragments_C3D4{x}(y,1),1);
        Fragments_C3D4_orignal{x}(d,2) =
C3D4_orignal(Fragments_C3D4{x}(y,1),2);
        Fragments_C3D4_orignal{x}(d,3) =
C3D4_orignal(Fragments_C3D4{x}(y,1),3);
        Fragments_C3D4_orignal{x}(d,4) =
C3D4_orignal(Fragments_C3D4{x}(y,1),4);
        Fragments_C3D4_orignal{x}(d,5) =
C3D4_orignal(Fragments_C3D4{x}(y,1),5);

    end
```

```
end


% Use the Fragments_C3D4_orignal to find Fragments_Nodes_orignal
for x = 1:size(Fragments_C3D4_orignal,2)

    e = 0;

    Nodes_orignal_temp = [];
    Nodes_orignal_temp = Fragments_C3D4_orignal{x}(:,2:5);
    Nodes_orignal_temp = Nodes_orignal_temp(:);
    Nodes_orignal_temp = unique(Nodes_orignal_temp);
    Nodes_orignal_temp = sort(Nodes_orignal_temp);

    for y = 1:size(Nodes_orignal_temp,1)

        e = e+1;

        Fragments_Nodes_orignal{x}(e,1) =
Nodes_orignal(Nodes_orignal_temp(y,1),1);
        Fragments_Nodes_orignal{x}(e,2) =
Nodes_orignal(Nodes_orignal_temp(y,1),2);
        Fragments_Nodes_orignal{x}(e,3) =
Nodes_orignal(Nodes_orignal_temp(y,1),3);
        Fragments_Nodes_orignal{x}(e,4) =
Nodes_orignal(Nodes_orignal_temp(y,1),4);


    end

end


% Write INP for each Fragment
for x = 1:size(Fragments,2)

    % Assign "Fragment_x.inp" to the FileName
    newFileName = strcat('Fragment_', num2str(x), '.inp');  % Assuming
the file extension is always '.inp'

    % Open the file for writing
    fileID = fopen(newFileName, 'w');

    fprintf(fileID, '%s\n', '*Heading');
    fprintf(fileID, '%s\n%s\n', '**Generated by B.Zhang','**This is for
fragment analysis');
    fprintf(fileID, '%s\n', '**PARTS');
    fprintf(fileID, '%s%d\n', '*Part, name=Fragment_', x);

    % Print Nodes info
    fprintf(fileID, '%s\n', '*Node');

    for y1 = 1:size(Fragments_Nodes_orignal{x},1)
        fprintf(fileID, '%10d, %10.8f, %10.8f, %10.8f\n',
Fragments_Nodes_orignal{x}(y1,:));
    end

    % Print C3D4 info
```

```
    fprintf(fileID, '%s\n', '*Element, type=C3D4');

    for y2 = 1:size(Fragments_C3D4_orignal{x},1)
        fprintf(fileID, '%10d, %10d, %10d, %10d, %10d\n',
Fragments_C3D4_orignal{x}(y2,:));
    end


    fprintf(fileID, '%s\n', '*End Part');
    fclose(fileID);

    disp(['Generate the Fragment_' num2str(x) '.inp']);

end


disp('Done!');
```

Appendix C

This appendix presents the 21 silica sand particles and 21 crushed glass particles reconstructed from μCT images, which were analysed in Chapter 4, along with their morphological characteristics such as flatness (FL), elongation (EL), convexity (C), and sphericity (S).

Appendix C.1. Silica sand particles – mesh representation.

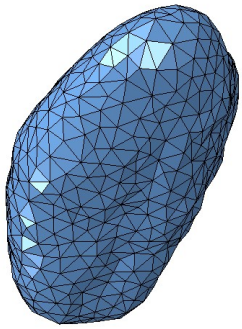		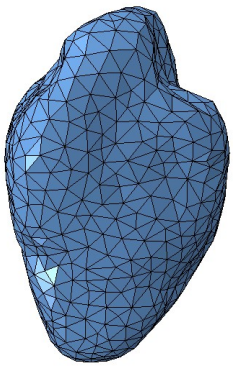		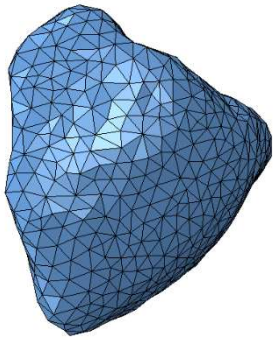	
FL: 0.212	C: 0.958	FL: 0.046	C: 0.953	FL: 0.178	C: 0.917
EL: 0.091	S: 0.892	EL: 0.216	S: 0.888	EL: 0.137	S: 0.815
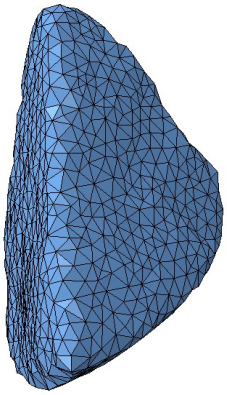		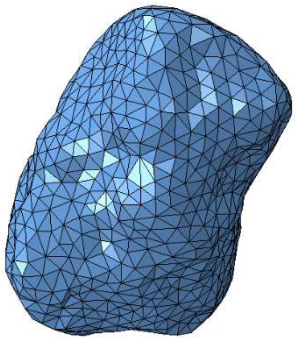		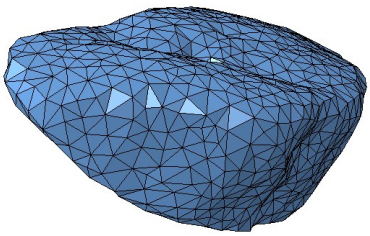	
FL: 0.009	C: 0.945	FL: 0.084	C: 0.916	FL: 0.198	C: 0.911
EL: 0.238	S: 0.793	EL: 0.197	S: 0.874	EL: 0.244	S: 0.799
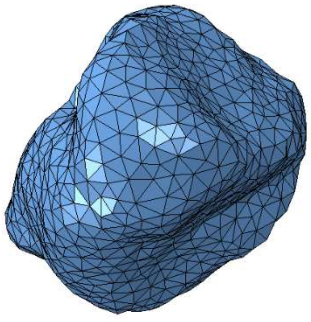		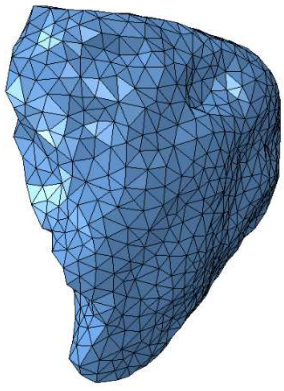		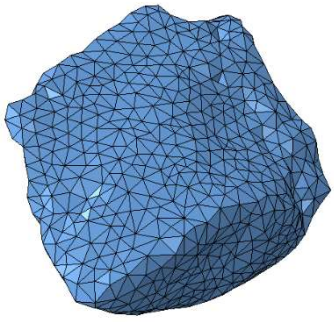	
FL: 0.069	C: 0.918	FL: 0.247	C: 0.899	FL: 0.343	C: 0.908
EL: 0.012	S: 0.875	EL: 0.043	S: 0.834	EL: 0.018	S: 0.763

Appendix C.2. Silica sand particles – mesh representation.

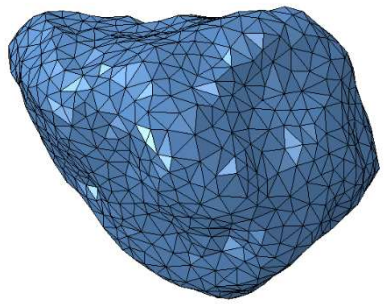		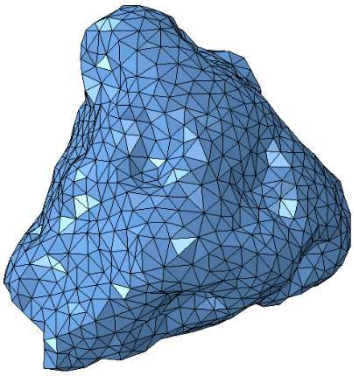		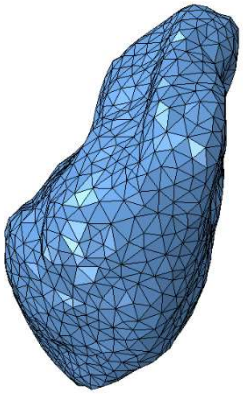	
FL: 0.154	C: 0.936	FL: 0.197	C: 0.829	FL: 0.005	C: 0.889
EL: 0.130	S: 0.867	EL: 0.045	S: 0.797	EL: 0.317	S: 0.824
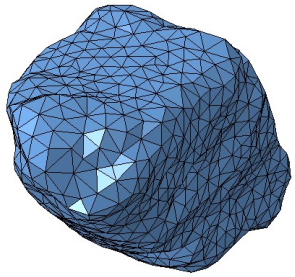		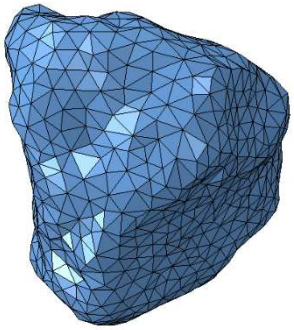		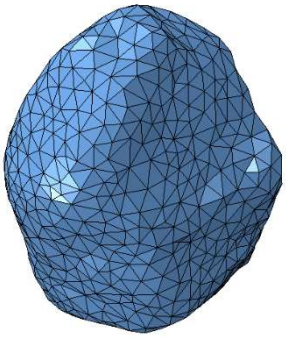	
FL: 0.017	C: 0.900	FL: 0.050	C: 0.919	FL: 0.030	C: 0.958
EL: 0.287	S: 0.832	EL: 0.098	S: 0.880	EL: 0.227	S: 0.910
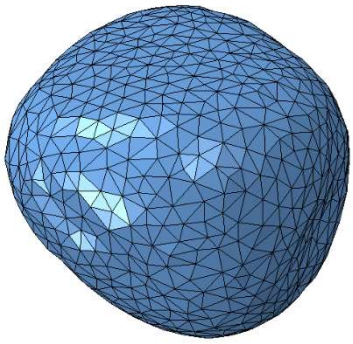		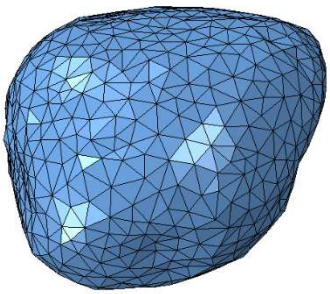		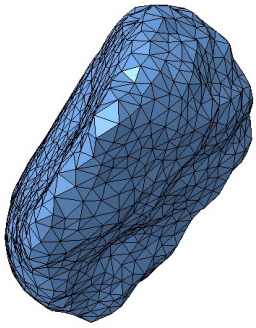	
FL: 0.032	C: 0.991	FL: 0.045	C: 0.983	FL: 0.162	C: 0.910
EL: 0.005	S: 0.957	EL: 0.038	S: 0.947	EL: 0.168	S: 0.810

Appendix C.3. Silica sand particles – mesh representation.

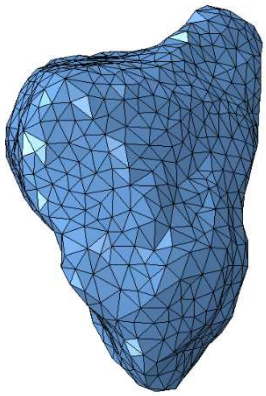		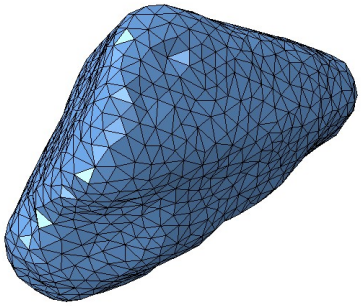		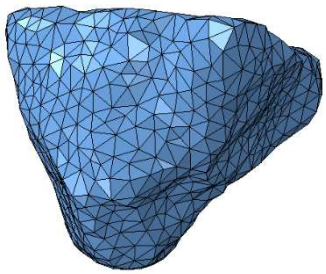	
FL: 0.098	C: 0.879	FL: 0.262	C: 0.937	FL: 0.082	C: 0.877
EL: 0.226	S: 0.825	EL: 0.101	S: 0.844	EL: 0.008	S: 0.830

Appendix C.4. Crushed glass particles – mesh representation.

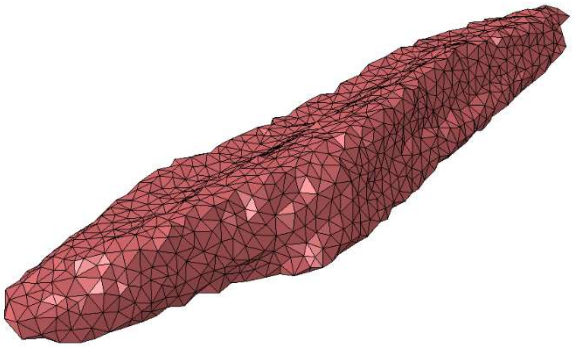		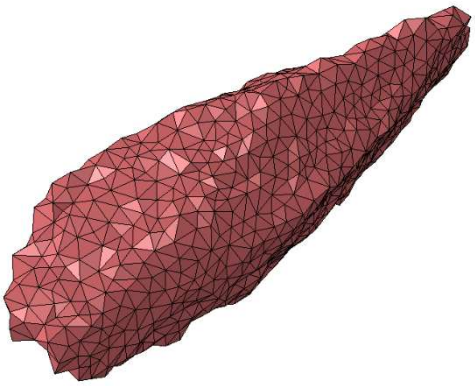	
FL: 0.162	C: 0.812	FL: 0.122	C: 0.865
EL: 0.601	S: 0.558	EL: 0.490	S: 0.657
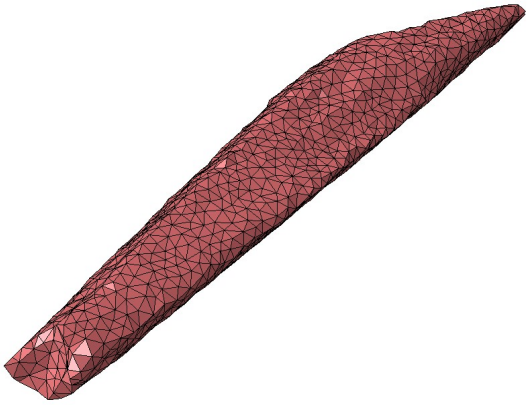		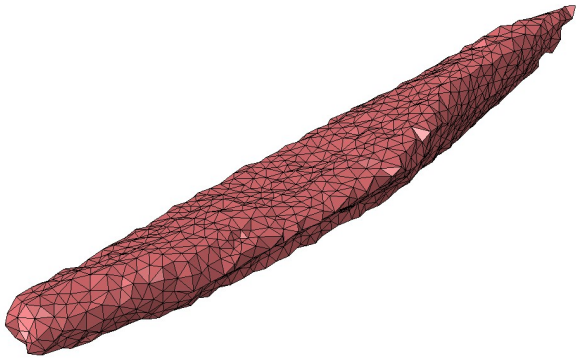	
FL: 0.113	C: 0.860	FL: 0.082	C: 0.784
EL: 0.718	S: 0.543	EL: 0.695	S: 0.548
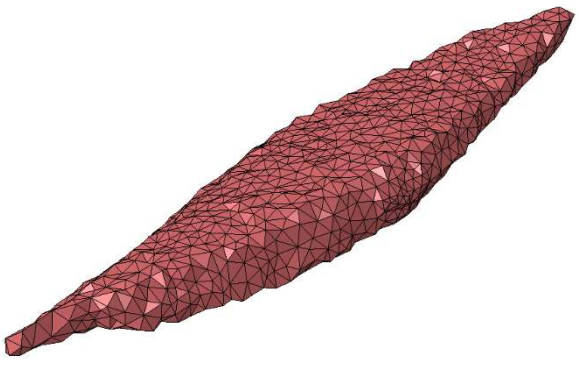		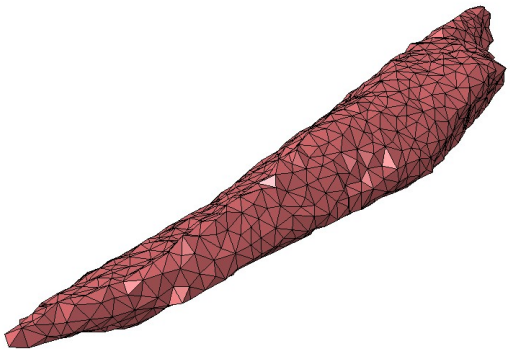	
FL: 0.218	C: 0.771	FL: 0.200	C: 0.809
EL: 0.582	S: 0.536	EL: 0.547	S: 0.577

Appendix C.5. Crushed glass particles – mesh representation.

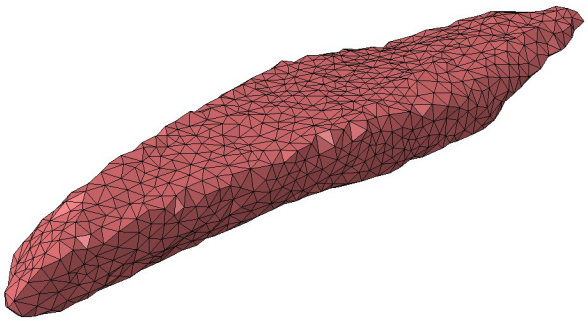		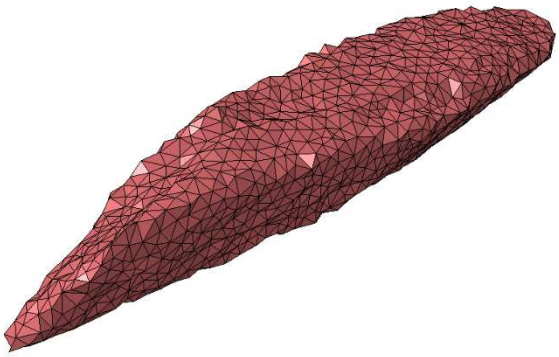	
FL: 0.215	C: 0.878	FL: 0.062	C: 0.817
EL: 0.559	S: 0.602	EL: 0.669	S: 0.579
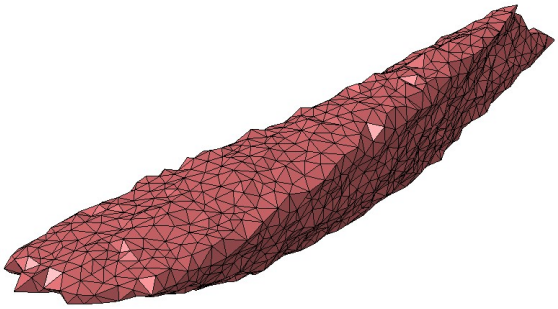		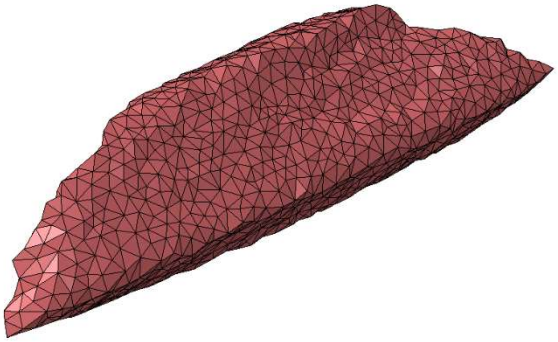	
FL: 0.053	C: 0.846	FL: 0.277	C: 0.869
EL: 0.654	S: 0.593	EL: 0.526	S: 0.582
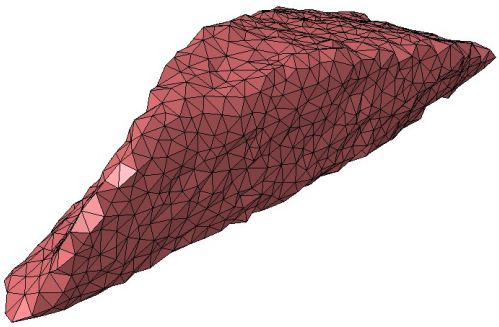		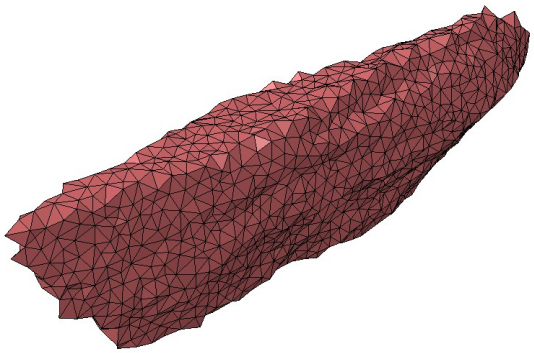	
FL: 0.008	C: 0.856	FL: 0.258	C: 0.812
EL: 0.569	S: 0.673	EL: 0.506	S: 0.543

Appendix C.6. Crushed glass particles – mesh representation.

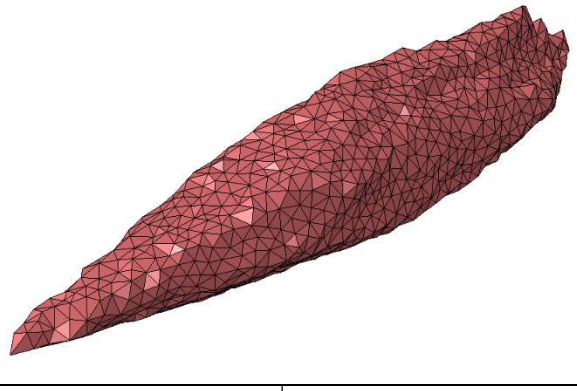		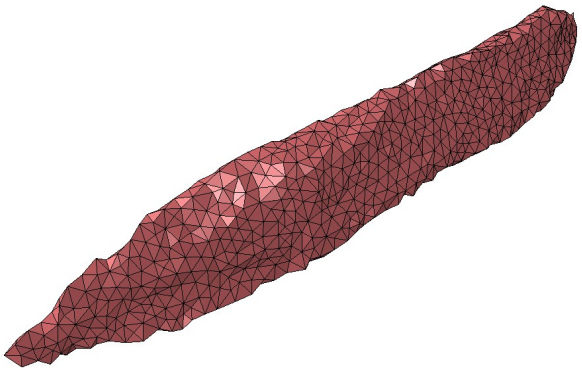	
FL: 0.055	C: 0.855	FL: 0.069	C: 0.833
EL: 0.669	S: 0.609	EL: 0.714	S: 0.558
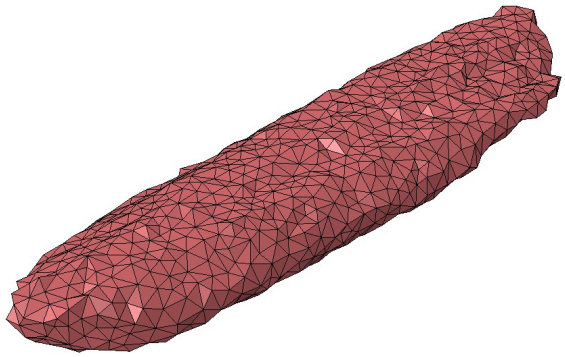		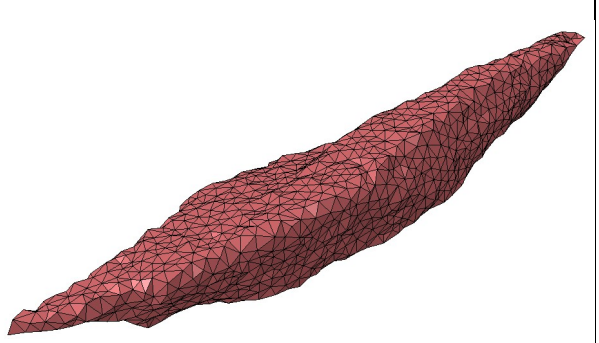	
FL: 0.149	C: 0.860	FL: 0.045	C: 0.813
EL: 0.587	S: 0.593	EL: 0.701	S: 0.582
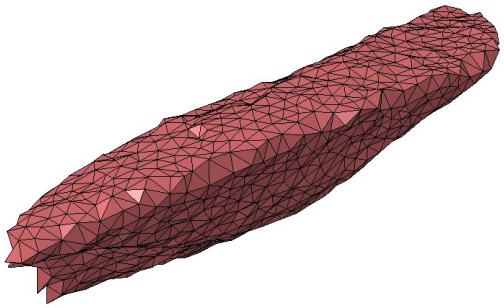		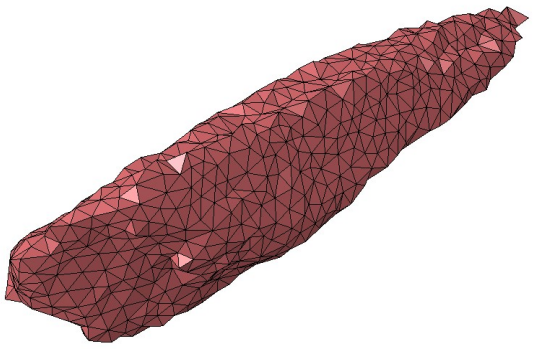	
FL: 0.196	C: 0.871	FL: 0.007	C: 0.864
EL: 0.457	S: 0.629	EL: 0.584	S: 0.653

Appendix C.7. Crushed glass particles – mesh representation.

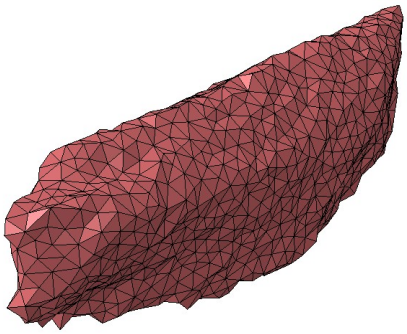		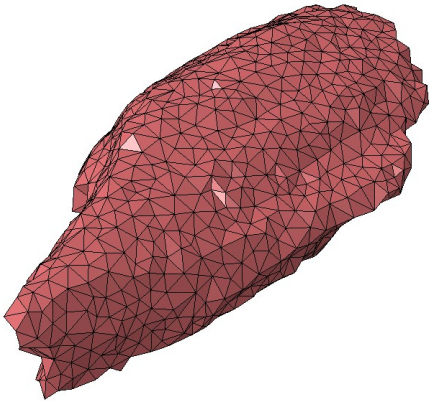	
FL: 0.173	C: 0.843	FL: 0.341	C: 0.854
EL: 0.469	S: 0.662	EL: 0.322	S: 0.670
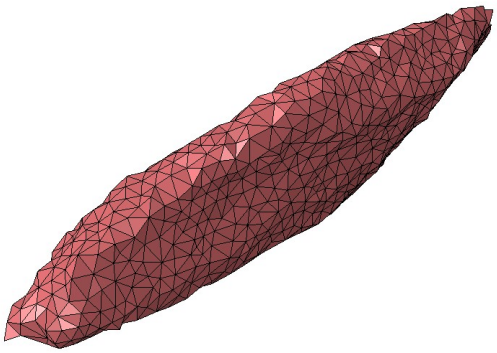			
FL: 0.200	C: 0.841		
EL: 0.510	S: 0.619		

Appendix D

This appendix provides a list of 37 representative rail surface profiles along with their corresponding roughness descriptors, as referenced in Chapter 5.

Profile ID	$R_a\ (\mu m)$	$R_q\ (\mu m)$	$R_{dq}\ (-)$	$R_{sk}\ (-)$	$R_{ku}\ (-)$
A-1	3.384	4.314	0.004	-0.119	3.662
A-2	9.037	12.092	0.011	-1.103	-1.103
B-1	20.228	25.399	0.019	-0.554	3.107
B-2	20.438	25.328	0.022	-0.563	3.058
B-3	20.279	25.595	0.019	-0.571	3.128
B-4	20.286	25.682	0.014	-0.584	3.181
B-5	20.229	25.267	0.019	-0.568	3.054
B-6	20.105	25.052	0.007	-0.554	2.998
B-7	19.858	24.672	0.013	-0.514	2.971
B-8	19.939	24.977	0.027	-0.606	3.025
B-9	19.758	24.804	0.018	-0.627	3.266
B-10	19.437	24.466	0.029	-0.742	3.688
B-11	19.795	24.765	0.018	-0.636	3.224
B-12	19.489	24.449	0.013	-0.626	3.247
B-13	19.406	24.243	0.018	-0.636	3.142
B-14	19.576	24.637	0.013	-0.623	3.220
B-15	19.510	24.260	0.018	-0.622	3.095
B-16	19.394	24.206	0.022	-0.699	3.220
B-17	19.224	24.113	0.013	-0.680	3.222
B-18	19.391	24.565	0.018	-0.659	3.235
B-19	19.557	24.488	0.013	-0.674	3.168
B-20	19.723	24.743	0.019	-0.612	3.067
B-21	19.592	24.569	0.013	-0.649	3.052
B-22	19.479	24.466	0.022	-0.617	2.971
B-23	19.470	24.397	0.018	-0.683	3.072
B-24	19.095	24.044	0.022	-0.620	2.972
B-25	19.314	24.064	0.018	-0.700	3.082
B-26	19.269	24.047	0.022	-0.668	3.016
B-27	19.073	23.836	0.017	-0.662	3.084
B-28	19.154	23.752	0.021	-0.675	3.065
B-29	19.011	23.797	0.017	-0.636	3.040
B-30	19.372	24.366	0.022	-0.741	3.156
B-31	19.340	24.307	0.017	-0.652	3.060
B-32	19.225	24.374	0.024	-0.735	3.046
B-33	19.075	23.889	0.021	-0.712	3.054
B-34	19.188	23.947	0.012	-0.664	3.041
B-35	19.008	23.763	0.018	-0.631	3.073